Institut für Erd- & Umweltwissenschaften
Mathematisch-Naturwissenschaftliche Fakultät
Universität Potsdam

Decadal changes in the snow regime of High Mountain Asia, 1987-2016

DISSERTATION

von

Taylor T. Smith

zur Erlangung des akademischen Grades

DOCTOR RERUM NATURALIUM
»Dr. rer. nat.«

in der Wissenschaftsdisziplin Fernerkundung

eingereicht an der
Mathematisch-Naturwissenschaftlichen Fakultät
der Universität Potsdam

Potsdam, September 2017

Abstract

More than a billion people rely on water from rivers sourced in High Mountain Asia (HMA), a significant portion of which is derived from snow and glacier melt. Rural communities are heavily dependent on the consistency of runoff, and are highly vulnerable to shifts in their local environment brought on by climate change. Despite this dependence, the impacts of climate change in HMA remain poorly constrained due to poor process understanding, complex terrain, and insufficiently dense in-situ measurements.

HMA's glaciers contain more frozen water than any region outside of the poles. Their extensive retreat is a highly visible and much studied marker of regional and global climate change. However, in many catchments, snow and snowmelt represent a much larger fraction of the yearly water budget than glacial meltwaters. Despite their importance, climate-related changes in HMA's snow resources have not been well studied.

Changes in the volume and distribution of snowpack have complex and extensive impacts on both local and global climates. Eurasian snow cover has been shown to impact the strength and direction of the Indian Summer Monsoon – which is responsible for much of the precipitation over the Indian Subcontinent – by modulating earth-surface heating. Shifts in the timing of snowmelt have been shown to limit the productivity of major rangelands, reduce streamflow, modify sediment transport, and impact the spread of vector-borne diseases. However, a large-scale regional study of climate impacts on snow resources had yet to be undertaken.

Passive Microwave (PM) remote sensing is a well-established empirical method of studying snow resources over large areas. Since 1987, there have been consistent daily global PM measurements which can be used to derive an estimate of snow depth, and hence snow-water equivalent (SWE) – the amount of water stored in snowpack. The SWE estimation algorithms were originally developed for flat and even terrain – such as the Russian and Canadian Arctic – and have rarely been used in complex terrain such as HMA.

This dissertation first examines factors present in HMA that could impact the reliability of SWE estimates. Forest cover, absolute snow depth, long-term average wind speeds, and hillslope angle were found to be the strongest controls on SWE measurement reliability. While forest density and snow depth are factors accounted for in modern SWE retrieval algorithms, wind speed and hillslope angle are not. Despite uncertainty in absolute SWE measurements and differences in the magnitude of SWE retrievals between sensors, single-instrument SWE time series were found to be internally consistent and suitable for trend analysis.

Building on this finding, this dissertation tracks changes in SWE across HMA using a statistical decomposition technique. An aggregate decrease in SWE was found (10.6 mm/yr), despite large spatial and seasonal heterogeneities. Winter SWE increased in almost half of HMA, despite general negative trends throughout the rest of the year. The elevation distribution of these negative trends indicates that while changes in SWE have likely impacted glaciers in the region, climate change impacts on these two pieces of the cryosphere are somewhat distinct.

Following the discussion of relative changes in SWE, this dissertation explores changes in the timing of the snowmelt season in HMA using a newly developed algorithm. The algorithm is shown to accurately track the onset and end of the snowmelt season (70% within 5 days of a control dataset, 89% within 10). Using a 29-year time series, changes in the onset, end, and duration of snowmelt are examined. While nearly the entirety of HMA has experienced an earlier end to the snowmelt season, large regions of HMA have seen a later start to the snowmelt season. Snowmelt periods have also decreased in almost all of HMA, indicating that the snowmelt season is generally shortening and ending earlier across HMA.

By examining shifts in both the spatio-temporal distribution of SWE and the timing of the snowmelt season across HMA, we provide a detailed accounting of changes in HMA's snow resources. The overall trend in HMA is towards less SWE storage and a shorter snowmelt season. However, long-term and regional trends conceal distinct seasonal, temporal, and spatial heterogeneity, indicating that changes in snow resources are strongly controlled by local climate and topography, and that inter-annual variability plays a significant role in HMA's snow regime.

ZUSAMMENFASSUNG

Mehr als eine Milliarde Menschen ist von Wasser aus Flüssen, welche im Hochgebirge Asiens (HA) abhängig. Diese werden, sich im Wesentlichen durch Schmelzwasser von Schnee und Gletschern gespeist. Gemeinden auf dem Land sind im hohem Maße auf die Beständigkeit des Wasserabflusses angewiesen, und folglich stark betroffen für durch Klimawandel hervorgerufene Veränderungen der Umwelt auf regionaler Ebene. Trotz dessen ist aufgrund mangelndem Prozessverständnisses, Terrainkomplexität und flächenhaft beschränkten In-situ-Messungen das Verständnis über den Einfluss des Klimawandels auf das HA begrenzt.

Die Gletscher des HA weisen mehr gefrorenes Wasser auf als alle anderen Regionen außerhalb des Nord- und Südpols. Der extensive Gletscherrückzug ist ein deutlich sichtbarer und weitgehend erforschter Marker für den Klimawandel auf regionaler und globaler Ebene. In vielen Einzugsgebieten machen jedoch Schnee und Schneeschmelzen einen sehr viel größeren Anteil des jährlichen Wasserbudgets aus als Gletscherschmelzwasser. Dennoch sind die klimaabhängigen Veränderungen auf Schneeressourcen im HA nicht ausreichend untersucht.

Veränderungen des Volumens und der Verteilung der Schneemasse hat komplexe und weitreichende Auswirkungen sowohl auf das regionale als auch auf das globale Klima. Es ist bekannt dass die eurasische von Schnee bedeckte Fläche die Erdoberflächenerwärmung verändert und somit einen Einfluss auf die Intensität und Ausrichtung des indischen Sommermonsuns hat, welcher wiederum die Hauptquelle für die Niederschlagswässer über dem indischen Subkontinent darstellt. Zeitliche Verschiebung der Schneeschmelze schränkt die Produktivität von Weidenländern ein, verringert die Abflussmengen, verändert den Sedimenttransport und beeinflusst die Ausbreitung von Vektorübertragenden Krankheiten. Trotz allem wurden über Klimafolgen auf Schneeressourcen noch keine weiträumigen regionalen Studien durchgeführt.

Passive Mikrowellenradiometer (PM) basierte Fernerkundung ist eine etablierte empirische Methode zur Untersuchung von Schneeressourcen in weit ausgedehnten Gebieten. Seit 1987 wurden täglich konsistente PM Messungen auf globaler Ebene durchgeführt, die zur Abschätzung der Schneehöhe verwendet werden können, und folglich den Anteil des Wassers in der Schneemasse wiederspiegeln – das Schneewasser Äquivalent (SWE). Algorithmen zur SWE Bestimmung wurden ursprünglich für flache und ebene Terrains wie die russische und kanadische Arktis entwickelt, und somit nur selten für komplexe Terrains wie das HA verwendet.

In dieser Studie werden Faktoren im HA untersucht, welche die Zuverlässigkeit des SWE Werte beeinflussen könnten. Bisher wurde angenommen, dass Waldbedeckung, absolute Schneehöhe, auf Langzeit betrachtete Durchschnittswindgeschwindigkeiten und Hangneigung die Hauptfaktoren darstellen, welche die SWE Messungen beeinflussen. In modernen Algorithmen zur SWE Bestimmung werde jedoch nur die Dichte der Waldbedeckung und die Schneehöhe als beeinflussende Faktoren eingesetzt. Trotz Unsicherheiten in absoluten SWE Messungen und sensorabhängigen Unterschieden in der Magnitude der Datenaufnahme, erwiesen sich SWE Zeitreihen der jeweilig einzelnen Messinstrumente als intern konsistent und adäquat für Trendanalysen.

Aufbauend auf diesen Ergebnissen werden in dieser Studie mit Hilfe von statistischen Dekompositionsverfahren die lokalen Veränderungen des SWE über dem gesamten HA untersucht. Trotz großer räumlicher und saisonaler Heterogenität, wurde eine Gesamtverringerung des SWE (10,6 mm/yr) festgestellt. Im Winter jedoch hat das SWE in etwa 50% des HAs trotz der negativen Trends im restlichen

Verlauf des Jahres zugenommen. Die Höhenverteilung der negativen Trends deutet darauf hin, dass Veränderungen im SWE sich nachweisbar auf die Gletscher in der Region auswirken. Die Auswirkung des Klimawandels auf die beiden Teile der Kryosphere ist jedoch jeweils etwas unterschiedlich.

Wie aus der Diskussion über die relativen Veränderungen im SWE hervorgeht, wird in dieser Studie mithilfe eines neuentwickelten Algorithmus der Veränderungen des zeitlichen Einsetzens der Schneeschmelzperiode im HA untersucht. Der Algorithmus zeigt eine hohe Genauigkeit in Bezug auf das Einsetzen und das Beenden der Schneeschmelze (70% innerhalb eines 5-tägigen Kontrolldatensatzes und 89% innerhalb eines 10-tägigen). Um Veränderungen im Beginn, Ende und Dauer der Schneeschmelze zu untersuchen wurde eine Zeitreihe, welche sich über 29 Jahre erstreckt, benutzt. Während im nahezu gesamten Gebiet des HA das Ende Schneeschmelzsaison verfrüht einsetzt, so ist in der Hälfte des Gebietes der Beginn dieser nach hinten verschoben. Die Schneeschmelzperioden haben im so gut wie gesamten Gebiet des HA abgenommen, was darauf hindeutet dass sich diese über dem gesamten HA generell verkürzt haben und frühzeitig beendet werden.

Durch die Untersuchung der räumlich-zeitlichen Verteilung des Schneevolumens und der Schneeschmelzperioden im gesamten HA konnten wir eine lückenlose Bilanz der Veränderungen der Schneeressourcen im HA erstellen. Der allgemeine Trend zeigt eine geringere Speicherung des SWE und kürzere Schneeschmelzperioden im gesamten HA. Langfristige und regionale Trends überdecken jedoch verschiedene saisonale, temporäre und räumliche Heterogenität, was wiederum zeigt dass Veränderungen der Schneebedeckung stark von lokalem Klima und der Topographie abhängen, und dass jährliche Schwankungen zu einem erheblichen Anteil zum Schneeregime des HA beitragen.

PUBLICATIONS AND AUTHOR CONTRIBUTIONS

This thesis is comprised of three independent studies published or in review in peer-reviewed journals. Individual studies are found in Chapters 4 to 6. One additional co-authored study is described in Appendix D.

Chapter 4 - Assessing uncertainty and sensor biases in passive microwave data across High Mountain Asia

Taylor Smith and Bodo Bookhagen

Both authors contributed to the design of the study. Taylor Smith processed and analyzed the data. Taylor Smith wrote the manuscript, with contributions from Bodo Bookhagen.
This study has been published in the peer-reviewed journal Remote Sensing of Environment:
Taylor Smith and Bodo Bookhagen. Assessing uncertainty and sensor biases in passive microwave data across High Mountain Asia. Remote Sensing of Environment, Volume 181, August 2016. Pages 174-185, ISSN 0034-4257, http://doi.org/10.1016/j.rse.2016.03.037.

Chapter 5 - Changes in seasonal snow-water equivalent distribution in High Mountain Asia, 1987-2009

Taylor Smith and Bodo Bookhagen

Taylor Smith and Bodo Bookhagen designed the study and contributed to the development of the methodology. Taylor Smith prepared and analyzed the data. Taylor Smith wrote the manuscript, with contributions from Bodo Bookhagen.
This article has been published at the peer-reviewed journal Science Advances:
Taylor Smith and Bodo Bookhagen. "Changes in seasonal snow water equivalent distribution in High Mountain Asia (1987 to 2009)", Science Advances 4: 1, (2018) http://doi.org/10.1126/sciadv.1701550.

Chapter 6 - Spatio-temporal Patterns of High Mountain Asia's Snowmelt Season Identified with an Automated Snowmelt Detection Algorithm, 1987-2016

Taylor Smith, Bodo Bookhagen, Aljoscha Rheinwalt

Taylor Smith and Bodo Bookhagen designed the study. All three authors contributed to the development of the methodology. Taylor Smith prepared and analyzed the data. Taylor Smith wrote the manuscript, with contributions from Bodo Bookhagen and Aljoscha Rheinwalt.
This article has been published at the peer-reviewed journal The Cryosphere:
Taylor Smith, Bodo Bookhagen, and Aljoscha Rheinwalt. "Spatio-temporal Patterns of High Mountain Asia's Snowmelt Season Identified with an Automated Snowmelt Detection Algorithm, 1987-2016". The Cryosphere 11 (2017): 2329-2343, https://doi.org/10.5194/tc-11-2329-2017.

Appendix D - Stable isotopes of modern surface waters show seasonal snowmelt amounts and identify moisture sources in the western Himalaya

Iris van der Veen, Hima J. Hassenruck-Gudipati, Taylor Smith, Eric Deal, Henry Wichura, Manfred R. Strecker, Bodo Bookhagen, Dirk Sachse

Taylor Smith provided the snow-water equivalent data and performed the regression analyses used throughout the publication.
This article is in review at a peer-reviewed journal.

ACKNOWLEDGMENTS

There is no one more deserving of thanks for this dissertation than Bodo Bookhagen. Thank you thank you thank you for the innumerable interesting discussions, your support through the last five years, and (of course) for bringing me with you to Germany. It has been an immensely stimulating experience to work with you over the course of this PhD, and I look forward to many future fruitful collaborations.

To my other co-authors, Aljoscha Rheinwalt and Forest Cannon, thank you for supporting the development of the publications that formed the core of my Masters and PhD work. It has been a pleasure working with you, and I hope to continue our interesting discussions into the future.

An immense thank you to Ben Purinton for being an adventure buddy and all-around support through my time in Berlin. Whether the discussion was scientific or otherwise, your feedback has been incredibly helpful. I would also like to thank Magda Patyniak for her help navigating German bureaucracy, and for providing a translation of the abstract in German.

Jessica Marter-Kenyon, your support through our time together in Santa Barbara and onwards has been invaluable. I look forward to finally getting around to publishing something together. To the rest of the Santa Barbara cohort – Kevin, Olaf, Daniel, Sarah, Kate, Nina, and co – thank you for helping me make it through two wonderful years in California.

Of course, I wouldn't have made it into and through this PhD without the support of past advisors. Peter Ryan, Ray Coish, Will Amidon, and Chris Condit, thank you for your support through my undergraduate career and beyond. It was a pleasure working together.

Finally, thank you to my family for instilling a love of science in me, and for supporting me through all of my adventures.

Contents

List of Figures

LIST OF TABLES

CHAPTER 1

Introduction and Motivation

Motivation

High Mountain Asia (HMA) provides food, water, and livelihoods for more than a billion people across a dozen countries. Both small and large communities are often highly dependent on the consistency of their local and regional climates; many lack the resources to respond to changes in the environment – especially to changes in their water resources.

Recent work has noted substantial changes in HMA's climate system, including increased temperatures (Vaughan et al., 2013), increased storm intensity (Singh et al., 2014; Yao et al., 2012; Bookhagen and Burbank, 2010; Malik et al., 2016; Fu, 2003; Palazzi et al., 2013), changes in the Indian Summer Monsoon (ISM) (Gautam et al., 2009; Menon et al., 2013; Kitoh et al., 2013), intensification of the Winter Westerly Disturbances (WWD) (Cannon et al., 2014, 2015), and substantial changes in glaciers throughout the region (Bolch et al., 2012; Kääb et al., 2012, 2015; Gardner et al., 2013; Kapnick et al., 2014; Yao et al., 2012; Scherler et al., 2011; Gardelle et al., 2012; Frey et al., 2014; Spiess et al., 2016). Many of these changes remain poorly understood due to lack of in-situ or empirical observation data in many areas. Satellite datasets, such as the Tropical Rainfall Measuring Mission (TRMM) (Huffman et al., 2007) and the Gravity Recovery and Climate Experiment (GRACE) (Tapley et al., 2004), and modeling efforts, such as High Asia Refined Analysis (HAR) (Maussion et al., 2014) and Asian Precipitation - Highly-Resolved Observational Data Integration Towards Evaluation (APHRODITE) (Yatagai et al., 2012), rarely agree on the magnitude and direction of changes in temperature and precipitation (Malik et al., 2016), and have trouble correctly quantifying high-elevation precipitation (Li et al., 2017; Immerzeel et al., 2015). Due to underdeveloped meteorological and hydrologic sensor networks in the region, quantification of these changes is still difficult (Sorg et al., 2012; Bookhagen and Burbank, 2010). Poor understanding of the interactions of major climate systems in HMA leads to disagreements in climate projections in global and regional models (Vaughan et al., 2013; Kapnick et al., 2014). Despite these caveats, reliance on interpolated weather station data and large-scale climate models is still high, and studies leveraging empirical data over large spatial scales are still scarce (Maussion et al., 2014; Kapnick et al., 2014).

Shrinking glaciers are a highly visible signal of climate change in HMA's cryosphere, and have been a particular focus of the climate research community (e.g., Cuffey and Paterson, 2010; Bolch et al., 2012; Kääb et al., 2012, 2015; Gardner et al., 2013; Immerzeel et al., 2010, 2013). Water stored in glaciers and seasonal snowpack is the primary source of household, agricultural, and industrial water in many parts of HMA – particularly for those communities situated at high elevations. Historically, water has been slowly released from snow and glaciers throughout the spring and summer, providing year-round water to both high-elevation and downstream communities. However, recent shifts in the climate regime of HMA have reduced the reliability of the yearly hydrological cycle. Many regions have seen increases in early season runoff alongside drastic decreases in late season runoff – particularly in those regions where glaciers have substantially retreated or disappeared. The Intergovernmental Panel on Climate Change (IPCC) forecasts that runoff in major river basins of HMA will increase through 2100 as glaciers continue to melt, and then drop off as glaciers disappear (Vaughan et al., 2013). However, these large-scale changes conceal regional, small-scale, and seasonal variation in climate change impacts which are already being felt in the region.

HMA's climate, and indeed the global climate, is strongly impacted by Eurasian snow cover (Bulygina et al., 2011; Vaughan et al., 2013; Hahn and Shukla, 1976; Bamzai and Shukla, 1999; Barnett et al., 1989). Changes in the distribution, timing, and volume of snow can modulate earth-surface heating and cooling, which is one of the primary drivers of major atmospheric weather systems, such as the ISM. As the ISM is the primary moisture source for much of the Indian Subcontinent, changes in the ISM are felt by hundreds of millions of people. Shifts in snow volume and snowmelt timing can also have significant impacts on the natural environment. For example, snowmelt changes can modify the timing of ephemeral wetlands, which are essential for many migratory species (Bookhagen, 2017), reduce the productivity of major rangelands by changing the length and timing of the growing season (Xu et al., 2009), and modify sediment transport in rivers (Wulf et al., 2012; Valentin et al., 2008), which in turn impacts water quality for human use (Palmer et al., 2008) and local fauna (Ficke et al., 2007).

Snow is the primary water reservoir for many communities in HMA, and provides more than 50% of the water budgets of many catchments (Bookhagen and Burbank, 2010; Shrestha et al., 2015; Huss et al., 2017). Snowpack is also highly responsive to warming climates, as it is present at low elevations and over wide areas. Small increases in temperature can drastically alter the hydrologic budget of a catchment by shifting precipitation events from snow to rain, which has been shown to reduce streamflow in snow-fed catchments (Berghuijs et al., 2014), and increase flooding from rain-on-snow events (Sturm et al., 2017). Snowmelt is particularly important in the summer months, when precipitation is low in many areas of HMA. Without the seasonal buffering capacity of snow-water storage, many communities would face periodic droughts. Even small changes in the timing of snowmelt can have drastic impacts on the planting and harvest seasons of important crops (Singh et al., 2011), growth patterns of grasses important for pastoral communities (Xu et al., 2009), the spread of vector-borne diseases (Githeko et al., 2000; Patz et al., 2005), and household food security (Lioubimtseva and Henebry, 2009; Singh et al., 2011). A shortening of the snowmelt season has already been observed in Central Asia (Dietz et al., 2014), the Himalaya (Lau et al., 2010; Panday et al., 2011), and the Upper Indus (Hasson et al., 2014).

Often, the communities that are most strongly impacted by climate change are those who are the least able to adapt to rapid changes in their environment (Vaughan et al., 2013). The dearth of quantitative data on climate changes and climate impacts in HMA severely limits the efficacy of local, regional, and global adaptation and mitigation efforts; changes in the spatial and temporal distribution of snow – as well as changes in the timing and length of the snowmelt season – are poorly constrained in HMA. The quantification of these changes is essential for long-term regional water planning, climate modeling, weather forecasting, and for contextualizing smaller-scale studies throughout HMA.

Objectives

This dissertation seeks to expand on methodologies for tracking snow dynamics from space, as well as to quantify recent changes in the snow regime of HMA. Passive microwave remote sensing data was chosen as the primary data source in this dissertation due to temporal and geographic extent of these data, which allow for regional and long-term assessments of changes in snow. The three primary research questions that this dissertation addresses are:

- What topographic, land-cover, and climate factors impact passive microwave snow-water equivalent estimations in the complex topography of HMA?
- What are the spatio-temporal patterns of recent changes in the distribution of snow-water storage across HMA?
- Have rising regional temperatures impacted the timing and duration of the snowmelt season in HMA?

This work has resulted in two published peer-reviewed journal articles and one additional article which is in review at the time of this dissertation's submission.

Outline

This dissertation begins with a general introduction to passive microwave remote sensing theory and algorithms (Chapter 2) and an overview of the geography and climate of the study area (Chapter 3). Chapters 4 through 6 then approach the individual research questions of this dissertation as independent studies published in peer-reviewed journals. Chapter 4 (research question 1) has been published under the title *"Assessing uncertainty and sensor biases in passive microwave data across High Mountain Asia"* by T. Smith and B. Bookhagen in the journal Remote Sensing of Environment (http://doi.org/10.1016/j.rse.2016.03.037). Chapter 5 (research question 2) has been published under the title *"Changes in seasonal snow water equivalent distribution in High Mountain Asia (1987 to 2009)"* by T. Smith and B. Bookhagen in the journal Science Advances (http://doi.org/10.1126/sciadv.1701550). Chapter 6 (research question 3) has been published with the title *"Spatio-temporal Patterns of High Mountain Asia's Snowmelt Season Identified with an Automated Snowmelt Detection Algorithm, 1987-2016"* by T. Smith, B. Bookhagen, and A. Rheinwalt in the journal The Cryosphere (https://doi.org/10.5194/tc-11-2329-2017). Chapter 7 contextualizes this dissertation work in the wider context of ongoing studies in HMA and provides concluding remarks.

CHAPTER 2

Passive Microwave Remote Sensing

Passive microwave (PM) data have been consistently used to estimate snow-water equivalent (SWE) from space since the launch of the Scanning Multichannel Microwave Radiometer (SMMR) satellite in 1978 (Chang et al., 1987; Derksen et al., 2004; Knowles et al., 2002). While the SMMR mission only collected data every other day, it demonstrated that the water content of snowpack could be estimated from space. It also demonstrated several important differences between PM and optical snow data retrieval. PM data penetrates clouds, can collect data at night, and is highly sensitive to the water content of the snowpack. This allows for consistent estimation of SWE, even in heavily cloud-covered areas, and is particularly important where winter cloud cover can be temporally and spatially extensive, such as in many parts of HMA.

Passive Microwave Instruments

Several subsequent satellite missions have included PM sensors, including the Special Sensor Microwave/Imager (SSMI, 1987-2009) (Wentz, 2013), Special Sensor Microwave Imager/Sounder (SSMIS, 2003-present) (Sun and Weng, 2008), Advanced Microwave Scanning Radiometer – Earth Observing System (AMSR-E, 2002-2011) (Ashcroft and Wentz, 2013), AMSR2 (2012-present) (Imaoka et al., 2010), Tropical Rainfall Measuring Mission (TRMM, 1997-2015) (Huffman et al., 2007) and the Global Precipitation Measurement Core Observatory (GPM, 2014-present) (GPM Science Team, 2014). Each of these sensors, by directly measuring the intensity of natural microwave radiation being emitted from the earth (Wentz, 1997), can be used to make estimates of snow depth and SWE at daily or sub-daily timesteps.

Special Sensor Microwave/Imager

The first SSMI sensor was launched aboard Defense Meteorological Satellite Program (DMSP) satellite F08 in June 1987, and has subsequently been flown on five other DMSP satellites (1987-present) (Hollinger et al., 1987; Wentz, 1997, 2013). SSMI collects data at four frequencies (19.35, 22.235, 37, and 85.5 GHz), in both vertical and horizontal polarizations – excepting the 22.235 GHz channel which only collects vertically polarized data. The DMSP satellites fly at an altitude of 860 ± 25 km, with an earth incidence angle of 53.1° and a scan angle range of ± 51.2° (Wentz, 1997; Smith and Bookhagen, 2016). This instrument setup allows data to be collected in a swath 1,400 km wide on the earth's surface, with sample spacing of 25 km for the 19.33, 22.235, and 37 GHz channels and 12.5 km for the 85.5 GHz channel. The SSMI series of satellites have overlapped in time, allowing for rigorous cross-calibration (Wentz, 2013). The SSMI sensor was not explicitly designed for snow measurement (Kelly et al., 2003); it lacks a low frequency (~10 GHz) channel, making estimating SWE in deep snow or in forested areas difficult. However, SSMI represents the longest single-instrument PM time series, which makes it the most suitable of the PM sensors discussed here for long-term studies of snow character.

Special Sensor Microwave Imager/Sounder

The first DMSP to carry SSMIS (F16) was launched in October 2003, and has been followed by three subsequent sensors (Smith and Bookhagen, 2016). The same frequency sensors are carried on the SSMIS as on the SSMI, excepting the 85.5 GHz channel which was replaced by a new 91.655 GHz channel, at both vertical and horizontal polarizations. SSMIS also includes several other channels which are not used for measuring snow properties – namely channels between 50 and 60 GHz for measuring atmospheric properties and 183.31 GHz channels for measuring tropospheric water (Sun and Weng, 2008). The scan angle was increased to ± 71.6°, while maintaining the same earth incidence angle of 53.1°. This increased the nominal swath width to 1707 km. As with SSMI, SSMIS is missing a low frequency channel which somewhat limits its utility for estimating SWE in forested or deep snow areas.

Several studies have focused on the inter-calibration of SSMI and SSMIS data, which were shown to exhibit slight differences both between satellites (ie, SSMI F08 to SSMI F11) and between instruments (ie, SSMI to SSMIS) (Cavalieri et al., 2012; Dai and Che, 2009; Dai et al., 2015). These satellite data retrieval differences, while slight, can have significant impacts on estimates of earth-surface environmental parameters. Inter-calibration concerns are discussed separately in each Chapter of this thesis, as different approaches to managing sensor biases are appropriate for different contexts.

Advanced Microwave Scanning Radiometer – Earth Observing System

AMSR-E was launched on May 4th, 2002, onboard the Aqua satellite (Kelly et al., 2003). It collects data at the 6.9, 10.65, 18.7, 23.8, 36.5, and 89.0 GHz channels, in both vertical and horizontal polarizations (again excepting the 23.8 channel which is only collected in vertical polarization). Aqua flies at an altitude of 705 km, allowing AMSR-E to collect data over a 1445 km swath (scan angle range ±61°) at an incidence angle of 55°, with a slightly improved spatial resolution over the SSMI series of sensors (Kelly et al., 2003). It ceased collecting data on October 4th, 2011. The near-polar orbit of AMSR-E allows it to sample nearly the entire earth twice each day (once at night and once during the day). The AMSR-E sensor measures a low frequency channel (10.65 GHz) which allows for better characterization of deep snow and snow in forested areas than the SSMI series of sensors.

Advanced Microwave Scanning Radiometer 2

AMSR2 has measured the same set of frequency bands as AMSR-E (and additionally the horizontally polarized 23.8 GHz channel), and is flown on the Japanese satellite GCOM-W1 (Imaoka et al., 2010). It also measures an additional 7.3 GHz channel at both vertical and horizontal polarizations. The instrument is otherwise almost identical to that flown on Aqua to maintain data continuity between the sensors. It was launched on May 18, 2012 and, at the time of the publication of this dissertation, is still in operation.

Global Precipitation Measurement

The GPM Core Observatory satellite was launched on February 27th, 2014 and is still in operation. It collects PM data at the 10.65, 18.7, 23.8, 36.5, 89, 166, and 183.31 GHz channels, in both vertical and horizontal polarization (excepting the 23.8 and 183.31 channels which are only collected in vertical polarization). While earlier sensors (SSMI, SSMIS, AMSR-E, AMSR2) all fly in polar orbits, GPM flies in an inclined, circular, non-sun-synchronous orbit (65° to the equator) at 407 km, providing a 904 km swath. The different orbit reflects divergent mission design parameters for GPM, which is primarily a precipitation mission. GPM has an earth incidence angle of 52.8°, with a scan angle range of $\pm 70°$. While the orbit parameters differ from those of the previous PM sensors, it still collects daily or pseudo-daily data for the study area of this dissertation, although at a less consistent temporal resolution than the other sensors.

Tropical Rainfall Measurement Mission

The TRMM satellite, which flew from 1997 to 2015, was also not explicitly designed to measure earth-surface parameters. However, it collected PM data at the 10.7, 19.4, 21.3, 37, and 85.5 GHz channels. As TRMM flew at 402 km, it boasted a higher spatial resolution over its 878 km swath width. Unfortunately, tests conducted during the compilation of Chapter 4 of this dissertation found that TRMM data – and in particular the 37 GHz channel – is not reliable for SWE estimation.

Passive Microwave Snow Measurement Theory

The PM data collected by the sensors listed in the previous Section can be used to estimate ground-surface properties, including snow depth. PM radiation measured at the satellite is referred to as 'brightness temperature' (Tb). In general, the radiation observed at the satellite can be characterized as:

$$Tb = (RT_{sky} + (1 - R)T_{surf})e^{-t} + T_{atm} \tag{2.1}$$

where t is the atmospheric transmissivity, R is the surface reflectivity, T_{sky} is the sky radiation, T_{surf} is the surface emission, and T_{atm} is the atmospheric component (Kelly, 2009). Both the sky and atmospheric components are small and can generally be omitted, leaving Tb directly related to surface features if atmospheric transmissivity is assumed to be close to one (Kelly, 2009). At long wavelengths (below ~20 GHz), microwave radiation is thought to penetrate snowpack with little scattering. At shorter wavelengths, snowpack acts as a volume scatterer which attenuates the passive microwave signal (Ulaby and Stiles, 1980). Thus, the relationship between the attenuated and unattenuated PM signals can be used to derive information about snowpack. However, several assumptions about the snowpack must be made in order to estimate snow depth and snow-water content.

Physically, dry snow can be considered as ice suspended in an air matrix. In dry snow, the primary mechanism of PM attenuation is volumetric scattering by the ice crystals which interact with microwave radiation emitted from the earth's surface, and thus cause some PM frequencies to be attenuated on their path towards the PM sensor (Tedesco et al., 2015; Tedesco, 2015). Wet snow is better characterized as a mixture of ice and liquid water (Tedesco, 2015). As the liquid water content of the snowpack increases, it absorbs the PM radiation emitted from the earth's surface, which means that the measured Tb at the satellite is emitted from the top of the liquid water layer as opposed to from the earth's surface (Fig. 2.1), and the depth of the snowpack can no longer be estimated (Tedesco et al., 2015). The change from scattering to absorption drastically increases the measured Tb at the PM sensor, and thus PM SWE estimates are based on the assumption of dry snow.

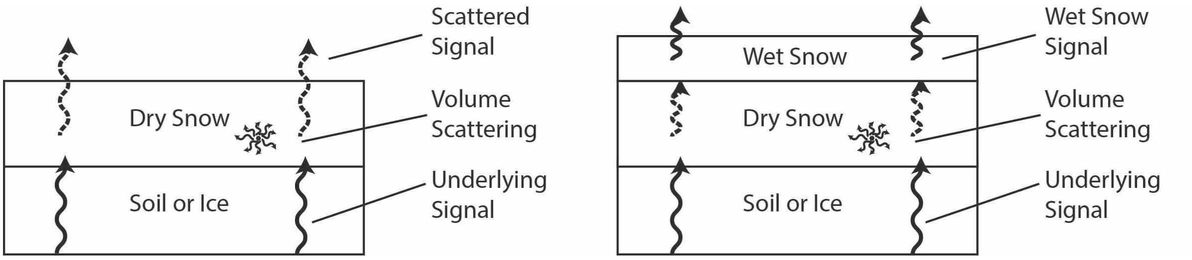

Figure 2.1 – Scattering behavior of wet and dry snow. Wet snow absorbs the underlying PM signal and emits a separate PM signal. Adapted from Tedesco et al. (2015).

The basic premise of PM SWE estimates is that the difference between a scattering (high frequency) and non-scattering (low frequency) signal is correlated with the depth of the scattering medium – in this case dry snow. Thus, as snow depth increases, so should the difference between the scattering and non-scattering PM frequencies. However, depth is not the only factor that impacts the scattering character of snowpack, and it is often impossible to determine whether a change in observed Tb is due to changes in snow depth or changes in the snowpack's physical structure. Changes in snow density and snowpack metamorphism are thus two of the largest sources of error in PM SWE estimation (Kelly et al., 2003).

Snow depth (number of snow grains along PM emission path), the size of the snow grains, and the density of the snowpack (how much of the snowpack volume is air) are thought to be the most important factors influencing high-frequency (~37 GHz) measurements (Kelly et al., 2003). To a lesser extent, sub-snow ground properties (e.g., surface roughness, surface temperature, and soil moisture) and snow temperature can influence Tb measurements (Hoekstra and Delaney, 1974). However, these factors are generally accounted for by using the difference between two PM frequencies for SWE estimation, and should not have outsized impacts on SWE estimation in this dissertation.

Many models theoretically relating snow properties to electromagnetic properties (e.g., Tb) make assumptions about snow grain homogeneity, snow-layer interfaces, and how spherical snow grains are in a given snowpack (e.g., Chang et al., 1976, 1982; Tedesco and Kim, 2006). These assumptions can lead to distinctly different interpretations of snowpack character between different models. Snow physical character – layering, grain size, and density – can change throughout a single PM pixel (~25 sq km) and through time. Thus, while modeling approaches help provide a basis for satellite-based PM SWE estimation, it is difficult to scale up these small-scale models to real world applications.

Throughout a snow season, the stratigraphy, density, and grain size of snow will change, with corresponding changes in measured Tb (Armstrong et al., 1993; Josberger and Mognard, 2002; DeWalle and Rango, 2008). The magnitude and character of these changes will be highly spatially and temporally variable, especially in the context of the complex topography of HMA. In HMA, some of the most important snowpack changes are compaction, the formation of depth hoar, and the formation of ice lenses. Compaction occurs naturally when new snow falls or as snow settles after deposition. Compaction can change snowpack stratigraphy by creating interfaces between distinct snow layers and by increasing snow density. Both compaction and stratigraphy have been shown to influence measured Tb at satellite sensors (e.g., Chang et al., 1987; Tedesco and Kim, 2006).

Depth hoar, or large, faceted snow crystals (Fig. 2.2), often forms throughout the snow season in the presence of temperature gradients within the snowpack which cause water vapor to be deposited on cold snow grains (Armstrong et al., 1993; Josberger and Mognard, 2002; Koenig and Forster, 2004; DeWalle and Rango, 2008). As depth hoar can be several times the size of the typical snow crystal, its interaction with PM radiation is substantially different and it can modify measured Tb significantly (Armstrong et al., 1993; Josberger and Mognard, 2002). Similarly, ice lenses – formed due to partial melt and refreezing of the snowpack or rain-on-snow events – impact PM measurements by changing the size and shape of PM scatterers in the snowpack and by acting as absorbers and reflectors rather than scatterers of PM radiation (Rees et al., 2010; Montpetit et al., 2013).

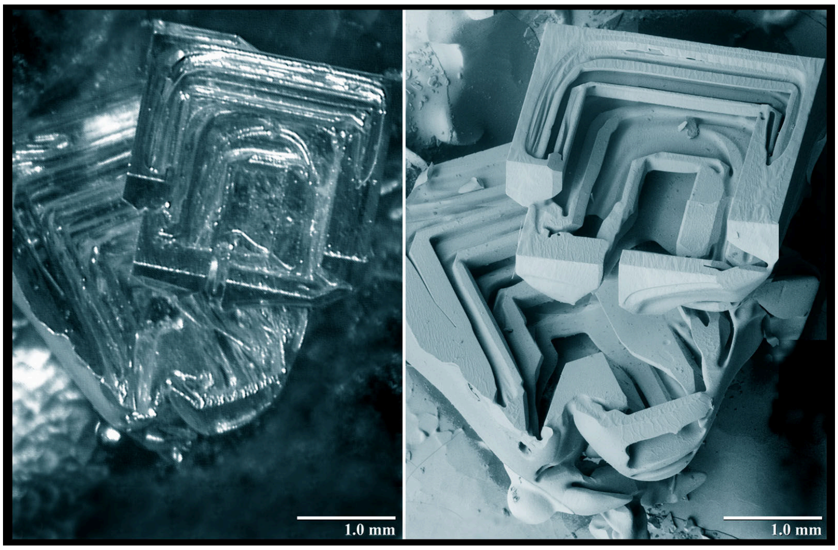

Figure 2.2 – Depth hoar as shown by visible light and scanning electron microscopy (courtesy Beltsville Agricultural Research Center Electron and Confocal Microscopy Unit). Depth hoar crystals are significantly larger than typical snow crystals, and thus their presence can substantially modify Tb measurements by satellite radiometers.

Each PM sensor collects data in both horizontal and vertical polarizations. Tb values at the two polarizations are often different, depending on the character of the snowpack (Rango et al., 1979; Mätzler, 1987, 1994; Foster et al., 2005). For the estimation of SWE, vertical polarization is generally used as it is slightly less sensitive to snowpack stratigraphy, more sensitive to snow depth, and more directly related to the upwelling radiation from the ground surface (Grody, 1991; Kelly et al., 2003). However, SWE estimates based on horizontal and vertical polarizations are similar, as SWE estimation techniques use the relative difference between two frequencies of the same polarization (Kelly et al., 2003). Snowmelt identification often uses a combination of horizontal and vertical polarizations (e.g., Abdalati and Steffen, 1995) which takes advantage of the depolarization of snow as it transitions to water, changes in the structure of the snowpack, and the formation of horizontal water layers at or near the top of snowpack.

While the processes behind snowpack metamorphism are understood theoretically and at a small scale (e.g., Tsang et al., 1985, 2000; Armstrong et al., 1993; Tedesco and Kim, 2006; Montpetit et al., 2013), scaling these models to match the resolution of a single PM pixel (~25 sq km) or applying them rigorously to global SWE estimates is impractical. Despite these problems, PM SWE estimates remain one of the most important sources of information on snowpack globally.

Utility of Passive Microwave Frequencies

Each sensor mentioned above carries a similar but unique set of frequencies. Each of these frequencies serves a distinct purpose, and is known to interact with snowpack in different ways.

The 6.93 GHz channel carried on AMSR-E and AMSR2 is used in some soil moisture algorithms (Njoku et al., 2003; Wang and Qu, 2009), but is known to be contaminated by radio frequencies, particularly in built-up and urban areas (Kelly, 2009) and is not used in modern SWE algorithms.

The ~10 and ~18 GHz channels are generally used as the un-attenuated signal in PM SWE algorithms. While snowpack does cause some attenuation of the PM signal at these frequencies (Smith and Bookhagen, 2016; Kelly, 2009), for medium (5 - 100 cm) snow depths, they are assumed to be interference-free. The attenuation of the ~36 GHz channel is known to interact pseudo-linearly with the depth of the snowpack (excepting caveats mentioned in the previous Section), and is thus used in SWE estimation algorithms.

The ~89 GHz channel is not sensitive to snow when SWE is greater than 20 mm. Its main utility is in detecting shallow snow in conjunction with the ~22 GHz channel which is sensitive to water vapor in the atmosphere (Kelly, 2009). The higher frequency channels carried on GPM are used for weather and precipitation characterization and are not used for SWE estimation.

Snow-Water Equivalent Algorithm Development

The initial algorithms for estimating SWE from PM data were developed by Chang et al. (1982, 1987), and have been improved over the course of the last 30 years (e.g., Grody, 1991; Sturm et al., 1995; Kelly et al., 2003; Kelly, 2009; Derksen, 2008; Armstrong and Brodzik, 2002; Takala et al., 2011; Tedesco and Narvekar, 2010; Cordisco et al., 2006; Andreadis and Lettenmaier, 2012). The algorithms are based on exploiting the difference between the brightness temperatures (Tb) at the ~18 and ~36 GHz channels of each PM sensor, such as in the original Chang equation (Chang et al., 1987):

$$SnowDepth = 1.59 * (Tb_{18H} - Tb_{36H}) \tag{2.2}$$

More recent work has added contributions from the ~10, ~23, and ~89 GHz channels available on more recent sensors, such as AMSR-E, AMSR2, and GPM (Kelly et al., 2003; Kelly, 2009; Tedesco et al., 2015; Smith and Bookhagen, 2016). These algorithms also account for the impacts of forest cover on PM data, such as in the algorithm proposed for AMSR-E data (Kelly, 2009):

$$SnowDepth = ff(SD_{ff}) + (1 - ff)SD_o \tag{2.3}$$

where ff is fractional forest cover, SD_{ff} is the snow depth of the forested fraction, and SD_o is the snow depth of the non-forested fraction. The parameters SD_{ff} and SD_o are calculated by:

$$SD_{ff} = p1 * (Tb_{18V} - Tb_{36V})/(1 - fd * 0.6) \tag{2.4}$$

$$SD_o = p1 * (Tb_{10V} - Tb_{36V}) + p2 * (Tb_{10V} - Tb_{18V}) \tag{2.5}$$

where $p1$ and $p2$ are defined as $1/log_{10}(Tb_{36V} - Tb_{36H})$ and $1/log_{10}(Tb_{18V} - Tb_{18H})$, and fd is forest density.

Some researchers have tuned the original equations proposed by Chang et al. (1982) to the conditions of a specific region (e.g., Che et al., 2008; Mizukami and Perica, 2012), by correcting for topography (Savoie et al., 2009), and by introducing forest cover corrections (Foster et al., 2005; Derksen, 2008). Despite improvements over the original algorithms that were developed and calibrated on wide, flat, and dry snow fields in Russia and Canada, SWE estimates remain unreliable in the absolute sense, particularly over complex terrain (Smith and Bookhagen, 2016; Mätzler and Standley, 2000; Dozier and Warren, 1982; Daly et al., 2012).

Topography has been shown to impact estimated SWE values (Dozier and Warren, 1982; Chang et al., 1991; Mätzler and Standley, 2000) by modifying the assumed satellite-to-ground path distance and angle, as well as by introducing constructive and destructive interference in the PM frequencies. For example, PM radiation emitted from two sides of a valley can interfere constructively or destructively depending on the angle of both valley faces and the relative view angle of the PM sensor. The problem is compounded by the polarized nature of PM data collections, where horizontally and vertically polarizations will modulate the impacts of topography differently. As with any satellite data, topography facing towards the satellite sensor will be preferentially sampled at the expense of topography facing away from the satellite.

Despite these caveats, PM data remains the only empirical method to estimate SWE over large areas of complex and inhospitable terrain, such as in HMA (e.g., Chang et al., 1982, 1987, 1991; Kelly et al., 2003; Kelly, 2009; Abdalati and Steffen, 1995; Hall et al., 2004; Drobot and Anderson, 2001; Joshi et al., 2001; Takala et al., 2003, 2008, 2009; Apgar et al., 2007; Monahan and Ramage, 2010; Tedesco, 2007; Liu et al., 2005; Armstrong and Brodzik, 2001). The lack of a well-maintained and spatially diverse sensor network in the region (Bookhagen and Burbank, 2010; Smith and Bookhagen, 2016; Sorg et al., 2012) – as well as the political, topographic, and climatic complexities of ground-data collection – leave few options for collecting spatially extensive and continuous SWE estimates in HMA.

Chapter 3

High Mountain Asia

Geographic Setting

The study area for this dissertation generally runs from 25-45N and 67.5-95E, and includes all or part of Mongolia, Kazakhstan, Kyrgyzstan, Uzbekistan, Tajikistan, Afghanistan, Pakistan, India, Nepal, Bhutan, Bangladesh, Myanmar, and China (Fig. 3.1A, inset). This area includes a diversity of climatic, topographic, and environmental zones; elevations run from nearly sea-level to over 8,000 m asl at the highest peaks in the world. The study area also includes several major mountain ranges – the Himalaya, Hindu Kush, Karakoram, Pamir, Tien Shan, and Kunlun Shan – which surround the Tibetan Plateau and are collectively known as High Mountain Asia (HMA).

Together, these mountain ranges contain the headwaters for rivers serving more than a billion people. The Syr Darya, Amu Darya, Indus, Tarim, Tibet, Yangtze, Salween, Tsangpo, and Ganges basins are entirely or partially sourced in HMA (Fig. 3.1A). While the higher elevation parts of HMA are often sparsely populated, the downstream areas of watersheds sourced in HMA play host to some of the most densely populated regions of the world (Fig. 3.1B). Combined, the Indus, Ganges, and Tsangpo basins provide water for more than 800 million people (Bolch et al., 2012), and the Yangtze provides water for an additional 600 million people (Immerzeel et al., 2010).

HMA is the most heavily glaciated region outside of the poles. The estimated 118,200 sq km of glaciated area has been rapidly losing mass over the past decades (Gardner et al., 2013). This mass loss has both impacted local communities (Vaughan et al., 2013) and has contributed to global sea-level rise (Gardner et al., 2013). However, these changes have been spatially heterogeneous and are strongly impacted by local topography and climate (Gardner et al., 2013; Gardelle et al., 2013; Kääb et al., 2012, 2015). The fate of HMA's glaciers remains hotly debated; in-situ data are sparse, and the role of differing climate and topographic settings in glacier response to climate change remains poorly understood. However, glaciated regions generally follow the very low temperature zones in the high-elevation areas in and bordering the Tibetan Plateau (Fig. 3.2).

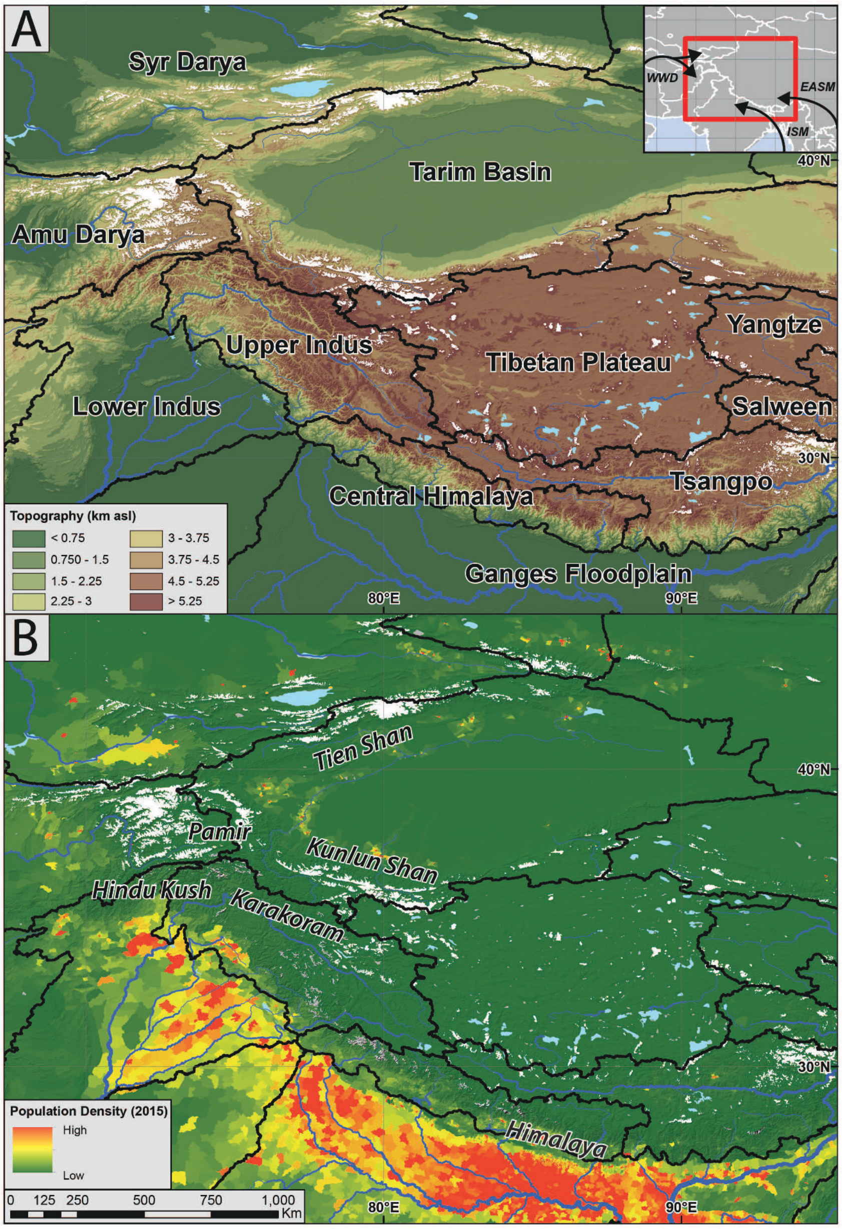

Figure 3.1 – (A) Topographic map of High Mountain Asia (HMA) with major catchment boundaries (black) derived from SRTM data (Jarvis et al., 2008). Major rivers scaled by discharge (blue) and glacier areas (white) from the Randolph Glacier Inventory v5 (Arendt et al., 2015). Inset map shows political boundaries, as well as wind direction of major weather systems (WWD: Winter Westerly Disturbances, ISM: Indian Summer Monsoon, EASM: East Asian Summer Monsoon). (B) Population density (2015) of HMA, derived from the Gridded Population of the World Version 4 (GPWv4) (CIESIN - Columbia University, 2016), with names of major mountain ranges. High-elevation and highly glaciated areas provide water for some of the most densely populated regions on earth.

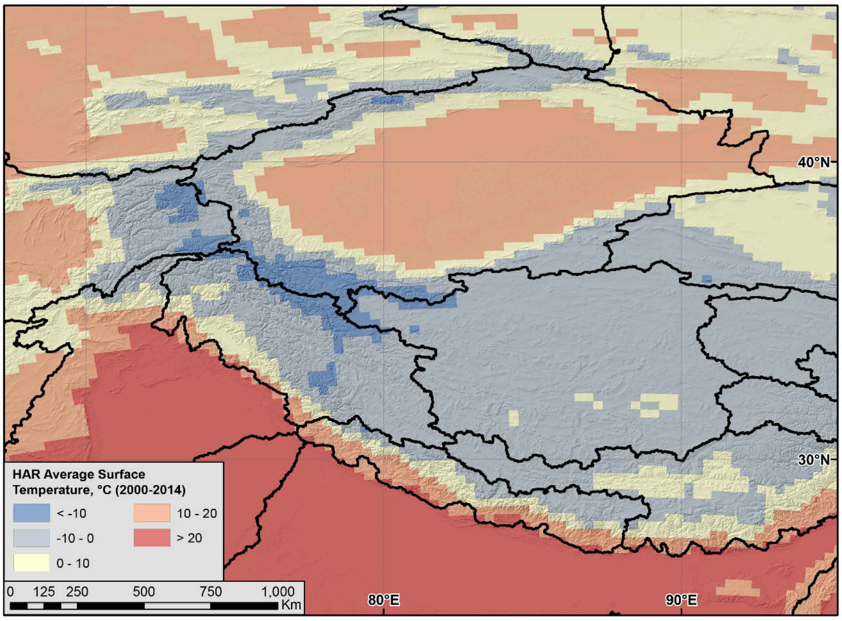

Figure 3.2 – Long-term (2000-2014) modeled average annual air temperature (°C) derived from High Asia Refined Analysis (HAR) (Maussion et al., 2014). The high-elevation Tibetan Plateau has average annual temperatures below zero, with some especially cold regions maintaining average annual temperatures below -10°C.

Major Climate Systems of HMA

HMA's climate is controlled by three major moisture sources: the Winter Westerly Disturbances (WWD), Indian Summer Monsoon (ISM), and East Asian Summer Monsoon (EASM) (Fig. 3.1A, inset). The interaction between these moisture sources and the complex topography of HMA creates a vast range of precipitation regimes and microclimates across the study region (e.g., Cannon et al., 2014; Kääb et al., 2012; Immerzeel and Bierkens, 2012; Immerzeel et al., 2015; Gardner et al., 2013; Kapnick et al., 2014; Barnett et al., 2005; Dahe et al., 2006; Takala et al., 2011; Cannon et al., 2017).

The ISM is a tropical monsoon system which generally extends from June to September (Kumar et al., 1995; Goswami et al., 1999; Goswami and Mohan, 2001; Menon et al., 2013), and is the result of periodic northward migrations of the Intertropical Convergence Zone (e.g., Boos and Kuang, 2010; Molnar et al., 2010) due to differential heating of Central Asia and the Indian Ocean. It is responsible for the majority of precipitation from north-central India and Nepal through Pakistan and moves north-west along the Himalayan Front (Bookhagen and Burbank, 2010). The primary moisture source of the ISM is the Bay of Bengal.

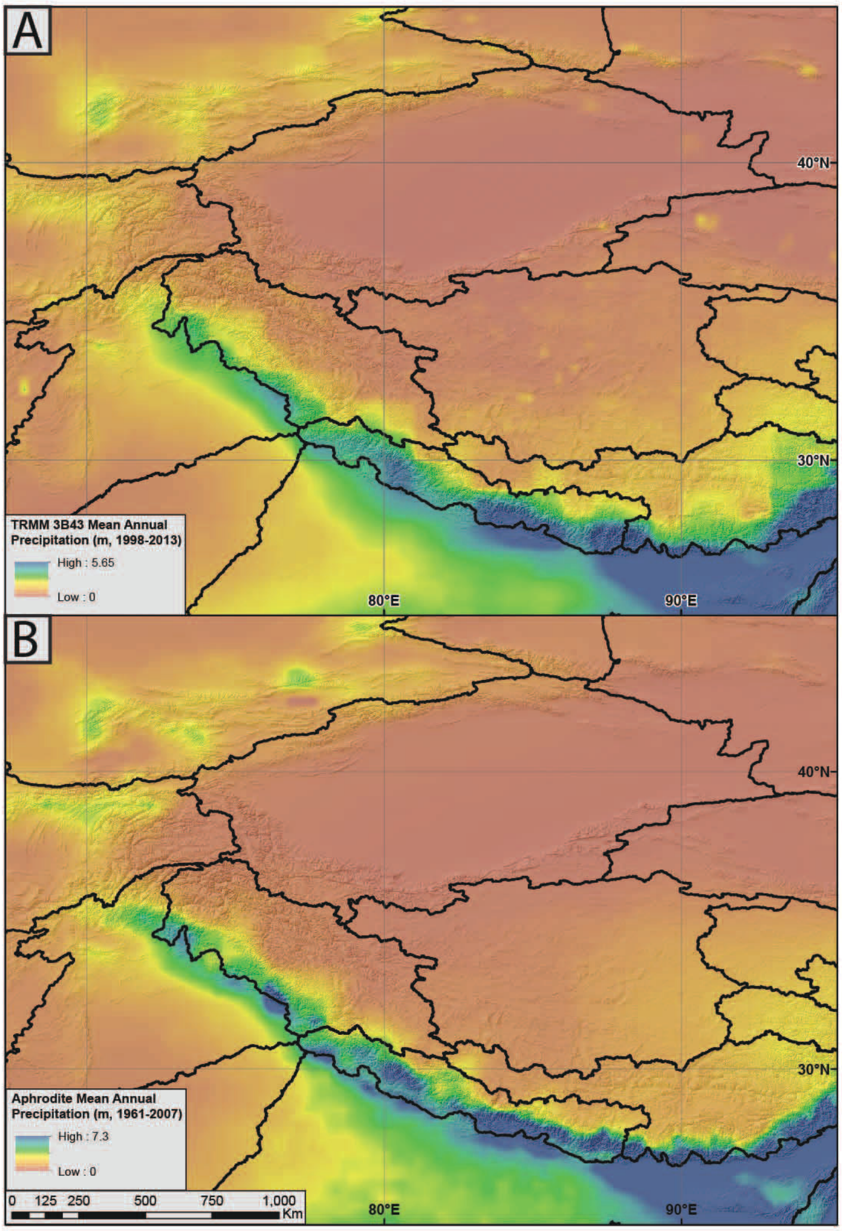

Figure 3.3 – (A) TRMM 3B43 (1998-2013, Huffman et al. (2007)) and (B) APHRODITE (1961-2007, Yatagai et al. (2012)) total annaul rainfall distributions across HMA with major catchment boundaries (black) derived from SRTM data (Jarvis et al., 2008). Clear precipitation gradients exist from the southeast moving along the Himalayan Front to the northwest in both datasets, with slight differences in volume and distribution. Satellite (TRMM) and interpolated station data (APHRODITE) produce similar precipitation patterns, but also maintain distinct differences.

The EASM is a sub-tropical monsoon system with multiple precipitation peaks in May and September-October (Yihui and Chan, 2005). It is primary over parts of Bhutan and the eastern Tibetan Plateau, and brings moisture from the South China Sea onto the mainland, eventually depositing moisture on the far eastern edge of the Tibetan Plateau (Yihui and Chan, 2005). The ISM and EASM, while separate phenomena, interact strongly (Zhu et al., 1990). Both the ISM and the EASM are influenced by El Niño-Southern Oscillation (ENSO), as well as other large-scale, global climate oscillations (Menon et al., 2013).

The WWD are driven by a low-level jet stream which brings moisture from as far west as the Mediterranean and generally last from December to March (Barlow et al., 2005; Palazzi et al., 2013; Cannon et al., 2014). As WWD move east, they are impacted by significant topographic blocking and capture, resulting in large-scale precipitation events. As these storms generally occur during cold months, they often result in heavy snowfall, particularly at high elevations and along topographic channels such as major valleys (Cannon et al., 2014; Lang and Barros, 2004).

Moisture in the southern and eastern regions of HMA is controlled by the interaction between the ISM and the EASM, which together provide the majority of moisture along the southern and eastern edges of the Tibetan Plateau (Barlow et al., 2005; Lang and Barros, 2004; Boos and Kuang, 2010). Inter-annual and inter-decadal variation in both the EASM and the ISM are driven by a combination of sea surface temperatures and snow cover across Eurasia and the Tibetan Plateau, which create temperature gradients and partially control the timing, direction, and strength of the ISM (Kumar et al., 1995).

The northern and western regions of HMA are more strongly influenced by the WWD (Barlow et al., 2005; Palazzi et al., 2013). While the WWD tend to carry less moisture than the ISM or the EASM, they occur during colder months and deposit more snow than either of the southern monsoons (cf. Figure 3.4). An additional climate system known as the Siberian High impacts only a small portion of HMA in the northern Tien Shan, where it serves as a blocking mechanism for the WWD (Sorg et al., 2012). The interaction of local topography with the interactions of the WWD and Siberian High creates distinct precipitation gradients in the Tien Shan, with decreasing precipitation from the northwest to southeast (cf. Fig. 3.3) (Sorg et al., 2012).

Climate Change in HMA's Cryosphere

HMA is already feeling the impacts of global warming, and will continue to face diverse climate change impacts in the coming decades (Vaughan et al., 2013; Bolch et al., 2012; Gardner et al., 2013). These changes will manifest as both changes to mean temperatures and precipitation levels, and changes in climate extreme events. Often, climate changes are enhanced by anthropogenic land cover changes (e.g., Charney, 1975; Charney et al., 1977). In general, HMA will warm over the coming decades – and in many cases will warm faster than the global average (Vaughan et al., 2013).

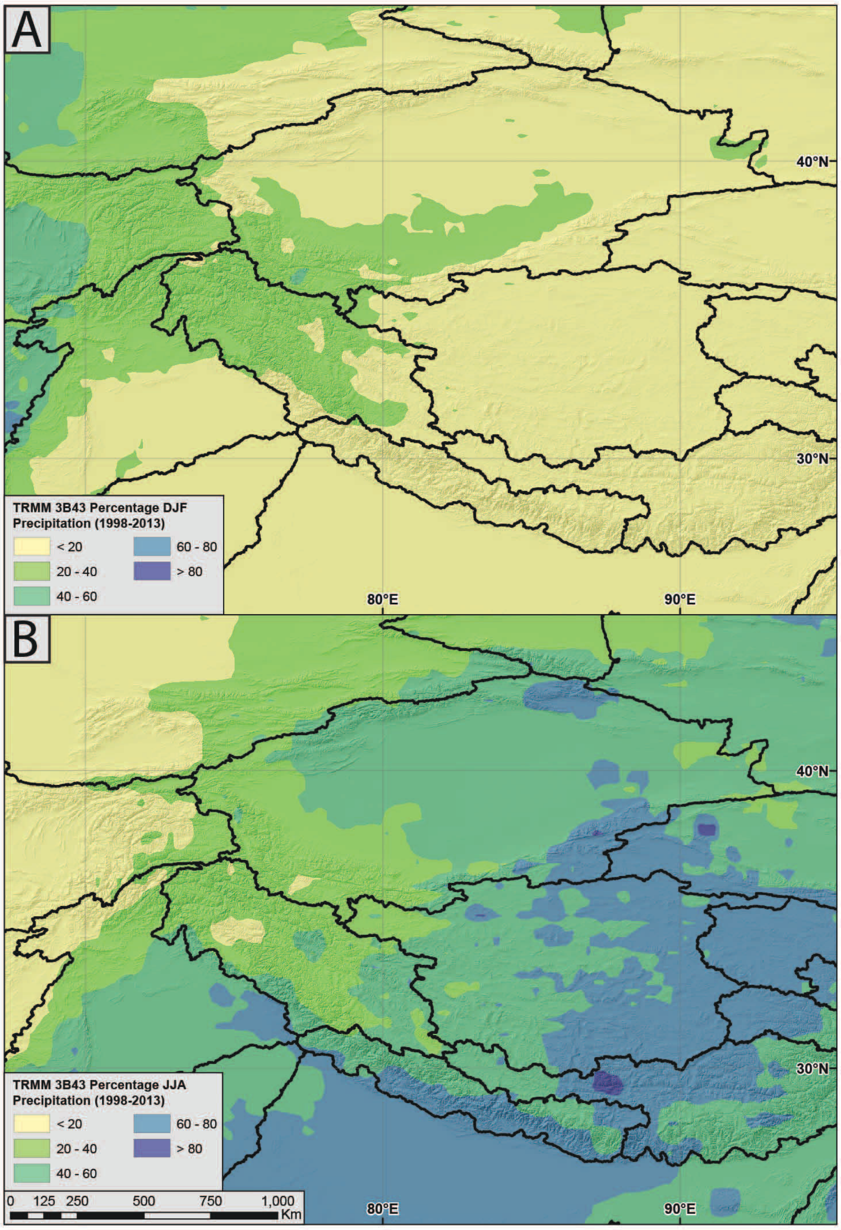

Figure 3.4 – TRMM 3B43 (1998-2013, Huffman et al. (2007)) seasonality in rainfall across High Mountain Asia (HMA) with major catchment boundaries (black) derived from SRTM data (Jarvis et al., 2008). Percentage of annual precipitation falling in (A) December-January-February (DJF) and (B) in June-July-August (JJA). A distinct DJF/JJA divide exists where the western areas of HMA receive more DJF precipitation and eastern areas receive more JJA precipitation.

Large-scale climate patterns – such as the ISM and WWD – have changed in strength and timing (e.g., Cannon et al., 2014, 2016; Gautam et al., 2009; Menon et al., 2013; Kitoh et al., 2013; Fu, 2003;

Ramanathan et al., 2005; Lau et al., 2010; Palazzi et al., 2013). For example, the ISM has increased in strength since the 1950s due to increases in moisture availability (Menon et al., 2013; Kitoh et al., 2013) and increased regional heat-trapping potential due to air pollution (Gautam et al., 2009; Ramanathan et al., 2005). In addition to climate change, shifts in Southeast Asia's landcover (i.e., deforestation, extensive irrigation and agriculture, urbanization) have modified regional weather and climate patterns (Fu, 2003; Gautam et al., 2009; Bookhagen and Burbank, 2010). Large-scale changes in ENSO patterns due to warming oceans have also impacted precipitation patterns in HMA (Bookhagen et al., 2005).

The WWD, while driven by very different atmospheric phenomena, have been increasing in strength over the past decades (Cannon et al., 2014, 2015; Norris et al., 2016; Treydte et al., 2006). This has driven both increases in mean regional precipitation and in the incidence of extreme storms. In the more northern reaches of the WWD (Tien Shan Mountains), massive changes in regional landcover, such as the introduction of cotton monoculture and subsequent infrastructural development in Central Asia in the 1960s, have had significant impacts on both water quality and regional weather patterns (Lioubimtseva et al., 2005). The increase in regional dust due to the dessication of the Aral Sea over the past decades is thought to have had significant influence on regional precipitation, and have had a compounding effect on regional climate warming (Lioubimtseva et al., 2005).

Shifts in large-scale weather patterns, when combined with regional warming above the global average (Vaughan et al., 2013), have strongly impacted HMA's cryosphere. Many recent studies have focused on changes in HMA's glaciers, whose retreat is a highly visible indicator of warming temperatures. In general, glaciers are retreating across HMA (e.g., Bolch et al., 2012; Kääb et al., 2012, 2015; Gardner et al., 2013) at variable rates controlled by topography, black carbon and other pollution (Scherler et al., 2011), debris cover (Scherler et al., 2011; Bolch et al., 2012; Racoviteanu et al., 2009), and precipitation regimes (Fujita, 2008; Kapnick et al., 2014). There exist, however, regions of glacier stability or even growth, such as the Karakoram (Hewitt, 2005; Gardelle et al., 2013; Kapnick et al., 2014; Wang et al., 2017; Gardner et al., 2013), Pamir (Gardelle et al., 2013), and Kunlun Shan (Shangguan et al., 2007; Gardner et al., 2013; Yao et al., 2012; Kääb et al., 2015). Due to lack of in-situ data, estimates of glacier change remain sparse and poorly constrained.

Warming spring temperatures, earlier snowmelt seasons, and an increasing lack of late-season water availability have been observed in Central Asia (Dietz et al., 2014), in the Himalaya (Lau et al., 2010; Panday et al., 2011) and in the Indus Basin (Hasson et al., 2014). Intensification of the snowmelt season has been observed in both model (Lutz et al., 2014) and empirical (Dietz et al., 2014; Bookhagen and Burbank, 2010; Stewart, 2009; Smith et al., 2017; Hasson et al., 2014) data. However, these changes are not monolithic, and general climate trends in HMA hide both small- and large-scale spatial and temporal variability in climate change impacts.

Chapter 4

Assessing uncertainty and sensor biases in passive microwave data across High Mountain Asia[†]

Taylor Smith[1], Bodo Bookhagen[1]

[1]*Institute of Earth and Environmental Sciences, Universität Potsdam, Germany*

Abstract

Snowfall comprises a significant percentage of the annual water budget in High Mountain Asia (HMA), but snow-water equivalent (SWE) is poorly constrained due to lack of in-situ measurements and complex terrain that limits the efficacy of modeling and observations. Over the past few decades, SWE has been estimated with passive microwave (PM) sensors with generally good results in wide, flat, terrain, and lower reliability in densely forested, complex, or high-elevation areas.

In this study, we use raw swath data from five satellite sensors – the Special Sensor Microwave/Imager (SSMI) and Special Sensor Microwave Imager/Sounder (SSMIS) (1987-2015, F08, F11, F13, F17), Advanced Microwave Scanning Radiometer - Earth Observing System (AMSR-E, 2002-2011), AMSR2 (2012-2015), and the Global Precipitation Measurement (GPM, 2014-2015) – in order to understand the spatial and temporal structure of native sensor, topographic, and land cover biases in SWE estimates in HMA. We develop a thorough understanding of the uncertainties in our SWE estimates by examining the impacts of topographic parameters (aspect, relief, hillslope angle, and elevation), land cover, native sensor biases, and climate parameters (precipitation, temperature, and wind speed). HMA, with its high seasonality, large topographic gradients and low relief at high elevations provides an excellent context to examine a wide range of climatic, land-cover, and topographic settings to better constrain SWE uncertainties and potential sensor bias.

Using a multi-parameter regression, we compare long-term SWE variability to forest fraction, maximal multi-year snow depth, topographic parameters, and long-term average wind speed across both individual sensor time series and a merged multi-sensor dataset. In regions where forest cover is extensive, it is the strongest control on SWE variability. In those regions where forest density is low (<5%), maximal snow depth dominates the uncertainty signal. In our regression across HMA, we find that forest fraction is the strongest control on SWE variabil-

---

[†] *published as Taylor Smith and Bodo Bookhagen. "Assessing uncertainty and sensor biases in passive microwave data across High Mountain Asia." Remote Sensing of Environment 181 (2016): 174-185.* http://www.sciencedirect.com/science/article/pii/S0034425716301419

ity (75.8%), followed by maximal multi-year snow depth (7.82%), 90th percentile 10-m wind speed of a 10-year December-January-February (DJF) time series (5.64%), 25th percentile DJF 10-m wind speed (5.44%), and hillslope angle (5.24%). Elevation, relief, and terrain aspect show very low influence on SWE variability (<1%). We find that the GPM sensor provides the most robust regression results, and can be reliably used to estimate SWE in our study region.

While forest cover and elevation have been integrated into many SWE algorithms, wind speed and long-term maximal snow depth have not. Our results show that wind redistribution of snow can have impacts on SWE, especially over large, flat, areas. Using our regression results, we have developed an understanding of sensor-specific SWE uncertainties and their spatial patterns. The uncertainty maps developed in this study provide a first-order approximation of SWE-estimate reliability for much of HMA, and imply that high-fidelity SWE estimates can be produced for many high-elevation areas.

Introduction

Tracking the accumulation and melt of snow is essential for weather forecasting, climate modeling, and water management applications. Estimates of snow depth (SD) and snow-water equivalent (SWE) provide additional information on the volume of water stored and released from snowpack, which is critical for managing flood risk, irrigation systems, and hydropower (Armstrong and Brodzik, 2002; Tedesco and Narvekar, 2010). Several methods have been used to estimate SD and SWE over large areas, such as modeling based on snow covered area (SCA) and a conversion factor (Bookhagen and Burbank, 2010; Immerzeel et al., 2009), estimating melt volume by backward calculation of snow clearance dates (Molotch and Margulis, 2008; Guan et al., 2013), direct measurements of SWE with in-situ climate stations, and SWE estimation with passive microwave (PM) data (Chang et al., 1982, 1987; Clifford, 2010; Daly et al., 2012; Pulliainen, 2006; Takala et al., 2009, 2011; Tedesco et al., 2015). SWE estimation with PM data is the only method which can estimate SWE over large areas, across all terrain types, and provide high-temporal resolution SWE estimates based on empirical relationships. High temporal-resolution data are imperative for accurately guaging snowmelt and downstream runoff (Anderton et al., 2002; Dozier et al., 2008; Painter et al., 2009).

Beginning in 1978 with the Scanning Multichannel Microwave Radiometer (SMMR) system, PM data has been used to measure snow parameters (Knowles et al., 2002; Chang et al., 1982). PM data has several significant advantages over optical remote sensing data for the collection of snow data, including cloud penetration, night-time data collection, and high sensitivity to water content in snowpack. For many snow-covered regions, winter storms can drastically limit optical data collection due to cloud cover. The Special Sensor Microwave/Imager (SSMI) (Wentz, 2013), Special Sensor Microwave Imager/Sounder (SSMIS) (Sun and Weng, 2008), Advanced Microwave Scanning Radiometer - Earth Observing System (AMSR-E) (Ashcroft and Wentz, 2013), AMSR2 (Imaoka et al., 2010), and Global Precipitation Measurement (GPM) (GPM Science Team, 2014) sensors each collect data at several microwave spectra, and can be used for the evaluation of snowpack at daily or greater resolution.

Several algorithms have been developed to estimate SD and SWE from PM data (e.g., Chang et al., 1987; Kelly et al., 2003; Pulliainen, 2006; Kelly, 2009; Tedesco and Narvekar, 2010; Takala et al., 2011). The majority of these algorithms exploit the difference between the brightness temperatures (Tb) at the ~18 and ~36 GHz channels. However, more recent algorithms, such as those proposed by Kelly (2009), also exploit the ~10, ~23, and ~89 GHz channels available on AMSR-E/2 and GPM, which can better resolve shallow snow conditions and are less sensitive to saturation of the PM signal at the ~18 GHz band (Derksen, 2008). Improvements on SWE estimation have also been made by tuning the original equations proposed by Chang et al. (1987) to specific regional conditions (Mizukami and Perica, 2012), correcting for elevation (Savoie et al., 2009), and by introducing a forest cover correction (Foster et al., 2005). While these methods have improved upon SWE estimation, they remain unreliable in complex topography (Tedesco et al., 2015).

Topographic relief can have strong impacts on sensed Tb values (Mätzler and Standley, 2000; Dozier and Warren, 1982). First, the path between the ground surface and the PM sensor is determined by the ground elevation, which can introduce a height-dependent bias (Savoie et al., 2009). Second, complex terrain can interact constructively, where the sensed Tb values are not only the PM radiation emitted by a flat surface, but the combination of interacting microwave signals from hillslopes which face each other. Third, topography can shadow parts of the satellite field of view, which preferentially samples those hillslopes which face the satellite. Last, land surface slope changes the relative look angle of the satellite, which can preferentially enhance or degrade the microwave signal from different areas of the same field of view, and modify the relative signal strengths of horizontally and vertically polarized Tb data (Dozier and Warren, 1982). In addition to topographic impacts, forest cover can significantly reduce the Tb difference term used by SWE algorithms (Chang et al., 1996; Foster et al., 2005). This is due to the attenuation of microwave signals as they pass through dense vegetation, which can reduce SWE estimates by as much as 50% (Brown, 1996; Vander Jagt et al., 2013).

While studies have examined the reliability of SWE data from several satellite platforms (i.e Imaoka et al., 2010; Armstrong and Brodzik, 2001, 2002; Brown, 1996; Chang et al., 1996; Dai et al., 2015; Foster et al., 2005; Langlois et al., 2011; Mizukami and Perica, 2012; Sun and Weng, 2008; Tedesco and Narvekar, 2010; Wang and Tedesco, 2007; Savoie et al., 2009; Dong et al., 2005), few large-scale analyses of SWE have been undertaken in High Mountain Asia (HMA), and none have examined the impacts of long-term maximal snow depth and wind redistribution on SWE variability.

As HMA lacks an extensive and reliable ground-weather station network, particularly at elevations above 3000 m, we do not rely on in-situ data to compare our satellite-based SWE estimates to those of any snow-monitoring stations. Instead, we focus on understanding the utility and limitations of satellite-based PM data – especially those factors which may reduce the reliability of SWE estimates – by examining a multi-frequency time series of PM data across a range of topographic, land cover, and climate settings.

Materials and Methods

In this study we use a multi-instrument time series of SSMI, SSMIS, AMSR-E, AMSR2, and GPM PM data from 2000-2015 in combination with topographic, land-cover, and climatic data.

Study Area

Our study area encompasses a wide range of climatic seasonality, elevation, topographic relief and hillslope angles. It includes not only high relief and high complexity areas typical of many mountain ranges, but also large areas

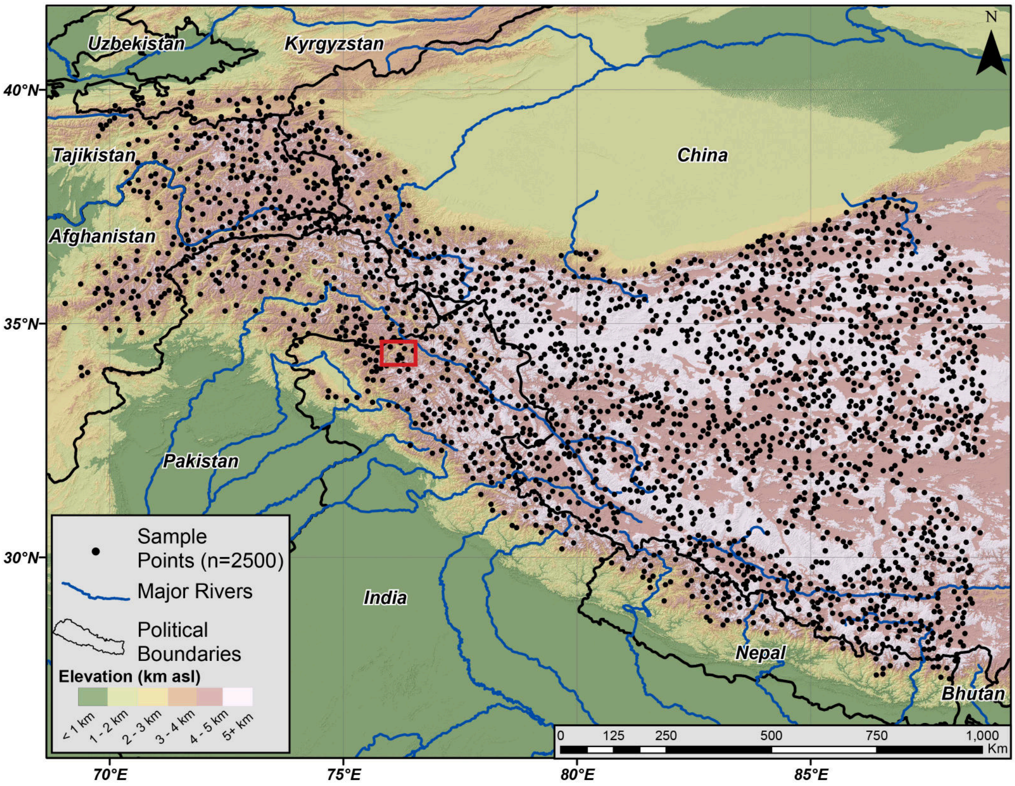

Figure 4.1 – Topographic map of High Mountain Asia (HMA) based on SRTM V4.1 data with political boundaries (black) and major rivers (blue). Black dots indicate randomly-generated sample points (n=2500) encompassing a wide range of land cover, topographic, and climate regimes. Red box indicates extent of Figure 4.3. For each sample point, we have extracted a multi-instrument time series of PM data, landscape characteristics (forest cover, hillslope angle, elevation, aspect, relief), and climate data (rainfall, temperature, wind speed).

of low relief at high elevation (i.e., the Tibetan Plateau). Low but variable forest density across the study region, in combination with the range of topographic characteristics, allows us to examine a range of factors which impact SWE estimation with PM data. We randomly generated 5000 points within our study area, and removed those close to major bodies of water. From this subset, we choose 2500 sample points which cover a wide range of elevation, relief, slope, and aspect settings (Fig. 4.1).

Topographic, Land Cover, and Climate Data

The 2000 Shuttle Radar Topography Mission V4.1 (SRTM) Digital Elevation Model (DEM) (~90-m, void-filled) was leveraged to provide elevation, hillslope angle, aspect, and 5-km radius relief (Jarvis et al., 2008) (Fig. 4.1). We then apply an averaging filter over a 20-km radius to the hillslope, elevation, and relief surfaces to minimize spatial-resolution differences and PM location uncertainties when comparing between 90-m and ~25-km resolution data (Fig. 4.2A,B).

High Asia Reanalysis (HAR) (2000-2014) provides 10-km resolution land-surface temperature at 2-m heights (product t2) at both daily and 3-hourly temporal resolution over 98% of the study area for the period 2000 to

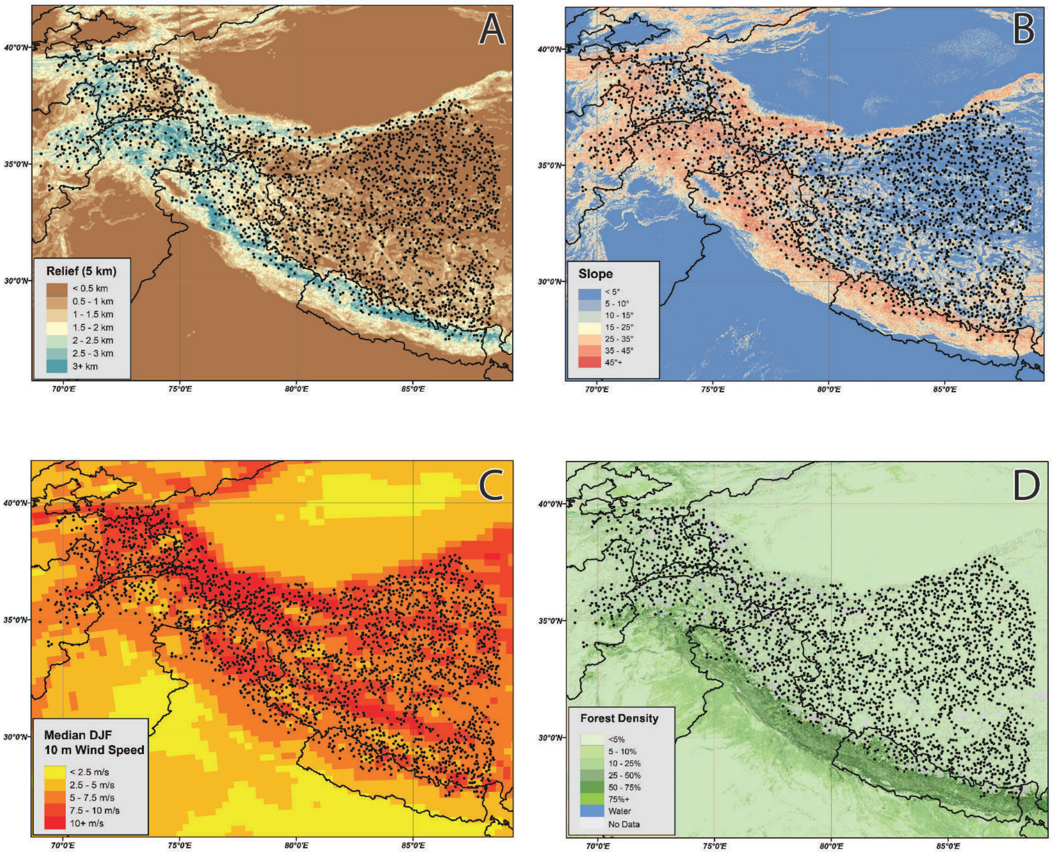

Figure 4.2 – Topographic and climatic characteristics of High Mountain Asia: (A) 5-km radius relief and (B) hillslope angle (degree), derived from SRTM V4.1 and averaged over a 20-km radius (Jarvis et al., 2008); (C) 14-year averaged December-January-February (DJF) median 10-m wind speed (m/s), derived from HAR (Maussion et al., 2014), and (D) forest density, derived from MOD44B (2000-2010, DiMiceli et al. (2011)). Black dots indicate random sample locations (cf. Figure 4.1).

2014 (Maussion et al., 2014). For those points which fall outside of the 10-km HAR domain, we use the 30-km product instead. We use the hourly product to create average daily daytime and nighttime temperatures, as well as bi-daily deviation values from the long-term average monthly temperatures. In addition to the HAR temperature product, we leverage the 10-m surface wind speed dataset (product ws10) to assess the impact of high-wind areas on SWE variability (Fig. 4.2C). We treat the HAR wind product as a 'static' dataset in our analysis by using long-term statistics derived from the 14-year time series of wind speed data, such as the long-term December-January-February (DJF) median, 25th and 90th percentile wind speeds at each pixel. By using percentiles as proxies for long-term trends in the climate data, we can more accurately compare trends in wind speed with trends in SWE and SWE variability over the whole time series instead of on a daily or hourly basis.

TRMM product 3B42 V7 (1997-2014) provides daily rainfall estimates at 0.25° × 0.25° resolution (Huffman et al., 2007). These data are used to isolate precipitation-free days and multi-day periods from the larger time series, with a sensed precipitation threshold of 0.1 mm/hr.

Fractional forest cover is derived from MODIS MOD12Q1 yearly data (2001-2012), following the Boston University IGBP classification scheme (Hansen et al., 2003). Forest density is derived from MODIS MOD44B global forest density yearly data (2000-2010, DiMiceli et al. (2011)). Both MOD12Q1 and MOD44B area averaged over a 20-km radius (Fig. 4.2D).

The AMSR EASEgrid SWE product (L3 v2, 2002-2011) provides SWE estimates at $0.25^\circ \times 0.25^\circ$ resolution across our entire study area (Tedesco et al., 2004). The EASEgrid product at daily resolution is used to visually compare the SWE estimation of a large-scale gridded products with the results of our point-level SWE analyses. We also use the AMSR EASEgrid product to examine the distribution of snow depth throughout our study area. In our analysis of SWE uncertainty, we use the 9-year daily resolution time series of SWE measurements to derive 95th percentile SWE volume estimates for each grid cell. These estimates serve as proxies for tracking areas which see frequent deep snow cover.

To identify time periods which should nominally have constant SWE (i.e., no changes in SWE), we choose those periods where (1) the HAR temperature does not rise above 0°C and (2) there is no sensed precipitation, as measured by TRMM. These periods are termed 'clear days' throughout this manuscript, and are used in sections 4.3 and 4.4 to examine native inter- and intra-sensor variability.

Passive Microwave Data

In this study we acquired ungridded, raw, swath data for SSMI and SSMIS (F08, F11, F13, F17, 1987-2015, Wentz (2013); Sun and Weng (2008)), AMSR-E (2002-2010, Ashcroft and Wentz (2013)), AMSR2 (2012-2015, Imaoka et al. (2010)), and GPM (2014-2015, GPM Science Team (2014)) satellites. The characteristics of each satellite are listed in Table 4.1.

We examined the potential of the TRMM Microwave Imager (TMI) instrument to measure SWE, but found the results unreliable. In particular, the 36V channel experienced highly variable Tb fluctuations, making SWE estimation with the TMI sensor problematic.

Swath Processing

We examine the raw, orbital PM data at each satellite's respective native sensor resolution and do not resample the data to an equally-spaced or consistent grid. By maintaining native resolution, we are able to increase our data density by using multiple imperfectly-overlapping swaths (Fig. 4.3). Native resolution also improves direct, point-by-point comparisons between horizontally and vertically polarized data points by avoiding any data resampling. In this study, we use 30,865,102 individual data points across five satellites and 2500 random sample locations to examine long-term aggregate and inter-sensor differences in PM data. We also process a subset of 14,804,414 data points which occur on 'clear days', or days which do not see temperatures above 0°C and have no sensed precipitation.

To examine the swath data at 2500 randomly chosen point locations across the study area, we implement a search algorithm to find the closest data point within each individual swath (maximum distance 0.1°, approx. 10 km) throughout the entire measurement period of each satellite. To test the influence of the chosen search distance on Tb values at any given point, we have examined whole time series Tb means and standard deviations against the distance from the sampling center point (Fig. A1 in the Supplement). Across search distances, the means and

Table 4.1 – Characteristics of PM sensors used, with native channel frequencies, spatial resolutions, processing algorithms, orbit frequencies, and satellite angular properties.

Satellite	Temporal Coverage	Channels (GHz)	Spatial Resolution (km^2)	Processing Level/Algorithm
SSMI	Aug 1987 - Apr 2009 (22 years)	19.35, 22, 36, 85	69x43, 60x40, 37x28, 16x14	FCDR V07
SSMI/S	Jan 2008 - Apr 2015 (7 years)	19.35, 22, 36, 92	69x43, 60x40, 37x28, 37x28	FCDR V07
AMSR-E	May 2002 - Oct 2011 (9 years)	6.93, 10.65, 18.7, 23.8, 36.5, 89	75x43, 51x29, 27x16, 27x16, 14x8, 6x4	L1B
AMSR2	Jul 2012 - Sep 2015 (3 years)	6.93, 7.3, 10.65, 18.7, 23.8, 36.5, 89	62x35, 62x35, 42x24, 22x14, 19x11, 12x7, 5x3	L1R
GPM	Feb 2014 - Jul 2015 (1.5 years)	10.65, 18.7, 23.8, 36.5, 89, 166, 183.31	32.2x19.4, 18.3x11.2, 15x9.2, 14.4x8.6, 7.3x4.4, 7.1x4.4, 7.2x4.4	L1B

Satellite	Number of Orbits (Descending/Ascending)	Average Observations per Month	Earth Incidence Angle (°)	Scan Angle Range (°)
SSMI	176,460/176,460	1411	53.1	±51.2
SSMI/S	41,896/41,896	901	53.1	±71.6
AMSR-E	49,083/49,079	868	55	±61
AMSR2	16,623/16,623	874	55	±61
GPM	3,919/3,919	435	52.8	±70

standard deviations do not change appreciably, indicating that while there may be some changes in the variability signal we see within a subsetted dataset, these changes are due to the reduction in data density and not due to variability in the satellite field of view over time.

In this way, we develop a time series of Tb values at each point location at native instrument spatial resolution (Fig. 4.3). Using the time of each individual capture in conjunction with the latitude and longitude of the point location, we derive the position of the sun relative to the horizon. In our analysis of SWE, we only use those points where the sun is below the horizon. While this method is more computationally expensive than using only the descending orbits of each satellite, it allows us to expand our dataset by including every data point which is captured at night, regardless of which orbit it falls in. It also allows us to examine intra-day differences in measured Tb through the daytime and nighttime subsets of the Tb time series.

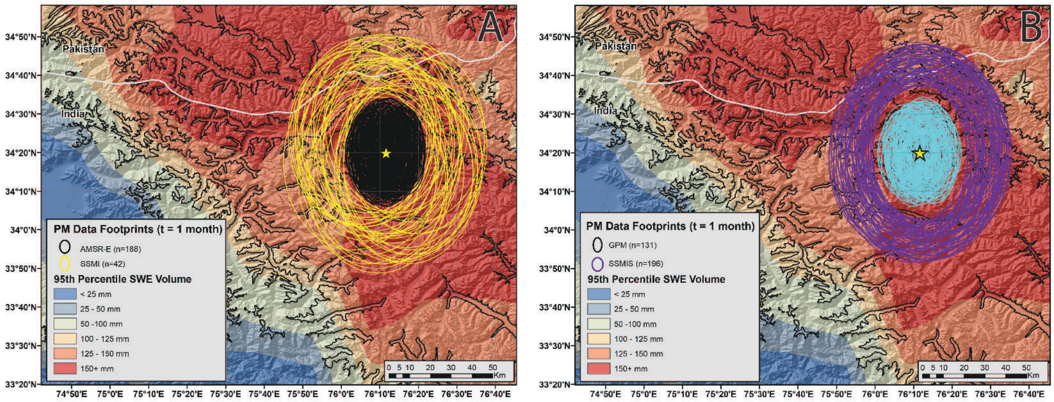

Figure 4.3 – Characteristic example of raw PM data points and their ellipsoidal geographic extent in NW India (cf. Figure 1). (A) One month of data from the SSMI (yellow, n=42) and AMSR-E (black, n=188) satellites; (B) SSMIS (purple, n=196) and GPM (turquoise, n=131). AMSR2 not shown, as the footprint size and density is comparable to AMSR-E. We show 9-year 95th percentile SWE volume from the AMSR EASEgrid as a background image to elucidate the 10-fold southwest-to-northeast SWE gradient in this area. Gray lines indicate international borders, black lines show the 4-km elevation contour.

Finally, we implement a correction to the SSMI/S data, as proposed by Dai et al. (2015), to normalize the SSMI/S data received from the multiple satellites (F08, F11, F13, F17). In this way, we ensure that each satellite dataset is as internally consistent as possible. We assume that the inter-calibration between AMSR-E and AMSR2 is of high quality, and thus do not perform any additional inter-calibration for the AMSR sensors.

SWE Estimation

Although several SWE estimation algorithms have been proposed (e.g., Chang et al., 1987; Kelly et al., 2003; Pulliainen, 2006; Kelly, 2009; Takala et al., 2011; Mizukami and Perica, 2012; Savoie et al., 2009; Tong et al., 2010), this study chooses to use only two of these to examine SD and SWE. The first method is based on the Chang equation:

$$SD[cm] = 1.59[cm/K] * (Tb_{18V} - Tb_{36V})[K] \tag{4.1}$$

This equation has seen wide use across the SSMI/S and AMSR-E platforms. To our knowledge, the Chang equation has never been used with GPM data to estimate SWE. However, due to the similar spectral ranges carried onboard AMSR-E/2 and GPM, we assume that the modified Chang equation, as proposed by Armstrong and Brodzik (2001), will work equally well for the GPM platform.

We also use a more complex algorithm – as initially developed for the AMSR-E satellite (Kelly et al., 2003; Kelly, 2009; Tedesco and Narvekar, 2010) – that includes a measure of forest cover and density. Both forest fraction and forest density have been shown to have strong impacts on SWE estimates, particularly in dense forests (DeWalle and

Rango, 2008; Langlois et al., 2011). This more complex algorithm also uses the ~10 GHz channel on AMSR-E/2 and GPM, and both the vertically and horizontally polarized ~18 and ~36 GHz channels

$$SD = ff(SD_{ff}) + (1 - ff)SD_o \tag{4.2}$$

where ff is fractional forest cover, SD_{ff} is the SD of the forested fraction, and SD_o is the SD of the non-forested fraction. SD_{ff} and SD_o are derived with

$$SD_{ff} = p1 * (Tb_{18V} - Tb_{36V})/(1 - fd * 0.6) \tag{4.3}$$

$$SD_o = p1 * (Tb_{10V} - Tb_{36V}) + p2 * (Tb_{10V} - Tb_{18V}) \tag{4.4}$$

where fd is forest density and $p1$ and $p2$ are $1/log_{10}(Tb_{36V} - Tb_{36H})$ and $1/log_{10}(Tb_{18V} - Tb_{18H})$, respectively. While neither the MOD12Q1 nor MOD44B products cover our entire time period, we forward- and back-estimate ff and fd by linear interpolation. This has a minimal impact on intra-sensor SWE estimation, and, as forest densities are generally low across the study region, does not significantly impact our results. While attenuation of the microwave signal in forests is a large problem in many parts of the world (e.g., Northern Canada, Foster et al. (2005)), our study region is very sparsely forested (Fig. 4.2D).

While both algorithms (Equations 4.1 and 4.2-4.4) produce reasonable SWE estimates, previous work has shown that differences in the SSMI and AMSR-E retrieval algorithms can result in strong bias, and in particular an elevation-dependent bias (Daly et al., 2012). We present results for several single-sensor SWE time series, across multiple sensor platforms. As can be seen in Figure 4.4, the *temporal patterns* of SWE are very similar across both algorithms, even if the absolute values of SWE are different. These similarities are emphasized by the black lines in Figure 4.4, which are smoothed by a 21-point Savitzky-Golay filter for display purposes (Savitzky and Golay, 1964). To simplify our discussion of intra-sensor and inter-sensor SWE variabilities and the impacts of different topographic factors, we choose to use the original Chang equation (Equation 6.1) for SWE estimation, along with a constant average snow density of 0.24 g/cm^3 conversion factor to transform SD into SWE (Takala et al., 2011).

Understanding Uncertainties in PM Data

To examine possible sources of uncertainty and variance in our SWE estimates, we have divided both the SWE and raw Tb data by time of day, position along the satellite scanline, and by several topographic parameters.

Time of Day

Previous studies (e.g., Chang et al., 1987, 1991; Armstrong and Brodzik, 2001) have noted that night time SWE estimates are more reliable than those taken during the day, as liquid water in the snowpack drastically alters the Tb gradient used for estimating SWE. However, most studies use only one of the descending or ascending orbits, depending on the location of their study areas and hence the time of satellite overpass. We instead choose to measure solar altitude on a point-by-point basis, to ensure that all of our measured Tb values occur when the sun is below

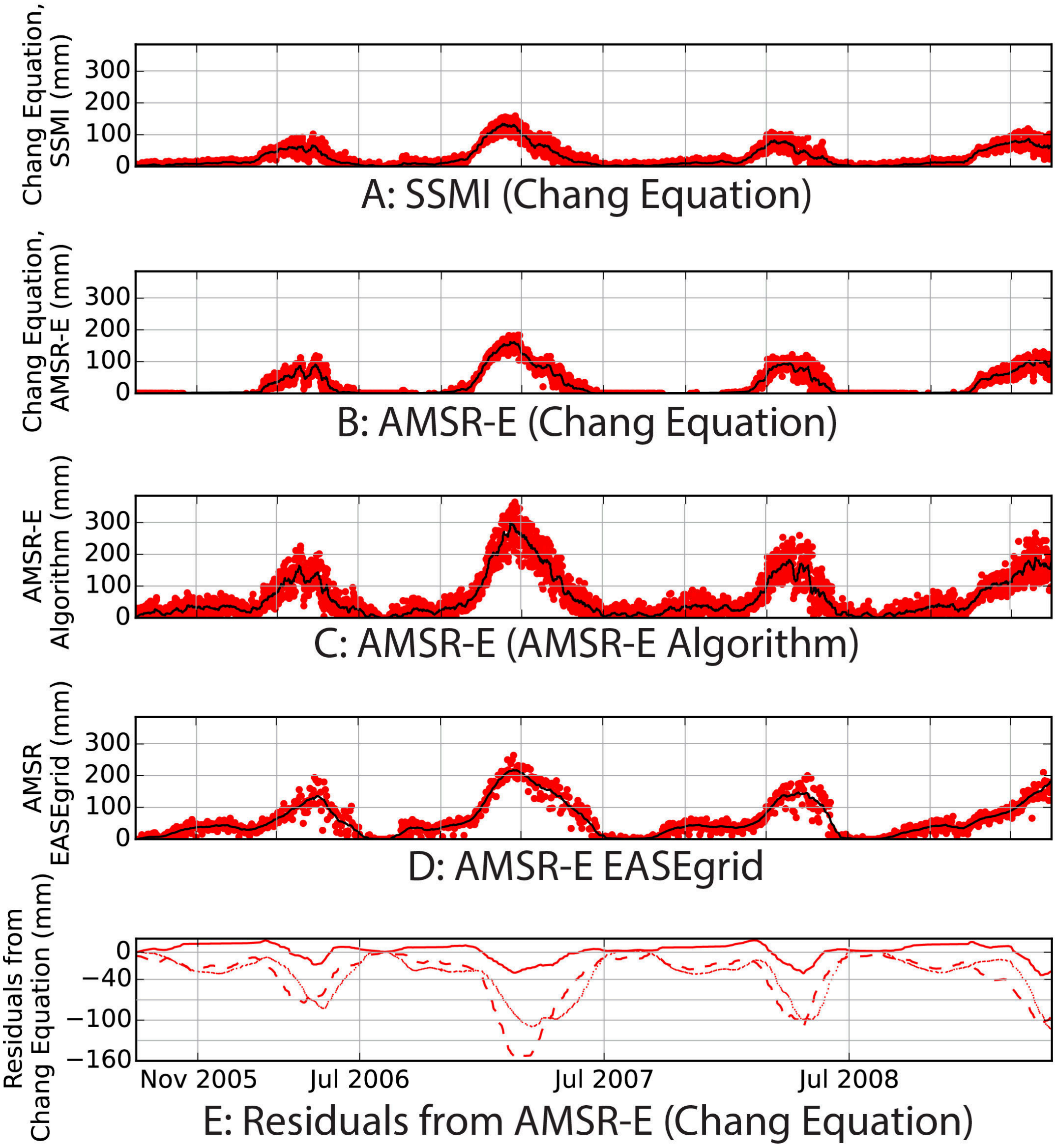

Figure 4.4 – Characteristic time series extracted for (76.1932°CE, 34.3335°CN, cf. Figure 4.3, 2005-2009) in the NW Himalaya for the AMSR-E platform. (A) SWE based on the Chang equation (Equation 6.1) (Chang et al., 1982) in mm, data from SSMI and (B) from AMSR-E, (C) SWE based on Forest Fraction (AMSR-E) algorithm (Equation 2.3) (Kelly et al., 2003), (D) SWE based on the AMSR-E EASEgrid product (Tedesco et al., 2004). Black lines smoothed using a 21 data-point Savitzky-Golay filter (Savitzky and Golay, 1964), and used in (E) to calculate residuals of Chang equation SSMI (solid line), AMSR-E algorithm (dashed line), and AMSR EASEgrid (dotted line), with respect to the Chang equation AMSR-E SWE estimates as shown in panel (B). Time series shows generally strong agreement on the *timing* of SWE buildup and melt, but disagreements on SWE volume.

the horizon. While 90+% of our points are derived from the descending orbits, we are also able to include some additional points from the ascending orbits during short periods of the year.

Scanline Position

To examine the impact of satellite look angle on SWE and Tb values, we take the index position (position along the scanline) of each measured data point, and normalize it by the length of the scanline (number of captures). As each satellite captures a different swath width, and thus number of points along a scanline, this allows us to normalize our scanline positions across satellite platforms. We then subset our data into quartiles to investigate possible bias derived from satellite look angle (i.e., Quartile 1 refers to the first 25% of the scanline, cf. Figure 4.5).

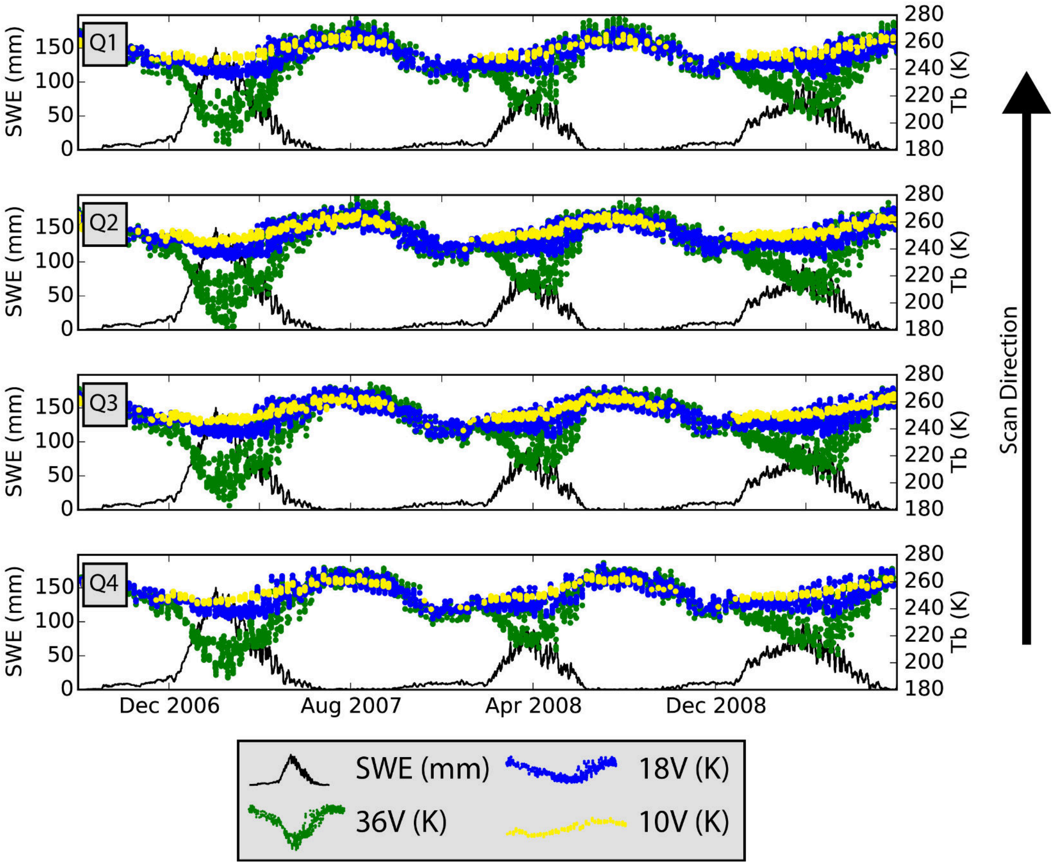

Figure 4.5 – Impacts of scanline position across the 10, 18, and 36V channels for AMSR-E data (76.1932°CE, 34.3335°CN, cf. Figure 4.3), divided into quartiles based on distance from satellite (black arrow indicates far to close range). SWE amount (left axis) in black, with raw 10V (yellow), 18V (blue), and 36V (green) Tb values (right axis). All channels show impact of SWE buildup, with largest impacts on the 36V channel, particularly in the spring melt periods.

As can be seen in Figure 4.5, Tb$_{10V}$, Tb$_{18V}$, and Tb$_{36V}$ remain relatively constant across all scanline positions. While there are some differences between each quartile, these impacts are not consistent across the study area, and show no discernible topographic pattern. Hence, while scanline position differences throughout a single-point time series may have minor impacts upon SWE variability, these impacts are not universal or constrained across many points, and thus are not considered a major factor in influencing SWE variability.

Topography

As with forest cover, topographic parameters have long been known to impact Tb and SWE measurements (Mätzler and Standley, 2000; Armstrong and Brodzik, 2001; Mizukami and Perica, 2012; Dong et al., 2005). However, as many SWE algorithms have been calibrated over wide, flat, and forested zones (e.g., Northern Canada, Siberia), the relationship between topographic parameters and SWE estimation remains unconstrained.

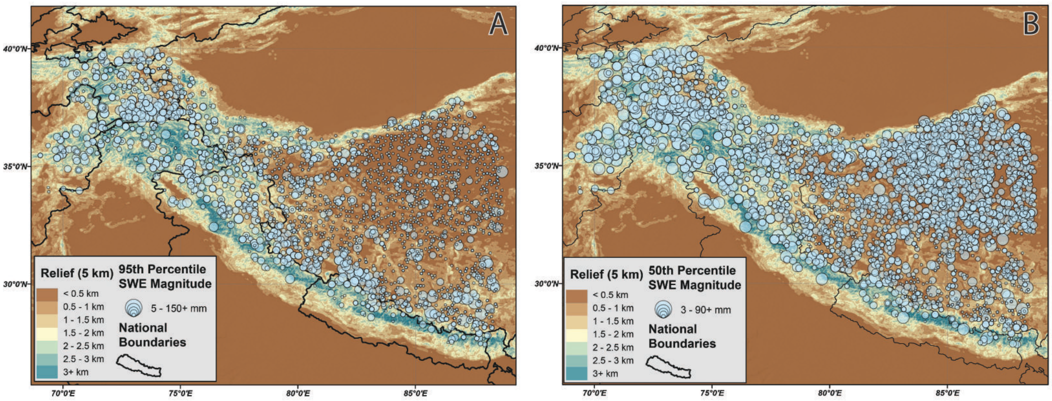

Figure 4.6 – (A) Multi-year maximal SWE, proxied by 95th percentile SWE volume, and (B) 50th percentile SWE volume, over the period 2000-2015, calculated from a merged dataset of daily values across all sensors. 5-km radius topographic relief in background.

Across all instruments, we see that relief and 95th percentile SWE volume are spatially correlated (Fig. 4.6). It is not clear whether this relationship stems from regional weather patterns, precipitation capture in complex terrain, or constructive interference in the PM spectrum over complex terrain. However, it is clear that both SWE volume and topographic parameters have impacts on SWE variability; examining whether these two impacts are manifestations of the same uncertainty in SWE measurements is outside the scope of this study.

Results

Linear Regressions

To explore the significance of several topographic and land cover indices on SWE variability, we performed a series of linear regressions on an aggregate and by-instrument basis. For each of our 2500 randomly chosen point locations, we extracted raw PM measurements within a radius of ~10-km (0.1°), and derived measures of both bulk SWE and clear-day SWE variability (defined as days where temperature does not rise above 0°C and there is less than 0.1-mm sensed precipitation) over the entire time series, which we then compare to the topographic parameters of each point (Fig. 4.7, Tables 4.2 and 4.3). Additional Figures and Tables for other topographic indices are available in the Supplement (Figs. A2-A6, Tables A1-A4).

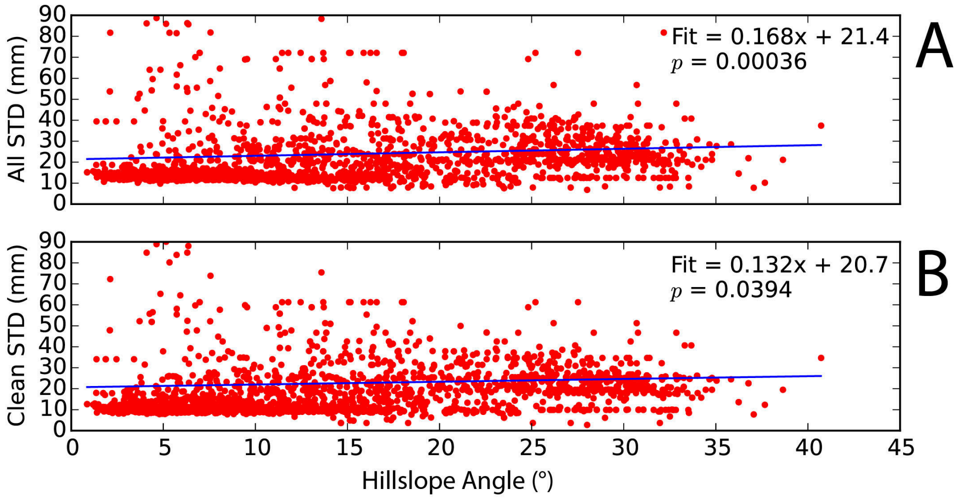

Figure 4.7 – Correlation between SWE variability (standard deviation, STD) and hillslope angle across all instruments and all sample points show in Figure 4.1 (n=2500). (A) Aggregate total variability on y-axis and (B) clear-day variability on the y-axis, with regression lines and p-values on each. Individual regression results available in Table 4.2.

When long-term variability in the SWE time series is compared to hillslope angle, we see significant ($p < 0.05$) results across all satellites (Table 4.2). When examining the entire time series, there is intrinsic variability in the SWE signal when snow falls between measurements. To control for this, we examine the SWE signal variability over only clear days. These results are also significant across all satellites, albeit with different regression slopes. This implies that hillslope angle has a direct influence on the reliability or consistency of SWE measurements, albeit with differences in regression coefficient related to PM instrument, the length of the sensed time series, and the temporal coverage of the time series. However, it is not clear whether the increase in SWE variability at steeper hillslopes in our study region is due solely to topographic impacts, or is also driven by regional weather patterns or other confounding effects.

Linear regressions for other topographic and land cover variables can be found in the Supplement (Tables A1-A4). No other topographic indices maintain an appreciable positive or negative relationship across multiple satellites. We find, however, a significant correlation between clear-day SWE variation and long-term wind patterns, as measured by HAR 10-m wind speed (Table 4.3).

For mean, median, 25th, 75th, and 90th percentile long-term DJF wind speeds, we see significant relationships, where consistently low-wind areas (low 25th percentile wind speeds) exhibit higher variance in SWE estimates (additional regression results available in the Supplement, Tables A1-A4). There are significant differences in the re-

Table 4.2 – Slopes of regressions against hillslope angle (n=2500), including p-values, t-values, and 95% confidence intervals (CI). Total individual points (all days/clear-day): All Satellites (30,865,102/14,804,414), SSMI (2,224,350/1,586,970), SSMIS (4,089,875/2,786,589), AMSR-E (15,302,564/7,284,209), AMSR2 (6,660,429/2,678,470), GPM (2,587,848/468,176). Bold values indicate statistically significant results (p <0.05).

Metric	All Satellites	SSMI	SSMI/S	AMSR-E	AMSR2	GPM
All-day Slope	0.168	0.491	0.359	0.17	0.45	0.322
All-day Slope p-values	0.00036	2.92e-109	4.5e-69	0.0261	4.63e-55	1.42e-28
All-day Slope t-values	3.57	23.4	18.1	2.23	16	11.2
All-day Slope CI	0.0905-0.245	0.457-0.526	0.327-0.392	0.0443-0.296	0.404-0.296	0.274-0.369
Clean-day Slope	0.311	0.141	0.463	6.64	0.458	0.109
Clean-day Slope p-values	5.43e-07	0.031	1.94e-108	9.83e-91	9.74e-75	1.42e-28
Clean-day Slope t-values	5.02	2.16	23.3	21.1	18.9	1.24
Clean-day Slope CI	0.209-0.412	0.0334-0.248	0.43-0.495	6.12-7.16	0.418-7.16	-0.0352-0.252

Table 4.3 – Slopes of regressions against 14-year 25th percentile 10-m DJF Wind Speed (n=2500), including p-values, t-values, and 95% confidence intervals (CI). Total individual points (all days/clear-day): All Satellites (30,865,102/14,804,414), SSMI (2,224,350/1,586,970), SSMIS (4,089,875/2,786,589), AMSR-E (15,302,564/7,284,209), AMSR2 (6,660,429/2,678,470), GPM (2,587,848/468,176). Bold values indicate statistically significant results (p <0.05).

Metric	All Satellites	SSMI	SSMI/S	AMSR-E	AMSR2	GPM
All-day Slope	-1.27	-0.28	-0.565	-1.37	-0.525	-1.11
All-day Slope p-values	1.57e-06	0.0327	2.03e-06	0.00146	0.00161	1.54e-11
All-day Slope t-values	-4.81	-2.14	-4.76	-3.19	-3.16	-6.78
All-day Slope CI	-1.71--0.838	-0.495--0.0643	-0.76--0.37	-2.08--0.662	-0.798--0.662	-1.38--0.842
Clean-day Slope	-1.12	-1.57	-0.306	13.9	-0.693	-1.64
Clean-day Slope p-values	0.00143	7.29e-06	0.013	5.86e-100	3.64e-06	1.54e-11
Clean-day Slope t-values	-3.19	-4.49	-2.48	22.2	-4.64	-2.86
Clean-day Slope CI	-1.69--0.541	-2.14--0.995	-0.508--0.103	12.9-15	-0.939-15	-2.59--0.696

gression slopes across different satellite platforms, in both Tables 4.2 and 4.3. We attribute this to differences in data capture time, data density, and the temporal range of the different satellite platforms. These differences indicate that any blended or multi-instrument SWE product must account for these differences to generate an accurate SWE estimate.

Discussion

Multiple Regression

To determine the relative impacts of several variables on clear-day SWE variability, we set up a multiple regression, with clear-day SWE standard deviation as the independent variable and maximal SWE volume, forest fraction, hillslope angle, relief, elevation and both 25th and 90th percentile DJF wind speeds as dependent variables. In this analysis, we use 95th percentile SWE volume, calculated over the entire time series, as a proxy for maximal SWE volume (Table 4.4). While SWE variation within a single PM footprint is likely to influence SWE variability, without significant in-situ data these impacts are hard to quantify. In this regression, we assume that some of the in-footprint variability is proxied by both topographic relief and by wind speeds, which could both impact the distribution of SWE within a single PM pixel.

Table 4.4 – Coefficients of Multiple Regressions for GPM (n=2500), including p-values, t-values, 95% confidence intervals (CI), and percentage of total variance. Bold values indicate statistically significant results (p <0.05).

Metric	Coefficient	p-value	t-value	Confidence Interval	Percent of Total
Forest Fraction	2.97	0.206	1.27	-1.63 - 7.57	75.8%
95th Percentile SWE	0.306	0	206	0.303 - 0.309	7.82%
90th Percentile Wind	0.22	2.13e-08	5.62	0.143 - 0.297	5.62%
25th Percentile Wind	-0.213	0.000953	-3.31	-0.34 - -0.087	5.44%
Hillslope Angle	0.205	6.84e-23	9.95	0.165 - 0.246	5.24%
Relief	-0.00236	9.93e-17	-8.36	-0.003 - -0.002	0.0603%
Elevation	-0.00224	4.86e-317	-44.4	-0.002 - -0.002	0.0572%

We observe that forest fraction is the strongest control on SWE variability (Table 4.4). This is followed by long-term 95th percentile SWE, 90th percentile DJF wind speed, 25th percentile DJF wind speed, hillslope angle, relief, and elevation. Interestingly, terrain slope has a $\sim$10 times greater effect upon SWE variability than terrain relief does in our study area (Table 4.4).

In our study region, there are relatively few geographic areas with significant forest cover (cf. Figure 4.2D). When a multiple regression is performed only on points with less than 5% forest fraction (the majority of our study area), the coefficients of regression for each of the other variables are nearly identical, as can be seen in Table A6 of the Supplement. This implies that forest fraction has very little impact upon the relationship between SWE variability and the other variables used in the multiple regression in HMA. We do not have enough sample points with dense forest cover to provide statistically significant results for a similar regression analysis on only those points with greater than 5% forest fraction.

While forest fraction is a factor controlled for in modern SWE estimation algorithms, wind speed, topographic slope, and maximal SWE volume are not. These factors will all have impacts on SWE estimation, and can help account for some of the uncertainty noted in SWE estimation studies (e.g., Mizukami and Perica, 2012; Dai et al., 2015; Foster et al., 2005; Tedesco and Narvekar, 2010). In particular, the sensitivity of SWE variance to 95th percentile

SWE implies that deep snow is still very difficult for PM SWE algorithms to estimate. Several studies have noted that SWE estimation becomes far less reliable at depths greater than 200-mm (e.g Vuyovich et al., 2014; Clifford, 2010; Andreadis and Lettenmaier, 2006; Tong et al., 2010; Dong et al., 2005). While both the Tb_{10V} and Tb_{18V} signals will be impacted by snow surface temperatures, several authors note that the Tb_{10V} signal is less influenced by deep snowpack than the Tb_{18V} (e.g., Kelly, 2009; Derksen, 2008; Tedesco et al., 2015; Tong et al., 2010).

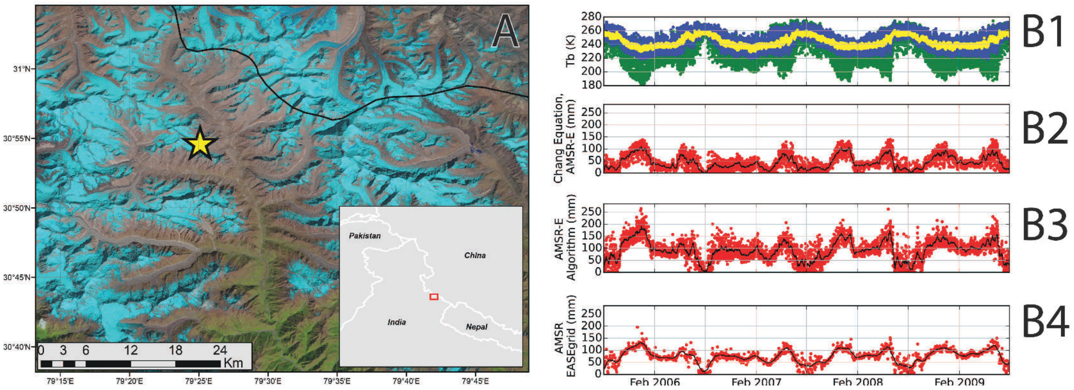

Figure 4.8 – (A) Landsat 8 Image (Oct 5, 2015, LC81450392015276LGN00), showing a point location in the western Himalaya (79.418247, 30.911184) surrounded by glaciers. (B1) Raw 10V (yellow), 18V (blue), and 37V (green) signal; (B2) Chang equation SWE estimates, with AMSR-E data; (B3) AMSR-E algorithm SWE estimates; (B4) AMSR EASEgrid SWE estimates. Illustrates how persistent snow cover can disrupt the 10V signal. SWE is also likely significantly underestimated in locations such as this with glacial ice or deep snow cover.

This effect is particularly pronounced in regions where there is constant or nearly-constant snow cover (e.g., Figure 4.8). Throughout the year, and in particular during the winter months, all three channels (Tb_{10V}, Tb_{18V}, and Tb_{36V}) are impacted by snow buildup, even though the Tb_{10V} and Tb_{18V} channels are treated as a 'bare-soil' signal by many algorithms (e.g., Chang et al., 1987; Kelly et al., 2003; Pulliainen, 2006; Kelly, 2009; Takala et al., 2011; Mizukami and Perica, 2012; Savoie et al., 2009; Derksen, 2008). This snow signal is captured by both the Chang equation (Fig. 4.8B2) and the AMSR-E SWE algorithm (Fig. 4.8B3), although it is unlikely that either estimate properly captures the *magnitude* of SWE. It is likely that those areas which see constant or nearly-constant snow cover develop larger snow crystals, which interfere more strongly with the Tb_{10V} and Tb_{18V} channels than fresh or seasonal snow. However, without in-situ data, it is difficult to separate these two interacting impacts.

While some point locations in our dataset see constant snow cover (cf. Figure 4.8), this effect is also visible in areas with seasonal snow cover (cf. Figure 4.5). Those points with constant deep snow cover are likely to *weaken* the relationship between maximal SWE depth and SWE variability by lowering the possible range of SWE values. Despite the potential for SWE signal saturation at high snow depths, we still see a strong positive correlation between 95th percentile SWE and SWE variability.

Both 90th and 25th percentile DJF 10-m wind speeds show strong impacts in our multiple regression. We attribute this effect – which is not consistent across all satellites – to wind-blown snow redistribution. Areas of high wind are typically topographically complex, and see wind-blown snow redistribution mostly in the form of avalanches which do not travel much further than the extent of a single PM pixel. These regions typically see more annual snow as well, which could confound the wind signal. However, low-wind areas, which correlate with large, flat regions in our study area, could see snow redistribution over a very large area, especially if there are few windbreaks.

Spatial Distribution of Uncertainties

Based on our multiple-regression analysis, we have developed a map showing the distribution of SWE uncertainty throughout our study area (Fig. 4.9). This is based on topographic parameters, HAR wind speed, land cover (MOD12Q1), and long-term 95th percentile SWE estimates derived from daily AMSR-E EASEgrid SWE measurements (2002-2011) (Tedesco et al., 2004), and does not include any uncertainties introduced by differing algorithms or 'instantaneous' ground conditions, such as precipitation or snow recrystallization. We use the AMSR-E EASEgrid to generate our SWE volume proxy as it covers the whole study area with a continuous surface at a comparable spatial resolution to the other input datasets.

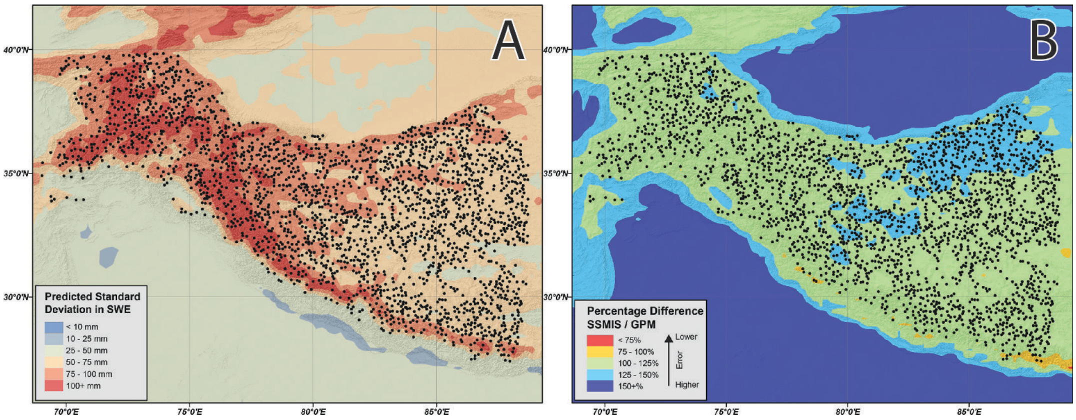

Figure 4.9 – Spatial distribution showing SWE uncertainties from PM data using (A) the multi-parameter estimated using regression coefficients from the GPM satellite (one year of data, Table 4.4). (B) Percentage difference between the uncertainty of the SSMIS satellite and the uncertainty of the GPM satellite (100% indicates equal uncertainty in both satellites, lower values indicate SSMIS is better) and black arrow in the legend indicates direction from high to low uncertainty. In general, the GPM satellite shows lower uncertainty across the entire study area. Additional comparisons available in the Supplement (Figs. A10-A15).

As can be seen in Figure 4.9, SWE uncertainty is strongly correlated with complex topography, as has been proposed in previous publications (Mizukami and Perica, 2012; Tedesco and Narvekar, 2010). However, the multiple regression also implies that topographic complexity is not the only controlling variable. For example, the north-central portions of the Tibetan Plateau, while topographically flat, see relatively high SWE variation due to the combination of higher snowfall totals than the south-eastern areas of the Plateau and more wind-related snow redistribution. These estimates can provide a first-order assessment of SWE measurement reliability throughout the world, and particularly in regions where ground-truth data are sparse. While a generalized uncertainty map combining the results of all of the satellite time series would be desirable, the multiple regression results on a by-satellite basis (available in the Supplement, Tables A5-16) indicate that there are important differences in regression coefficients across satellites. When considered in aggregate, these differences dilute the uncertainty signatures of each individual satellite. As each satellite responds slightly differently to topographic, land cover, and climatic factors, in both positive and negative directions, the aggregate regression encompasses a wider spread of uncertainties, and thus shows the least significant correlations (see Supplement, Figures A10-A15 and Tables A5-A16). The different responses of each satellite are likely due to differences in spatial, temporal, and spectral resolution and instrument hardware.

Despite these differences in uncertainty, all five satellites are able to track the *patterns* of SWE over our multi-year time series (cf. Figure 4.10). The largest differences between SWE amounts on an annual basis come when SWE amounts are greatest – for example in 2007 and 2010 – and when the SWE time series does not encompass the entire 3-month DJF period – for example in 2002 (cf. Figure 4.10).

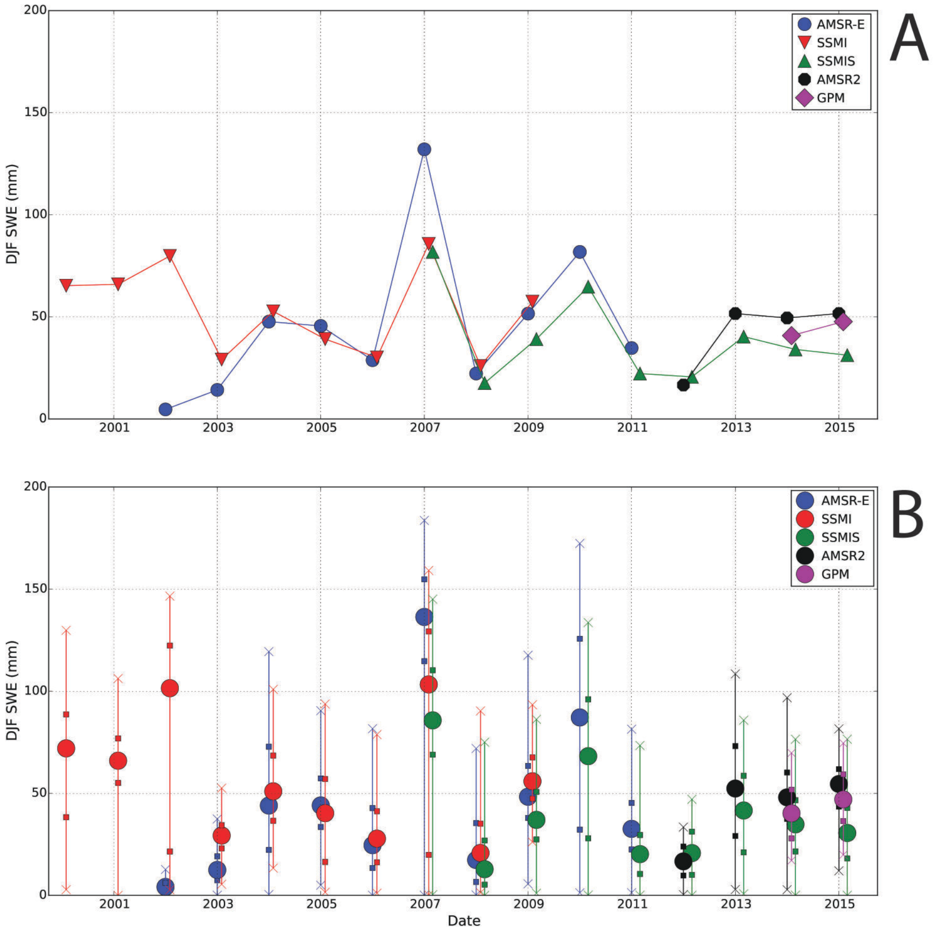

Figure 4.10 – (A) Annual DJF mean SWE amounts at a single point (cf. Figure 4.3), as sensed by SSMI (red), AMSR-E (blue), SSMIS (green), AMSR2 (black), and GPM (magenta). (B) Annual DJF median SWE amounts with DJF minima and maxima (Xs) and first and third quartiles (squares) for each. Illustrates that while each instrument senses slightly different SWE *amounts*, the inter-annual patterns of SWE are consistent across the satellites.

In our analysis, spectral resolution has the least influence on differences in SWE volume uncertainty across satellite platforms, as we use only two bands (Tb_{18V} and Tb_{36V}) in our calculations of SWE. These bands are present across all satellites, albeit with slight differences in exact channel frequency (Table 4.1). These channel differences are controlled for in the application of the Chang Equation (Equation 6.1), after Armstrong and Brodzik (2001). Differences in the temporal range and resolution of each satellite dataset could influence our calculated uncertainties, particularly due to differences in snow cover during multiple winter periods. For example, AMSR-E (2002-2011) has several different winters of data, while GPM (2014-2015) only has data from a single complete winter. However, there is high variation in both the regression coefficients and p-values when the multiple regressions are performed on a year-by-year basis. The coefficients tend to oscillate around a multi-year norm, indicating that while the multi-year regressions provide the long-term mean coefficients, the highest significance uncertainty signal will come from those data with a shorter observation period, such as GPM.

As the spatial resolutions of GPM and AMSR-E/2 are higher than those of SSMI/S (e.g., Figure 4.3), there is less intrinsic terrain variability in a single GPM/AMSR pixel than in a single SSMI/S pixel. This implies that, all other factors being equal, the SWE estimates from GPM and AMSR-E/2 will be of a higher quality (cf. Figure 4.9, and Figures A10-A15 in the Supplement). As these sensors also gather additional spectral frequencies, they are also suitable for more complicated SWE algorithms, such as those shown in Equations 2.3-2.5.

Discussion of Additional SWE Uncertainties

The above regressions have noted some possible topographic, land cover, and weather-related SWE measurement uncertainty sources. However, there are several other possible uncertainty sources, which have been accounted for to varying degrees in previous work.

The first possible source of uncertainty, which is difficult to control for, is inter- and intra-sensor biases. Some studies, such as Dai et al. (2015), have identified SWE biases between the various satellites of the SSMI/S constellation. Intercalibration of multiple satellites is challenging due to the dearth of wide-scale and long-term SWE ground measurements. Additionally, the Tb_{18V} channel present on all of the studied satellites is considered as a clean soil signal from the snow-covered earth in the Chang equation. However, the influence of SWE buildup can be seen clearly in this channel, for example in Figures 4.5 and 4.8. While modern algorithms also take advantage of the Tb_{10V} signal for deep-snow estimation (e.g., Kelly, 2009; Tedesco and Narvekar, 2010; Derksen, 2008), Figure 4.8 also shows SWE influence on that channel. Therefore, there will be inherent bias in any SWE estimation, especially in deep-snow situations.

Previous work has also implicated high relief areas as low SWE confidence areas (Mätzler and Standley, 2000; Tedesco and Narvekar, 2010). This is due to relief not only influencing the size of the satellite footprint through shadowing, but also changing the relative satellite look angle and angle of incidence for polarization. Our results indicate that topographic parameters do indeed influence SWE reliability, although it is not clear whether overshadowing, satellite look angle, polarization changes, or a secondary impact of topography such as precipitation capture are most responsible for changes in SWE reliability. Additionally, terrain slope has a much larger impact upon SWE variability than terrain relief does in our study area (Table 4.4).

Conclusion

This study presents a multi-parameter uncertainty assessment of passive microwave (PM) snow-water equivalent (SWE) estimation using the Special Sensor Microwave/Imager (SSMI), Special Sensor Microwave Imager/Sounder (SSMIS), Advanced Microwave Scanning Radiometer - Earth Observing System (AMSR-E), AMSR2, and Global Precipitation Measurement (GPM) satellites. We identify and assess a suite of possible uncertainty sources in the raw PM data, as well as in the SWE estimations from multiple overlapping time series. We use these uncertainty sources to develop a multi-parameter estimation of inherent unreliability in SWE estimates across High Mountain Asia, including the Tibetan Plateau and the Himalaya. We find that forest fraction is the strongest control on SWE variability, followed by long-term maximal SWE volume, wind speed, and hillslope angle. Elevation, relief, and terrain aspect show very low influence on SWE variability. While forest cover and topographic parameters have been integrated into many SWE algorithms, wind speed and long-term maximal SWE volume have not. The results derived here show that wind-redistribution of snow can have impacts on SWE, especially over large, flat, areas. The uncertainty map developed here provides a first-order approximation of SWE-estimate reliability for much of High Asia, and implies that high-fidelity SWE estimates can be produced for a range of elevation zones and terrain types. We find that each individual satellite shows differences in SWE variability, with the more modern sensors (GPM, AMSR-E/2) providing the most robust SWE estimates, expressed in this analysis as low SWE variability.

Supporting Information

(see Appendix A).

CHAPTER 5

Changes in seasonal snow-water equivalent distribution in High Mountain Asia, 1987-2009[†]

TAYLOR SMITH[1], BODO BOOKHAGEN[1]

[1] *Institute of Earth and Environmental Sciences, Universität Potsdam, Germany*

Abstract

Snow meltwaters account for the majority of the yearly water budgets of many catchments in High Mountain Asia (HMA). Here we examine trends in snow-water equivalents (SWE) using passive microwave data (1987-2009). We find an overall decrease in SWE in HMA, despite regions of increased SWE in the Pamir, Kunlun Shan, Eastern Himalaya and Eastern Tien Shan. While the average decline in annual SWE across HMA (contributing area: 2,641 x 10^3 sq km) is low (average: -0.3%), annual SWE losses conceal distinct seasonal and spatial heterogeneities across the study region. For example, the Tien Shan has seen both strong increases in winter SWE and sharp declines in spring and summer SWE. In the majority of catchments, the most negative SWE trends are found in mid-elevation zones, which often correspond to the regions of highest snow-water storage and are somewhat distinct from glaciated areas. Negative changes in SWE storage in these mid-elevation zones have strong implications for downstream water availability.

Introduction

The impacts of climate change on High Mountain Asia (HMA) have been the subject of intense debate over the past decade (Bolch et al., 2012; Kääb et al., 2012; Kang et al., 2010; Immerzeel et al., 2010; Gardner et al., 2013; Hewitt, 2005; Malik et al., 2016), and remain largely unconstrained due to the lack of in-situ observational data in many areas, particularly those at high elevations (Bookhagen and Burbank, 2010). Large-scale satellite datasets, such as the Global Precipitation Measurement (GPM) (GPM Science Team, 2014), Tropical Rainfall Measurement Mission (TRMM) (Huffman et al., 2007), and the Gravity Recovery and Climate Experiment (GRACE) (Tapley et al., 2004) missions, and modeling efforts, such as High Asia Refined Analysis (HAR) (Maussion et al., 2014) and Asian Precipitation - Highly-Resolved Observational Data Integration Towards Evaluation (APHRODITE)

[†] *published as Taylor Smith and Bodo Bookhagen. "Changes in seasonal snow water equivalent distribution in High Mountain Asia (1987 to 2009)", Science Advances 4: 1, (2018)* *http://doi.org/10.1126/sciadv.1701550*

(Yatagai et al., 2012), show spatially and temporally heterogeneous trends in temperature and precipitation in the region (Malik et al., 2016). Global and regional climate models also disagree on climate projections for much of HMA, due to relatively poor understanding of the interactions between large-scale climate systems active in the region, such as the Indian Summer Monsoon (ISM), East Asian Summer Monsoon (EASM), and the Winter Westerly Disturbances (WWD) (Kapnick et al., 2014).

Climatic shifts in HMA have spatial, altitudinal, and temporal components and are not evenly felt across the region. The total yearly precipitation in the ISM region (cf. Fig. 5.1, inset) has not changed significantly over the past decades, but extensive changes in the spatial and intensity distributions of rainfall have been observed (Malik et al., 2016; Bookhagen and Burbank, 2010; Singh et al., 2014; Yao et al., 2012). Similarly, the timing and intensity of major precipitation events related to the WWD has shifted over the past 30 years (Cannon et al., 2014). As whether precipitation falls as rain or snow is determined by air temperature, changes in the timing of storm events can have large impacts on the amount of snow that falls in HMA (Lutz et al., 2014) and downstream water availability (Berghuijs et al., 2014). Consistent runoff is essential for year-round water provision for more than a billion people who rely on water sourced in HMA (Vaughan et al., 2013).

Many studies have noted extensive glacial retreat across HMA (Bolch et al., 2012; Kääb et al., 2012; Gardner et al., 2013; Scherler et al., 2011; Sorg et al., 2012), with a few notable exceptions, such as the so-called Karakoram Anomaly (Hewitt, 2005; Gardelle et al., 2012). Heterogeneity in glacier response to climate change has been attributed to hypsometric and precipitation variation (Hewitt, 2005), differences in debris cover (Scherler et al., 2011), snow-cover shielding (Kapnick et al., 2014), and precipitation seasonality (Fujita, 2008; Fujita and Nuimura, 2011). Extensive research has been focused on retreating glaciers as a symbol of regional climate change, even though the majority of meltwater in much of HMA is generated by snowmelt (Bookhagen and Burbank, 2010; Ghosh et al., 2012; Shrestha et al., 2015; Wulf et al., 2016; Jeelani et al., 2012; Immerzeel et al., 2010). Due to large spatial heterogeneity in snow cover, a regional assessment is difficult; very little in-situ data are available to constrain large uncertainties in modeled trends.

In this study, we leverage passive microwave (PM) data from the Special Sensor Microwave Imager (SSMI, 1987-2009), spatially averaged from raw swath data following Smith and Bookhagen (Smith and Bookhagen, 2016), to assess whether there have been any significant trends in snow-water equivalent (SWE) across HMA from October 1987 to October 2009. We consider a set of 6,680 grid cells with 0.25 decimal degree (dd) spatial resolution (approx. 4,175 x 10^3 sq km), with on average 8,340 measurements each (average of 1.03 measurements/day for 22 complete October-to-October years), across 10 major catchments, with a special focus on the Syr Darya, Amu Darya, Tarim, Indus, Ganges/Brahmaputra, and Tibetan Plateau catchments (Fig. 5.1). Together these catchments serve more than a billion people, many of whom depend heavily on seasonal snowmelt. In some catchments, such as the Indus and Amu Darya, nearly 50% of the yearly water budget is derived from snowmelt (Bookhagen and Burbank, 2010; Shrestha et al., 2015). The Syr Darya, Tarim, and Tibet catchments receive more than two thirds of their yearly water budget as snow (Barnett et al., 2005; Huss et al., 2017). Across the study region, the majority of the snowpack is at high elevations and is often poorly measured by sparse weather station coverage (e.g., Fig. 5.2). Our data provide

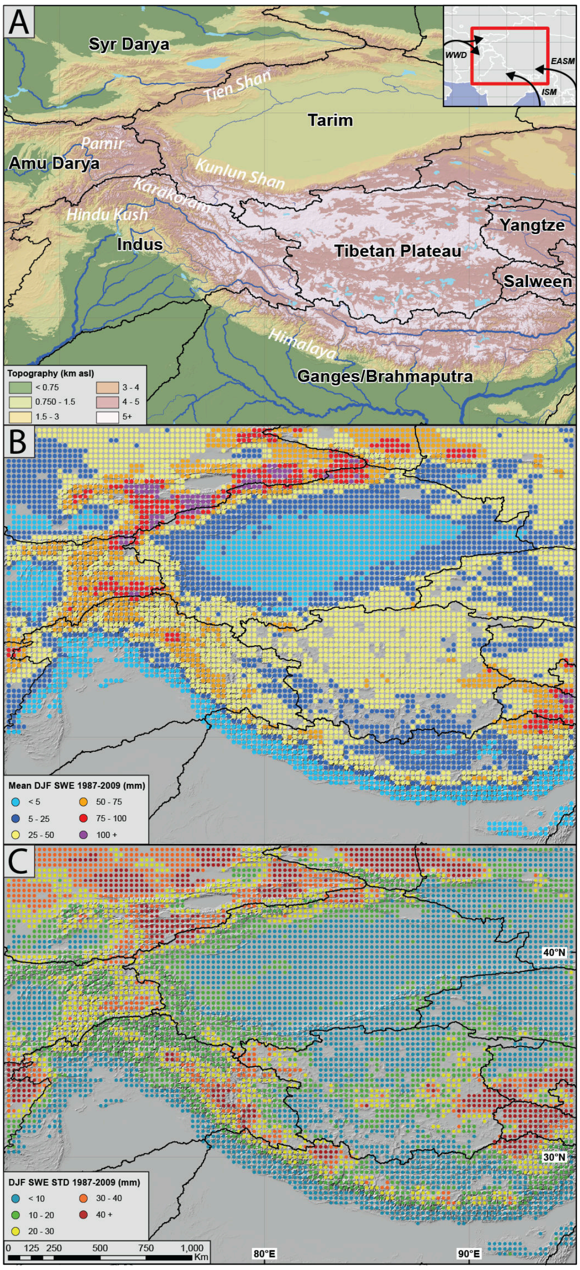

Figure 5.1 – Study Area. (A) Topographic map of High Mountain Asia (HMA) with major catchment boundaries (black) derived from SRTM data (Jarvis et al., 2008), and names of major mountain ranges. Inset map shows political boundaries, as well as wind direction of major weather systems (WWD: Winter Westerly Disturbances, ISM: Indian Summer Monsoon, EASM: East Asian Summer Monsoon). (B) 22-year average December-January-February (DJF) daily SWE volume across the study area, as derived from SSMI data. (C) DJF SWE standard deviation. Each point represents a 0.25 x 0.25 decimal degree (dd) grid cell.

information on SWE that may be poorly parameterized in regional and global models at a spatial scale that is not available to in-situ studies.

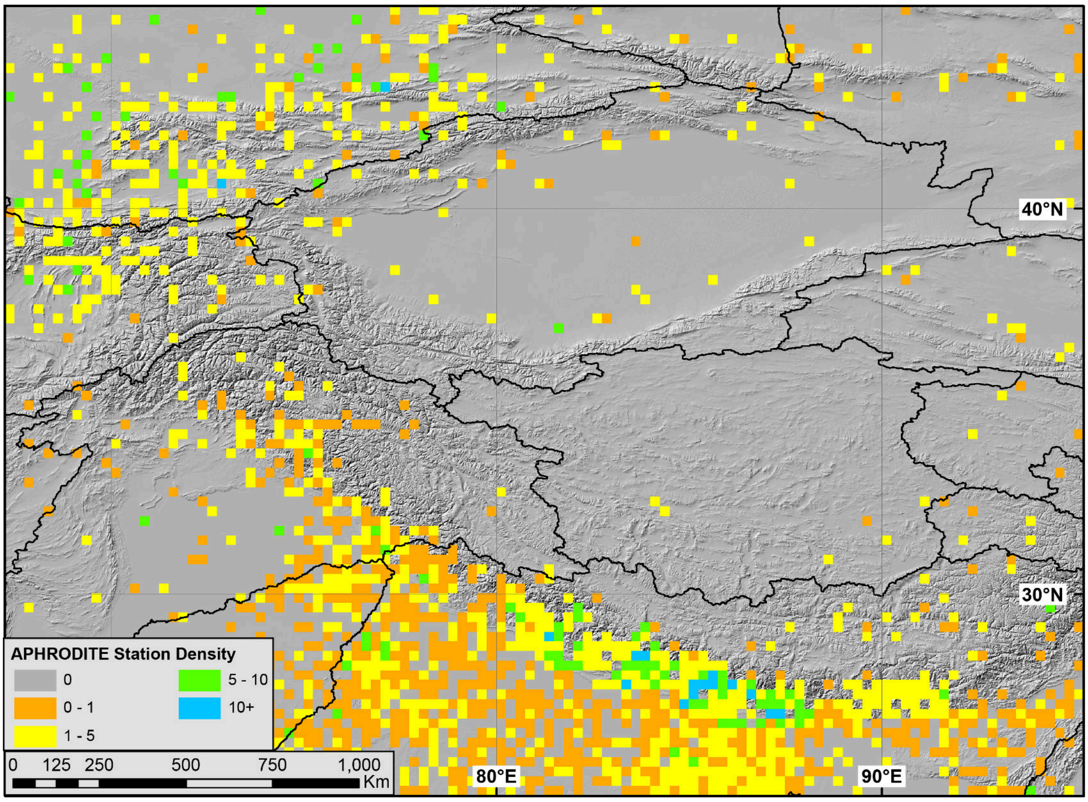

Figure 5.2 – Asian Precipitation - Highly-Resolved Observational Data Integration Towards Evaluation (APHRODITE) station density (Yatagai et al., 2012). Shown are average gridcell station densities over the past 47 years (1961-2007). Illustrates the low station density in the core of HMA (Tibetan Plateau), and that the highest elevations are severely under-represented. Note that these stations almost exclusively measure rainfall; there exist very few snow-monitoring stations in HMA.

Our results are provided with the caveats that (1) the climatically-short study period limits attribution of the trends, and (2) passive microwave SWE estimates are impacted by a wide range of uncertainties – particularly in deep snow and complex terrain, and increasingly lack physical bases as snow depths increase (Smith and Bookhagen, 2016; Takala et al., 2011; Kelly, 2009). Our results therefore provide an assessment of relative changes in SWE over the study period – and the spatial and temporal distribution of those changes – rather than concrete changes in water storage in HMA.

Spatio-temporal Patterns in Regional Snow Cover

Average winter (December-January-February, DJF) SWE ranges from zero up to more than 140 mm in some high-elevation areas. In particular, the Tien Shan, Pamir, and Hindu Kush see significant snow buildup above 2 km elevation (Fig. 5.1B). These high-SWE areas generally follow the track of the WWDs as they move northeast from the Arabian Sea and deposit snow along high-elevation topographic breaks (Fig. 5.1A, inset). Southern HMA also receives snow from the tail end of the ISM as it moves north and west towards the Indus. As each region of HMA is impacted by different climatic systems – and the impacts of climate change are spatially diverse – trends in SWE are not uniform. While annual trends (1987-2009) in SWE (cf. Fig. 5.3) are generally negative across HMA, there are distinct seasonal and elevation heterogeneities.

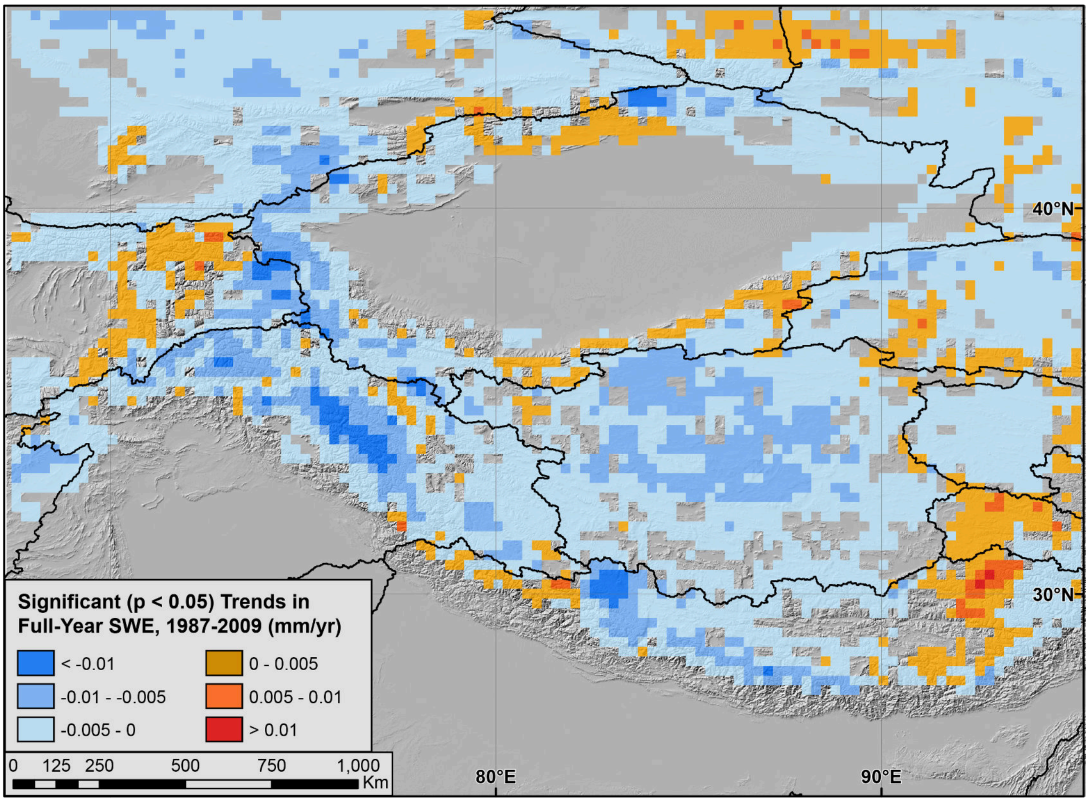

Figure 5.3 – Annual trends in SWE volume (1987-2009), as derived from SSMI data, with major regional watersheds (black outlines). Parts of the Tien Shan, the Kunlun Shan, and parts of the central and eastern Himalaya see overall positive SWE signals in the study period. All points shown are significant ($p < 0.05$).

In general, SWE in HMA is decreasing across the period March-August (Fig. 5.4B,C), but some areas, particularly in the Pamir-Tien Shan region, exhibit a significant positive DJF trend over our study period (Fig. 5.4A). A smaller geographic area, mainly in the Himalaya, Karakoram, and Kunlun Shan, shows increasing trends in fall (September-October-November, SON) SWE (Fig. 5.4D).

DJF and SON SWE trends are generally negative from the Hindu Kush in the northern Indus catchment, along the Himalayan Front, and through the Tibetan Plateau. The exception to this is along the border between the Indus and Ganges catchments (Gharwal), where positive SWE trends are observed. Increases in SON/DJF SWE in this region are possibly linked to changes in the WWD, which has resulted in increased snowfall in parts of the

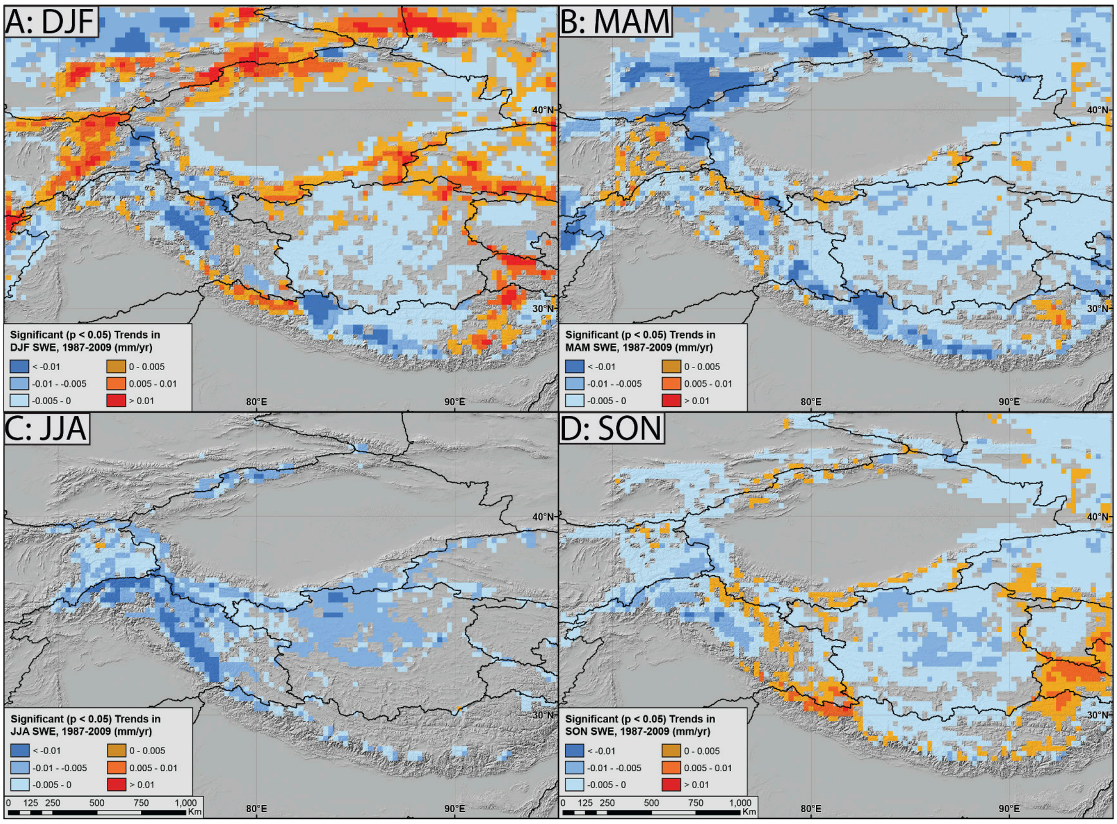

Figure 5.4 – Seasonality in SWE Trends. Significant (p <0.05) (A) December-January-February (DJF), (B) March-April-May (MAM), (C) June-July-August (JJA), and (D) September-October-November (SON) trends in SWE volume (1987-2009), as derived from SSMI data, with major catchments (black outlines, cf. Fig. 5.1A). We limit our analysis to regions where the seasonal average SWE is greater than 5 mm to remove spurious results in areas with shallow or infrequent snow cover. MAM and JJA trends across HMA are overwhelmingly negative, excepting a few isolated regions. DJF trends are more widely positive, and are also present in SON in the western Himalaya, the Tien Shan and the Kunlun Shan.

Indus (Tahir et al., 2011; Cannon et al., 2014; Norris et al., 2016), and are strong enough to show positive annual SWE trends in opposition to the general decrease in SWE in HMA (cf. Fig. 5.3).

The northwestern region of HMA, following the track of the WWD (cf. Fig. 5.1A, inset) through the Amu Darya catchment towards the Tien Shan into the north-western Tarim has also seen increasing DJF SWE over the study period, which is in line with measured increases in precipitation in the Pamir and parts of the Tien Shan (Sorg et al., 2012; Aizen et al., 1997), and increased snow cover in western China (Dahe et al., 2006). This is particularly true along the border between the Syr Darya and Tarim catchments in the Tien Shan, despite decreasing trends in mean annual precipitation as measured by sparse in-situ climate stations (Sorg et al., 2012). These trends align well with a proposed increase in the strength of the WWD over the past 30 years (Cannon et al., 2014, 2016), and observed increases in DJF precipitation in northern Pakistan (Pamir-Karakoram) (Archer and Fowler, 2004; Treydte et al., 2006). The full extent of changes in SWE, and in particular the positive SWE trends at high elevations, had not yet been observed outside of model data.

Spring (March-April-May, MAM) SWE trends are distinctly negative, excepting where some of the high-elevation regions of the Pamir-Karakoram (northern Indus and Amu Darya catchments) show positive SWE trends (Fig. 5.4B), which may be related to the positive regional DJF trends. The dramatic DJF-MAM trend reversal in the Tien Shan could indicate that increasing spring temperatures have led to faster spring runoff despite increased winter snowpack – a trend that has already been observed in snow cover, but not SWE, changes in Central Asia (Sorg et al., 2012; Aizen et al., 1997; Smith et al., 2017). Higher air temperatures across HMA could also induce a shift from snow to rain, which would also reduce SWE storage.

Trends in summer (June-July-August, JJA) SWE are negative across the study region, where enough SWE is present to allow for trend analysis (Fig. 5.4C). This is in line with projections of increased temperatures in HMA (Yao et al., 2012), which drive earlier melting of snow (Xu et al., 2017; Smith et al., 2017), and increase the ratio of liquid precipitation to snowfall in much of the region (Lutz et al., 2014). The decline in summer SWE in the Himalaya is consistent with observed changes in the precipitation distribution of the ISM (Singh et al., 2014; Palazzi et al., 2013) and melt rate enhancement from decreases in snow albedo due to aerosol contamination (Lau et al., 2010).

When these trends are considered together, they imply an intensification of the yearly hydrological cycle, where winter storms deposit more snow, particularly at high elevations, while warming summer temperatures cause rapid melting. Under this scenario, late-spring to early-fall water storage will decrease, with potentially dire implications for year-round water provision in many communities that rely directly on the slow melting of large snowfields for dry-season water provision (Vaughan et al., 2013).

Aggregated Trends Across Elevations

While seasonal trend analysis provides valuable information on potential changes in local hydrologic budgets, it does not account for whether these changes occur in low- or high-SWE areas, and what the elevation distribution of these changes is. We aggregate SWE trend and distribution data on a catchment scale and segment it into a succession of 5th-percentile elevation slices to illustrate the variation of trends across elevation zones (Fig. 5.5). Catchment-aggregated trend statistics can be found in Tables B1-B5.

Across all catchments, there is a strong, non-linear, elevation-SWE relationship; the nature and magnitude of these relationships – as well as each individual catchment's glacier and SWE distribution – are distinct, and contextualized by the unique topographic and climatic setting of each catchment. High-elevation DJF snow and glacier coverage is nearly complete, although actual catchment hypsometries vary significantly (Figs. B1-B6). The highest SWE-volume elevation slice in each catchment occurs below the maximal catchment elevation in the majority of catchments (Fig. 5.5A).

In the northern, lower-elevation, regions of HMA (Amu Darya, Syr Darya, and Tarim catchments), positive SWE changes are limited to DJF (Figs. B1-B3). In particular, the Syr Darya catchment has experienced strong increases in high-elevation DJF SWE (Figs. 5.4A, B1), while also having some of the strongest negative trends in MAM SWE (Table B3). The Tarim and Amu Darya catchments also see positive DJF trends – albeit with different eleva-

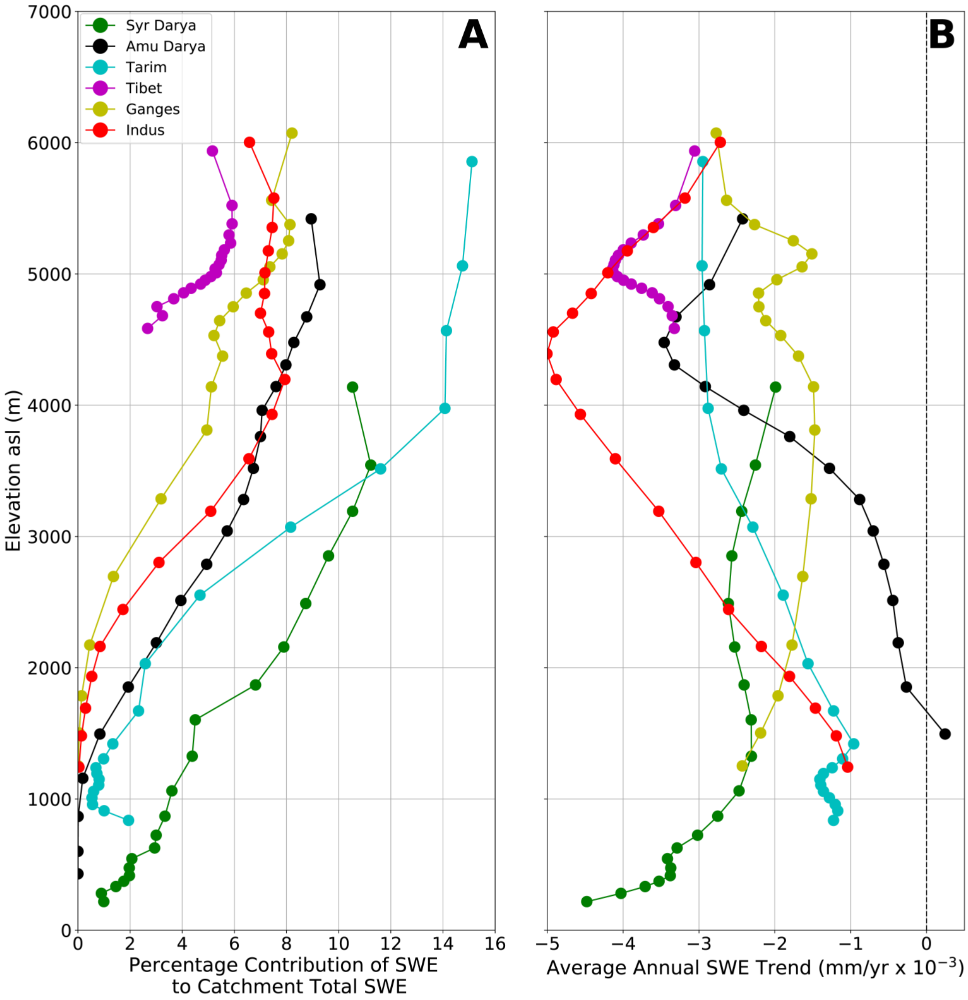

Figure 5.5 – SWE Contribution and SWE trend synthesis: (A) Elevation distribution of SWE in each catchment, where each point shows percentage of total-catchment SWE at each 5th percentile elevation bin. (B) Mean SWE trend at each 5th percentile elevation bin. In the majority of catchments, maximum SWE occurs below the maximum catchment elevation, despite differences in catchment hypsometry. Each catchment is characterized by a unique elevation-trend relationship. The Indus, Amu Darya, and Tibetan Plateau catchments see the most negative SWE trends at their mid-elevations. The Ganges in the central Himalaya sees the most negative trends at the highest elevations.

tion distributions – and negative MAM-JJA trends. The Amu Darya and Tarim, however, see less negative MAM SWE trends, implying more persistence of SWE into the spring melt season in these catchments than in the Syr Darya. Across all three catchments, however, full-year SWE trends remain negative, excepting at the very lowest parts of the Amu Darya (Fig.5.5, Table B1).

The central and southern HMA catchments (Tibet, Indus, Ganges/Brahmaputra) store much less low-elevation SWE than the northern catchments. To simplify the discussion of SWE trends for these catchments, we have focused on elevations above 1,000 m, where the vast majority of snowfall occurs. All three catchments exhibit a mid-elevation decrease in their SWE trends, where mid-elevation trends are more negative than those at higher or lower elevations (Fig. 5.5B). The only catchment out of the six examined in this study where the most negative SWE trends occur at the highest elevations is the Ganges/Brahmaputra (Fig. 5.5B, yellow line). This is in line with increased temperatures in low-precipitation, high-elevation zones of the Himalaya (Bolch et al., 2012; Pepin et al., 2015). It is likely that the decreasing SWE trends in this area at high elevations have also influenced glacial declines, which are some of the fastest in HMA (Bolch et al., 2012).

Implications for Glaciers

Many recent studies (Bolch et al., 2012; Kääb et al., 2012, 2015; Gardner et al., 2013; Kapnick et al., 2014; Yao et al., 2012; Scherler et al., 2011; Gardelle et al., 2012; Frey et al., 2014) have examined glaciers in HMA across several spatial scales. Glacier retreat rates are not uniform across HMA; some distinct regions of rapid decline, stability, and even growth exist. Two regions where studies have shown stability or glacier growth are the Karakoram (Hewitt, 2005; Gardelle et al., 2012; Wang et al., 2017) and the Kunlun Shan (Gardner et al., 2013; Yao et al., 2012; Kääb et al., 2015). Our data show positive trends in DJF, MAM, and SON SWE for parts or all of both regions, which indicates that increases in winter SWE storage could be partially responsible for glacier stability and growth in these regions. These positive SWE regions generally match the increased precipitation regions found by Yao et al. (Yao et al., 2012) and are consistent with the proposed increase in the strength of the WWD (Cannon et al., 2014). Previous work has argued that HMA's glaciers are more strongly impacted by changes in precipitation seasonality than by changes in annual precipitation (Fujita, 2008; Fujita and Nuimura, 2011; Kapnick et al., 2014). In the cold and dry Kunlun Shan, glaciers are less sensitive to rising regional temperatures, and thus the trend towards wintertime SWE increases (Fig. 5.4A) could help explain some of the observed glacial thickening. As many glaciers are fed by avalanching as well as direct snowfall (Scherler et al., 2011), changes in high-elevation precipitation are an important factor to account for when estimating future glacier mass budgets.

Strongly negative summer SWE trends are found in the central Indus catchment (Jammu-Kashmir region), and correspond with some of the most rapidly shrinking glaciers in the region (Kääb et al., 2012). These wasting rates are confirmed in further studies that found that the western and central Himalaya have some of the highest glacier wasting rates in HMA (Gardner et al., 2013; Yao et al., 2012). This implies a more intense melt period in the summer, potentially due to increased temperatures in the region (Vaughan et al., 2013). Monsoon-fed glaciers along the Himalayan front could also be impacted by rising summer temperatures, which would favor rain over snowfall and reduce glacier albedo by limiting the persistence of fresh snow.

Spatially and temporally variable glacier retreat rates were found for the central Tien Shan using a suite of orthorectified satellite images (Narama et al., 2010). Further work noted that while there was an overall decrease of glacial mass in the Tien Shan, some high elevation glaciers, particularly those on the eastern inner edge of the Tien Shan, have stable or slightly positive mass balances (Farinotti et al., 2015). This area agrees well with both positive DJF SWE anomalies (cf. Fig. 5.4A) and overall positive SWE trends (cf. Fig. 5.3). However, Gardner et al. (Gardner et al., 2013) using Ice, Cloud and land Elevation Satellite (ICESat) data, found overall negative trends for glaciers in the Tien Shan. It is possible that the poor sampling frequency of ICESat led to an overestimation of glacier wasting rates in the region, or that the increases in SWE observed in this study are not translated into glacier ice in the predominantly summer-accumulation Tien Shan glaciers, and thus do not have a strong impact upon glacier mass balances in this region (Fujita and Nuimura, 2011).

Spatially diverse water storage trends across HMA have also been noted in GRACE data. For example, negative gravity anomaly trends are smaller in the Tien Shan than in the Karakoram or Himalaya (Matsuo and Heki, 2010). Positive storage anomalies were also found in the Pamir, Tien Shan, eastern Himalaya (Moiwo et al., 2011), and eastern Kunlun Shan (Jacob et al., 2012). These gravity anomalies, which were attributed to changes in glaciers, may also represent a change in seasonal snow-water storage patterns. Changes in seasonal water distribution have also been observed in GRACE data; positive and negative seasonal water storage anomalies correlate well with the positive and negative anomalies present in the SWE data shown in this study. While the overall trend in the GRACE data are negative, some areas have seasonally positive mass signatures.

Regional Impact

Climate models have trouble correctly estimating SWE buildup in high-elevation areas due to a dearth of calibration data, complex topography, and poor measurement of snowfall and SWE with current generation weather satellites, which negatively impacts model parameterization and calibration (Kapnick et al., 2014). For example, in the Tien Shan, only three stations exist above 3,000 m, and these stations fail to show significant correlations with reanalysis data (Sorg et al., 2012) (Fig. 5.2). The data presented here indicate that there have been unmeasured changes in HMA's SWE distribution; these changes have important implications for both glaciers and downstream water provision.

The aggregated data show a HMA-wide annual net loss in SWE (-10.60 mm/yr (average: -0.3%) over 2,641 x 10^3 sq km, including only trends with p <0.05 and areas above 500 m asl) over the period 1987-2009 (Figs. 5.3, 5.5, Table B1). While there have been positive changes in SWE in some areas of HMA, particularly in the winter and at the highest elevations (cf. Figs. 5.3, 5.5, Table B2), these changes are outweighed by the net losses in the medium and low-elevation zones of each catchment (Fig. 5.5B). Unfortunately, due to the poor performance of SWE algorithms in complex terrain (Smith and Bookhagen, 2016; Takala et al., 2011), converting these changes into absolute discharge or sea-level contributions is not feasible. While SWE data have been shown to be internally consistent (Smith and Bookhagen, 2016), absolute SWE volume measurement is not precise (Tedesco and Narvekar, 2010). However, significant observations about the areal and elevation distribution of SWE and relative SWE changes can still be made from the data.

The highest SWE totals in many catchments occur below the maximum catchment elevation (Figs. 5.5,5.6). This implies that while the negative SWE trends at the highest elevations are important, particularly for glaciers, downstream meltwater discharge is more strongly impacted by SWE trends at the middle elevations of each catchment. SWE trends in the mid-elevation zones of the Indus and Ganges – between 4,000 and 5,000 m asl – are more negative than trends at lower and higher elevations (Fig. 5.5). As the mid-elevations are less heavily glaciated than high-elevation zones (cf. Fig. 5.6), it is likely that changes in glaciers and snowfields will be somewhat distinct. Figure 5.6 indicates that the impacts of SWE changes will be unevenly felt even in neighboring catchments, as the majority of the SWE in the Indus is stored at significantly lower elevations than in the Ganges. SWE trends at the

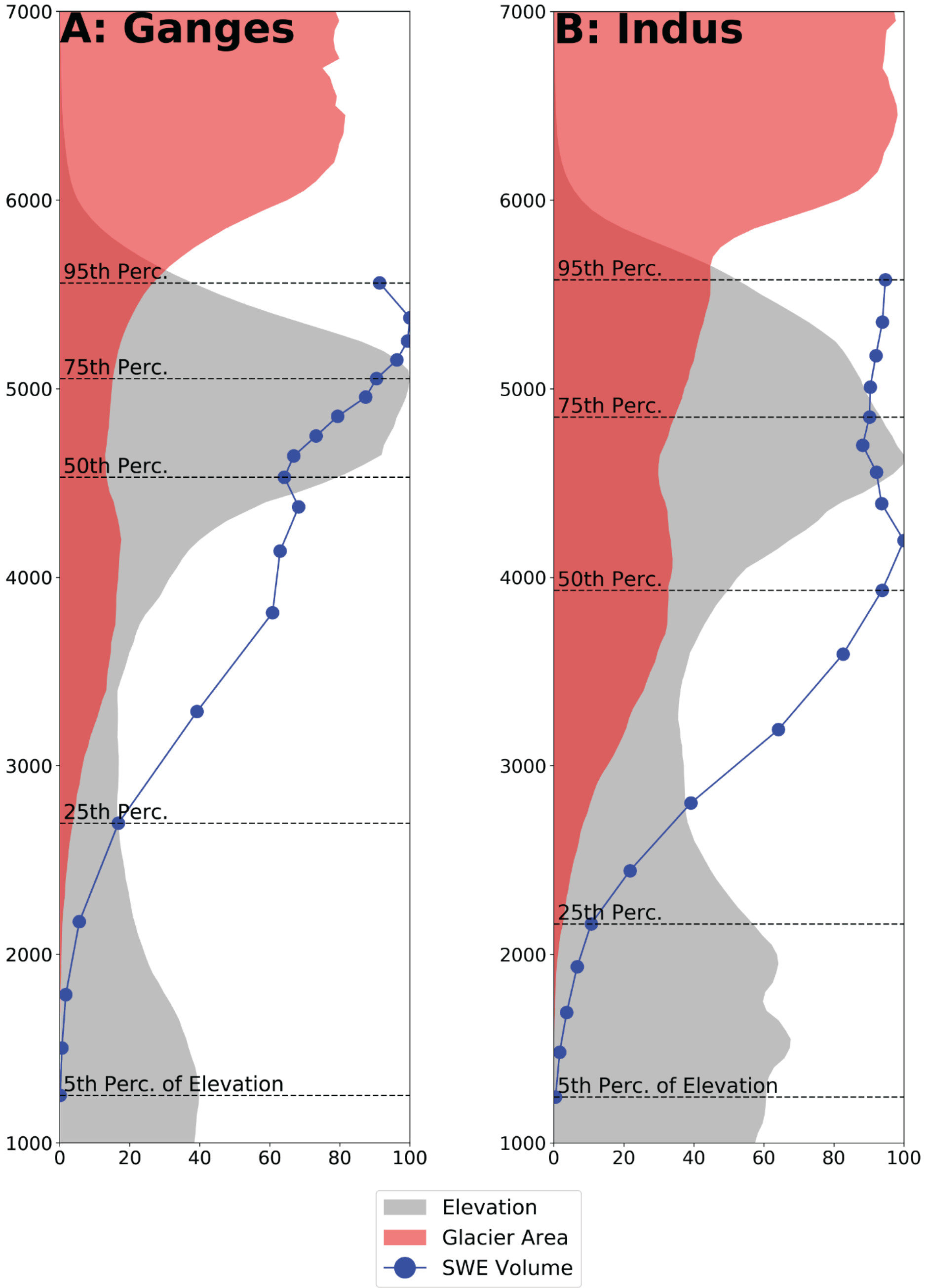

Figure 5.6 – (A) Ganges and (B) Indus catchments, showing catchment hypsometry (grey) (Jarvis et al., 2008), percentage glaciated area (red) (Arendt et al., 2015), and catchment-wide normalized SWE distribution (blue). Red lines indicate catchment elevation percentiles. Illustrates the differences in SWE distribution between catchments, although both show SWE maxima below their elevation peaks. The altitude of SWE maxima are also minimally overlapping with glacier areas, indicating that snow and glacier meltwaters are often distinct and are affected by different climatic processes.

highest elevations are often less negative than lower-elevation trends, indicating that snow in colder, high-elevation zones may be partially shielded from regional climate changes.

While the trend values presented here (cf. Figs. 5.3, 5.4, Tables B1-B5) are individually small, the changes in SWE volume over each point represent gains and losses in SWE over a $\sim$625 sq km area, meaning that each millimeter of SWE change is equivalent to 6.25 x 10^8 liters of water. When statistically significant trends are aggregated at a watershed scale, the annual changes in water resources range from -0.46 mm/yr (average: -0.14%) in the Amu Darya to -2.9 mm/yr (average: -0.41%) in Tibet (Table B1). Although these trends are small in comparison to the total volume of snowpack in HMA, they indicate that changes in HMA's cryosphere are not confined to glaciers. While changes in SWE are less likely to be felt in monsoon-dominated areas, regions which rely heavily on snowmelt – particularly during low-rainfall pre-monsoon months – will feel the effects of diminished snow-water storage.

This work provides a first step towards understanding changes in SWE in HMA and underlines the strength of seasonal and regional variations in the hydrological regime. It also presents evidence that changes in glaciers and snowfields are somewhat distinct due to differences in their elevation distributions. We also find that trends in SWE are not linearly related to elevation, and are highly heterogeneous between catchments. As these changes will affect household water availability, as well as hydropower and agricultural infrastructure, understanding the interplay between snow and glaciers in regional water budgets will continue to be important for the vast downstream populations of HMA.

Methods

SWE Data Processing

We generate a 0.25 decimal degree (dd) grid from 25-45N and 67.5-95E which encompasses a wide range of topographic and climatic settings, as well as several major mountain ranges, which allows us to track large-scale patterns in SWE (Fig. 6.1). In this study, we acquired ungridded, raw, swath data for SSMI (F08, F11, F13, 1987-2009) (Wentz, 2013). We then extract a time series at native sensor resolution for each of our sample points, as described in Smith and Bookhagen (Smith and Bookhagen, 2016). In short, we aggregate all measurements within a 0.125 dd radius of each point in the 0.25-dd grid, and then generate a spatially weighted mean value for each swath at that point. Our time series is made up of on average 1.03 measurements/day over the study period. This process does not involve regridding the raw swath data or resampling the data to daily or otherwise even time-steps, and thus preserves as much of the raw, empirical signal as possible.

From this dataset we remove points adjacent to major water bodies, as water is known to interfere with PM SWE estimation (Kelly, 2009). We also remove those points which do not see frequent or extensive snow accumulation, as the seasonal decomposition methods used in this study are not well-suited to sporadic and irregular time series. We choose to examine only the SSMI dataset, as previous studies have noted differences in PM SWE retrievals between instruments (Smith and Bookhagen, 2016). While this time series is climatically short, it is internally consistent and is thus suitable for trend analysis.

We note that passive-microwave derived SWE measurements have large uncertainties – especially in mountainous environments (Smith and Bookhagen, 2016; Chang et al., 1991; Clifford, 2010). These uncertainties are mainly due to forest cover, topographic complexity, and signal saturation in deep snowpack. The majority of our study area is above the treeline, meaning we do not expect significant vegetation-induced uncertainties. Terrain complexity can modify the assumed path between the PM sensor and the ground surface, and thus impact measured Tb values (Mätzler and Standley, 2000; Smith and Bookhagen, 2016). However, terrain complexity, as modeled by slope and relief, was shown to have a small impact on SWE uncertainty in the study region relative to the impacts of forest density (Smith and Bookhagen, 2016). We examine here changes internal to single point locations which will be impacted by the same set of terrain-related SWE uncertainties throughout the study period.

Passive microwave signal saturation in deep snow and over glaciers has been well documented (Takala et al., 2011; Tedesco and Narvekar, 2010). This saturation occurs even in pixels where only some area exceeds the signal saturation depth, as the estimated SWE for a PM pixel is sensitive to total snow depth within that pixel (Vander Jagt et al., 2013). However, when glacier areas are removed from our analysis (defined here as any pixel with more than 25% glacier cover), the large-scale spatial patterns and elevation relationships are maintained (cf. Fig. B7). In this study we do not attempt to create a well-calibrated SWE product for all of HMA, as the SWE magnitudes are likely influenced by signal saturation. We instead focus on examining changes internal to the SWE time series over our study period in order to examine the spatial patterns of positive and negative relative SWE changes.

As the SWE data are drawn from a single continuous measurement record, each year of data is likely to be impacted by similar measurement errors (i.e., saturation depths at a given point will be similar between years, terrain-related SWE error will be consistent). Given this, analysis of SWE data can still yield valuable information on changes in SWE internal to each location's SWE distribution. Our trends thus provide valuable information on the *direction* rather than the *magnitude* of SWE trends, and the spatial pattern of those trends. We thus present our results with the caveat that our results are representative of *relative* differences in SWE trends between regions and across large spatial scales.

Trend Analysis and Significance Testing

First, we remove shallow and infrequent snow-covered areas by applying a long-term average SWE threshold of 5 mm to each annual and seasonal analysis. The 5 mm limit is derived from previous studies, which have noted that the detection of shallow snow below 5 cm depths is unreliable (Kelly et al., 2003; Kelly, 2009). We tested using additional metrics to remove shallow SWE areas or misclassified snow cover areas, such as the Cross-Polarized Gradient Ratio (Abdalati and Steffen, 1995; Smith et al., 2017), but found minimal changes in our results.

We then removed the seasonal signal of snow accumulation and melt from each individual point in this subset dataset using Seasonal Trend Decomposition by Loess (STL) (Cleveland et al., 1990; Donner et al., 2012). This procedure effectively removes the seasonal oscillations from our data, leaving only the 'residual', multi-year, SWE signal at a given point location. To decompose the full-year signal, we resample our data to a daily timestep and apply a 365 day decomposition window. To decompose the seasonal signals, we break our time series into seasonal components, and decompose each season individually on a 90-92 day window, depending on the length of the seasonal period. The Loess filter we use is adaptive, in that the full-year signal that is removed from the data varies from year to year. A full description of the parameters used for the STL filter used in this study are available in the Supplement.

We first test the de-seasoned data using a Mann-Kendall (MK) test (Mann, 1945; Kendall, 1948) – a non-parametric test often used for testing for trends in time series data – and only consider those areas which exhibit a statistically significant ($p<0.05$) monotonically increasing or decreasing trend. We then perform a linear regression on the de-seasoned data to examine changes in SWE over the study period (Figs. 5.3, 5.4). When these trends are compared to straightforward linear regressions performed on the original dataset without detrending, the direction of the slope is the same, but the magnitude of the slope varies slightly. The main difference is in the significance of the results, where the seasonally detrended data are more statistically reliable. Similarly, if the linear regression is replaced with a weighted regression where the weights are related to the inverse of the SWE amount, the large-scale trend patterns are similar, albeit with different trend magnitudes (cf. Figs. B8-B10).

Elevation Analysis

To examine elevation dependence in both our SWE trends and estimated SWE volumes, we segment each catchment into five-percentile zones, and use those elevation zones to subset our data. The total sum of each five-percentile slice is compared to the catchment-wide total SWE in Figure 5.5A, and the average of all statistically significant SWE trends within each elevation slice is plotted in Figure 5.5B. Catchment-wide trends thus reflect only *statistically significant* data, and should be properly contextualized by examining the pixel-level data presented in Figures 5.3 and 5.4.

The hypsometries presented in Figure 5.6 (grey) are generated from the SRTM V4.1 (Jarvis et al., 2008) dataset aggregated to 50 m elevation bins. Glacier outlines from the Randolph Glacier Inventory V5.0 (Arendt et al., 2015) are used to extract glacier elevation distributions from the SRTM V4.1. These elevations are then aggregated into 50 m elevation bins, and compared to the size of the same SRTM elevation bin to derive glacier coverage at each elevation slice (Fig. 5.6, red polygon). Snow volumes, derived as in Figure 5.5, are normalized to the maximum single-slice snow volume to provide a relative measure of SWE volume across each catchment's elevation range (Fig. 5.6, blue line).

Supporting Information

(see Appendix B).

CHAPTER 6

Spatio-temporal Patterns of High Mountain Asia's Snowmelt Season Identified with an Automated Snowmelt Detection Algorithm, 1987-2016†

TAYLOR SMITH[1], BODO BOOKHAGEN[1], ALJOSCHA RHEINWALT[1]

[1]*Institute of Earth and Environmental Sciences, Universität Potsdam, Germany*

Abstract

High Mountain Asia (HMA) – encompassing the Tibetan Plateau and surrounding mountain ranges – is the primary water source for much of Asia, serving more than a billion downstream users. Many catchments receive the majority of their yearly water budget in the form of snow, which is poorly monitored by sparse in-situ weather networks. Both the timing and volume of snowmelt play critical roles in downstream water provision, as many applications – such as agriculture, drinking-water generation, and hydropower – rely on consistent and predictable snowmelt runoff. Here, we examine passive microwave data across HMA with five sensors (SSMI, SSMIS, AMSR-E, AMSR2, and GPM) from 1987-2016 to track the timing of the snowmelt season – defined here as the time between maximum passive microwave signal separation and snow clearance. We validated our method against climate-model surface temperatures, optical remote-sensing snow-cover data, and a manual control dataset (n=2100, 3 variables at 25 locations over 28 years); our algorithm is generally accurate within 3-5 days. Using the algorithm-generated snowmelt dates, we examine the spatiotemporal patterns of the snowmelt season across HMA. The climatically short (29 year) time series, along with complex inter-annual snowfall variations, makes determining trends in snowmelt dates at a single point difficult. We instead identify trends in snowmelt timing by using hierarchical clustering of the passive microwave data to determine trends in self-similar regions. We make the following four key observations: (1) The end of the snowmelt season is trending almost universally earlier in HMA (negative trends). Changes in the end of the snowmelt season are generally between 2 and 8 days/decade over the 29-year study period (5 - 25 days total). The length of the snowmelt season is thus shrinking in many, though not all, regions of HMA. Some areas exhibit later peak signal separation (positive trends), but with a generally smaller magnitudes than trends

---

† *published as Taylor Smith, Bodo Bookhagen, and Aljoscha Rheinwalt. "Spatio-temporal Patterns of High Mountain Asia's Snowmelt Season Identified with an Automated Snowmelt Detection Algorithm, 1987-2016". The Cryosphere 11 (2017): 2329-2343, https://doi.org/10.5194/tc-11-2329-2017*

in snowmelt end. (2) Areas with long snowmelt periods, such as the Tibetan Plateau, show the strongest compression of the snowmelt season (negative trends). These trends are apparent regardless of the time period over which the regression is performed. (3) While trends averaged over three decades indicate generally earlier snowmelt seasons, data from the last 14 years (2002-2016) exhibit positive trends in many regions, such as parts of the Pamir and Kunlun Shan. Due to the short nature of the time series, it is not clear whether this change is a reversal in a long-term trend or simply inter-annual variability. (4) Some regions with stable or growing glaciers – such as the Karakoram and Kunlun Shan – see slightly later snowmelt seasons and longer snowmelt periods. It is likely that changes in the snowmelt regime of HMA account for some of the observed heterogeneity in glacier response to climate change. While the decadal increases in regional temperature have in general led to earlier and shortened melt seasons, changes in HMA's crysophere have been spatially and temporally heterogeneous.

Introduction

More than a billion people across Asia rely directly or indirectly on water sourced from melting snow in High Mountain Asia (HMA) (Bookhagen and Burbank, 2010; Bolch et al., 2012; Kääb et al., 2012; Kang et al., 2010; Immerzeel et al., 2010; Gardner et al., 2013; Hewitt, 2005; Malik et al., 2016). Many catchments receive the majority of their yearly water budget in the form of snow – particularly at high elevations (Barnett et al., 2005). Both the volume of snowfall and the timing of snowmelt play crucial roles in the efficacy of water provision for downstream users, as many applications – such as agriculture and hydropower – rely on consistent and predictable water availability. Many areas also rely on snowmelt to provide a water buffer late in the year when direct precipitation is rare. Any changes in the onset, length, or intensity of the snowmelt season will impact the water security of both high-elevation and downstream communities.

Passive microwave (PM) data has been used to estimate snow depth and snow-water equivalent (SWE) since the launch of the Scanning Multichannel Microwave Radiometer (SMMR) in 1978. Consistent, pseudo-daily measurements became available in 1987 with the launch of the Special Sensor Microwave/Imager (SSMI) series of sensors (Wentz, 2013). PM data are highly sensitive to liquid water present in the snowpack, and is thus a valuable tool for tracking the onset of snowmelt across large, inhospitable, and unmonitored regions. PM data also have the advantage of functioning despite cloud cover, which is ubiquitous in much of HMA during both winter and the Indian Summer Monsoon (ISM) season. Using satellite-derived PM measurements, several authors have tracked the onset, duration, and spatial extent of snowmelt events using a range of approaches including the cross-polarized gradient ratio (XPGR) (Abdalati and Steffen, 1995; Hall et al., 2004), the advanced horizontal range algorithm (Drobot and Anderson, 2001), Gaussian edge detection (Joshi et al., 2001), channel differences (Takala et al., 2003), artificial neural networks (Takala et al., 2008, 2009), diurnal temperature brightness (Tb) variations (Apgar et al., 2007; Monahan and Ramage, 2010; Tedesco, 2007), wavelet-based approaches (Liu et al., 2005), and median filtering of raw PM data (Xiong et al., 2017).

In this study, we adapted a previously published algorithm (Abdalati and Steffen, 1995) that relied on the establishment of a single cutoff threshold for identifying melt phases in Greenland to the more complex and diverse snow regimes of HMA. This algorithm was chosen due to (1) speed of calculation, (2) consistency across the large study area, and (3) reliance on only night-time data, which is less influenced by sporadic daytime melt-refreeze cycles. While previous studies have successfully measured snowmelt in large and homogeneous environments such as Greenland and Antarctica, we found these algorithms as originally formulated ineffective in the highly variable topography and snow dynamics of HMA – particularly when a single passive microwave pixel can encompass several terrain types which may melt at different speeds. Here we present an enhanced and generalized algorithm building on previous work to improve on snowmelt detection in HMA. We then apply this algorithm to PM data from 1987-2016, and use the derived snowmelt dates to examine spatio-temporal snowmelt patterns across the entire HMA region.

Geographic Setting

HMA contains several mountain ranges – the Himalaya, Pamir, Karakoram, Hindu Kush, Tien Shan, and Kunlun Shan – from which flow several large rivers serving more than a dozen countries (Fig. 6.1). Many of these catchments, such as the Tibetan Plateau, Tarim, Syr Darya, Amu Darya, and Indus, rely on snowmelt for more than 50% of their yearly water budget (Bookhagen and Burbank, 2010; Shrestha et al., 2015). Many communities – particularly those at high elevations or those that depend on surface water for agriculture – are highly reliant on the timing of snowmelt. An early snowmelt season can create a late-season 'water gap' when a dry spell is caused by snow meltwaters disappearing before the start of the next rainy season. These water gaps can also negatively impact flora and fauna which depend heavily on the timing of the appearance of ephemeral water bodies (Bookhagen, 2017). The timing and volume of snowmelt thus has important implications for the environment, direct household water use, agriculture, and hydropower.

Several interacting moisture sources, including the Winter Westerly Disturbances (WWD), Indian Summer Monsoon (ISM), and East Asian Summer Monsoon (EASM), are responsible for the wide range of snowfall regimes across HMA (Fig. 6.1, inset). The interaction of these climatic regimes with the complex topography of HMA – particularly the vast elevation gradients – creates a diverse set of snowfall regimes (Cannon et al., 2014; Kääb et al., 2012; Immerzeel and Bierkens, 2012; Gardner et al., 2013; Kapnick et al., 2014; Barnett et al., 2005; Dahe et al., 2006; Takala et al., 2011; Cannon et al., 2017).

Materials and Methods

Datasets

We leverage a combined time series of SSMI (1987-2009), Special Sensor Microwave Imager/Sounder (SSMIS) (2008-2016), Advanced Microwave Scanning Radiometer - Earth Observing System (AMSR-E, 2002-2011), AMSR2 (2012-2016), and Global Precipitation Measurement (GPM, 2014-2016) data, processed to 0.25 decimal degree (dd) resolution by interpolating raw PM swath data at a series of point locations as described in Smith and Bookhagen (2016) (see Supplementary Table S1 for a full dataset listing). In essence, we group all measurements within a 0.125° dd radius of each point on a 0.25° dd grid and generate a spatially weighted mean value for each swath at that point. The dataset is comprised of 6,399 point locations, with on average 26,000 PM measurements each (long-term average of 2.4 measurements/day for 29 years, with more measurements during the 2002-2016 period).

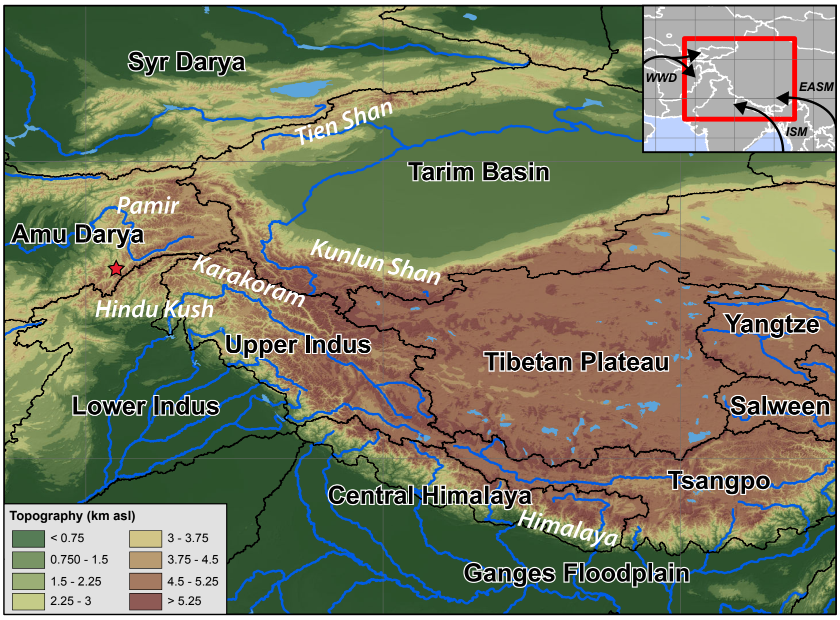

Figure 6.1 – Topographic map of the study area across High Mountain Asia (HMA), with major catchment boundaries (black lines and labels in black font with white border) and major mountain ranges (white font). Inset map shows wind direction of major Asian weather systems (WWD: Winter Westerly Disturbances, ISM: Indian Summer Monsoon, EASM: East Asian Summer Monsoon) on top of political boundaries. Red star indicates the location used for Figures 6.2 and 6.3.

PM measurements are converted to snow-water equivalent (SWE) using the Chang equation (Eq. 6.1) (Chang et al., 1987), with modifications for non-SSMI platforms as proposed by Armstrong and Brodzik (2001), and a constant snow density of 0.24 g/cm^3 as proposed by Takala et al. (2011).

$$SD[cm] = 1.59[cm/K] * (Tb_{18V} - Tb_{36V})[K] \tag{6.1}$$

Studies have noted that SWE estimates from the Chang equation have high uncertainties (e.g., Kelly et al., 2003; Kelly, 2009; Tedesco and Narvekar, 2010; Daly et al., 2012), particularly in dense forests. However, as much of our study area is non-forested – and we use SWE only as a rough estimate of snow volume – we choose to rely on the simple Chang equation rather than a more complex algorithm for SWE estimation.

As control data, we analyze Moderate Resolution Imaging Spectroradiometer (MODIS) percentage snow-covered area (product MOD10C1 V6, 2001-2016, (Hall and Riggs, 2016)) and High Asia Refined Analysis (HAR) surface temperature (tsk, 2000-2014, (Maussion et al., 2014)). While these datasets only cover a subset of our study period, they are among the few independent control datasets available across the entire study area.

Snowmelt Tracking Algorithm

The shift from dry snow, which can be physically characterized as snow crystals in an air background, to wet snow, which replaces the air matrix with water, shifts the primary interaction between PM radiation and the snowpack from volumetric (dry snow) to surface (wet snow) scattering. These scattering changes are reflected in the temperature brightness (Tb) data, and allow wet and dry snow to be differentiated, as the transition from dry to wet snow drastically increases the measured Tb – particularly in the scattering (Tb_{37V}) channel. The XPGR, as originally described by Abdalati and Steffen (1995), is defined as:

$$XPGR = (Tb_{19H} - Tb_{37V})/(Tb_{19H} + Tb_{37V}) \tag{6.2}$$

This algorithm takes advantage of both the channel difference between the Tb_{19} and Tb_{37} GHz channels as well as the depolarization effects of snowmelt, which increases the differences between the horizontally and vertically polarized channels (Abdalati and Steffen, 1995). In the original application of the XPGR on the Greenland Ice Sheet, a static value of -0.025 was shown to indicate the presence of liquid water in the snowpack, and hence used to separate the year into melting and non-melting phases (Abdalati and Steffen, 1995). We find that for the majority of HMA, the -0.025 threshold is not effective in identifying the onset of snowmelt, as the XPGR-snowmelt relationship is highly variable through time and space.

We modify the XPGR method here to track maximum passive microwave signal separation – or the yearly maximum XPGR, referred to from here on as MXPGR. As the context of seasonal snowmelt in HMA is quite different from that of Greenland, and sufficiently long-term and spatially diverse in-situ snowmelt data are lacking, we use the MXPGR as a proxy for snowmelt onset to track changes in the snowmelt season year-over-year. Thus, while we do not use the classical literature definition of snowmelt – presence of liquid water in the snowpack – we track a consistent metric related to physical snowpack changes that can be broadly interpreted as the onset of the snowmelt season.

However, the MXPGR is not effective for tracking the cessation of snowmelt. To track the end of snowmelt, we leverage two additional datasets: (1) the raw Tb_{37V} time series, which rapidly increases as snowpack thins, and (2) a SWE time series calculated from the Tb_{19} and Tb_{37} GHz channels (Chang et al., 1987; Kelly et al., 2003; Tedesco et al., 2015; Smith and Bookhagen, 2016).

We first use a simple peak-finding algorithm, which identifies peaks as points which are larger than their two neighboring samples, to generate a list of potential peaks in the XPGR data. Next, we take the average XPGR value within $\pm$ 2 days of each peak to determine not only the simple yearly maximum XPGR, but the highest and temporally widest peak in our XPGR data – termed here the MXPGR. We flag years which have multiple strong and temporally distinct XPGR peaks as unconstrained for snowmelt onset estimation, as the algorithm has trouble consistently identifying the MXPGR in these cases.

To determine the end of the snowmelt season, we choose either the date of the yearly maximum Tb_{37V} value, which corresponds to the thinnest snowpack or to a 'bare earth' signal, or the first date where 4 out of 5 days have been within 2 cm of the yearly SWE minimum. We choose the yearly SWE minimum instead of zero as our SWE threshold for snow clearance because some regions in HMA have a defined melt season but rarely reach zero SWE. This also helps control for uncertainty in shallow SWE measurements, as detecting shallow snow (<5 cm) with PM data is still difficult (Kelly et al., 2003; Armstrong and Brodzik, 2001). A full description of our melt detection algorithm is available in the Supplement (Figs. C1-C4).

Manual Control Dataset Generation

Unfortunately, large-scale and several-decades long snowmelt onset and end date records are not available for HMA. Instead, we use HAR (Maussion et al., 2014) and MODIS (Hall and Riggs, 2016) data alongside a manually generated set of control dates for the snowmelt season, determined from the SWE, XPGR, and Tb_{37V} signals by the researchers. We visually identified major peaks (MXPGR), as well as the cessation of snowmelt, by inspection of the time series. We chose a random sample of 25 point locations across our study area, and identify snowmelt dates for each year of the time series (n=1400). We use the calculated length of the snowmelt period (days between the MXPGR and the end of the snowmelt season) as an additional control variable (n=700).

Hierarchical Clustering

Hierarchical clustering is a method used to correlate time series data by intrinsic similarity (Corpet, 1988; Johnson, 1967; Jain et al., 1999; Murtagh and Contreras, 2012; Rheinwalt et al., 2015), which has been used extensively in the environmental research community. We generate clusters from those time series which share the most temporal overlap, or where the periodicity of Tb values have the largest coherence, regardless of their spatial correlation.

We choose the XPGR time series as our clustering variable, as the XPGR is the most sensitive to melt dynamics, integrates multiple Tb frequencies, and is not sensitive to SWE calibration issues. To improve the robustness of our clustering, we combine the disparate single-instrument PM time series into a single coherent time series which leverages the full temporal extent of each dataset (1987-2016), using the following three steps: (1) We standardize the PM signals of the suite of instruments used in this study to a single set of dates, artificially created at daily resolution from the minimum and maximum dates across all satellite datasets, by resampling all individual satellite time series to a daily time step and dropping dates without data. (2) We homogenize the disparate PM time series based on the overlapping portions of individual satellite time series, using linear regression. The results of these regressions can be seen in Tables C2-C5, with an example regression at a single point shown in Figure 6.2. (3) In order to reduce noise in our cluster analysis, we resample our merged XPGR time series to a 5-day temporal resolution (pentad).

Next, we normalize each merged pentad time series (1987-2016) to a Gaussian distribution, using a percentile mapping approach (Rheinwalt, 2017). We then estimate the Pearson correlation coefficient to classify regions of self-similarity in our XPGR time series (Rheinwalt, 2016). This method computes a Pearson correlation coefficient between each time series, and based on the resulting correlation matrix, computes a set of linkages using the angle between time series in vector space (Murtagh and Contreras, 2012). We use the maximum distance (complete linkage) to split the linkage matrix, which is favorable because it ensures a minimum intra-cluster correlation. An average linkage scheme was tested and produced heterogeneous cluster sizes with outliers. We choose our cluster threshold from the hierarchical clustering dendrogram (Fig. C6), which maximizes cluster size while minimizing

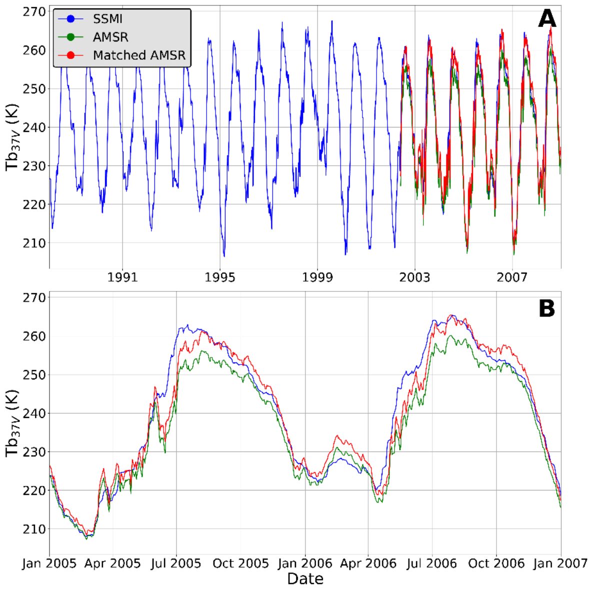

Figure 6.2 – (A) Sample time series showing SSMI (blue) and AMSR-E (green) Tb_{37V} frequencies, with linearly matched modified AMSR-E Tb (red), 1987-2009. Data taken from 71.25E, 36.75N (cf. Fig. 6.1). (B) The same data as panel A but for two seasons (2005-2007).

cluster internal diversity (Fig. C7). We emphasize that the correlation is based on the temporal co-evolution of the time series, and is less sensitive to the relative magnitudes of peaks and troughs between data points. For an oscillating time series, the magnitude of the Pearson correlation coefficient is driven by the synchronization of peak timing, especially in normalized time series. The combination of several sensors in this study may impact the magnitudes of the resultant time series, but will not have an outsized effect on the timing, and thus clustering, of our time series.

Results

Melt Algorithm Validation

3.1.1 Comparison with Manual Control Dataset

The agreement between manually clicked snowmelt dates and algorithm-derived snowmelt dates is generally within 3 days, with 70% or more of MXGPR and snowmelt end dates falling within 5 days of the control dataset (Table 6.1). We find the lowest standard deviation for the end of melt, which is to be expected given that the end of snowmelt is determined by both snow clearance and the Tb_{37V} signal, and thus is more tightly constrained than the MXPGR date. The MXPGR date, while having a low average offset, has a high standard deviation as the algorithm sometimes has trouble correctly choosing the MXPGR when a snow season has several large storms, or several periods of melting and refreezing (cf. Fig. 6.3). Thus, errors in identification of MXGPR will naturally have a higher standard deviation due to the presence of more relatively large misclassification errors.

Diverse snow seasons are shown from an example location (71.25E, 36.75N), over six years of data (Fig. 6.3). Despite clear inter-annual variations in the temporal distribution of SWE, there exists high correlation between

Table 6.1 – Summary statistics comparing manual control dataset and algorithm dataset (n=2100, 28 snowmelt seasons at 25 locations).

Variable	Mean Offset (days)	Mean Absolute Offset (days)	Standard Deviation	RMSE	Percentage of Algorithm Dates Within 3/5/10 Days of Control Dates
MXPGR	-0.23	5.51	16.71	16.71	68 / 80 / 90 %
Snowmelt End	-1.3	5.0	9.74	9.82	49 / 70 / 89 %
Snowmelt Period	-0.25	7.44	16.1	16.1	47 / 64 / 82 %

the algorithm-derived melt dates and our manually chosen melt dates. In the sample data, the first and third snow seasons have multiple peaks which could possibly be related to the true onset of the snowmelt season, and these years are flagged as unconstrained. The second and fourth years of data have a simple structure with a well-defined peak and a pseudo-linear melt during the spring season. The fifth year of data has a strong late-season XPGR peak, implying that there was significant snow buildup after an initial early season XPGR peak and melt phase. The last year of data shows a mismatch between the algorithm and control datasets, where it is difficult to determine the best candidate for the MXPGR. The algorithm picks the wider XPGR peak (earlier in the season), while we chose the thin but high peak later in the season as more closely following the end of snow buildup. Across all years of data shown here, the snowmelt end date is well matched between the algorithm and manual datasets.

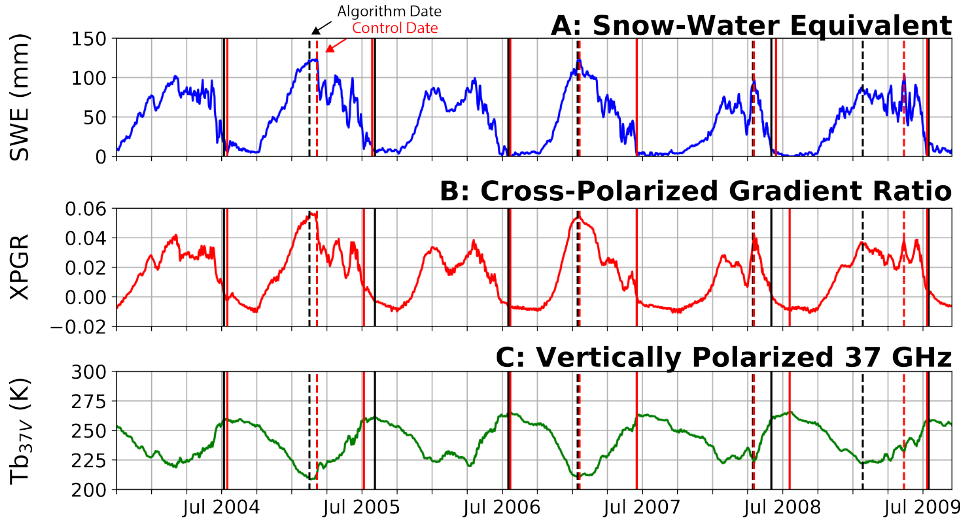

Figure 6.3 – Sample data from 71.25E, 36.75N (cf. Fig. 6.1) showing: (A) Snow-Water Equivalent (SWE) based on the Chang algorithm (Chang et al., 1987), (B) Cross-Polarized Gradient Ratio (XPGR), and (C) vertically polarized temperature brightness at 37 GHz (Tb_{37V}) measurements. MXPGR (dashed lines) and end of melt (solid lines) are black for algorithm dates, and red for control dates. Lack of red lines indicates temporal overlap of algorithm and control dates. Years with multiple distinct peaks (e.g., 2004, 2006) are flagged as unconstrained, and not used for further analysis.

3.1.2 Comparison with MODIS Snow Cover Data

The MODIS sensor onboard Terra (product MOD10C1 V006, (Hall and Riggs, 2016)) provides an additional estimate of snow cover from an optical, instead of PM, instrument. While MODIS cannot provide accurate measurements of fractional snow covered area (SCA) in the presence of clouds, it represents an independent control on the snowmelt end date (Fig. 6.4). In Figure 6.4A, the MODIS snow-clearance date is defined as the first day when five out of seven days have less than 5% SCA, and the data are cloud free. Only those dates where there is no cloud cover within seven days of the end of the snowmelt season are used in Figure 6.4B, which illustrates the consistently low SCA fraction at our algorithm-derived end of the snowmelt season.

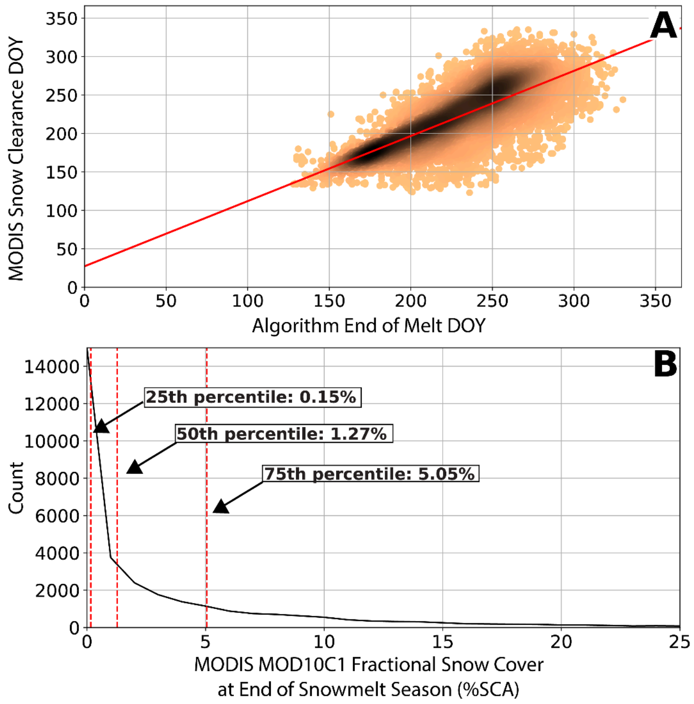

Figure 6.4 – (A) Comparison of MODIS MOD10C1 (Hall and Riggs, 2016) and algorithm-derived end of the snowmelt season days of year, with darker areas indicating high point densities. We find strong agreement between the snowmelt end dates derived from both datasets (slope = 0.85, R^2 = 0.58, n = 34,468), despite the presence of outliers. (B) MODIS snow covered area fraction at the algorithm-derived end of the snowmelt season. This shows, for example, that over all algorithm-determined snowmelt end dates, the median SCA was 1.27%, and that SCA is below 5% in the majority of cases. Areas with snowmelt periods of less than 20 days are removed from this analysis.

While the agreement between algorithm and MODIS snowmelt end days is generally high (cf. Fig. 6.4A), there remain significant outliers. It is likely that some larger outliers are due to poorly flagged clouds in the MODIS dataset (cf. Fig. C1). We rely here on the MOD10C1 product, as other snow cover products such as NOAA Global Multisensor Automated Snow and Ice Mapping System (Romanov, 2017) utilize a combination of optical and passive microwave data, and thus do not represent a truly independent control dataset.

3.1.3 Comparison with HAR Surface Temperature Data

HAR provides surface temperature at hourly intervals from 2000-2014 at 30 km spatial resolution over the entire study area (Maussion et al., 2014). Using this data, we derive (1) the full-day average surface temperature, (2) the average daytime surface temperature, and (3) the daily surface temperature range at each MXPGR date (Fig. 6.5).

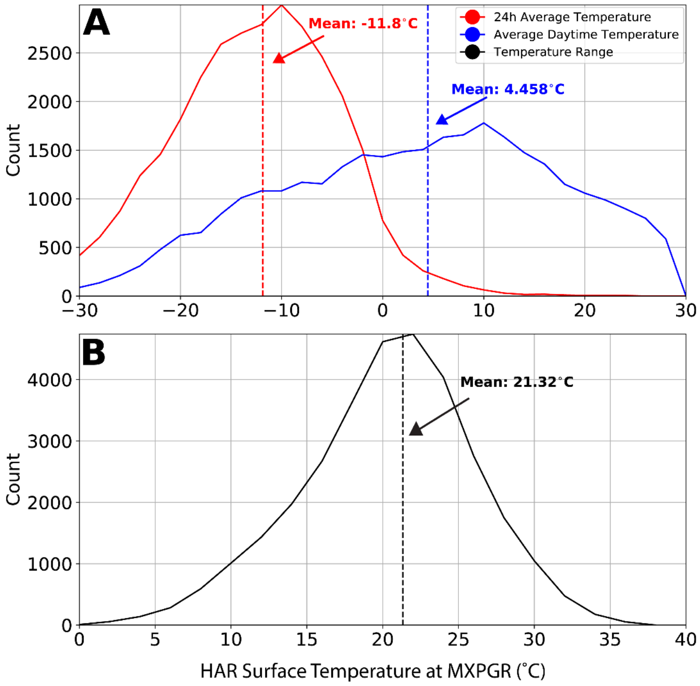

Figure 6.5 – (A) HAR full-day average surface temperature (red), daytime average surface temperature (blue), and (B) daily surface temperature range (black) at the algorithm-derived MXPGR date (n = 31,583). Full-day and daytime average temperatures show distinctly different distributions, with full-day temperatures averaging below 0°C and daytime temperatures above. This relationship, as well as the large daily temperature range, imply that the algorithm-derived MXPGR dates occur at or near the transition from sub-freezing to above-freezing temperatures.

While the relationship between surface temperature and MXPGR isn't as clearly defined as the comparison between MODIS SCA and snowmelt end, the highly variable surface temperature and positive daytime temperatures at the MXPGR dates imply that the MXPGR is likely linked to melt-refreeze cycles, snowpack metamorphism, or the presence of liquid water in the snowpack.

Application: Spatial Patterns of Snowmelt Period

We apply our algorithm on a pixel-by-pixel and year-by-year basis to identify the onset of the snowmelt season – here proxied by the MXPGR – as well as the end of the snowmelt season. We also use the number of days between the MXPGR and the end of the snowmelt season to calculate the snowmelt period for each year. The long-term average snowmelt period is shown in Figure 6.6.

The length of the snowmelt season varies significantly across HMA (Fig. 6.7). In many low-elevation areas, such as the Ganges Plain, and low-SWE areas, such as the central Tarim Basin, the snowmelt period is very short. Higher-

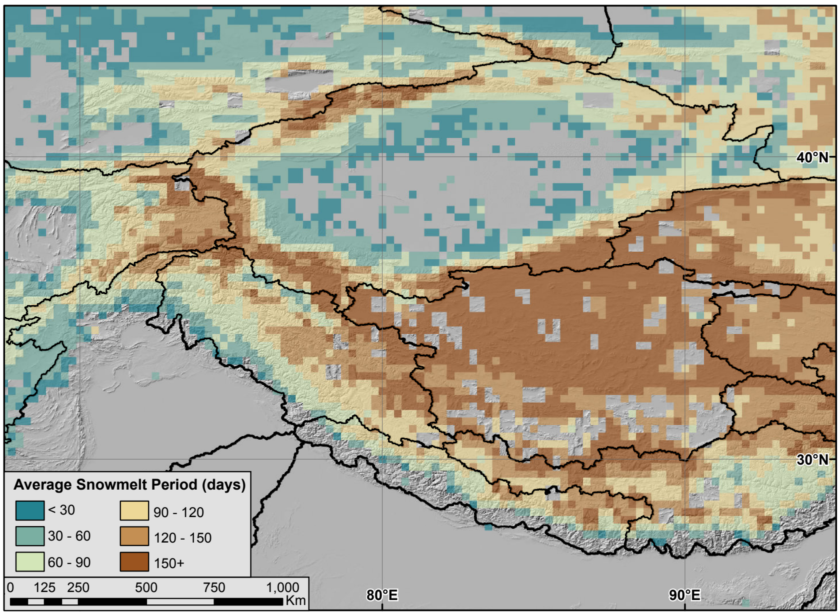

Figure 6.6 – Average snowmelt period across HMA from 1987-2016. Snowmelt period ranges from less than a month to several months, depending on geographic location, elevation, and local and regional climatic conditions. Locations with long-term average snowmelt periods less than 20 days are removed. Topographic hillshade in background. Grey areas indicate water bodies, low-SWE areas, and short snowmelt period areas that are excluded from the analysis.

elevation zones, and in particular the Tibetan Plateau, see snowmelt periods of several months. While both elevation and the amount of SWE impact snowmelt, these are not the sole determinants of the length of the snowmelt season (Fig. 6.7). Each of the major catchments (cf. Fig. 6.1) has a unique MXPGR, snowmelt end date, and snowmelt-period distribution, based on the various climate and topographic forcings present in each catchment.

Hierarchical Clusters

Cluster selection criteria can be seen in Figures S6-7. We choose our dendrogram cutoff (distance threshold in vector space) based on a combination of the number of generated clusters, the internal variation within those clusters, and the average resultant cluster size. In our case, we choose a distance cutoff of 1 radian from the complete linkage matrix (minimum intra-cluster correlation 0.525), which results in 285 clusters (Fig. 6.8).

While the hierarchical clusters are not based on any explicit spatial relationships, many of the clusters fall into spatially coherent groups. For example, the Pamir Knot and Tarim Basin both form large, coherent clusters based on the similarity of their snowfall and snowmelt patterns. The large number of small clusters throughout the Himalaya indicate that the region is not climatically uniform, and small-scale variations in topography and climate have strong impacts on the snowmelt regime.

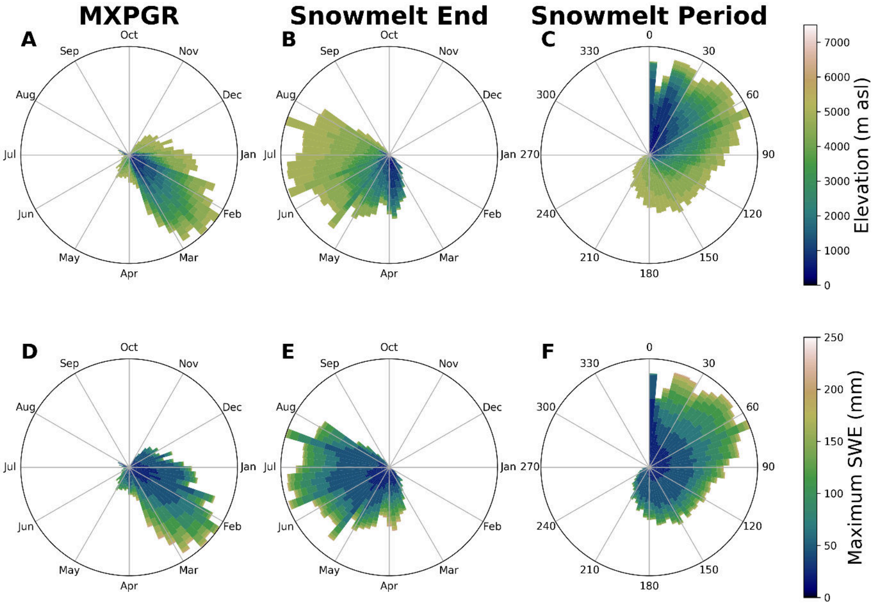

Figure 6.7 – MXPGR (A,D), snowmelt end (B,E), and snowmelt period (C,F) for the entire study area, colored by elevation (A-C) and snow depth (D-F) bins. Radial bin heights (radial distance from the center) indicate relative number of pixels at each day of year (i.e. area). While very short snowmelt periods show a distinct low-elevation, low-SWE bias, in general melt onset and end dates are well distributed throughout elevation zones and SWE amounts.

Discussion

Spatial Melt Patterns from Hierarchical Clustering

As can be seen in Figure 6.3, there exists significant inter-annual variation in the timing the snowmelt season. This is particularly true of areas impacted by the WWD, which often have multiple snowfall events starting in winter and lasting until spring (Cannon et al., 2014). As one year may receive a small late season storm, and thus see a maximum in the spring, while the next year may receive a large summer storm, and thus peak in the summer, analyzing trends at a single point in space is difficult.

To mitigate the influence of inter-annual variation in determining long-term trends in the timing of the snowmelt season, we group our data into self-similar clusters using hierarchical clustering. We do not filter our generated clusters based on size or self-similarity, as we do not use our clusters to generate a single averaged or representative time series for each cluster, as is often done in climate analyses. Due to inter-annual variations in SWE and the timing of the snowmelt season, fitting a linear regression through only 29 years of data does not provide statistically significant results for the majority of HMA. Instead, we use our clusters to group sets of algorithmically-derived snowmelt dates, and fit linear models on a cluster-by-cluster basis. By leveraging the snowmelt dates of a set of time

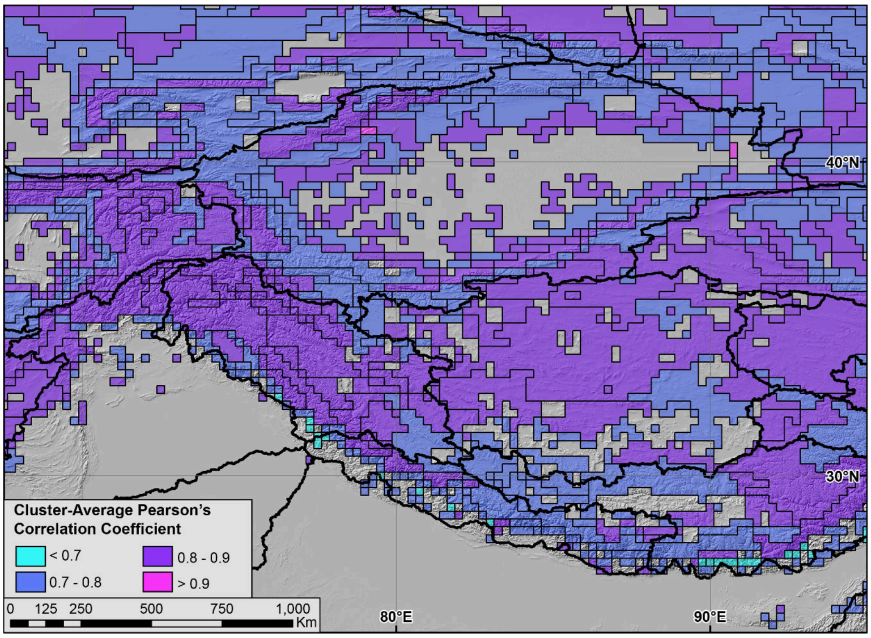

Figure 6.8 – Hierarchical clusters (black outlines), as determined from the rank-order correlation coefficients of the 5-day resampled, merged, and linearly matched XPGR data (1987-2016). Colors indicate cluster-average internal diversity (average Pearson's correlation coefficient between members in the same cluster). Grey areas indicate water bodies, low-SWE areas excluded from the analysis, or areas with irregular PM signals which fail to cluster.

series in parallel, we are able to identify statistically significant changes in the timing of the snowmelt season, as well as changes in the length of the snowmelt period (Fig. 6.9). To reduce noise from low-SWE and very short snowmelt period areas, we remove areas from the subsequent analyses with long-term average melt periods of less than 20 days. We also remove MXPGR dates that are flagged as unconstrained (when there are multiple candidate dates) to limit the impact of unreliable data on our analysis.

MXPGR is trending earlier (negative trend) in HMA outside of a small band running from the Karakoram through the interior Tibetan Plateau (Fig. 6.9A). In another snowmelt study leveraging SSMI and QuickSCAT data in HMA, Xiong et al. (2017) find a similar distribution of positive and negative snowmelt onset trends. However, a direct comparison with their results is difficult due to differences in the temporal and spatial resolution of source data, filtering methods, and statistical treatment of SWE trends. Negative snowmelt onset trends have also been previously observed in Central Asia (Lioubimtseva and Henebry, 2009; Dietz et al., 2014), the Himalaya (Lau et al., 2010; Panday et al., 2011), and the Tibetan Plateau (Xu et al., 2017).

A complex pattern of regionally increasing and decreasing spring snow depth in the Tibetan Plateau has been observed since the 1970s (Zhang et al., 2004; Che et al., 2008; Wang et al., 2013), which could help account for the mixed MXPGR trends observed in the Tibetan Interior. High-elevation zones in the upper Indus catchment, running from the Karakorum in a south-eastward direction, have seen increased precipitation over the past decades due to increases in the strength of the WWD (Cannon et al., 2015; Norris et al., 2016; Treydte et al., 2006).

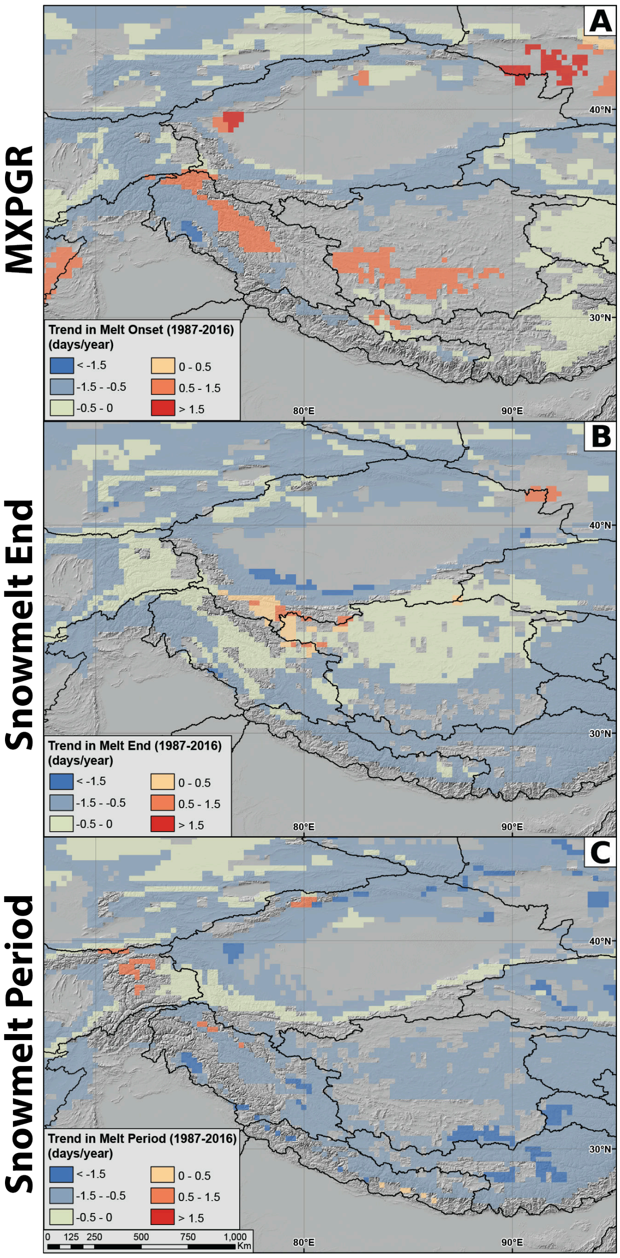

Figure 6.9 – Significant ($p < 0.05$) trends in date of (A) MXPGR, (B) snowmelt end, and (C) snowmelt period, 1987-2016 for the cluster areas (cf. Fig. 6.8). The MXPGR is generally moving earlier outside of the Tibetan Plateau-Karakoram region, and moving slightly later in a high-elevation zone running from the Karakoram through the Tibetan Plateau interior, as well as parts of the Himalaya. The end of the melt season is moving earlier in the vast majority of HMA, at varying rates. Consequently, snowmelt period is also shrinking in much of HMA, with the exception of small parts of the Pamir, Karakoram, and Tien Shan.

Temperatures in HMA are increasing faster than the global average (Vaughan et al., 2013; Lau et al., 2010), and are likely the primary driver of the almost universal earlier snowmelt end dates as seen in Figure 6.9B. Increased temperatures have likely both reduced overall SWE amounts, by causing more precipitation to fall as rain, and decreased SWE persistence into the spring and summer months. These changes have helped drive a 2-8 day/decade earlier end to the snowmelt season (Fig. 6.9B).

The length of the snowmelt season is shortening in much of HMA, with the exception of small areas in the Pamir, Tien Shan, and Karakoram regions (Fig. 6.9C). We attribute this to a combination of increased WWD storm intensity, and increases in late season storms, which could help extend the snowmelt season slightly later into the year (Cannon et al., 2016; Norris et al., 2015; Kapnick et al., 2014). In general, however, the snowmelt season is shortening throughout HMA. Intensification of the spring runoff regime in HMA has been observed in both model (Lutz et al., 2014) and empirical (Dietz et al., 2014; Bookhagen and Burbank, 2010; Stewart, 2009) data.

Temporal Heterogeneity in Snowmelt Trends

Not only are changes in the snowmelt regime spatially complex (e.g., Fig. 6.9), but they exhibit distinct temporal heterogeneity as well.

Changes in MXPGR do not have a bias towards early or late onset snow regimes (Fig. 6.10A). The end of the snowmelt season is almost universally negative (earlier), excepting a few isolated areas in the Kunlun Shan (cf. Fig. 6.9). The majority of locations show negative (shorter) trends in snowmelt period. Strong negative changes in the snowmelt period are biased towards areas with long melt seasons (120 days or more). This implies that high-elevation areas, such as the Tibetan Plateau, and high-SWE areas, such as the Karakoram, will see a relatively stronger compression in the length of the snowmelt season. While changes in the MXPGR date are partially responsible, the main driver of shorter snowmelt periods is the earlier end of the snowmelt season across most of HMA.

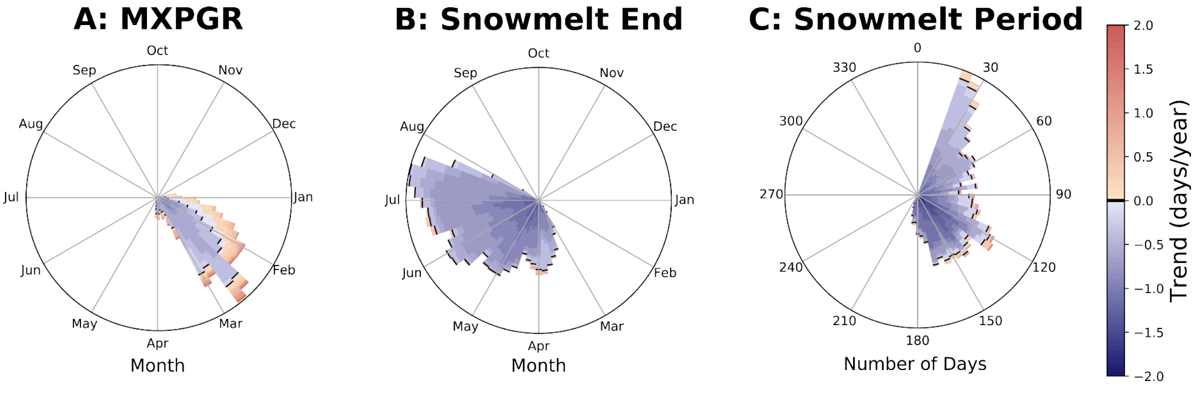

Figure 6.10 – 29-year average (A) MXPGR, (B) snowmelt end, and (C) snowmelt period, colored by trend (1987-2016), with radial bin heights (radial distance from the center) indicating relative number of pixels (i.e. area) at each day of year. Black lines indicate zero trend. Data taken only from areas with statistically significant trends ($p < 0.05$, cf. Fig 6.9). Changes in snowmelt end date are positive in very few areas. Negative changes in snowmelt period (shortening) are relatively larger in long snowmelt-period areas.

Several-decade long trends conceal short-term fluctuations in the snowmelt regime of HMA. To assess the impact of the analysis timeframe on our regression results, we analyzed trends with window sizes ranging from four years to 28 years, across all possible start-year and window-size combinations, averaged over the entire study area (Fig. 6.11).

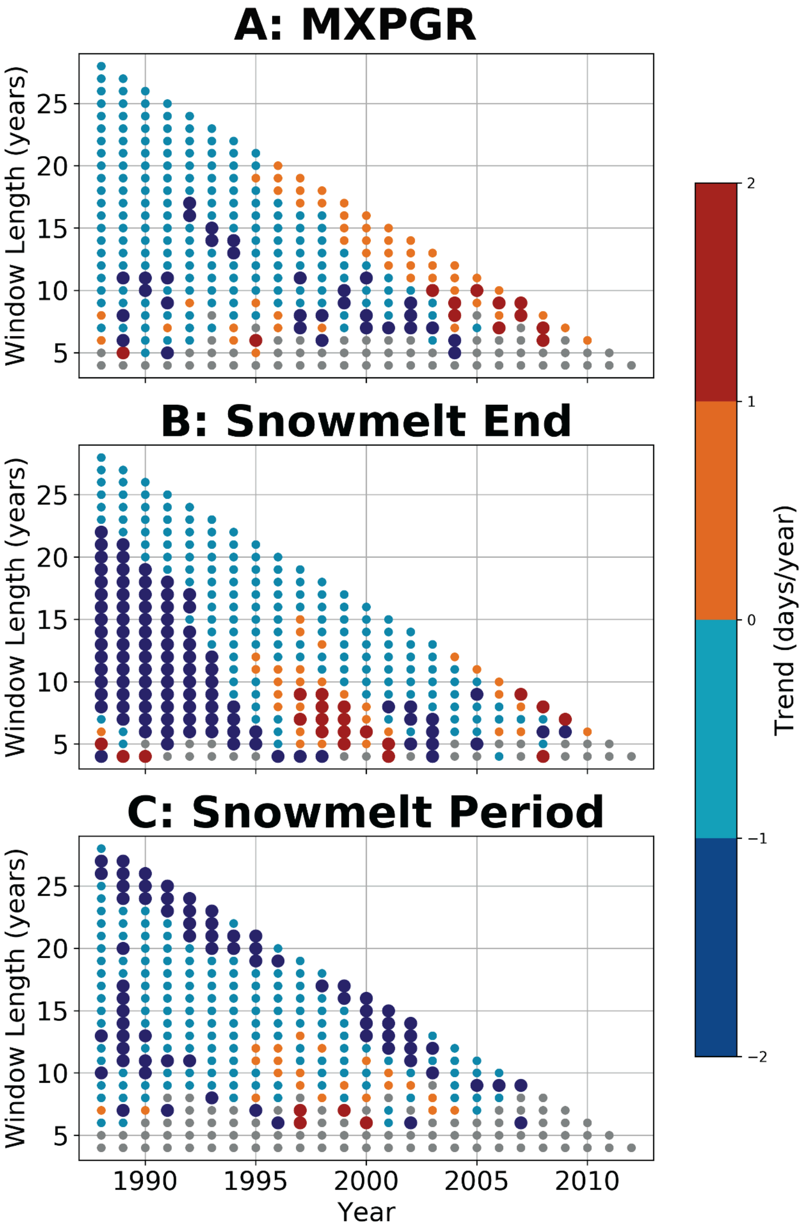

Figure 6.11 – Impact of window length on measured trends in (A) MXPGR, (B) snowmelt end, and (C) snowmelt period over the entire study area. Each dot represents trends over a single window size (4 to 28 year) and start year (1988-2012) combination. Regressions are performed using the same clusters as shown in Figure 6.8. Only statistically significant trends (p <0.05) are included in this analysis; gray dots indicate lack of significant trend. Larger dots indicate positive or negative trends larger than 1 day per year. Trends in snowmelt period and snowmelt end dates are generally negative regardless of which years the trend is assessed over, excepting short periods in the late 1990s and 2000s. MXPGR dates are positive over short time periods starting in the late 1990s, and negative over earlier time periods and longer time windows.

Trends are universally negative for the MXPGR and the end of the snowmelt season, as well as for the snowmelt period, between 1988 and 1995, regardless of the timeframe over which the regression is performed. While there were some short positive trends in snowmelt end date (5-10 years) starting in the mid 1990s, trends in end dates and snowmelt period are generally negative. Although long-term trends in MXPGR date (longer than 20 years) are negative, recent trends (after 2002) are positive when considered at timeframes of 5-10 years. This implies that while the three-decade trend in MXPGR dates has been negative, the trend has become more variable in the past decade.

It is clear that decadal trends (cf. Fig. 6.9) are not consistent throughout the entire study period (cf. Fig. 6.11). When trends in the first half (1988-2002) and second half (2002-2016) of the data are compared, distinct regional patterns are apparent (Fig. 6.12).

The lack of statistically significant trends limits some interpretations, particularly with regards to changes in the snowmelt period. Nowhere in HMA are MXPGR trends consistent in both analysis periods. While many snowmelt end dates have remained negative in both time periods, trends in parts of the Pamir and Karakoram have moved from negative to positive, and those in the Tien Shan have become less negative (cf. Fig. C8). A similar story is apparent when MXPGR dates are considered, where the Tien Shan and parts of the Pamir have moved from negative to positive trends. Unfortunately, due the the climatically short nature of the dataset, it is not clear whether this change represents inter-annual variability or a reversal of a long-term trend.

Hydrologic Implications

The spatially and topographically complex changes in MXPGR, snowmelt end, and snowmelt period make interpretation of downstream impacts difficult. The long-term trend in HMA of a shortened and earlier melt season will impact downstream populations who rely on the consistent timing and volume of spring and summer runoff (Archer and Fowler, 2004; Barnett et al., 2005). Already the impacts of precipitation intensification and shifts in the snowmelt season have been felt in many regions (Barnett et al., 2005; Stewart, 2009). These trends are likely to continue as temperatures rise across HMA, and each major catchment will feel the impacts of a shortened snowmelt season, regardless of changes in the start and end dates of melt.

Many regions rely on glaciers as their only water source between the end of snowmelt and the beginning of major precipitation systems (Bolch et al., 2012). This important water reserve is certain to be impacted by, and reflect changes in, the snowmelt regime of HMA, as the timing of precipitation has been shown to be an important factor in the response of glaciers to climate change (Maussion et al., 2014; Wang et al., 2017). While many regions have seen rapid glacier retreat (Bolch et al., 2012; Kääb et al., 2012, 2015; Scherler et al., 2011) there exist regions of glacier stability and even growth, such as the Karakoram (Hewitt, 2005; Gardelle et al., 2012) and Kunlun Shan (Gardner et al., 2013; Yao et al., 2012). Our results (cf. Fig. 6.9) show longer snowmelt periods in parts of the Pamir, later snowmelt end dates in parts of the Karakoram and Kunlun Shan, and relatively less negative trends in snowmelt end in the Pamir when compared with the rest of HMA. These regions overlap with both the 'Karakoram Anomaly' and positive glacier mass balances in parts of the Kunlun Shan and Pamir, implying that changes in the timing of the snowmelt season could be partially responsible for regional heterogeneity in glacier change.

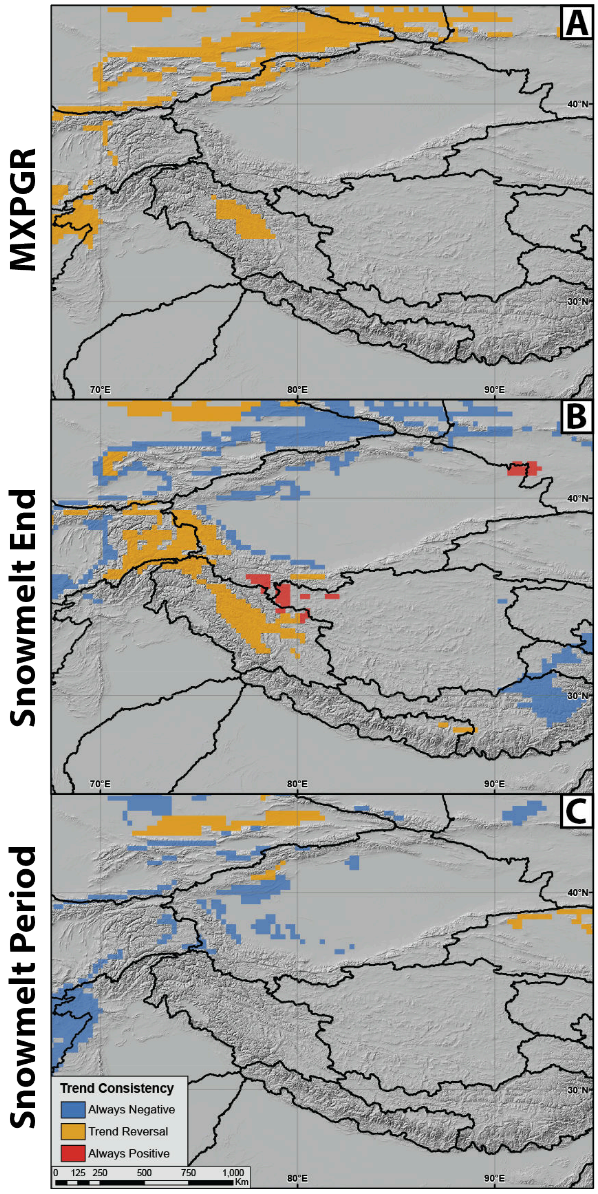

Figure 6.12 – Impact of analysis period (1988-2002 or 2002-2016) on measured trends in (A) MXPGR, (B) snowmelt end, and (C) snowmelt period. Grey areas indicate lack of statistically significant (p <0.05) trends at one or both analysis periods. Much of HMA lacks significant shorter-term trends in MXPGR and snowmelt period, highlighting the complexities and inter-annual variation in the snowmelt season. While northern HMA has maintained a negative trend in snowmelt end throughout both analysis timeframes, a large region running from the Pamir east has had a reversed trend from negative to positive in the last decade. Regression results at both individual timeframes are available in the Supplement (Fig. C8).

The majority of HMA, however, exhibits a three-decade long trend towards an earlier end of the snowmelt season. Earlier snow clearance increases the absorption of solar radiation, and thus stores more heat at high elevations and generates a positive feedback (Willis et al., 2002). As seasonal snow is removed earlier from glacier regions, glacier melt will accelerate. In general, glaciers in HMA are decreasing in volume and shrinking, which fits with the observed long-term decrease in snowmelt end dates (cf. Figs. 6.9, 6.10, 6.11), despite clear spatial and temporal heterogeneity in these trends (cf. Fig. 6.12).

Caveats of the Method

Our algorithm-derived snowmelt end dates and those derived from the independent MOD10C1 product show close alignment, indicating that the algorithm is well-suited to identifying the end of the snowmelt season (cf. Fig. 6.4). The identification and interpretation of the MXPGR, however, is more difficult. While previous work has used the XPGR to identify the presence of liquid water in snowpack, this relationship has not been confirmed with in-situ data in HMA. While it is likely that XPGR peaks are linked to melt-refreeze cycles, liquid water, or other snowpack metamorphism, these conclusions lack true in-situ controls. This uncertainty, combined with the periods of melt and refreeze and late-season storms in much of HMA, make linking MXPGR to the onset of the snowmelt season difficult. The multiple peaks and troughs in the XPGR data also hamper the identification of a single strong peak to classify as the MXPGR. Without rigorous measurements of surface air temperature or in-situ monitoring of snowmelt, the efficacy of our algorithm for identifying snowmelt onset cannot be directly confirmed.

Despite these drawbacks, MXPGR dates are correlated with the day of year that HAR temperatures first start to increase and MODIS SCA is maximal (Fig. C2), and provide a single consistent proxy for the onset of the snowmelt season in this vast and largely unmonitored area. Furthermore, MXPGR is associated with days with a high temperature range and on-average positive daytime surface temperatures (cf. Fig. 6.5). This implies that rising daytime temperatures, in conjunction with solar radiation, are linked to MXPGR dates in our study area. However, as we lack a direct control dataset for snowmelt onset, and there is a high degree of variance in the HAR surface temperature-MXPGR relationship, MXPGR dates and trends therein should be considered as less reliable than trends in snowmelt end dates.

Conclusions

This study presents a snowmelt tracking algorithm based on the cross-polarized gradient ratio, native passive microwave (PM) signal, and a rough estimate of snow-water equivalent (SWE). We do not rely on static thresholds to classify the snowmelt season across our diverse study region, but instead rely on identifying the snowmelt signal from intrinsic properties of each individual time series. The algorithm leverages passive microwave data from the Special Sensor Microwave/Imager (SSMI), Special Sensor Microwave Imager/Sounder (SSMIS), Advanced Microwave Scanning Radiometer - Earth Observing System (AMSR-E), AMSR2, and Global Precipitation Measurement (GPM) satellites (1987-2016) to track the characteristics of the snowmelt season across High Mountain Asia (HMA). We examine large-scale spatial patterns in the snowmelt regime and identify trends in the timing of snowmelt across HMA over the past three decades using hierarchical clustering.

We find the following four key points: (1) The snowmelt season is ending earlier in much of HMA (negative trend), with magnitudes between 2 and 8 days/decade (5-25 days total over 29 years). The length of the snowmelt season is shortening in the majority of HMA, despite some regions of delayed snowmelt onset. (2) Negative changes to the end of the snowmelt season are felt most strongly in areas with long snowmelt seasons (as averaged over three decades), such as the Tibetan Plateau and high-SWE areas in the Himalaya, Karakoram, and Tien Shan. (3) While three-decade long trends indicate earlier end dates for the snowmelt season, recent (2002-2016) trends are positive (later snowmelt end dates) in many regions of HMA. These changes could be due to inter-annual variability or a reversal in the long-term trend. (4) Areas with slightly longer snowmelt seasons or later MXPGR dates overlap with regions of positive glacier mass balance, such as the Pamir and Kunlun Shan. This implies that changes to the snowmelt regime of HMA could help account for some of the observed regional glacier changes. In general, however, regional warming has led to earlier and shortened melt seasons in much of HMA. These changes are spatially and temporally complex, and will require further local and high-spatial resolution assessments to fully understand changes in HMA's cryosphere.

Code Availability

The code used in this study is available online at: https://github.com/UP-RS-ESP/SnowmeltTracking

Supporting Information

(see Appendix C).

CHAPTER 7

Discussion and Conclusions

The main goal of this dissertation was to identify and quantify recent changes in HMA's cryosphere. This set of studies was conducted across a large region spanning much of central and southern Asia, centered around the Tibetan Plateau. As water sourced in this region is essential for the livelihoods of more than a billion people, understanding and quantifying changes in snow – the primary water source in many regions of HMA – is of utmost importance. While there exist regional studies on glaciers (e.g., Bolch et al., 2012; Gardner et al., 2013; Kääb et al., 2012, 2015) and smaller-scale studies on snow-cover (e.g., Archer and Fowler, 2004; Treydte et al., 2006), the full extent of changes in HMA's snow regime had not yet been well explored.

HMA contains diverse topographic, environmental, and climatic zones which create vastly different snow regimes. Changes in HMA's climate have impacts not only on nearby regions, but also affect global circulation patterns. However, there remains a dearth of high-quality, consistent, and long-term climate records in the region. In many cases, in-situ climate networks are out-dated, unreliable, or simply do not exist. Station and satellite climate data often disagree, due to issues of scale, time of collection, and measurement accuracy (cf. Fig. 3.3). Collection of ground data is also complicated by difficult terrain, complex political situations, and harsh climates. Recent work has focused on using remotely sensed (e.g., Kääb et al., 2015; Chang and Rango, 2000) and modeled (e.g., Maussion et al., 2014; Yatagai et al., 2012) datasets to address these data gaps, but the empirical, large-scale and high-temporal resolution studies on HMA's cryosphere required to constrain snowmelt runoff are still lacking (Anderton et al., 2002; Dozier et al., 2008).

Passive microwave SWE algorithms were originally developed on flat and sparsely vegetated terrain (Chang et al., 1982, 1987), and are less reliable over densely forested or complex terrain (Takala et al., 2011; Tedesco and Narvekar, 2010; Tedesco et al., 2015; Kelly et al., 2003; Kelly, 2009; Mätzler and Standley, 2000; Dozier and Warren, 1982). As a first step, this dissertation examined what topographic, land-cover, and climatic factors influence PM SWE estimate reliability in HMA. Using this improved understanding of the capabilities and limitations of SWE estimation in HMA, changes in both the spatial and temporal distribution of SWE across HMA were then explored. Lastly, a novel method of tracking the onset and end of the snowmelt season using PM data was devised. Chapters 4 through 6 are comprised of three separate manuscripts which examine each of the three research questions of this dissertation in detail. This Chapter contextualizes these studies in the broader literature on climate change in HMA, and discusses the implications of changes in HMA's cryosphere for regional hydrology.

Limitations of Passive Microwave Data

The first study of this dissertation (Chapter 4) documents several important characteristics of PM sensors which influence the estimation of SWE. As PM SWE estimates are influenced by a range of sensor, topographic, climate, and land-cover characteristics, a thorough understanding of what conclusions can and cannot be drawn from PM SWE data is an essential first step towards constraining changes in HMA's snow regime.

Biases in SWE Estimates

Several authors have examined factors influencing PM SWE estimates (e.g., Dozier and Warren, 1982; Foster et al., 2005; Tedesco and Narvekar, 2010; Mizukami and Perica, 2012; Derksen, 2008; Savoie et al., 2009; Mätzler and Standley, 2000). While radiative transfer theory shows that PM data becomes unreliable in areas of deep snow (SWE >150 mm) (e.g., Tedesco and Narvekar, 2010; Takala et al., 2011; Mizukami and Perica, 2012), the impacts of most climatic and topographic metrics on SWE remained unconstrained. To assess the influence of these factors, a method of isolating only those days where there was no sensed precipitation (derived from TRMM (Huffman et al., 2007)) and air temperatures remained below zero (derived from HAR (Maussion et al., 2014)) was developed and used to assess how variable these nominally consistent SWE measurements were.

The parameters used to examine SWE consistency were long-term snow depth, forest cover, wind speed, slope, elevation, relief and aspect. Previous work has identified problems with SWE retrieval related to snow depth (Foster et al., 2005; Rango et al., 1979) and forest cover (Derksen, 2008). Our results confirmed that these two factors show the strongest correlation with SWE inconsistency. Deep snow was shown to impact not only the ~18 GHz channel used in the original SWE retrieval algorithm (Chang et al., 1987, 1991), but also the ~10 GHz channel used explicitly to help control for deep snowcover in more modern algorithms (Kelly et al., 2003; Kelly, 2009) (cf. Fig. 4.8). It is likely that both depth-related attenuation (Mizukami and Perica, 2012) and the formation of depth hoar and ice lenses during long periods of constant snow cover impact measurements at the ~10 and ~18 GHz channels.

Wind speed had never before been analyzed as a potential driver of variability in SWE measurements. For the first time, we showed that both high (90th percentile) and low (25th percentile) wind speeds are correlated with consistency of SWE measurements. We posit that high wind areas tend to be high-elevation and high-relief, and that wind redistribution of SWE generally occurs within the extent of a single PM pixel (~25 sq km). However, as these areas also receive more SWE generally, it is difficult to distinguish the impacts of precipitation capture and wind-redistribution. Conversely, low-wind areas (25th percentile) can see wind redistribution of SWE over a much larger area. As these areas tend to be lower SWE, however, it is difficult to identify an exact causal relationship.

SWE modeling efforts, such as GlobSWE (Luojus et al., 2013) and HAR (Maussion et al., 2014), and empirical retrievals such as using AMSR-E (Chang and Rango, 2000) offer SWE estimates in mountainous terrain only with severe caveats. Previous work has shown that at very high elevations, such as those found on the Tibetan Plateau, SWE estimates are influenced by the relatively thinner atmosphere (Savoie et al., 2009). We show in our study, however, that while hillslope angle has a small impact on SWE retrieval variability, elevation, aspect, and relief have very little influence. Further, we note that one major influence on SWE retrievals globally – forest cover – is a relatively minor consideration in much of the study area due to the high-elevation terrain and sparse tree cover.

Differences between PM Sensors

Several satellites, both current and past, have flown with PM sensors. Each of these satellites has had a different set of data collection goals, onboard sensors, and spatial resolutions. An important finding of Chapter 4 was that while both the GPM and TRMM missions collect the requisite PM frequencies to measure SWE, only GPM SWE estimates can be considered alongside more specialized PM sensors, such as SSMI/S and AMSR-E/2 (Smith and Bookhagen, 2016). The ~36 GHz vertically polarized channel onboard TRMM displayed too much variability to provide consistent and accurate SWE measurements. Chapter 4, however, showed that GPM data can be used to estimate SWE.

Although each satellite dataset used in this dissertation carries a PM sensor with a different spectral resolution, each sensor agrees on the timing and relative volume of SWE buildup and melt (cf. Figs. 4.4, 4.10). This implies that even if SWE measurements are poorly correlated to in-situ snow depth measurements, as has been shown in several studies (e.g., Mizukami and Perica, 2012; Dai et al., 2015; Foster et al., 2005; Tedesco and Narvekar, 2010), trends in relative SWE and the general timing of the snow season are consistent throughout any given time series and between any combination of sensors. This key finding forms one of the core building blocks for the rest of our analyses, which exploit the consistency in SWE time series to look at changes in SWE intrinsic to given spatial locations.

Novel Methods for Tracking SWE and Snowmelt Changes

This dissertation adapted three important methods from neighboring disciplines to the context of tracking changes in HMA's cryosphere. While each of these methods has previously been used in related fields, this dissertation presents several important adaptations and improvements that allowed long-term trends in snow to be examined with PM data.

Seasonal Trend Decomposition

Seasonal Trend Decomposition (STL) is a method of decomposing a time series into trend, seasonal, and residual components (Cleveland et al., 1990). In its original application, it was used to examine long-term trends in carbon dioxide by removing yearly oscillations. It has since been used in several other natural science applications, such as in tracking sea-level changes (Donner et al., 2012), monitoring forest health (Verbesselt et al., 2010), and in analyzing temporal patterns in groundwater extraction (Shamsudduha et al., 2009).

It is used in this dissertation to isolate long-term changes in SWE storage from seasonal and inter-annual variation. In Chapter 5, both annual (cf. Fig. 5.3) and seasonal (cf. Fig. 5.4) SWE trends are examined. We find that while both the detrended and original time series produce the same results in terms of the direction of slope, the detrended data are more tightly constrained and offers a more statistically robust treatment of long-term changes in SWE without the influence of seasonality.

Snowmelt Tracking Algorithm

Several authors have developed algorithms for tracking snowmelt using PM data (e.g., Abdalati and Steffen, 1995; Hall et al., 2004; Drobot and Anderson, 2001; Joshi et al., 2001; Takala et al., 2003, 2008, 2009; Apgar et al., 2007; Monahan and Ramage, 2010; Tedesco, 2007; Liu et al., 2005). In Chapter 6, the method originally developed by Abdalati and Steffen (1995), which leverages the combined impacts of channel and polarization differences between the horizontally and vertically polarized ~18 GHz and ~37 GHz channels, was modified and applied to HMA. In the original application, static thresholds were used to track snowmelt over large, homogeneous areas of Greenland. Chapter 6 extends this method to use dynamic time series cutoffs, which allows the method to be applied across diverse terrain without forcing pre-conceived melt thresholds onto the dataset. The algorithm was shown to effectively track snowmelt onset and end across a wide range of snow regimes and despite large inter-annual variation in SWE buildup and drawdown, even in the large, spatially heterogeneous context of HMA.

Hierarchical Clustering for Snowmelt Trend Detection

While the newly developed snowmelt tracking algorithm was found to be effective for identifying snowmelt onset and end across HMA, there was simply too much seasonal variation between snowfall seasons to track long-term trends on a point-by-point basis, as had been done in Chapter 5. To overcome the high inter-annual variability in snowmelt seasons, a complex networks approach was leveraged to aggregate the snowmelt data.

Hierarchical clustering has been used extensively to group time series information by intrinsic self-similarity (Corpet, 1988; Johnson, 1967; Jain et al., 1999; Murtagh and Contreras, 2012; Rheinwalt et al., 2015). In essence, clusters of points are identified which share the same periodicity, regardless of the absolute magnitude of their peaks and troughs. This method leads to two important developments. First, the whole length of the PM data collection (1987-2016) can be used to derive clusters instead of only single-instrument time series. While the absolute magnitudes of measured SWE between sensors are not always compatible (Smith and Bookhagen, 2016), the tight temporal co-evolution of their time series allows multi-instrument time series to be effectively clustered with this method. Second, assessing changes in snowmelt onset, end, and period within self-similar clusters reduced the influence of inter-annual and small-scale spatial variability on the detection of snowmelt trends. This method yielded statistically significant results, albeit at reduced spatial resolution.

Recent Changes in HMA's Cryosphere

The combination of the novel methods developed in Chapters 5 and 6 with long-term SWE data in HMA has helped constrain the impacts of climate change on HMA's cyrosphere.

Temperatures in HMA are increasing faster than the global average (Vaughan et al., 2013; Lau et al., 2010). Many studies have examined glaciers as an indicator of regional warming in HMA (e.g., Bolch et al., 2012; Kääb et al., 2012, 2015; Gardner et al., 2013). The mechanisms behind the spatial heterogeneity in glacier losses in HMA remain poorly understood, although recent studies have implicated spatially divergent temperature and precipitation trends as possible drivers of regional glacier differences, as well as changes in precipitation seasonality (Fujita, 2008; Fujita and Nuimura, 2011; Kapnick et al., 2014). This dissertation explores poorly understood changes in HMA's snow regime which control the water security of many communities, and which have likely partially contributed to regional heterogeneity in glacier change.

An overall decrease in SWE storage in HMA was found in Chapter 5, with an annual aggregate decline of 10.6 mm/yr over the entire study area. However, annual losses in SWE hide distinct seasonal and spatial differences, where winter SWE has increased in almost half of HMA in contrast to general negative SWE trends throughout the rest of the year. The mechanism behind these SWE changes is not well defined, but likely includes contributions from aerosol contamination (Lau et al., 2010), changes in precipitation phase (Lutz et al., 2014), changes in the strengths of the WWD (Cannon et al., 2014, 2015) and ISM (Singh et al., 2014; Palazzi et al., 2013), and increases in regional temperatures which lead to both more atmospheric water storage and decreased SWE persistence (Vaughan et al., 2013; Yao et al., 2012; Trenberth, 2011). The elevation distribution of these changes indicates that the impacts of climate change on glaciers and snow will be related but distinct in HMA.

Following the exploration of SWE trends in Chapter 5, changes in the timing of the snowmelt season were explored in Chapter 6. In general, the end of the snowmelt season is occurring earlier across HMA, and the length of the snowmelt season is shrinking; these changes are not biased towards early or late snowmelt-onset regions (cf. Fig. 6.10). Warming temperatures increase the rate of snowmelt and can drive a precipitation shift from snow to rain. The onset of snowmelt, however, is occurring later in some parts of HMA, indicating that snowmelt changes in HMA are not monolithic. There exist large temperature, elevation, and precipitation gradients which drive regional differences in the response of HMA's cryosphere to regional warming. The diverse mountain ranges examined in the study area have responded to climate change differently and must be contextualized individually.

Tien Shan

Studies disagree on the fate of glaciers in the Tien Shan (Sorg et al., 2012; Narama et al., 2010; Gardner et al., 2013; Farinotti et al., 2015). Large-scale studies note only glacier mass loss in the Tien Shan (e.g., Gardner et al., 2013), although Farinotti et al. (2015) found regions of both growing and retreating glaciers in the Tien Shan, with high spatial heterogeneity. More glacier mass loss was noted in the western (outer) than the eastern (inner) regions of the Tien Shan (Sorg et al., 2012), which agrees generally with the distributions of positive DJF SWE trends found in the Tien Shan (cf. Fig. 5.4), and the increased strength of the WWD (Cannon et al., 2014, 2015). Large regional decreases in March-April-May (MAM) SWE, however, indicate that this increased December-January-February (DJF) SWE is not maintained into the spring. Recent work has also proposed that predominantly summer-accumulation type glaciers, such as those in the Tien Shan, are more likely to lose mass under warming climates (Fujita, 2008; Fujita and Nuimura, 2011), which could reconcile the increase in DJF SWE with regionally declining glaciers.

Changes in snowmelt onset, end, and period are distinctly negative, excepting a small area of larger snowmelt periods in the north eastern Tien Shan. This result agrees well with previous observations which noted earlier snowmelt throughout Central Asia (Dietz et al., 2014). It also confirms the strongly negative MAM SWE trends (cf. Fig. 5.4), which, when combined with the positive DJF SWE trends, indicate that the Tien Shan has experienced earlier and stronger spring snowmelt.

Pamir, Karakoram, and Kunlun Shan

Recent studies have noted glacier stability or even mass increases in the Pamir (Gardelle et al., 2013), Karakoram (Hewitt, 2005; Gardelle et al., 2012; Scherler et al., 2011; Kääb et al., 2015), and Kunlun Shan (Shangguan et al., 2007; Ding et al., 2006; Kääb et al., 2015). Increased winter precipitation has been proposed as a possible mechanism behind these changes (Gardelle et al., 2012; Kapnick et al., 2014; Yao et al., 2012; Fujita, 2008; Fujita and Nuimura, 2011), but has not been confirmed with empirical data. This dissertation work indicates that changes in glaciers are well matched with changes in the timing of snow buildup and melt in the Pamir-Karakoram-Kunlun Shan region.

Increasing precipitation (Sorg et al., 2012; Aizen et al., 1997; Archer and Fowler, 2004; Treydte et al., 2006) and increased snow cover (Dahe et al., 2006; Che et al., 2008) had been previously observed in the Pamir-Karakoram-Kunlun Shan area. This aligns well with our results (cf. Fig. 5.4) which indicate that winter SWE has increased in the Pamir, Kunlun Shan, and parts of the Karakoram over the past decades. These areas have also seen increases in MAM and September-October-November (SON) SWE, in opposition to the general trend towards losses in spring and fall SWE in the rest of HMA. The Pamir and Kunlun Shan are two of the areas where slight increases in the length of the snowmelt season were observed (cf. Fig. 6.9), and where full-year SWE trends are positive (cf. Fig. 5.3). When these factors are considered together, it is likely that increases in the strength of the WWD and in the strength of late-season storms (Cannon et al., 2014, 2015; Kapnick et al., 2014) are responsible for some of the changes in the SWE distribution. However, the Karakoram is the only region out of the three which sees slightly later snowmelt onset, indicating that changes in SWE are not evenly felt across the study region, and that climate change impacts are heterogeneous even among regions impacted by the same large-scale climate patterns.

Himalaya and Hindu Kush

While much of the Himalaya's water budget is monsoon-driven, there exists a precipitation gradient moving west along the front of the Himalaya, where the western reaches of the Himalaya-Hindu Kush region have a much higher snowmelt and glacier contribution to their water budgets (Bookhagen and Burbank, 2010). Even in those regions where rainfall is primary, seasonal snowmelt is an important water source for mountain communities. These communities rely heavily on the consistency of snow and glacier melt to meet dry-season water needs (Vaughan et al., 2013).

Glaciers in the Himalaya-Hindu Kush are generally retreating (Bolch et al., 2012; Gardner et al., 2013; Kääb et al., 2012, 2015); in many cases, retreat is accelerating and small glaciers are disappearing (Armstrong et al., 2010). The reasons behind these changes are multi-faceted and poorly constrained, although debris cover, topography, and precipitation regime are factors known to impact glacier stability.

Previous work has noted earlier snowmelt in the Himalaya (Lau et al., 2010; Panday et al., 2011); this is generally confirmed in this dissertation. In parts of the eastern Himalaya, a slight increase full-year SWE is observed, despite negative trends in snowmelt onset, end, and period. This implies a slight increase in snow persistence in parts of the eastern Himalaya and could be related to increased incursion of large storms into the dry Tibetan Plateau interior. Trends in snowmelt end date and snowmelt period are distinctly negative across the entire region, excepting a few isolated pixels in the central Himalaya.

This central Himalayan area along the border with the Indus and Ganges shows positive SON and DJF SWE trends. This region receives moisture from both the ISM and WWD; precipitation at the end of the monsoon season could account for some of the increases in SON SWE, which remains through the winter. These positive SWE trends are strong enough to show a positive trend at the yearly scale, in opposition to the general decrease in SWE in HMA (cf. Fig. 5.3).

Tibetan Plateau

Despite slightly later snowmelt onset in parts of the Tibetan Plateau (cf. Fig. 6.9), SWE trends in the central Tibetan Plateau are negative at both annual (cf. Fig. 5.3) and seasonal (cf. Fig. 5.4) scales. The far eastern reaches of the Tibetan Plateau, towards the headwaters of the Salween and the northeastern reaches of the Brahmaputra, show both increases in yearly SWE and DJF/MAM/SON SWE. This confirms the results of Zhang et al. (2004) who noted that the eastern Tibetan Plateau has seen increasing snow depths, and in particular, increasing spring snow depths since the 1970s.

Empirical study of the Tibetan Plateau's cryosphere is difficult due to the general lack of ground-truth data above 5,000 m (Kang et al., 2010) and insufficiently dense in-situ climate monitoring networks (cf. Fig. 5.2). While the general utility of remote sensing datasets for monitoring snow in Tibet has been explored (Che et al., 2008; Pu et al., 2007; Kang et al., 2010; Zhang et al., 2004), relatively little work has explored changes in snow cover in the region. Discussion of snow cover changes in Tibet is complicated by the vastly different areas considered as the Tibetan Plateau between studies, of which some consider only the endorreic Tibetan Plateau catchment, while others include areas as far away as the Tien Shan.

The general earlier snowmelt clearance and shorter snowmelt periods observed in this dissertation align well with the decreases in glacier mass and permafrost stability seen in the Tibetan Plateau (Kang et al., 2010). Negative SWE trends in the low-SWE central Tibetan Plateau are likely driven by increasing regional temperatures. Increases in SWE along the eastern, northern, and western borders of the Tibetan Plateau are likely driven by slightly increasing precipitation in the region (Kang et al., 2010; Zhang et al., 2004), coupled with generally low temperatures that allow snow persistence despite increasing regional temperatures.

Implications of Changes in HMA's Cryosphere

There exist clear regional differences in climate change impacts on HMA's cryosphere. There also exist temporal heterogeneities in snowmelt trends, where several-decade-long trends hide inter-annual and inter-decadal variations (cf. Figs. 6.11-6.12). The heterogeneity in snowmelt trends over the past decade indicates that the snow regime of HMA has become more variable in recent years. In particular, large regions of the Tien Shan, Pamir, and Karakoram have seen reversals from negative to positive trends in snowmelt onset and end dates when the periods 1988-2002 and 2002-2016 are considered separately (cf. Figs. C8, 6.12). Poor treatment of SWE in climate models (Maussion et al., 2014), and lack of in-situ measurements (Sorg et al., 2012) limit analysis of snowpack over shorter timeframes. More in-depth studies will be required to constrain whether this is a reversal in a long-term trend or simply inter-annual variability impacting the climatically short time series examined in this dissertation.

Long-term trends across HMA, however, indicate a shift towards shorter and earlier snowmelt seasons. This has already had, and will continue to have, strong impacts upon communities which rely on consistency in the volume and timing of snowmelt for year-round water provision (Stewart, 2009; Archer and Fowler, 2004; Barnett et al., 2005; Bolch et al., 2012). Earlier snowmelt will also drive changes in glaciers, as snow-free high-elevation areas are able to store more heat from incoming solar radiation (Willis et al., 2002). The timing of snowfall and snowmelt have previously been noted as an important constraint on glacial change (Maussion et al., 2014; Wang et al., 2017; Kapnick et al., 2014; Fujita, 2008; Fujita and Nuimura, 2011). As regional temperatures continue to warm, it is likely that the changes in HMA's cryosphere observed in this dissertation will accelerate, and will be strongly felt by both high-elevation communities and those downstream who depend on water sourced in HMA.

Conclusions

The aim of this dissertation was to develop a coherent, empirically based, and spatially extensive picture of recent changes in HMA's cryosphere. To this end, *the reliability of PM SWE estimates in the complex topography of HMA* was explored. This study was undertaken using a suite of five sensors in conjunction with climatic, topographic, and land-cover datasets at a large spatial scale. The improved understanding of the capabilities of PM SWE estimates was then used to develop two studies exploring changes in HMA's cryosphere. The first study assessed *recent spatio-temporal patterns of SWE change across HMA*. Following this, a novel algorithm to *explore spatio-temporal changes in the timing of the snowmelt season across HMA* was developed. The following conclusions can be drawn from these studies:

1. PM data are impacted by a wide range of topographic, land cover, and climatic factors. The two factors which contribute the most to SWE variability in nominally constant-SWE times – forest cover and PM signal attenuation in deep snow – are controlled for in modern SWE algorithms. Wind redistribution of SWE contributes to SWE variance in HMA, and is poorly controlled for in the sparsely monitored HMA region. Hillslope angle was the only topographic factor shown to have a significant impact on SWE estimate reliability.

2. Each PM sensor measures slightly different frequencies, and thus provides slightly different SWE estimates. While these estimates can diverge in magnitude, the timing of snow buildup and draw down are preserved between sensors. Relative SWE magnitudes within single-sensor time series are also preserved, indicating that while PM SWE estimates will not always agree with ground measurements, they represent an internally consistent and temporally continuous measurement of SWE.

3. Long-term annual SWE trends are negative in much of HMA (cf. Fig. 5.3), although some regions – such as the Pamir, Kunlun Shan, and eastern Tibetan Plateau – have seen increased SWE. The seasonal distribution of SWE has also changed significantly over the past decades. The central Himalaya, Pamir, Tien Shan, and Kunlun Shan have seen increased winter SWE; spring SWE trends are only positive in the Pamir, Karakoram, and Kunlun Shan.

4. The onset, end, and length of the snowmelt season can be tracked using a dynamic, time-series-derived, metric. The mean offset between the algorithm-derived onset and end dates and manually controlled dates is within one day. The average absolute offset is within one week, with almost 90% of onset and end dates within 10 days of the control dataset.

5. Snowmelt onset is split between positive changes from the Karakoram through the Tibetan Plateau, and negative changes in the rest of HMA. Snowmelt end dates are almost universally negative, excepting a high-elevation, low-temperature region along the Karakoram-Kunlun Shan. Only a few isolated regions in the Pamir, Karakoram, and Tien Shan see longer snowmelt periods. These long-term trends conceal inter-annual variability, where more recent (2002-2016) snowmelt trends are positive or less negative than long-term trends in many regions.

6. The combined changes in seasonal SWE distribution and the timing of the snowmelt season will impact the environment and inhabitants of HMA. Glaciers have been shown to be retreating in much of HMA, with a few notable exceptions. The spatial distribution of glacier changes agrees well with the changes in HMA's cyrosphere observed in this dissertation, implying that changes in SWE and snowmelt are a potential control on glacier response to climate change. The combined changes in SWE and snowmelt will be felt by high-elevation communities and downstream users who rely on the consistency of snowmelt volume and timing for agriculture, livelihoods, and water provision.

References

Abdalati, W. and Steffen, K.: Passive microwave-derived snow melt regions on the Greenland Ice Sheet, Geophysical Research Letters, 22, 787–790, 1995.

Aizen, V. B., Aizen, E. M., Melack, J. M., and Dozier, J.: Climatic and hydrologic changes in the Tien Shan, central Asia, Journal of Climate, 10, 1393–1404, 1997.

Anderton, S., White, S., and Alvera, B.: Micro-scale spatial variability and the timing of snow melt runoff in a high mountain catchment, Journal of Hydrology, 268, 158–176, 2002.

Andreadis, K. M. and Lettenmaier, D. P.: Assimilating remotely sensed snow observations into a macroscale hydrology model, Advances in Water Resources, 29, 872–886, 2006.

Andreadis, K. M. and Lettenmaier, D. P.: Implications of representing snowpack stratigraphy for the assimilation of passive microwave satellite observations, Journal of Hydrometeorology, 13, 1493–1506, 2012.

Apgar, J. D., Ramage, J. M., McKenney, R. A., and Maltais, P.: AMSR-E algorithm for snowmelt onset detection in sub-arctic heterogeneous terrain, Hydrological processes, 21, 1587–1596, 2007.

Archer, D. R. and Fowler, H.: Spatial and temporal variations in precipitation in the Upper Indus Basin, global teleconnections and hydrological implications, Hydrology and Earth System Sciences Discussions, 8, 47–61, 2004.

Arendt, A., Bolch, T., Cogley, J., Gardner, A., Hagen, J., Hock, R., Kaser, G., Pfeffer, W., Moholdt, G., Paul, F., et al.: Randolph Glacier Inventory [v5.0]: A Dataset of Global Glacier Outlines. Global Land Ice Measurements from Space, Boulder Colorado, USA, Digital Media, 2015.

Armstrong, R. and Brodzik, M.: Recent Northern Hemisphere snow extent: A comparison of data derived from visible and microwave satellite sensors, Geophysical Research Letters, 28, 3673–3676, 2001.

Armstrong, R. L. and Brodzik, M. J.: Hemispheric-scale comparison and evaluation of passive-microwave snow algorithms, Annals of Glaciology, 34, 38–44, 2002.

Armstrong, R. L., Chang, A., Rango, A., and Josberger, E.: Snow depths and grain-size relationships with relevance for passive microwave studies, Annals of Glaciology, 17, 171–176, 1993.

Armstrong, R. L. et al.: The glaciers of the Hindu Kush-Himalayan region: a summary of the science regarding glacier melt/retreat in the Himalayan, Hindu Kush, Karakoram, Pamir, and Tien Shan mountain ranges., International Centre for Integrated Mountain Development (ICIMOD), 2010.

Ashcroft, P. and Wentz, F.: AMSR-E/aqua L2A global swath spatially-resampled brightness temperatures V003, [2002–2010]., Boulder, Colorado USA: National Snow and Ice Data Center, 2013.

Bamzai, A. S. and Shukla, J.: Relation between Eurasian snow cover, snow depth, and the Indian summer monsoon: An observational study, Journal of Climate, 12, 3117–3132, 1999.

Barlow, M., Wheeler, M., Lyon, B., and Cullen, H.: Modulation of daily precipitation over southwest Asia by the Madden–Julian oscillation, Monthly weather review, 133, 3579–3594, 2005.

Barnett, T., Dümenil, L., Schlese, U., Roeckner, E., and Latif, M.: The effect of Eurasian snow cover on regional and global climate variations, Journal of the Atmospheric Sciences, 46, 661–686, 1989.

Barnett, T. P., Adam, J. C., and Lettenmaier, D. P.: Potential impacts of a warming climate on water availability in snow-dominated regions, Nature, 438, 303–309, 2005.

Beltsville Agricultural Research Center Electron and Confocal Microscopy Unit: Comparison of depth hoar crystal using light (video) and Low Temperature Scanning Electron Microscopy, URL http://www.anri.barc.usda.gov/emusnow/default.htm,accessedvia:https://commons.wikimedia.org/wiki/File:LightLTSEM.jpg.

Berghuijs, W., Woods, R., and Hrachowitz, M.: A precipitation shift from snow towards rain leads to a decrease in streamflow, Nat. Clim. Change, 4, 583–586, 2014.

Bolch, T., Kulkarni, A., Kääb, A., Huggel, C., Paul, F., Cogley, J., Frey, H., Kargel, J., Fujita, K., Scheel, M., et al.: The state and fate of Himalayan glaciers, Science, 336, 310–314, 2012.

Bookhagen, B.: Chapter 11: The influence of Hydrology and Glaciology on Wetlands in the Himalaya, in: Bird Migration Across the Himalayas: Wetland Functioning Amidst Mountains and Glaciers, edited by Prins, H. and Namgail, T., Cambridge University press, 2017.

Bookhagen, B. and Burbank, D. W.: Toward a complete Himalayan hydrological budget: Spatiotemporal distribution of snowmelt and rainfall and their impact on river discharge, Journal of Geophysical Research: Earth Surface (2003–2012), 115, 2010.

Bookhagen, B., Thiede, R. C., and Strecker, M. R.: Abnormal monsoon years and their control on erosion and sediment flux in the high, arid northwest Himalaya, Earth and Planetary Science Letters, 231, 131–146, 2005.

Boos, W. R. and Kuang, Z.: Dominant control of the South Asian monsoon by orographic insulation versus plateau heating, Nature, 463, 218–222, 2010.

Brown, R.: Evaluation of methods for climatological reconstruction of snow depth and snow cover duration at Canadian meteorological stations, in: Proc. Eastern Snow Conf., 53d Annual Meeting, pp. 55–65, 1996.

Bulygina, O., Groisman, P. Y., Razuvaev, V., and Korshunova, N.: Changes in snow cover characteristics over Northern Eurasia since 1966, Environmental Research Letters, 6, 045 204, 2011.

Cannon, F., Carvalho, L., Jones, C., and Bookhagen, B.: Multi-annual variations in winter westerly disturbance activity affecting the Himalaya, Climate Dynamics, pp. 1–15, 2014.

Cannon, F., Carvalho, L. M., Jones, C., and Norris, J.: Winter westerly disturbance dynamics and precipitation in the western Himalaya and Karakoram: a wave-tracking approach, Theoretical and Applied Climatology, pp. 1–18, 2015.

Cannon, F., Carvalho, L., Jones, C., Hoell, A., Norris, J., Kiladis, G., and Tahir, A.: The influence of tropical forcing on extreme winter precipitation in the western Himalaya, Climate Dynamics, 2016.

Cannon, F., Carvalho, L. M. V., Jones, C., Norris, J., Bookhagen, B., and Kiladis, G. N.: Effects of Topographic Smoothing on the Simulation of Winter Precipitation in High Mountain Asia, Journal of Geophysical Research: Atmospheres, pp. n/a–n/a, doi: 10.1002/2016JD026038, URL http://dx.doi.org/10.1002/2016JD026038, 2016JD026038, 2017.

Cavalieri, D. J., Parkinson, C. L., DiGirolamo, N., and Ivanoff, A.: Intersensor calibration between F13 SSMI and F17 SSMIS for global sea ice data records, IEEE Geoscience and remote sensing letters, 9, 233–236, 2012.

Chang, A., Foster, J., Hall, D., Rango, A., and Hartline, B.: Snow water equivalent estimation by microwave radiometry, Cold Regions Science and Technology, 5, 259–267, 1982.

Chang, A., Foster, J., and Hall, D.: Nimbus-7 SMMR derived global snow cover parameters, Annals of glaciology, 9, 39–44, 1987.

Chang, A., Foster, J., and Rango, A.: Utilization of surface cover composition to improve the microwave determination of snow water equivalent in a mountain basin, Remote Sensing, 12, 2311–2319, 1991.

Chang, A., Foster, J., and Hall, D.: Effects of forest on the snow parameters derived from microwave measurements during the BOREAS winter field campaign, Hydrological Processes, 10, 1565–1574, 1996.

Chang, A. T. and Rango, A.: Algorithm theoretical basis document (ATBD) for the AMSR-E snow water equivalent algorithm, NASA/GSFC, Nov, 2000.

Chang, T., Gloersen, P., Schmugge, T., Wilheit, T., and Zwally, H.: Microwave emission from snow and glacier ice, Journal of Glaciology, 16, 23–39, 1976.

Charney, J., Quirk, W. J., Chow, S.-h., and Kornfield, J.: A comparative study of the effects of albedo change on drought in semi–arid regions, Journal of the Atmospheric Sciences, 34, 1366–1385, 1977.

Charney, J. G.: Dynamics of deserts and drought in the Sahel, Quarterly Journal of the Royal Meteorological Society, 101, 193–202, 1975.

Che, T., Xin, L., Jin, R., Armstrong, R., and Zhang, T.: Snow depth derived from passive microwave remote-sensing data in China, Annals of Glaciology, 49, 145–154, 2008.

CIESIN - Columbia University: Gridded Population of the World, Version 4 (GPWv4): Population Density Adjusted to Match 2015 Revision UN WPP Country Totals., URL http://dx.doi.org/10.7927/H4HX19NJ, 2016.

Cleveland, R. B., Cleveland, W. S., McRae, J. E., and Terpenning, I.: STL: A seasonal-trend decomposition procedure based on loess, Journal of Official Statistics, 6, 3–73, 1990.

Clifford, D.: Global estimates of snow water equivalent from passive microwave instruments: history, challenges and future developments, International Journal of Remote Sensing, 31, 3707–3726, 2010.

Cordisco, E., Prigent, C., and Aires, F.: Snow characterization at a global scale with passive microwave satellite observations, Journal of Geophysical Research: Atmospheres, 111, 2006.

Corpet, F.: Multiple sequence alignment with hierarchical clustering, Nucleic acids research, 16, 10 881–10 890, 1988.

Cuffey, K. M. and Paterson, W. S. B.: The physics of glaciers, Academic Press, 2010.

Dahe, Q., Shiyin, L., and Peiji, L.: Snow cover distribution, variability, and response to climate change in western China, Journal of climate, 19, 1820–1833, 2006.

Dai, L. and Che, T.: Cross-platform calibration of SMMR, SSM/I and AMSR-E passive microwave brightness temperature, in: The Sixth International Symposium on Digital Earth, pp. 784 103–784 103, International Society for Optics and Photonics, 2009.

Dai, L., Che, T., and Ding, Y.: Inter-Calibrating SMMR, SSM/I and SSMI/S Data to Improve the Consistency of Snow-Depth Products in China, Remote Sensing, 7, 7212–7230, 2015.

Daly, S. F., Vuyovich, C. M., Deeb, E. J., Newman, S. D., Baldwin, T. B., and Gagnon, J. J.: Assessment of the snow conditions in the major watersheds of Afghanistan using multispectral and passive microwave remote sensing, Hydrological Processes, 26, 2631–2642, 2012.

Derksen, C.: The contribution of AMSR-E 18.7 and 10.7 GHz measurements to improved boreal forest snow water equivalent retrievals, Remote Sensing of Environment, 112, 2701–2710, 2008.

Derksen, C., Brown, R., and Walker, A.: Merging conventional (1915–92) and passive microwave (1978–2002) estimates of snow extent and water equivalent over central North America, Journal of Hydrometeorology, 5, 850–861, 2004.

DeWalle, D. R. and Rango, A.: Principles of snow hydrology, Cambridge University Press, 2008.

Dietz, A. J., Conrad, C., Kuenzer, C., Gesell, G., and Dech, S.: Identifying changing snow cover characteristics in Central Asia between 1986 and 2014 from remote sensing data, Remote Sensing, 6, 12 752–12 775, 2014.

DiMiceli, C., Carroll, M., Sohlberg, R., Huang, C., Hansen, M., and Townshend, J.: Annual global automated MODIS vegetation continuous fields (MOD44B) at 250 m spatial resolution for data years beginning day 65, 2000-2010, collection 5 percent tree cover, USA: University of Maryland, College Park, MD, 2011.

Ding, Y., Liu, S., Li, J., and Shangguan, D.: The retreat of glaciers in response to recent climate warming in western China, Annals of Glaciology, 43, 97–105, 2006.

Dong, J., Walker, J. P., and Houser, P. R.: Factors affecting remotely sensed snow water equivalent uncertainty, Remote Sensing of Environment, 97, 68–82, 2005.

Donner, R., Ehrcke, R., Barbosa, S., Wagner, J., Donges, J., and Kurths, J.: Spatial patterns of linear and nonparametric long-term trends in Baltic sea-level variability, Nonlinear Processes in Geophysics, 19, 95–111, 2012.

Dozier, J. and Warren, S. G.: Effect of viewing angle on the infrared brightness temperature of snow, Water Resources Research, 18, 1424–1434, doi: 10.1029/WR018i005p01424, URL http://dx.doi.org/10.1029/WR018i005p01424, 1982.

Dozier, J., Painter, T. H., Rittger, K., and Frew, J. E.: Time–space continuity of daily maps of fractional snow cover and albedo from MODIS, Advances in Water Resources, 31, 1515–1526, 2008.

Drobot, S. D. and Anderson, M. R.: An improved method for determining snowmelt onset dates over Arctic sea ice using scanning multichannel microwave radiometer and Special Sensor Microwave/Imager data, 2001.

Farinotti, D., Longuevergne, L., Moholdt, G., Duethmann, D., Mölg, T., Bolch, T., Vorogushyn, S., and Güntner, A.: Substantial glacier mass loss in the Tien Shan over the past 50 years, Nature Geoscience, 2015.

Ficke, A. D., Myrick, C. A., and Hansen, L. J.: Potential impacts of global climate change on freshwater fisheries, Reviews in Fish Biology and Fisheries, 17, 581–613, 2007.

Foster, J. L., Sun, C., Walker, J. P., Kelly, R., Chang, A., Dong, J., and Powell, H.: Quantifying the uncertainty in passive microwave snow water equivalent observations, Remote Sensing of environment, 94, 187–203, 2005.

Frey, H., Machguth, H., Huss, M., Huggel, C., Bajracharya, S., Bolch, T., Kulkarni, A., Linsbauer, A., Salzmann, N., and Stoffel, M.: Estimating the volume of glaciers in the Himalayan–Karakoram region using different methods, The Cryosphere, 8, 2313–2333, 2014.

Fu, C.: Potential impacts of human-induced land cover change on East Asia monsoon, Global and Planetary Change, 37, 219–229, 2003.

Fujita, K.: Effect of precipitation seasonality on climatic sensitivity of glacier mass balance, Earth and Planetary Science Letters, 276, 14–19, 2008.

Fujita, K. and Nuimura, T.: Spatially heterogeneous wastage of Himalayan glaciers, Proceedings of the National Academy of Sciences, 108, 14 011–14 014, 2011.

Gardelle, J., Berthier, E., and Arnaud, Y.: Slight mass gain of Karakoram glaciers in the early twenty-first century, Nature geoscience, 5, 322–325, 2012.

Gardelle, J., Berthier, E., Arnaud, Y., and Kääb, A.: Region-wide glacier mass balances over the Pamir-Karakoram-Himalaya during 1999-2011, Cryosphere, 7, 2013.

Gardner, A. S., Moholdt, G., Cogley, J. G., Wouters, B., Arendt, A. A., Wahr, J., Berthier, E., Hock, R., Pfeffer, W. T., Kaser, G., et al.: A reconciled estimate of glacier contributions to sea level rise: 2003 to 2009, Science, 340, 852–857, 2013.

Gautam, R., Hsu, N., Lau, K.-M., and Kafatos, M.: Aerosol and rainfall variability over the Indian monsoon region: distributions, trends and coupling, in: Annales Geophysicae, vol. 27, pp. 3691–3703, Copernicus GmbH, 2009.

Ghosh, S., Das, D., Kao, S.-C., and Ganguly, A. R.: Lack of uniform trends but increasing spatial variability in observed Indian rainfall extremes, Nature Climate Change, 2, 86–91, 2012.

Githeko, A. K., Lindsay, S. W., Confalonieri, U. E., and Patz, J. A.: Climate change and vector-borne diseases: a regional analysis, Bulletin of the World Health Organization, 78, 1136–1147, 2000.

Goswami, B. and Mohan, R. A.: Intraseasonal oscillations and interannual variability of the Indian summer monsoon, Journal of Climate, 14, 1180–1198, 2001.

Goswami, B., Krishnamurthy, V., and Annmalai, H.: A broad-scale circulation index for the interannual variability of the Indian summer monsoon, Quarterly Journal of the Royal Meteorological Society, 125, 611–633, 1999.

GPM Science Team: GPM GMI Level 1B Brightness Temperatures, version 03, Greenbelt, MD, USA: NASA Goddard Earth Science Data and Information Services Center (GES DISC), 2014.

Grody, N. C.: Classification of snow cover and precipitation using the Special Sensor Microwave Imager, 1991.

Guan, B., Molotch, N. P., Waliser, D. E., Jepsen, S. M., Painter, T. H., and Dozier, J.: Snow water equivalent in the Sierra Nevada: Blending snow sensor observations with snowmelt model simulations, Water Resources Research, 49, 5029–5046, 2013.

Hahn, D. G. and Shukla, J.: An apparent relationship between Eurasian snow cover and Indian monsoon rainfall, Journal of the Atmospheric Sciences, 33, 2461–2462, 1976.

Hall, D. K. and Riggs, G. A.: MODIS/Terra Snow Cover Daily L3 Global 0.05Deg CMG, Version 6, URL http://dx.doi.org/10.5067/MODIS/MOD10C1.006.27.6.2017, 2016.

Hall, D. K., Williams Jr, R. S., Steffen, K., and Chien, J. Y.: Analysis of summer 2002 melt extent on the Greenland Ice Sheet using MODIS and SSM/I data, in: Geoscience and Remote Sensing Symposium, 2004. IGARSS'04. Proceedings. 2004 IEEE International, vol. 5, pp. 3029–3032, IEEE, 2004.

Hansen, M., DeFries, R., Townshend, J., Carroll, M., Dimiceli, C., and Sohlberg, R.: Global percent tree cover at a spatial resolution of 500 meters: First results of the MODIS vegetation continuous fields algorithm, Earth Interactions, 7, 1–15, 2003.

Hasson, S., Lucarini, V., Khan, M. R., Petitta, M., Bolch, T., and Gioli, G.: Early 21st century snow cover state over the western river basins of the Indus River system, Hydrology and Earth System Sciences, 18, 4077–4100, doi: 10.5194/hess-18-4077-2014, URL http://www.hydrol-earth-syst-sci.net/18/4077/2014/, 2014.

Hewitt, K.: The Karakoram anomaly? Glacier expansion and the'elevation effect,'Karakoram Himalaya, Mountain Research and Development, 25, 332–340, 2005.

Hoekstra, P. and Delaney, A.: Dielectric properties of soils at UHF and microwave frequencies, Journal of geophysical research, 79, 1699–1708, 1974.

Hollinger, J., Lo, R., Poe, G., Savage, R., and Pierce, J.: Special sensor microwave/imager user's guide, NRL Tech. Rpt, 1987.

Huffman, G. J., Bolvin, D. T., Nelkin, E. J., Wolff, D. B., Adler, R. F., Gu, G., Hong, Y., Bowman, K. P., and Stocker, E. F.: The TRMM multisatellite precipitation analysis (TMPA): Quasi-global, multiyear, combined-sensor precipitation estimates at fine scales, Journal of Hydrometeorology, 8, 38–55, 2007.

Huss, M., Bookhagen, B., Huggel, C., Jacobsen, D., Bradley, R., Clague, J., Vuille, M., Buytaert, W., Cayan, D., Greenwood, G., Mark, B., Milner, A., Weingartner, R., and Winder, M.: Towards mountains without permanent snow and ice, Earth's Future, pp. n/a–n/a, doi: 10.1002/2016EF000514, URL http://dx.doi.org/10.1002/2016EF000514, 2016EF000514, 2017.

Imaoka, K., Kachi, M., Kasahara, M., Ito, N., Nakagawa, K., and Oki, T.: Instrument performance and calibration of AMSR-E and AMSR2, International Archives of the Photogrammetry, Remote Sensing and Spatial Information Science, 38, 13–18, 2010.

Immerzeel, W. and Bierkens, M.: Asia's water balance, Nature Geoscience, 5, 841–842, 2012.

Immerzeel, W., Pellicciotti, F., and Bierkens, M.: Rising river flows throughout the twenty-first century in two Himalayan glacierized watersheds, Nature geoscience, 6, 742–745, 2013.

Immerzeel, W., Wanders, N., Lutz, A., Shea, J., and Bierkens, M.: Reconciling high-altitude precipitation in the upper Indus basin with glacier mass balances and runoff, Hydrology and Earth System Sciences, 19, 4673, 2015.

Immerzeel, W. W., Droogers, P., De Jong, S., and Bierkens, M.: Large-scale monitoring of snow cover and runoff simulation in Himalayan river basins using remote sensing, Remote sensing of Environment, 113, 40–49, 2009.

Immerzeel, W. W., Van Beek, L. P., and Bierkens, M. F.: Climate change will affect the Asian water towers, Science, 328, 1382–1385, 2010.

Jacob, T., Wahr, J., Pfeffer, W. T., and Swenson, S.: Recent contributions of glaciers and ice caps to sea level rise, Nature, 482, 514–518, 2012.

Jain, A. K., Murty, M. N., and Flynn, P. J.: Data clustering: a review, ACM computing surveys (CSUR), 31, 264–323, 1999.

Jarvis, A., Reuter, H. I., Nelson, A., Guevara, E., et al.: Hole-filled SRTM for the globe Version 4, available from the CGIAR-CSI SRTM 90m Database (http://srtm.csi.cgiar.org), 2008.

Jeelani, G., Feddema, J. J., Veen, C. J., and Stearns, L.: Role of snow and glacier melt in controlling river hydrology in Liddar watershed (western Himalaya) under current and future climate, Water Resources Research, 48, 2012.

Johnson, S. C.: Hierarchical clustering schemes, Psychometrika, 32, 241–254, 1967.

Josberger, E. G. and Mognard, N. M.: A passive microwave snow depth algorithm with a proxy for snow metamorphism, Hydrological Processes, 16, 1557–1568, 2002.

Joshi, M., Merry, C. J., Jezek, K. C., and Bolzan, J. F.: An edge detection technique to estimate melt duration, season and melt extent on the Greenland ice sheet using passive microwave data, Geophysical Research Letters, 28, 3497–3500, 2001.

Kääb, A., Berthier, E., Nuth, C., Gardelle, J., and Arnaud, Y.: Contrasting patterns of early twenty-first-century glacier mass change in the Himalayas, Nature, 488, 495–498, 2012.

Kääb, A., Treichler, D., Nuth, C., and Berthier, E.: Brief Communication: Contending estimates of 2003–2008 glacier mass balance over the Pamir–Karakoram–Himalaya, The Cryosphere, 9, 557–564, 2015.

Kang, S., Xu, Y., You, Q., Flügel, W.-A., Pepin, N., and Yao, T.: Review of climate and cryospheric change in the Tibetan Plateau, Environmental Research Letters, 5, 015 101, 2010.

Kapnick, S. B., Delworth, T. L., Ashfaq, M., Malyshev, S., and Milly, P.: Snowfall less sensitive to warming in Karakoram than in Himalayas due to a unique seasonal cycle, Nature Geoscience, 7, 834–840, 2014.

Kelly, R.: The AMSR-E snow depth algorithm: Description and initial results, Journal of the Remote Sensing Society of Japan, 29, 307–317, 2009.

Kelly, R. E., Chang, A. T., Tsang, L., and Foster, J. L.: A prototype AMSR-E global snow area and snow depth algorithm, Geoscience and Remote Sensing, IEEE Transactions on, 41, 230–242, 2003.

Kendall, M. G.: Rank correlation methods., Griffin, 1948.

Kitoh, A., Endo, H., Krishna Kumar, K., Cavalcanti, I. F., Goswami, P., and Zhou, T.: Monsoons in a changing world: a regional perspective in a global context, Journal of Geophysical Research: Atmospheres, 118, 3053–3065, 2013.

Knowles, K., Njoku, E., Armstrong, R., and Brodzik, M. J.: Nimbus-7 SMMR Pathfinder daily EASE-Grid brightness temperatures, Digital Media, 2002.

Koenig, L. S. and Forster, R. R.: Evaluation of passive microwave snow water equivalent algorithms in the depth hoar-dominated snowpack of the Kuparuk River Watershed, Alaska, USA, Remote sensing of Environment, 93, 511–527, 2004.

Kumar, K. K., Soman, M., and Kumar, K. R.: Seasonal forecasting of Indian summer monsoon rainfall: a review, Weather, 50, 449–467, 1995.

Lang, T. J. and Barros, A. P.: Winter storms in the central Himalayas, Journal of the Meteorological Society of Japan. Ser. II, 82, 829–844, 2004.

Langlois, A., Royer, A., Dupont, F., Roy, A., Goïta, K., and Picard, G.: Improved corrections of forest effects on passive microwave satellite remote sensing of snow over boreal and subarctic regions, Geoscience and Remote Sensing, IEEE Transactions on, 49, 3824–3837, 2011.

Lau, W. K., Kim, M.-K., Kim, K.-M., and Lee, W.-S.: Enhanced surface warming and accelerated snow melt in the Himalayas and Tibetan Plateau induced by absorbing aerosols, Environmental Research Letters, 5, 025 204, 2010.

Li, L., Gochis, D. J., Sobolowksi, S., and Mesquita, M. d. S.: Evaluating the present annual water budget of a Himalayan headwater river basin using a high-resolution atmosphere-hydrology model, Journal of Geophysical Research: Atmospheres, 2017.

Lioubimtseva, E. and Henebry, G. M.: Climate and environmental change in arid Central Asia: Impacts, vulnerability, and adaptations, Journal of Arid Environments, 73, 963–977, 2009.

Lioubimtseva, E., Cole, R., Adams, J., and Kapustin, G.: Impacts of climate and land-cover changes in arid lands of Central Asia, Journal of Arid Environments, 62, 285–308, 2005.

Liu, H., Wang, L., and Jezek, K. C.: Wavelet-transform based edge detection approach to derivation of snowmelt onset, end and duration from satellite passive microwave measurements, International Journal of Remote Sensing, 26, 4639–4660, 2005.

Luojus, K., Pulliainen, J., Takala, M., Lemmetyinen, J., Kangwa, M., Smolander, T., and Derksen, C.: Algorithm Theoretical Basis Document - SWE Algorithm, URL http://www.globsnow.info/docs/GS2_SWE_ATBD.pdf, 2013.

Lutz, A., Immerzeel, W., Shrestha, A., and Bierkens, M.: Consistent increase in High Asia's runoff due to increasing glacier melt and precipitation, Nature Climate Change, 4, 587–592, 2014.

Malik, N., Bookhagen, B., and Mucha, P. J.: Spatiotemporal patterns and trends of Indian monsoonal rainfall extremes, Geophysical Research Letters, 43, 1710–1717, 2016.

Mann, H. B.: Nonparametric tests against trend, Econometrica: Journal of the Econometric Society, pp. 245–259, 1945.

Matsuo, K. and Heki, K.: Time-variable ice loss in Asian high mountains from satellite gravimetry, Earth and Planetary Science Letters, 290, 30–36, 2010.

Mätzler, C.: Applications of the interaction of microwaves with the natural snow cover, Remote sensing reviews, 2, 259–387, 1987.

Mätzler, C.: Passive microwave signatures of landscapes in winter, Meteorology and Atmospheric Physics, 54, 241–260, 1994.

Mätzler, C. and Standley, A.: Technical note: Relief effects for passive microwave remote sensing, International Journal of Remote Sensing, 21, 2403–2412, 2000.

Maussion, F., Scherer, D., Mölg, T., Collier, E., Curio, J., and Finkelnburg, R.: Precipitation Seasonality and Variability over the Tibetan Plateau as Resolved by the High Asia Reanalysis*, Journal of Climate, 27, 1910–1927, 2014.

Menon, A., Levermann, A., and Schewe, J.: Enhanced future variability during India's rainy season, Geophysical Research Letters, 40, 3242–3247, 2013.

Mizukami, N. and Perica, S.: Towards improved snow water equivalent retrieval algorithms for satellite passive microwave data over the mountainous basins of western USA, Hydrological Processes, 26, 1991–2002, 2012.

Moiwo, J. P., Yang, Y., Tao, F., Lu, W., and Han, S.: Water storage change in the Himalayas from the Gravity Recovery and Climate Experiment (GRACE) and an empirical climate model, Water Resources Research, 47, 2011.

Molnar, P., Boos, W. R., and Battisti, D. S.: Orographic controls on climate and paleoclimate of Asia: thermal and mechanical roles for the Tibetan Plateau, Annual Review of Earth and Planetary Sciences, 38, 77–102, 2010.

Molotch, N. P. and Margulis, S. A.: Estimating the distribution of snow water equivalent using remotely sensed snow cover data and a spatially distributed snowmelt model: A multi-resolution, multi-sensor comparison, Advances in Water Resources, 31, 1503–1514, 2008.

Monahan, P. A. and Ramage, J.: AMSR-E melt patterns on the Southern Patagonia Icefield, Journal of Glaciology, 56, 699–708, 2010.

Montpetit, B., Royer, A., Roy, A., Langlois, A., and Derksen, C.: Snow microwave emission modeling of ice lenses within a snowpack using the microwave emission model for layered snowpacks, IEEE Transactions on Geoscience and Remote Sensing, 51, 4705–4717, 2013.

Murtagh, F. and Contreras, P.: Algorithms for hierarchical clustering: an overview, Wiley Interdisciplinary Reviews: Data Mining and Knowledge Discovery, 2, 86–97, 2012.

Narama, C., Kääb, A., Duishonakunov, M., and Abdrakhmatov, K.: Spatial variability of recent glacier area changes in the Tien Shan Mountains, Central Asia, using Corona (˜ 1970), Landsat (˜ 2000), and ALOS (˜ 2007) satellite data, Global and Planetary Change, 71, 42–54, 2010.

Njoku, E. G., Jackson, T. J., Lakshmi, V., Chan, T. K., and Nghiem, S. V.: Soil moisture retrieval from AMSR-E, IEEE transactions on Geoscience and remote sensing, 41, 215–229, 2003.

Norris, J., Carvalho, L. M., Jones, C., and Cannon, F.: WRF simulations of two extreme snowfall events associated with contrasting extratropical cyclones over the western and central Himalaya, Journal of Geophysical Research: Atmospheres, 120, 3114–3138, 2015.

Norris, J., Carvalho, L. M., Jones, C., Cannon, F., Bookhagen, B., Palazzi, E., and Tahir, A. A.: The spatiotemporal variability of precipitation over the Himalaya: evaluation of one-year WRF model simulation, Climate Dynamics, pp. 1–26, 2016.

Painter, T. H., Rittger, K., McKenzie, C., Slaughter, P., Davis, R. E., and Dozier, J.: Retrieval of subpixel snow covered area, grain size, and albedo from MODIS, Remote Sensing of Environment, 113, 868–879, 2009.

Palazzi, E., Hardenberg, J., and Provenzale, A.: Precipitation in the Hindu-Kush Karakoram Himalaya: Observations and future scenarios, Journal of Geophysical Research: Atmospheres, 118, 85–100, 2013.

Palmer, M. A., Reidy Liermann, C. A., Nilsson, C., Flörke, M., Alcamo, J., Lake, P. S., and Bond, N.: Climate change and the world's river basins: anticipating management options, Frontiers in Ecology and the Environment, 6, 81–89, 2008.

Panday, P. K., Frey, K. E., and Ghimire, B.: Detection of the timing and duration of snowmelt in the Hindu Kush-Himalaya using QuikSCAT, 2000–2008, Environmental Research Letters, 6, 024 007, 2011.

Patz, J. A., Campbell-Lendrum, D., Holloway, T., and Foley, J. A.: Impact of regional climate change on human health, Nature, 438, 310–317, 2005.

Pepin, N., Bradley, R. S., Diaz, H. F., Baraer, M., Caceres, E. B., Forsythe, N., Fowler, H., Greenwood, G., Hashmi, M. Z., Liu, X. D., Miller, J. R., Ning, L., Ohmura, A., Palazzi, E., Rangwala, I., Schöner, W., Severskiy, I., Shahgedanova, M., Wang, M. B., Williamson, S. N., and Yang, D. Q.: Elevation-dependent warming in mountain regions of the world, Nature Climate Change, 5, 424–430, 2015.

Pu, Z., Xu, L., and Salomonson, V. V.: MODIS/Terra observed seasonal variations of snow cover over the Tibetan Plateau, Geophysical Research Letters, 34, 2007.

Pulliainen, J.: Mapping of snow water equivalent and snow depth in boreal and sub-arctic zones by assimilating spaceborne microwave radiometer data and ground-based observations, Remote sensing of Environment, 101, 257–269, 2006.

Racoviteanu, A. E., Paul, F., Raup, B., Khalsa, S. J. S., and Armstrong, R.: Challenges and recommendations in mapping of glacier parameters from space: results of the 2008 Global Land Ice Measurements from Space (GLIMS) workshop, Boulder, Colorado, USA, Annals of Glaciology, 50, 53–69, 2009.

Ramanathan, V., Chung, C., Kim, D., Bettge, T., Buja, L., Kiehl, J., Washington, W., Fu, Q., Sikka, D., and Wild, M.: Atmospheric brown clouds: Impacts on South Asian climate and hydrological cycle, Proceedings of the National Academy of Sciences of the United States of America, 102, 5326–5333, 2005.

Rango, A., Chang, A., and Foster, J.: The utilization of spaceborne microwave radiometers for monitoring snowpack properties, Hydrology Research, 10, 25–40, 1979.

Rees, A., Lemmetyinen, J., Derksen, C., Pulliainen, J., and English, M.: Observed and modelled effects of ice lens formation on passive microwave brightness temperatures over snow covered tundra, Remote Sensing of Environment, 114, 116–126, 2010.

Rheinwalt, A.: Python C-extension for memory efficient and multithreaded Pearson product-moment correlation coefficient estimation using OpenMP, https://github.com/UP-RS-ESP/CorrCoef, 2016.

Rheinwalt, A.: Normalize time series by quantile normalization to the normal distribution., https://github.com/UP-RS-ESP/Normalize, 2017.

Rheinwalt, A., Goswami, B., Boers, N., Heitzig, J., Marwan, N., Krishnan, R., and Kurths, J.: Teleconnections in Climate Networks: A Network-of-Networks Approach to Investigate the Influence of Sea Surface Temperature Variability on Monsoon Systems, in: Machine Learning and Data Mining Approaches to Climate Science, pp. 23–33, Springer, 2015.

Romanov, P.: Global Multisensor Automated satellite-based Snow and Ice Mapping System (GMASI) for cryosphere monitoring, Remote Sensing of Environment, 196, 42–55, 2017.

Savitzky, A. and Golay, M. J.: Smoothing and differentiation of data by simplified least squares procedures., Analytical chemistry, 36, 1627–1639, 1964.

Savoie, M. H., Armstrong, R. L., Brodzik, M. J., and Wang, J. R.: Atmospheric corrections for improved satellite passive microwave snow cover retrievals over the Tibet Plateau, Remote Sensing of Environment, 113, 2661–2669, 2009.

Scherler, D., Bookhagen, B., and Strecker, M. R.: Spatially variable response of Himalayan glaciers to climate change affected by debris cover, Nature Geoscience, 4, 156–159, 2011.

Shamsudduha, M., Chandler, R., Taylor, R., and Ahmed, K.: Recent trends in groundwater levels in a highly seasonal hydrological system: the Ganges-Brahmaputra-Meghna Delta, Hydrology and Earth System Sciences, 13, 2373–2385, 2009.

Shangguan, D., Shiyin, L., Yongjian, D., Jing, L., Yong, Z., Lianfu, D., Xing, W., Changwei, X., and Gang, L.: Glacier changes in the west Kunlun Shan from 1970 to 2001 derived from Landsat TM/ETM+ and Chinese glacier inventory data, Annals of Glaciology, 46, 204–208, 2007.

Shrestha, M., Koike, T., Hirabayashi, Y., Xue, Y., Wang, L., Rasul, G., and Ahmad, B.: Integrated simulation of snow and glacier melt in water and energy balance-based, distributed hydrological modeling framework at Hunza River Basin of Pakistan Karakoram region, Journal of Geophysical Research: Atmospheres, 120, 4889–4919, 2015.

Singh, D., Tsiang, M., Rajaratnam, B., and Diffenbaugh, N. S.: Observed changes in extreme wet and dry spells during the South Asian summer monsoon season, Nature Climate Change, 4, 456–461, 2014.

Singh, S. P., Bassignana-Khadka, I., Karky, B. S., Sharma, E., et al.: Climate change in the Hindu Kush-Himalayas: the state of current knowledge., International Centre for Integrated Mountain Development (ICIMOD), 2011.

Smith, T. and Bookhagen, B.: Assessing uncertainty and sensor biases in passive microwave data across High Mountain Asia, Remote Sensing of Environment, 181, 174–185, 2016.

Smith, T., Bookhagen, B., and Rheinwalt, A.: Spatiotemporal Patterns of High Mountain Asia's Snowmelt Season Identified with an Automated Snowmelt Detection Algorithm, 1987–2016, The Cryosphere, 2017.

Sorg, A., Bolch, T., Stoffel, M., Solomina, O., and Beniston, M.: Climate change impacts on glaciers and runoff in Tien Shan (Central Asia), Nature Climate Change, 2, 725–731, 2012.

Spiess, M., Schneider, C., and Maussion, F.: MODIS-derived interannual variability of the equilibrium-line altitude across the Tibetan Plateau, Annals of Glaciology, 57, 140–154, 2016.

Stewart, I. T.: Changes in snowpack and snowmelt runoff for key mountain regions, Hydrological Processes, 23, 78–94, 2009.

Sturm, M., Holmgren, J., and Liston, G. E.: A seasonal snow cover classification system for local to global applications, Journal of Climate, 8, 1261–1283, 1995.

Sturm, M., Goldstein, M. A., and Parr, C.: Water and life from snow: A trillion dollar science question, Water Resources Research, 2017.

Sun, N. and Weng, F.: Evaluation of special sensor microwave imager/sounder (SSMIS) environmental data records, Geoscience and Remote Sensing, IEEE Transactions on, 46, 1006–1016, 2008.

Tahir, A. A., Chevallier, P., Arnaud, Y., and Ahmad, B.: Snow cover dynamics and hydrological regime of the

Hunza River basin, Karakoram Range, Northern Pakistan, Hydrology and Earth System Sciences, 15, 2275–2290, doi: 10.5194/hess-15-2275-2011, URL http://www.hydrol-earth-syst-sci.net/15/2275/2011/, 2011.

Takala, M., Pulliainen, J., Huttunen, M., and Hallikainen, M.: Estimation of the beginning of snow melt period using SSM/I data, in: Geoscience and Remote Sensing Symposium, 2003. IGARSS'03. Proceedings. 2003 IEEE International, vol. 4, pp. 2841–2843, IEEE, 2003.

Takala, M., Pulliainen, J., Huttunen, M., and Hallikainen, M.: Detecting the onset of snow-melt using SSM/I data and the self-organizing map, International Journal of Remote Sensing, 29, 755–766, 2008.

Takala, M., Pulliainen, J., Metsämäki, S. J., and Koskinen, J. T.: Detection of snowmelt using spaceborne microwave radiometer data in Eurasia from 1979 to 2007, Geoscience and Remote Sensing, IEEE Transactions on, 47, 2996–3007, 2009.

Takala, M., Luojus, K., Pulliainen, J., Derksen, C., Lemmetyinen, J., Kärnä, J.-P., Koskinen, J., and Bojkov, B.: Estimating northern hemisphere snow water equivalent for climate research through assimilation of space-borne radiometer data and ground-based measurements, Remote Sensing of Environment, 115, 3517–3529, 2011.

Tapley, B. D., Bettadpur, S., Watkins, M., and Reigber, C.: The gravity recovery and climate experiment: Mission overview and early results, Geophysical Research Letters, 31, 2004.

Tedesco, M.: Snowmelt detection over the Greenland ice sheet from SSM/I brightness temperature daily variations, Geophysical Research Letters, 34, 2007.

Tedesco, M.: Electromagnetic properties of components of the cryosphere, Remote Sensing of the Cryosphere, pp. 17–30, 2015.

Tedesco, M. and Kim, E. J.: Intercomparison of electromagnetic models for passive microwave remote sensing of snow, IEEE Transactions on Geoscience and Remote Sensing, 44, 2654–2666, 2006.

Tedesco, M. and Narvekar, P. S.: Assessment of the NASA AMSR-E SWE Product, Selected Topics in Applied Earth Observations and Remote Sensing, IEEE Journal of, 3, 141–159, 2010.

Tedesco, M., Kelly, R., Foster, J. L., and Chang, A. T.: AMSR-E/Aqua Daily L3 Global Snow Water Equivalent EASE-Grids. Version 2. 2002-2011. Boulder, Colorado USA: NASA National Snow and Ice Data Center Distributed Active Archive Center., doi: 10.5067/AMSR-E/AE_DYSNO.002, URL http://dx.doi.org/10.5067/AMSR-E/AE_DYSNO.002, 2004.

Tedesco, M., Derksen, C., Deems, J. S., and Foster, J. L.: Remote sensing of snow depth and snow water equivalent, Remote Sensing of the Cryosphere, pp. 73–98, 2015.

Tong, J., Dery, S. J., Jackson, P. L., and Derksen, C.: Testing snow water equivalent retrieval algorithms for passive microwave remote sensing in an alpine watershed of western Canada, Canadian Journal of Remote Sensing, 36, S74–S86, 2010.

Trenberth, K. E.: Changes in precipitation with climate change, Climate Research, 47, 123–138, 2011.

Treydte, K. S., Schleser, G. H., Helle, G., Frank, D. C., Winiger, M., Haug, G. H., and Esper, J.: The twentieth century was the wettest period in northern Pakistan over the past millennium, Nature, 440, 1179–1182, 2006.

Tsang, L., Kong, J. A., and Shin, R. T.: Theory of microwave remote sensing, URL https://ntrs.nasa.gov/search.jsp?R=19850058641, 1985.

Tsang, L., Chen, C.-T., Chang, A. T., Guo, J., and Ding, K.-H.: Dense media radiative transfer theory based on quasicrystalline approximation with applications to passive microwave remote sensing of snow, Radio Science, 35, 731–749, 2000.

Ulaby, F. T. and Stiles, W. H.: The active and passive microwave response to snow parameters: 2. Water equivalent of dry snow, Journal of Geophysical Research: Oceans, 85, 1045–1049, 1980.

Valentin, C., Agus, F., Alamban, R., Boosaner, A., Bricquet, J.-P., Chaplot, V., De Guzman, T., De Rouw, A., Janeau, J.-L., Orange, D., et al.: Runoff and sediment losses from 27 upland catchments in Southeast Asia: Impact of rapid land use changes and conservation practices, Agriculture, Ecosystems & Environment, 128, 225–238, 2008.

Vander Jagt, B. J., Durand, M. T., Margulis, S. A., Kim, E. J., and Molotch, N. P.: The effect of spatial variability on the sensitivity of passive microwave measurements to snow water equivalent, Remote Sensing of Environment, 136, 163–179, 2013.

Vaughan, D., Comiso, J., Allison, I., Carrasco, J., Kaser, G., Kwok, R., Mote, P., Murray, T., Paul, F., Ren, J., Rignot, E., Solomina, O., Steffen, K., and Zhang, T.: Observations: Cryosphere. In: Climate Change 2013: The Physical Science Basis., Contribution of Working Group I to the Fifth Assessment Report of the IPCC., 2013.

Verbesselt, J., Hyndman, R., Newnham, G., and Culvenor, D.: Detecting trend and seasonal changes in satellite image time series, Remote sensing of Environment, 114, 106–115, 2010.

Vuyovich, C. M., Jacobs, J. M., and Daly, S. F.: Comparison of passive microwave and modeled estimates of total watershed SWE in the continental United States, Water Resources Research, 50, 9088–9102, 2014.

Wang, J. and Tedesco, M.: Identification of atmospheric influences on the estimation of snow water equivalent from AMSR-E measurements, Remote Sensing of Environment, 111, 398–408, 2007.

Wang, L. and Qu, J. J.: Satellite remote sensing applications for surface soil moisture monitoring: A review, Frontiers of Earth Science in China, 3, 237–247, 2009.

Wang, Q., Yi, S., and Sun, W.: Precipitation-driven glacier changes in the Pamir and Hindu Kush mountains, Geophysical Research Letters, 2017.

Wang, T., Peng, S., Lin, X., and Chang, J.: Declining snow cover may affect spring phenological trend on the Tibetan Plateau, Proceedings of the National Academy of Sciences, 110, E2854–E2855, 2013.

Wentz, F. J.: A well-calibrated ocean algorithm for special sensor microwave/imager, Journal of Geophysical Research: Oceans, 102, 8703–8718, 1997.

Wentz, F. J.: SSM/I version-7 calibration report, Remote Sensing Systems Rep, 11012, 46, 2013.

Willis, I. C., Arnold, N. S., and Brock, B. W.: Effect of snowpack removal on energy balance, melt and runoff in a small supraglacial catchment, Hydrological Processes, 16, 2721–2749, 2002.

Wulf, H., Bookhagen, B., and Scherler, D.: Climatic and geologic controls on suspended sediment flux in the Sutlej River Valley, western Himalaya, Hydrology and Earth System Sciences, 16, 2193, 2012.

Wulf, H., Bookhagen, B., and Scherler, D.: Differentiating between rain, snow, and glacier contributions to river discharge in the western Himalaya using remote-sensing data and distributed hydrological modeling, Advances in Water Resources, 88, 152–169, 2016.

Xiong, C., Shi, J., Cui, Y., and Peng, B.: Snowmelt Pattern Over High-Mountain Asia Detected From Active and Passive Microwave Remote Sensing, IEEE Geoscience and Remote Sensing Letters, 2017.

Xu, J., Grumbine, R. E., Shrestha, A., Eriksson, M., Yang, X., Wang, Y., and Wilkes, A.: The melting Himalayas: cascading effects of climate change on water, biodiversity, and livelihoods, Conservation Biology, 23, 520–530, 2009.

Xu, W., Ma, L., Ma, M., Zhang, H., and Yuan, W.: Spatial–temporal variability of snow cover and depth in the Qinghai–Tibetan Plateau, Journal of Climate, 30, 1521–1533, 2017.

Yao, T., Thompson, L., Yang, W., Yu, W., Gao, Y., Guo, X., Yang, X., Duan, K., Zhao, H., Xu, B., et al.: Different glacier status with atmospheric circulations in Tibetan Plateau and surroundings, Nature Climate Change, 2, 663–667, 2012.

Yatagai, A., Kamiguchi, K., Arakawa, O., Hamada, A., Yasutomi, N., and Kitoh, A.: APHRODITE: Constructing a long-term daily gridded precipitation dataset for Asia based on a dense network of rain gauges, Bulletin of the American Meteorological Society, 93, 1401–1415, 2012.

Yihui, D. and Chan, J. C.: The East Asian summer monsoon: an overview, Meteorology and Atmospheric Physics, 89, 117–142, 2005.

Zhang, Y., Li, T., and Wang, B.: Decadal change of the spring snow depth over the Tibetan Plateau: the associated circulation and influence on the east Asian summer monsoon*, Journal of Climate, 17, 2780–2793, 2004.

Zhu, B., Yihui, D., and Huibang, L.: A review of the atmospheric general circulation and monsoon in East Asia, Journal of Meteorological Research, 4, 399–416, 1990.

APPENDIX A

Appendix A - Supplementary Materials for Chapter 4

Impact of Search Distance

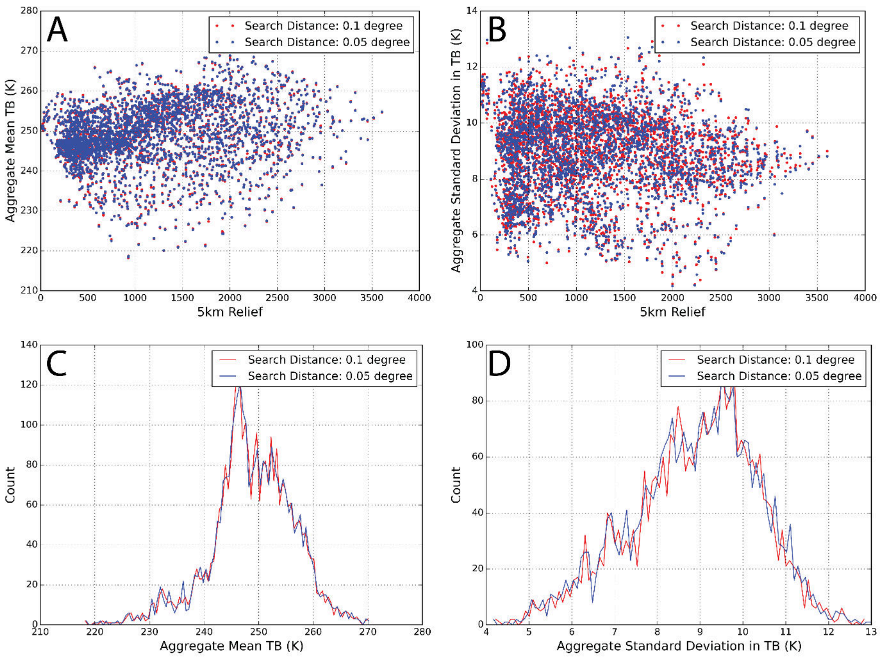

Figure A1 – Raw (A-B) and aggregate (C-D) 18 GHz, vertically polarized, Temperature Brightness characteristics (mean and standard deviations) using two search distances (0.1 decimal degree (dd) and 0.05 dd). Slight reductions in variability are seen for some areas when a smaller search distance is used (which we attribute to lower variance in a smaller dataset), but in general the two datasets are similar, indicating that search distance does not have an impact upon our results.

Individual Instrument Regressions vs Hillslope Angle

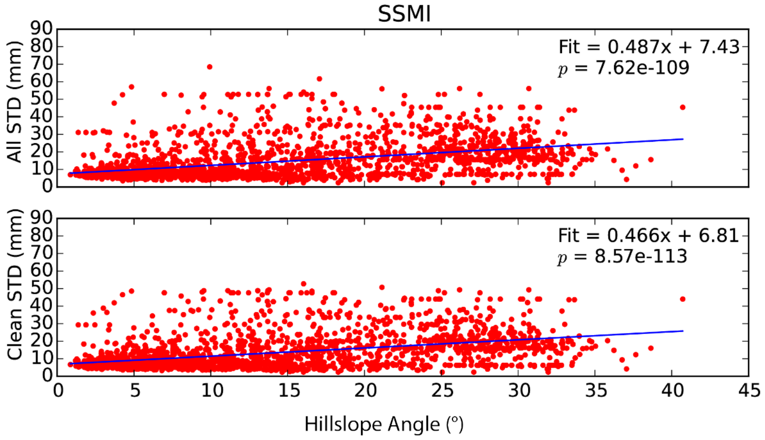

Figure A2 – Correlation between SSMI SWE variability (standard deviation, STD) and hillslope angle across all sample points show in Figure 4.1 (n=2500). (A) Aggregate total variability on y-axis, and (B) clean-day variability on the y-axis, with regression lines and *p*-values on each.

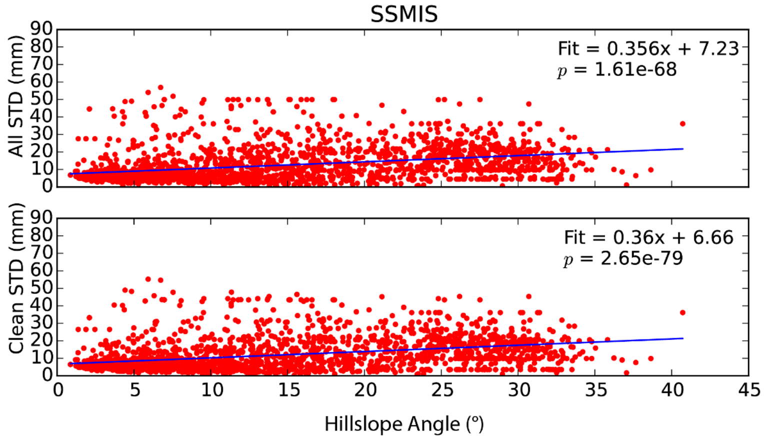

Figure A3 – Correlation between SSMIS SWE variability (standard deviation, STD) and hillslope angle across all sample points show in Figure 4.1 (n=2500). (A) Aggregate total variability on y-axis, and (B) clean-day variability on the y-axis, with regression lines and *p*-values on each.

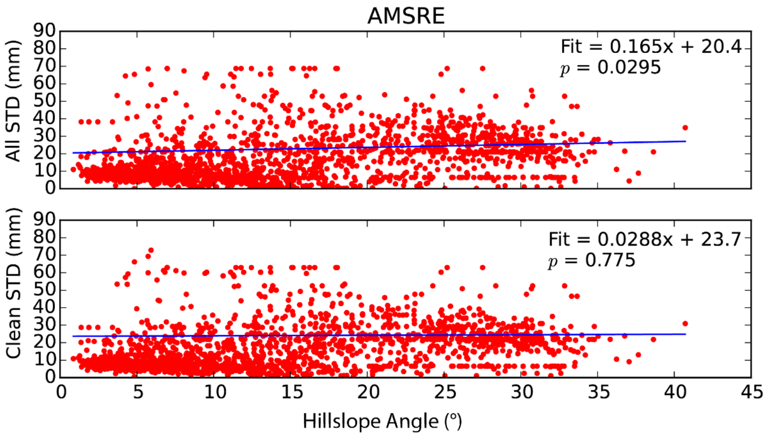

Figure A4 – Correlation between AMSR-E SWE variability (standard deviation, STD) and hillslope angle across all sample points show in Figure 4.1 (n=2500). (A) Aggregate total variability on y-axis, and (B) clean-day variability on the y-axis, with regression lines and *p*-values on each.

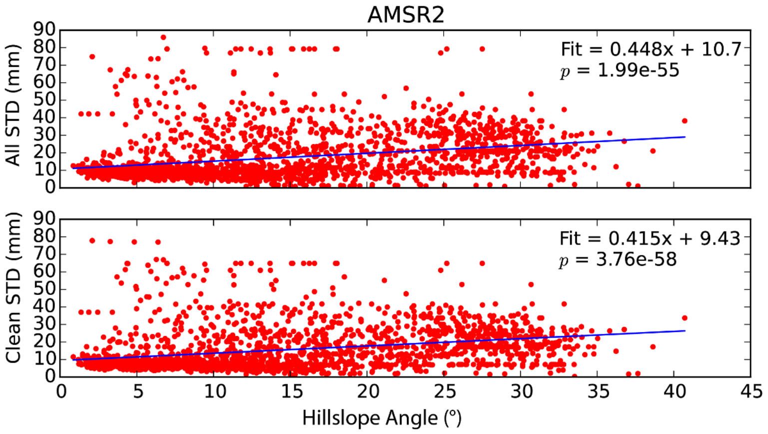

Figure A5 – Correlation between AMSR2 SWE variability (standard deviation, STD) and hillslope angle across all sample points show in Figure 4.1 (n=2500). (A) Aggregate total variability on y-axis, and (B) clean-day variability on the y-axis, with regression lines and *p*-values on each.

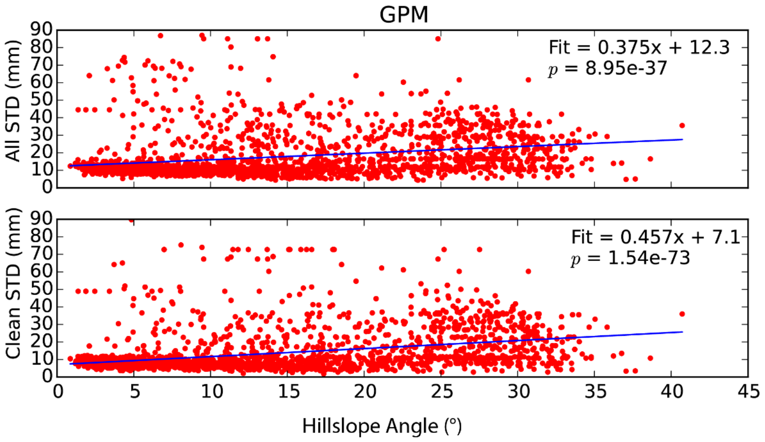

Figure A6 – Correlation between GPM SWE variability (standard deviation, STD) and hillslope angle across all sample points show in Figure 4.1 (n=2500). (A) Aggregate total variability on y-axis, and (B) clean-day variability on the y-axis, with regression lines and p-values on each.

Comparison of SWE Volume and Topographic Indices

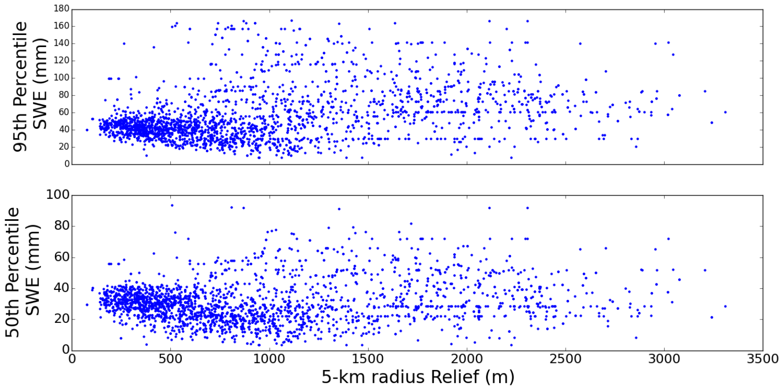

Figure A7 – Correlation between 95th percentile SWE volume (A) and 50th percentile SWE volume (B) and 5-km relief across all sample points show in Figure 4.1 (n=2500). Shows slight negative relationship below 1000-m of relief, and then increasing variability.

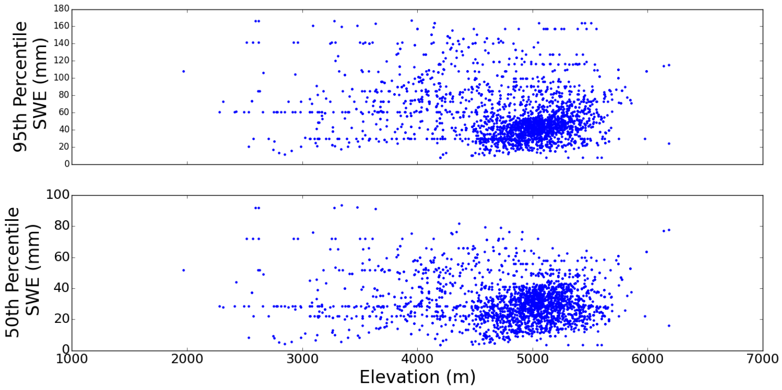

Figure A8 – Correlation between 95th percentile SWE volume (A) and 50th percentile SWE volume (B) and elevation across all sample points show in Figure 4.1 (n=2500). Shows positive relationship in majority of points, with high levels of noise, particularly below 4000-m.

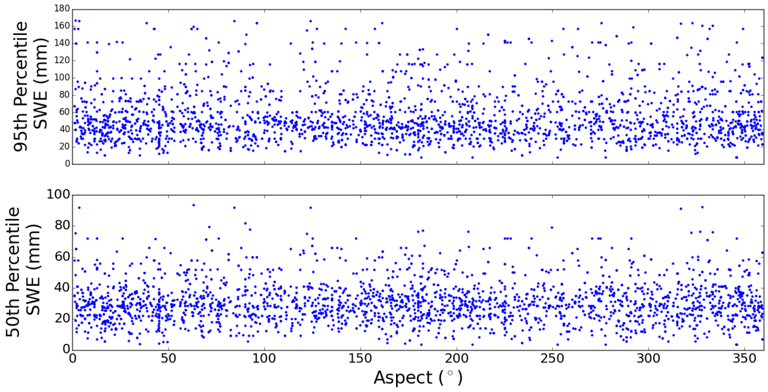

Figure A9 – Correlation between 95th percentile SWE volume (A) and 50th percentile SWE volume (B) and terrain aspect across all sample points show in Figure 4.1 (n=2500). Shows no significant trend.

Multiple Regressions for All Satellites, with Spatial Distributions

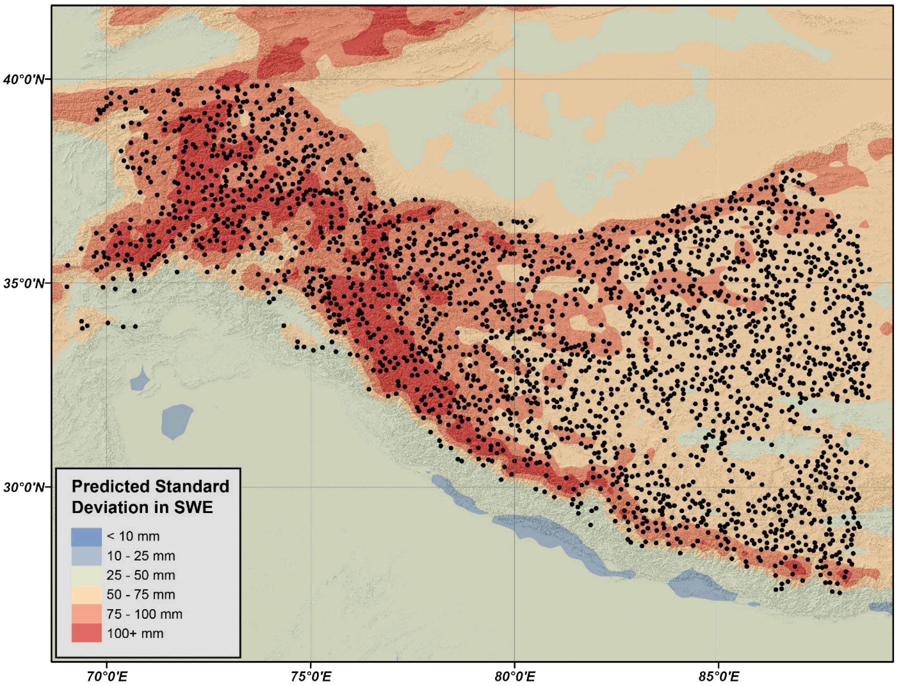

Figure A10 – Spatial distribution showing SWE uncertainties from PM data using GPM (Table A5, cf. Figure 9 in manuscript).

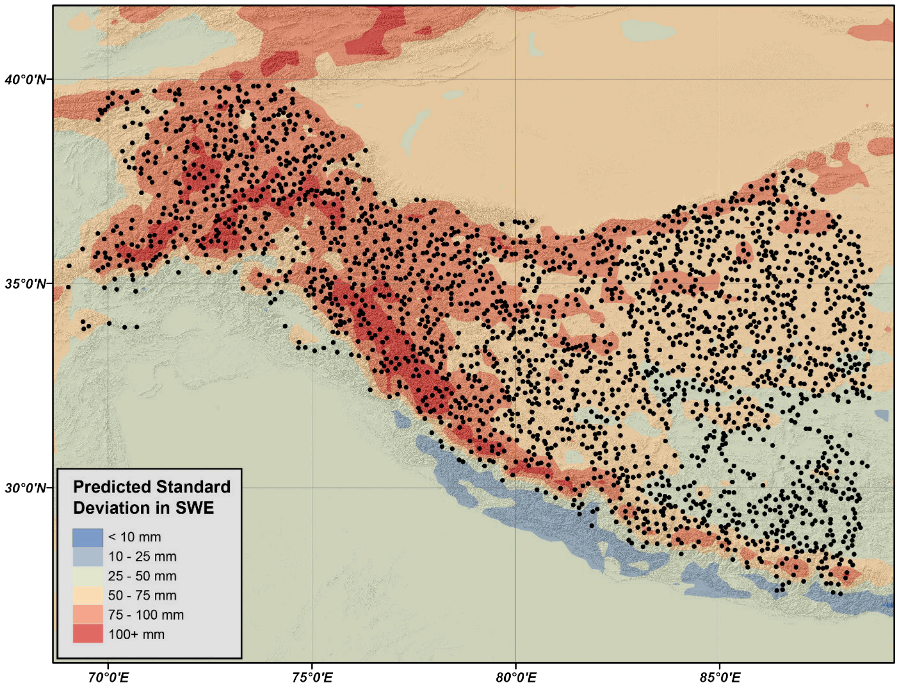

Figure A11 – Spatial distribution showing SWE uncertainties from PM data using AMSR-E (Table A7).

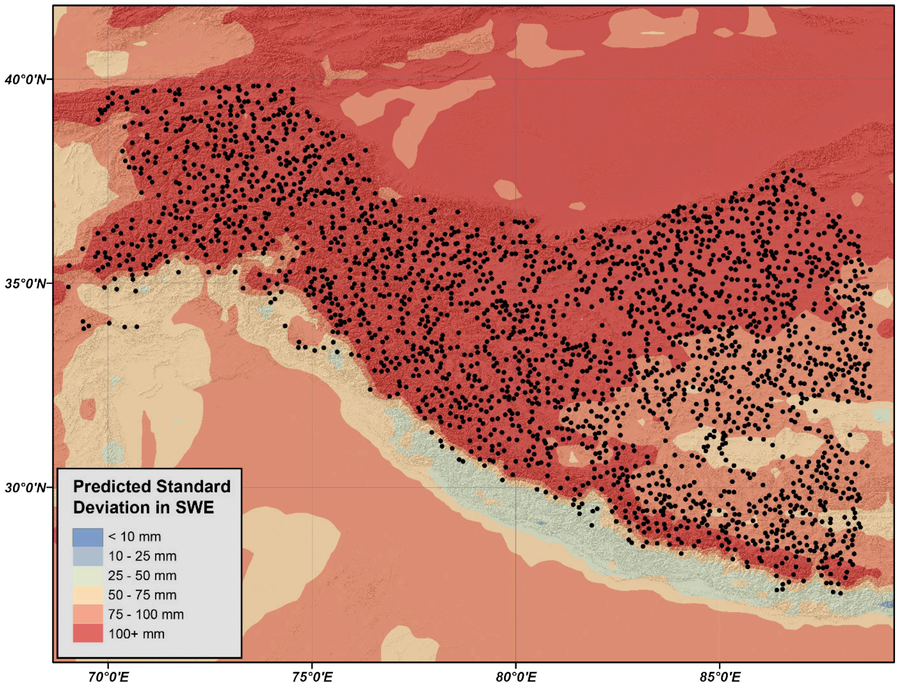

Figure A12 – Spatial distribution showing SWE uncertainties from PM data using AMSR2 (Table A9).

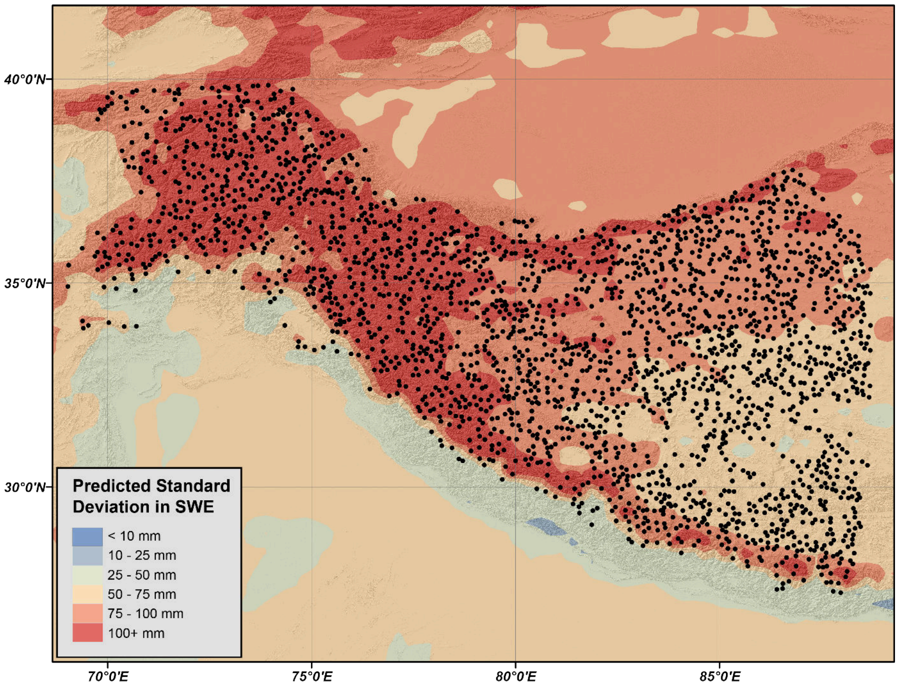

Figure A13 – Spatial distribution showing SWE uncertainties from PM data using SSMI (Table A11).

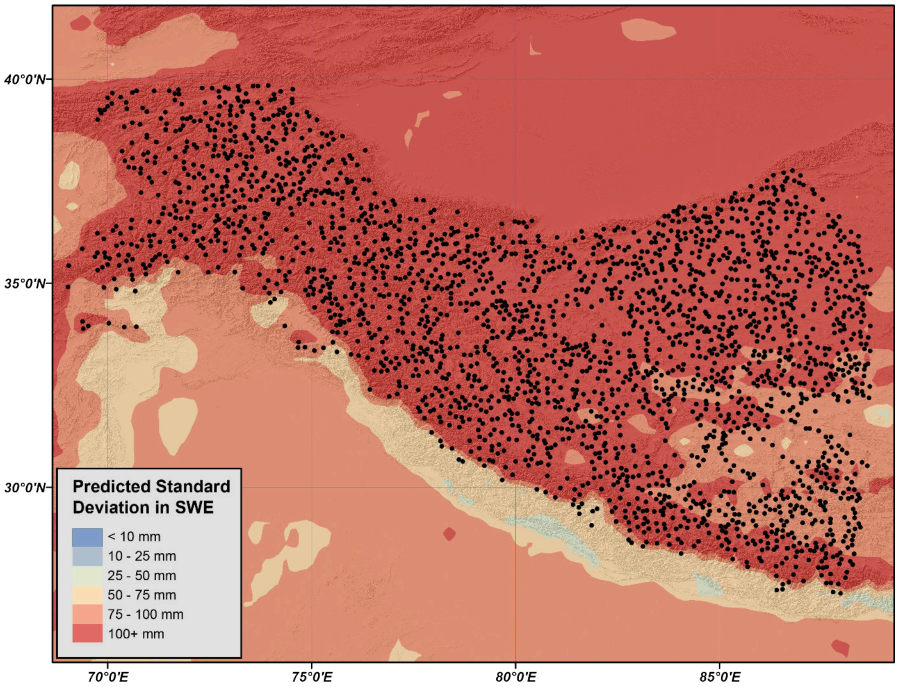

Figure A14 – Spatial distribution showing SWE uncertainties from PM data using SSMIS (Table A13).

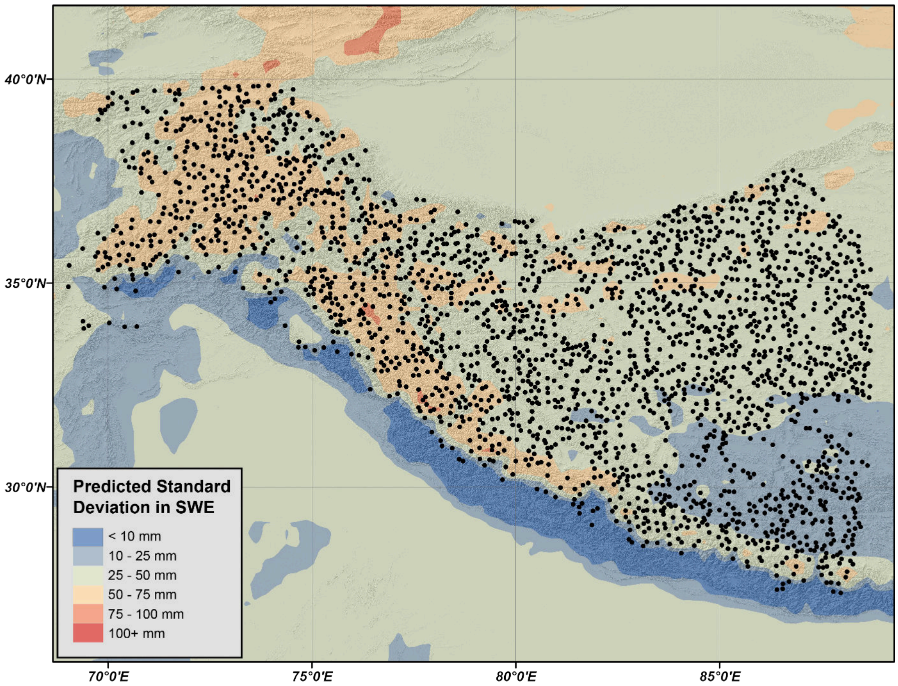

Figure A15 – Spatial distribution showing SWE uncertainties from PM data using all satellites (Table A15).

Results from Linear Regressions

Table A1 – Slopes of regressions against Elevation (n=2500), including p-values, t-values, and 95% confidence intervals (CI). Bold values indicate statistically significant results ($p < 0.05$).

Metric	All Satellites	SSMI	SSMI/S	AMSR-E	AMSR2	GPM
Slope	-0.00276	-0.0052	-0.00343	-0.00309	-0.00349	-0.00325
Slope p-values	0.000161	6.49e-49	6.31e-26	0.00949	2.27e-14	9.36e-13
Slope t-values	-3.78	-15	-10.7	-2.6	-7.68	-7.18
Slope CI	-0.00396 - -0.00156	-0.00577 - -0.00463	-0.00396 - -0.0029	-0.00505 - -0.00113	-0.00423 - -0.00113	-0.00399 - -0.0025
Clean-day Slope	-0.00389	-0.00266	-0.00482	28.2	-0.00436	-0.00347
Clean-day Slope p-values	5.62e-05	0.00395	1.74e-49	1.06e-76	2.88e-27	9.36e-13
Clean-day Slope t-values	-4.04	-2.88	-15.1	19.2	-10.9	-2.36
Clean-day Slope CI	-0.00548 - -0.0023	-0.00418 - -0.00114	-0.00534 - -0.0043	25.8 - 30.6	-0.00502 - 30.6	-0.00589 - -0.00105

Table A2 – Slopes of regressions against Relief (n=2500), including p-values, t-values, and 95% confidence intervals (CI). Bold values indicate statistically significant results ($p < 0.05$).

Metric	All Satellites	SSMI	SSMI/S	AMSR-E	AMSR2	GPM
Slope	0.00241	0.0066	0.00463	0.00264	0.00612	0.00428
Slope p-values	0.000205	8.6e-103	6.82e-60	0.0122	2.53e-53	1.41e-26
Slope t-values	3.72	22.6	16.8	2.51	15.7	10.8
Slope CI	0.00134 - 0.00348	0.00612 - 0.00708	0.00418 - 0.00508	0.000909 - 0.00438	0.00548 - 0.00438	0.00363 - 0.00493
Clean-day Slope	0.00437	0.00146	0.00623	7.11	0.00621	0.00117
Clean-day Slope p-values	3.44e-07	0.114	2.82e-101	4.72e-105	6.46e-71	1.41e-26
Clean-day Slope t-values	5.11	1.58	22.4	22.9	18.4	0.83
Clean-day Slope CI	0.00296 - 0.00577	-5.82e-05 - 0.00298	0.00578 - 0.00669	6.6 - 7.62	0.00566 - 7.62	-0.00115 - 0.00349

Table A3 – Slopes of regressions against 90th percentile DJF 10-m wind speed (n=2500), including p-values, t-values, and 95% confidence intervals (CI). Bold values indicate statistically significant results ($p < 0.05$).

Metric	All Satellites	SSMI	SSMI/S	AMSR-E	AMSR2	GPM
Slope	-0.351	0.365	0.121	-0.288	0.219	-0.198
Slope p-values	0.0214	1.21e-06	0.0773	0.245	0.0221	0.0372
Slope t-values	-2.3	4.87	1.77	-1.16	2.29	-2.08
Slope CI	-0.602 - -0.1	0.241 - 0.488	0.00838 - 0.234	-0.696 - 0.12	0.0615 - 0.12	-0.355 - -0.0417
Clean-day Slope	-0.0796	-0.367	0.437	9.41	0.205	-0.379
Clean-day Slope p-values	0.693	0.0653	1.54e-10	8.22e-38	0.0145	0.0372
Clean-day Slope t-values	-0.395	-1.84	6.43	13.1	2.45	-1.31
Clean-day Slope CI	-0.411 - 0.252	-0.695 - -0.0396	0.325 - 0.549	8.22 - 10.6	0.0671 - 10.6	-0.857 - 0.0981

Table A4 – Slopes of regressions against 50th percentile DJF 10-m wind speed (n=2500), including p-values, t-values, and 95% confidence intervals (CI). Bold values indicate statistically significant results ($p < 0.05$).

Metric	All Satellites	SSMI	SSMI/S	AMSR-E	AMSR2	GPM
Slope	-0.81	0.133	-0.161	-0.813	-0.0658	-0.629
Slope p-values	0.00022	0.22	0.103	0.0224	0.632	4.1e-06
Slope t-values	-3.7	1.23	-1.63	-2.29	-0.479	-4.62
Slope CI	-1.17 - -0.45	-0.0454 - 0.311	-0.323 - 0.00138	-1.4 - -0.228	-0.292 - -0.228	-0.853 - -0.405
Clean-day Slope	-0.554	-0.8	0.265	11.9	-0.133	-0.809
Clean-day Slope p-values	0.0557	0.00592	0.00743	5.03e-62	0.277	4.1e-06
Clean-day Slope t-values	-1.91	-2.75	2.68	17.1	-1.09	-1.85
Clean-day Slope CI	-1.03 - -0.0777	-1.28 - -0.322	0.102 - 0.427	10.8 - 13.1	-0.333 - 13.1	-1.53 - -0.0885

Results from Multiple Regressions

Table A5 – Coefficients of Multiple Regressions for GPM (n=2500), including p-values, t-values, and 95% confidence intervals (CI). Bold values indicate statistically significant results (p <0.05).

Metric	Coefficient	p-value	t-value	Confidence Interval	Percent of Total
95th Percentile SWE	0.306	0	206	0.303 - 0.309	7.82
Forest Fraction	2.97	0.206	1.27	-1.63 - 7.57	75.8
Hillslope Angle	0.205	6.84e-23	9.95	0.165 - 0.246	5.24
Relief	-0.00236	9.93e-17	-8.36	-0.003 - -0.002	0.0603
Elevation	-0.00224	4.86e-317	-44.4	-0.002 - -0.002	0.0572
25th Percentile Wind	-0.213	0.000953	-3.31	-0.34 - -0.087	5.44
90th Percentile Wind	0.22	2.13e-08	5.62	0.143 - 0.297	5.62

Table A6 – Coefficients of Multiple Regressions for GPM, without Forest Fraction (n=2438), including p-values, t-values, and 95% confidence intervals (CI). Bold values indicate statistically significant results (p <0.05).

Metric	Coefficient	p-value	t-value	Confidence Interval	Percent of Total
95th Percentile SWE	0.306	0	205	0.303 - 0.309	31.9
Hillslope Angle	0.21	2.22e-23	10.1	0.169 - 0.25	21.9
Relief	-0.00238	1.11e-16	-8.35	-0.003 - -0.002	0.248
Elevation	-0.00224	7.54e-313	-44.1	-0.002 - -0.002	0.233
25th Percentile Wind	-0.219	0.000715	-3.39	-0.346 - -0.092	22.9
90th Percentile Wind	0.219	2.93e-08	5.56	0.142 - 0.297	22.9

Table A7 – Coefficients of Multiple Regressions for AMSR-E (n=2500), including p-values, t-values, and 95% confidence intervals (CI). Bold values indicate statistically significant results (p <0.05).

Metric	Coefficient	p-value	t-value	Confidence Interval	Percent of Total
95th Percentile SWE	0.318	0	116	0.313 - 0.324	7.07
Forest Fraction	-3.66	0.823	-0.223	-35.9 - 28.5	81.4
Hillslope Angle	-0.125	0.385	-0.868	-0.408 - 0.158	2.79
Relief	0.00164	0.404	0.834	-0.002 - 0.006	0.0365
Elevation	0.000723	0.0291	2.18	7.38e-05 - 0.001	0.0161
25th Percentile Wind	-0.284	0.526	-0.634	-1.16 - 0.595	6.31
90th Percentile Wind	-0.105	0.701	-0.384	-0.641 - 0.431	2.34

Table A8 – Coefficients of Multiple Regressions for AMSR-E, without Forest Fraction (n=2438), including p-values, t-values, and 95% confidence intervals (CI). Bold values indicate statistically significant results (p <0.05).

Metric	Coefficient	p-value	t-value	Confidence Interval	Percent of Total
95th Percentile SWE	0.318	0	115	0.313 - 0.324	37.9
Hillslope Angle	-0.125	0.392	-0.856	-0.413 - 0.162	15
Relief	0.00167	0.405	0.833	-0.002 - 0.006	0.199
Elevation	0.000727	0.0298	2.17	7.11e-05 - 0.001	0.0867
25th Percentile Wind	-0.285	0.53	-0.629	-1.17 - 0.603	33.9
90th Percentile Wind	-0.108	0.695	-0.391	-0.652 - 0.435	12.9

Table A9 – Coefficients of Multiple Regressions for AMSR2 (n=2500), including *p*-values, *t*-values, and 95% confidence intervals (CI). Bold values indicate statistically significant results (p <0.05).

Metric	Coefficient	*p*-value	*t*-value	Confidence Interval	Percent of Total
95th Percentile SWE	0.308	0	340	0.306 - 0.309	4.1
Forest Fraction	7.05	2.67e-06	4.71	4.11 - 9.99	94
Hillslope Angle	0.0482	0.000262	3.66	0.022 - 0.074	0.642
Relief	-0.000376	0.0366	-2.09	-0.001 - -2.34e-05	0.00502
Elevation	-0.000194	2.89e-10	-6.33	0 - 0	0.00259
25th Percentile Wind	-0.0837	0.0415	-2.04	-0.164 - -0.003	1.12
90th Percentile Wind	0.0108	0.665	0.433	-0.038 - 0.06	0.144

Table A10 – Coefficients of Multiple Regressions for AMSR2, without Forest Fraction (n=2438), including *p*-values, *t*-values, and 95% confidence intervals (CI). Bold values indicate statistically significant results (p <0.05).

Metric	Coefficient	*p*-value	*t*-value	Confidence Interval	Percent of Total
95th Percentile SWE	0.308	0	338	0.306 - 0.309	66.4
Hillslope Angle	0.0488	0.000255	3.66	0.023 - 0.075	10.5
Relief	-0.000374	0.0396	-2.06	-0.001 - -1.78e-05	0.0808
Elevation	-0.000194	3.57e-10	-6.3	0 - 0	0.042
25th Percentile Wind	-0.0909	0.0278	-2.2	-0.172 - -0.01	19.6
90th Percentile Wind	0.0157	0.534	0.621	-0.034 - 0.065	3.38

Table A11 – Coefficients of Multiple Regressions for SSMI (n=2500), including p-values, t-values, and 95% confidence intervals (CI). Bold values indicate statistically significant results (p <0.05).

Metric	Coefficient	p-value	t-value	Confidence Interval	Percent of Total
95th Percentile SWE	0.301	0	127	0.296 - 0.306	3.31
Forest Fraction	7.95	0.00689	2.7	2.19 - 13.7	87.5
Hillslope Angle	0.263	7.77e-24	10.2	0.212 - 0.314	2.89
Relief	-0.00247	3.6e-12	-6.99	-0.003 - -0.002	0.0272
Elevation	-0.000646	1.65e-26	-10.8	-0.001 - -0.001	0.0071
25th Percentile Wind	-0.478	3.3e-09	-5.94	-0.635 - -0.32	5.25
90th Percentile Wind	0.0964	0.0508	1.95	0 - 0.193	1.06

Table A12 – Coefficients of Multiple Regressions for SSMI, without Forest Fraction (n=2438), including p-values, t-values, and 95% confidence intervals (CI). Bold values indicate statistically significant results (p <0.05).

Metric	Coefficient	p-value	t-value	Confidence Interval	Percent of Total
95th Percentile SWE	0.301	0	127	0.296 - 0.306	25.9
Hillslope Angle	0.266	8.95e-24	10.2	0.215 - 0.317	22.9
Relief	-0.0025	3.55e-12	-6.99	-0.003 - -0.002	0.215
Elevation	-0.000644	6.07e-26	-10.7	-0.001 - -0.001	0.0554
25th Percentile Wind	-0.491	1.64e-09	-6.05	-0.65 - -0.332	42.2
90th Percentile Wind	0.102	0.0407	2.05	0.004 - 0.2	8.78

Table A13 – Coefficients of Multiple Regressions for SSMIS (n=2500), including p-values, t-values, and 95% confidence intervals (CI). Bold values indicate statistically significant results (p <0.05).

Metric	Coefficient	p-value	t-value	Confidence Interval	Percent of Total
95th Percentile SWE	0.304	0	280	0.302 - 0.306	5.25
Forest Fraction	5.16	0.000107	3.88	2.55 - 7.76	89.1
Hillslope Angle	0.12	4.47e-24	10.2	0.097 - 0.143	2.07
Relief	-0.00107	1.87e-11	-6.75	-0.00 1- -0.001	0.0186
Elevation	-5.03e-05	0.0613	-1.87	0 - 2.38e-06	0.000869
25th Percentile Wind	-0.205	2.07e-08	-5.62	-0.277 - -0.134	3.55
90th Percentile Wind	0.00202	0.928	0.0904	-0.042 - 0.046	0.0348

Table A14 – Coefficients of Multiple Regressions for SSMIS, without Forest Fraction (n=2438), including p-values, t-values, and 95% confidence intervals (CI). Bold values indicate statistically significant results (p <0.05).

Metric	Coefficient	p-value	t-value	Confidence Interval	Percent of Total
95th Percentile SWE	0.304	0	278	0.302 - 0.306	48.2
Hillslope Angle	0.119	2.04e-23	10.1	0.096 - 0.143	19
Relief	-0.00106	6.19e-11	-6.57	-0.001 - -0.001	0.168
Elevation	-4.49e-05	0.0982	-1.65	-9.8e-05 - 8.31e-06	0.00712
25th Percentile Wind	-0.206	2.52e-08	-5.59	-0.278 - -0.134	32.7
90th Percentile Wind	-5.19e-06	1	-0.00023	-0.044 - 0.044	0.000824

Table A15 – Coefficients of Multiple Regressions for a combined product of all satellites (n=2500), including p-values, t-values, and 95% confidence intervals (CI). Bold values indicate statistically significant results ($p < 0.05$).

Metric	Coefficient	p-value	t-value	Confidence Interval	Percent of Total
95th Percentile SWE	0.303	0	56.5	0.293 - 0.314	6.99
Forest Fraction	2.91	0.867	0.167	-31.3 - 37.1	67.1
Hillslope Angle	-0.34	0.0267	-2.22	-0.641 - -0.039	7.84
Relief	0.00289	0.167	1.38	-0.001 - 0.007	0.0667
Elevation	0.00181	3.2e-07	5.13	0.001 - 0.003	0.0418
25th Percentile Wind	-0.748	0.116	-1.57	-1.68 - 0.185	17.2
90th Percentile Wind	0.0315	0.913	0.109	-0.537 - 0.6	0.727

Table A16 – Coefficients of Multiple Regressions for a combined product of all satellites, without Forest Fraction (n=2438), including p-values, t-values, and 95% confidence intervals (CI). Bold values indicate statistically significant results ($p < 0.05$).

Metric	Coefficient	p-value	t-value	Confidence Interval	Percent of Total
95th Percentile SWE	0.303	0	56.2	0.293 - 0.314	21.3
Hillslope Angle	-0.345	0.0269	-2.21	-0.65 - -0.039	24.2
Relief	0.00297	0.161	1.4	-0.001 - 0.007	0.209
Elevation	0.00182	3.93e-07	5.09	0.001 - 0.003	0.128
25th Percentile Wind	-0.745	0.121	-1.55	-1.69 - 0.197	52.3
90th Percentile Wind	0.0277	0.925	0.0941	-0.549 - 0.604	1.94

Appendix B

Appendix B - Supplementary Materials for Chapter 5

Catchment-averaged SWE Trend Characteristics

To generate the following trend statistics, we aggregate all statistically-significant ($p<0.05$) trends above 500 m asl at either the whole-HMA or individual-catchment scale. We then calculate the minimum, average, maximum, and sum of trends, and report the total contributing area for these statistics. Percentage change at each point is calculated by dividing 22-year SWE change by long-term average SWE. The mean of these pixel-wise percent changes is then reported in the Tables below.

Table B1 – Full Year catchment-aggregated SWE Trends above 500 m asl. Data applicable only for statistically significant trends.

Catchment	Min Trend (mm/yr)	Ave Trend (mm/yr)	Max Trend (mm/yr)	Trend Sum (mm/yr)	Percentage Change	Contributing Area (sq km)
All HMA	-0.020	-0.003	0.011	-10.599	-0.293%	2,641,250
Syr Darya	-0.011	-0.003	0.005	-1.507	-0.368%	364,375
Amu Darya	-0.016	-0.002	0.006	-0.459	-0.143%	163,125
Tarim	-0.020	-0.002	0.007	-1.413	-0.256%	378,750
Tibet	-0.009	-0.004	0.004	-2.874	-0.411%	473,750
Ganges	-0.016	-0.002	0.011	-0.884	-0.301%	271,250
Indus	-0.015	-0.004	0.005	-2.047	-0.342%	317,500

Table B2 – DJF catchment-aggregated SWE Trends above 500 m asl. Data applicable only for statistically significant trends.

Catchment	Min Trend (mm/yr)	Ave Trend (mm/yr)	Max Trend (mm/yr)	Trend Sum (mm/yr)	Percentage Change	Contributing Area (sq km)
All HMA	-0.147	-0.000	0.123	-1.253	-0.293%	2,201,875
Syr Darya	-0.079	0.002	0.092	0.875	-0.584%	283,750
Amu Darya	-0.108	0.013	0.064	3.003	0.235%	145,000
Tarim	-0.147	0.001	0.088	0.546	-0.120%	443,125
Tibet	-0.044	-0.005	0.068	-3.136	-0.473%	356,875
Ganges	-0.122	-0.011	0.085	-4.835	-1.163%	271,250
Indus	-0.109	-0.020	0.063	-6.238	-1.017%	195,000

Table B3 – MAM catchment-aggregated SWE Trends above 500 m asl. Data applicable only for statistically significant trends.

Catchment	Min Trend (mm/yr)	Ave Trend (mm/yr)	Max Trend (mm/yr)	Trend Sum (mm/yr)	Percentage Change	Contributing Area (sq km)
All HMA	-0.131	-0.022	0.037	-87.178	-2.332%	2,450,625
Syr Darya	-0.103	-0.040	-0.008	-21.488	-4.106%	336,875
Amu Darya	-0.114	-0.018	0.037	-3.247	-1.412%	111,250
Tarim	-0.119	-0.021	0.028	-11.417	-2.482%	337,500
Tibet	-0.045	-0.018	0.011	-13.730	-1.821%	470,625
Ganges	-0.131	-0.025	0.034	-10.037	-2.582%	253,125
Indus	-0.086	-0.019	0.030	-8.269	-1.385%	275,000

Table B4 – JJA catchment-aggregated SWE Trends above 500 m asl. Data applicable only for statistically significant trends.

Catchment	Min Trend (mm/yr)	Ave Trend (mm/yr)	Max Trend (mm/yr)	Trend Sum (mm/yr)	Percentage Change	Contributing Area (sq km)
All HMA	-0.094	-0.032	0.025	-36.789	-6.497%	719,375
Syr Darya	-0.046	-0.028	-0.013	-0.532	-7.623%	11,875
Amu Darya	-0.057	-0.023	0.025	-3.537	-3.689%	94,375
Tarim	-0.081	-0.030	-0.006	-6.680	-5.256%	138,125
Tibet	-0.063	-0.032	-0.006	-10.018	-8.593%	193,125
Ganges	-0.046	-0.023	0.008	-1.711	-5.832%	45,625
Indus	-0.094	-0.041	-0.006	-12.154	-6.576%	183,125

Table B5 – SON catchment-aggregated SWE Trends above 500 m asl. Data applicable only for statistically significant trends.

Catchment	Min Trend (mm/yr)	Ave Trend (mm/yr)	Max Trend (mm/yr)	Trend Sum (mm/yr)	Percentage Change	Contributing Area (sq km)
All HMA	-0.059	-0.009	0.057	-28.698	-1.328%	1,960,625
Syr Darya	-0.023	-0.009	0.013	-1.641	-2.233%	116,875
Amu Darya	-0.048	-0.014	0.014	-2.982	-2.118%	128,750
Tarim	-0.038	-0.009	0.023	-3.926	-1.469%	262,500
Tibet	-0.041	-0.016	0.028	-11.765	-1.723%	447,500
Ganges	-0.045	0.001	0.057	0.206	-0.197%	208,750
Indus	-0.059	-0.011	0.045	-3.759	-1.590%	222,500

By-Catchment Seasonal Trends

All data reported in the Figures in this Section is drawn from statistically significant yearly or seasonal trends ($p<0.05$).

Syr Darya Seasonal Trends

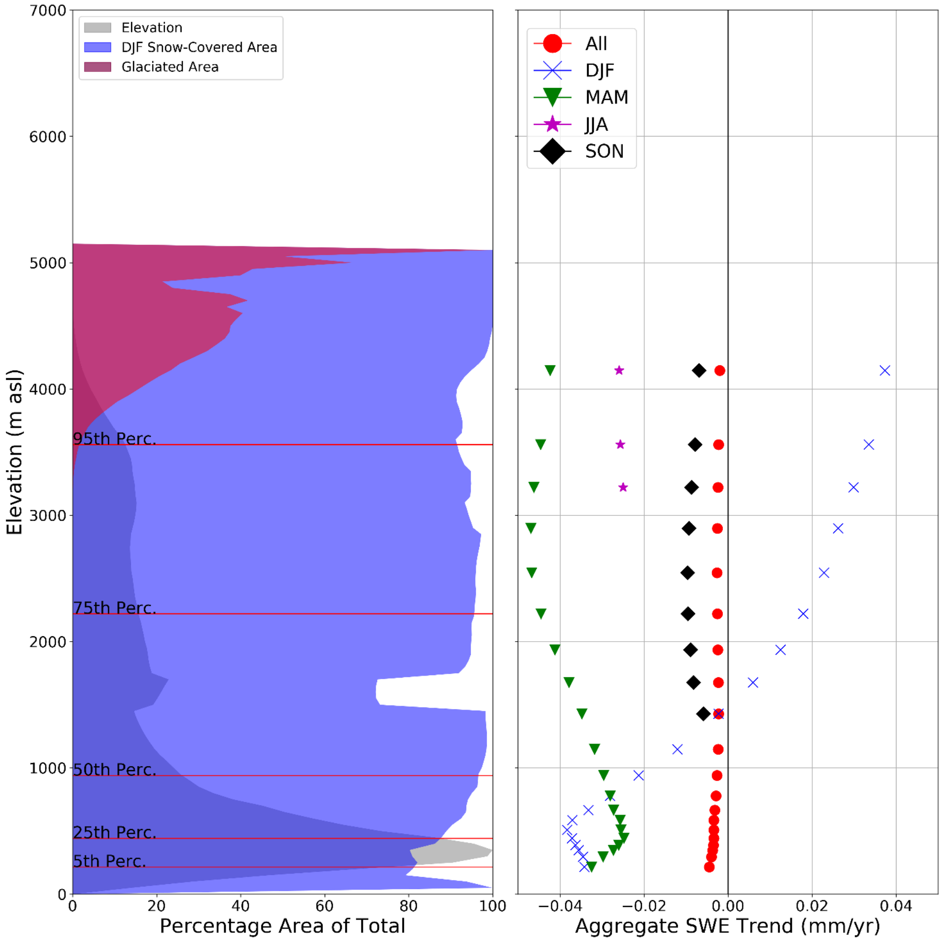

Figure B1 – (A) Catchment hypsometry (grey), percentage glaciated area (red), and percentage DJF snow covered area (blue). Red lines indicate catchment elevation percentiles. (B) Seasonal and yearly SWE trends by 5th percentile elevation slice, between the 5th and 99.5th percentiles.

Amu Darya Seasonal Trends

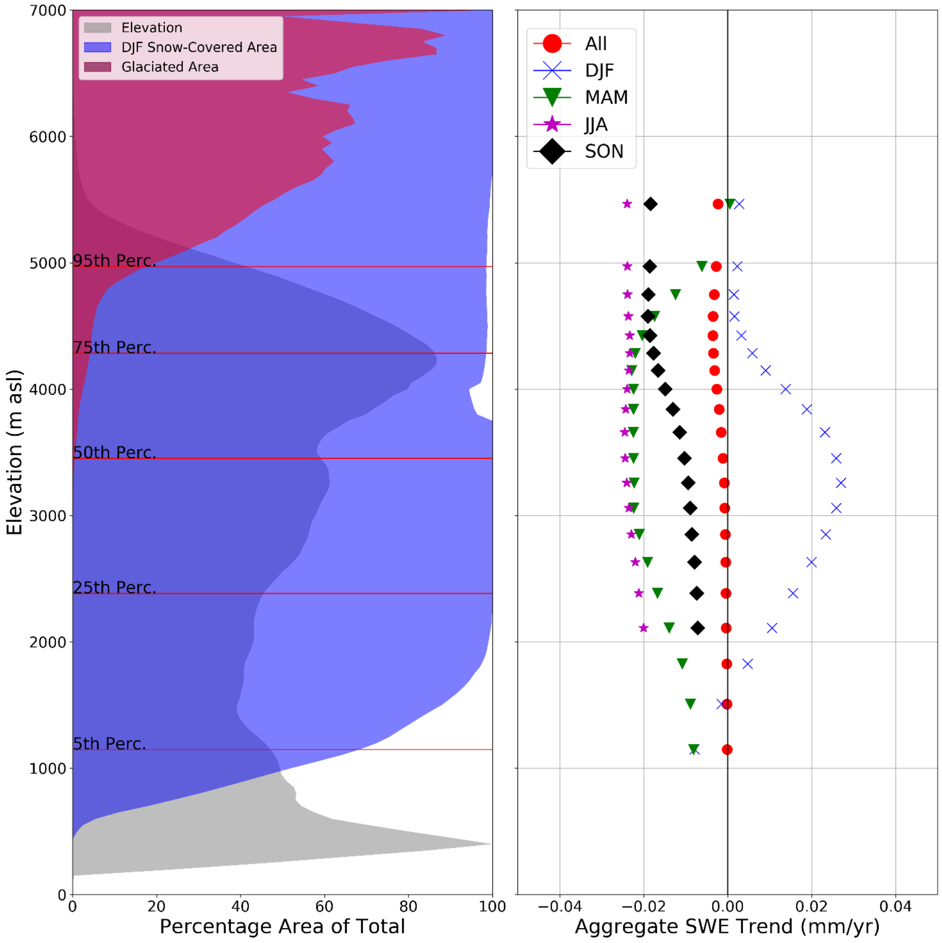

Figure B2 – (A) Catchment hypsometry (grey), percentage glaciated area (red), and percentage DJF snow covered area (blue). Red lines indicate catchment elevation percentiles. (B) Seasonal and yearly SWE trends by 5th percentile elevation slice, between the 5th and 99.5th percentiles.

Tarim Seasonal Trends

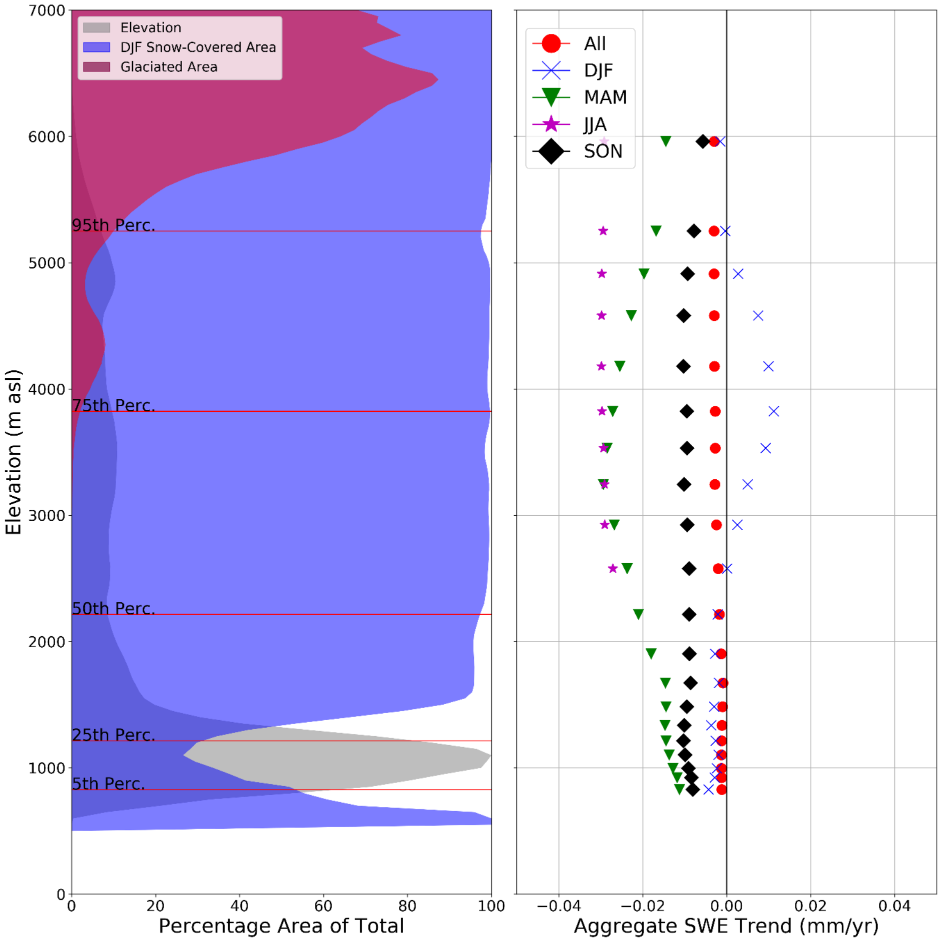

Figure B3 – (A) Catchment hypsometry (grey), percentage glaciated area (red), and percentage DJF snow covered area (blue). Red lines indicate catchment elevation percentiles. (B) Seasonal and yearly SWE trends by 5th percentile elevation slice, between the 5th and 99.5th percentiles.

Tibetan Plateau Seasonal Trends

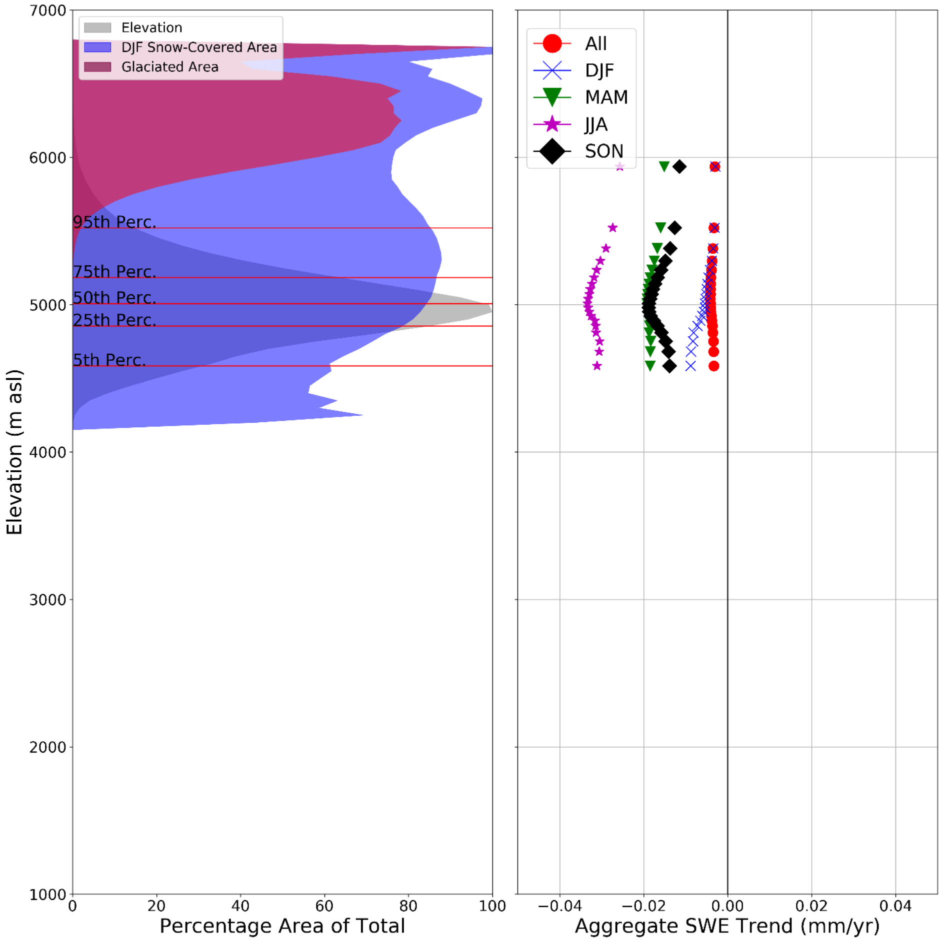

Figure B4 – (A) Catchment hypsometry (grey), percentage glaciated area (red), and percentage DJF snow covered area (blue). Red lines indicate catchment elevation percentiles. (B) Seasonal and yearly SWE trends by 5th percentile elevation slice, between the 5th and 99.5th percentiles.

Ganges Seasonal Trends

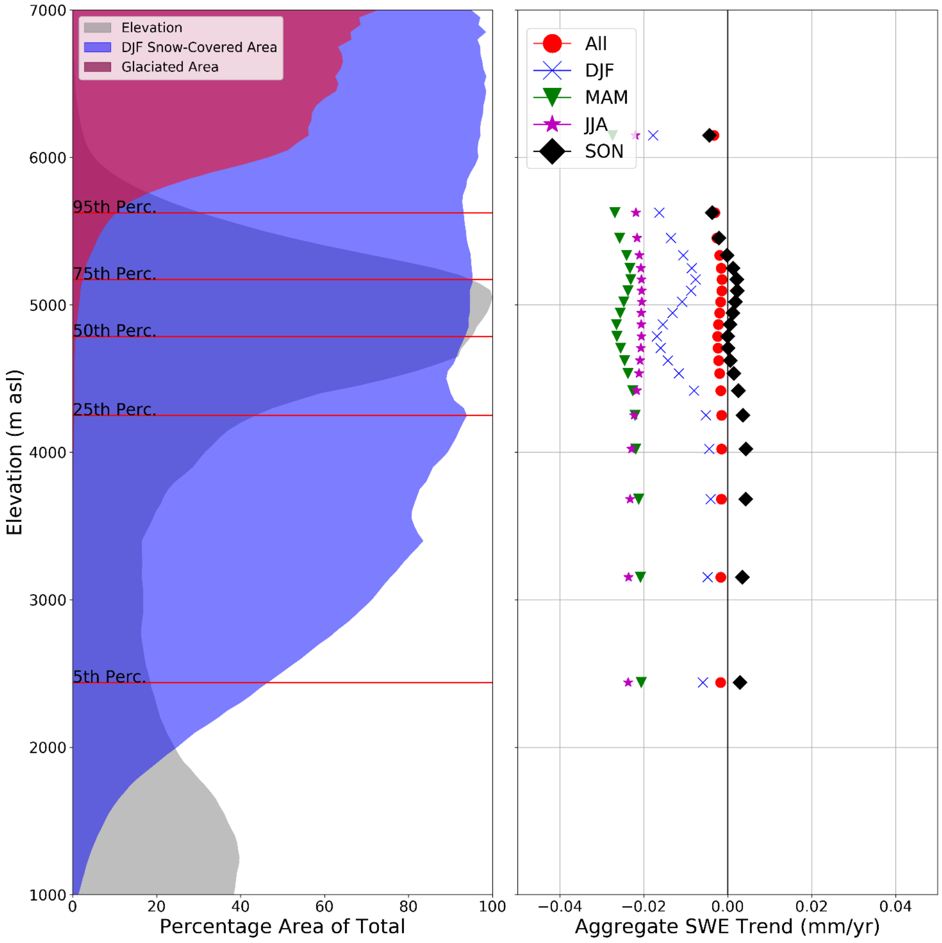

Figure B5 – (A) Catchment hypsometry (grey), percentage glaciated area (red), and percentage DJF snow covered area (blue). Red lines indicate catchment elevation percentiles. (B) Seasonal and yearly SWE trends by 5th percentile elevation slice, between the 5th and 99.5th percentiles.

Indus Seasonal Trends

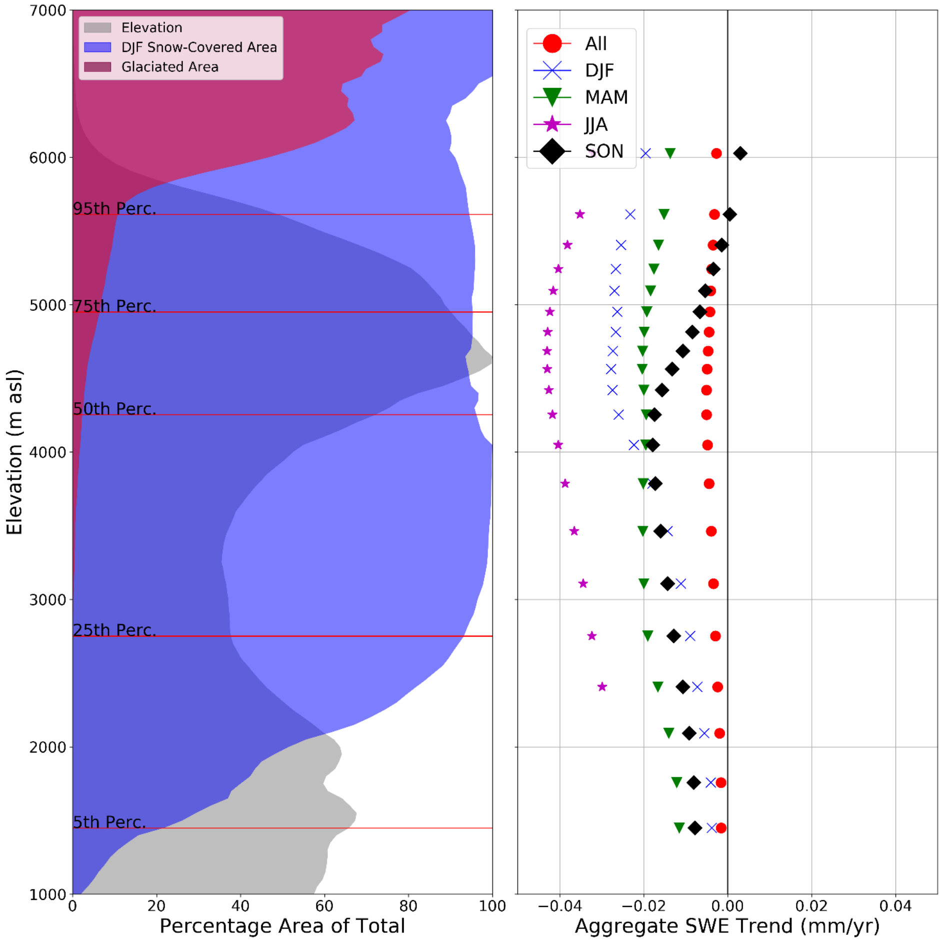

Figure B6 – (A) Catchment hypsometry (grey), percentage glaciated area (red), and percentage DJF snow covered area (blue). Red lines indicate catchment elevation percentiles. (B) Seasonal and yearly SWE trends by 5th percentile elevation slice, between the 5th and 99.5th percentiles.

Seasonal Trend Decomposition Coefficients

The code below describes the fitting parameters as implemented in this study, using the pyloess module (https://github.com/lucidfrontier45/pyloess), modeled after the results of (Cleveland et al., 1990).

```python
from pyloess import stl

def nt_calc(f,ns):
  '''Calcualte the length of the trend smoother based on Cleveland et al., 1990'''
  nt = (1.5*f)/(1-1.5*(1/ns)) + 1 #Force fractions to be rounded up
  if int(nt) % 2. == 1:
    return int(nt)
  elif int(nt) % 2. == 0:
    return int(nt) + 1

def nl_calc(f):
  '''Calcualte the length of the low-pass filter based on Cleveland et al., 1990'''
  if int(f) % 2. == 1:
    return int(f)
  elif int(f) % 2. == 0:
    return int(f) + 1

#f here is the period of the seasonal component (365 for yearly, ~90 for seasonal)

##### From pyloess.py, line ~480, and Cleveland et al. (1990)
#np = f             # period of seasonal component
ns = 7              # length of seasonal smoother
nt = nt_calc(f,ns)  # length of trend smoother
nl = nl_calc(f)     # length of low-pass filter
isdeg = 1           # Degree of locally-fitted polynomial in seasonal smoothing.
itdeg = 1           # Degree of locally-fitted polynomial in trend smoothing.
ildeg = 1           # Degree of locally-fitted polynomial in low-pass smoothing.
nsjump = None       # Skipping value for seasonal smoothing.
ntjump = 1          # Skipping value for trend smoothing. If None, ntjump= 0.1*nt
nljump = 1          # Skipping value for low-pass smoothing. If None, nljump= 0.1*nl
robust = True       # Flag indicating whether robust fitting should be performed.
ni = 1              # Number of loops for updating the seasonal and trend  components.
no = 3              # Number of iterations of robust fitting. The value of no should
          #be a nonnegative integer. If the data are well behaved without
          #outliers, then robustness iterations are not needed. In this case
          #set no=0, and set ni=2 to 5 depending on how much security
          #you want that  the seasonal-trend looping converges.
          #If outliers are present then no=3 is a very secure value unless
          #the outliers are radical, in which case no=5 or even 10 might
          #be better.  If no>0 then set ni to 1 or 2.
          #If None, then no is set to 15 for robust fitting, to 0 otherwise.

result = stl(timeseries, f, ns, nt, nl, isdeg, itdeg, ildeg, nsjump, ntjump, nljump, robust, ni,
    no)
```

Impact of Glaciers on Trend Patterns

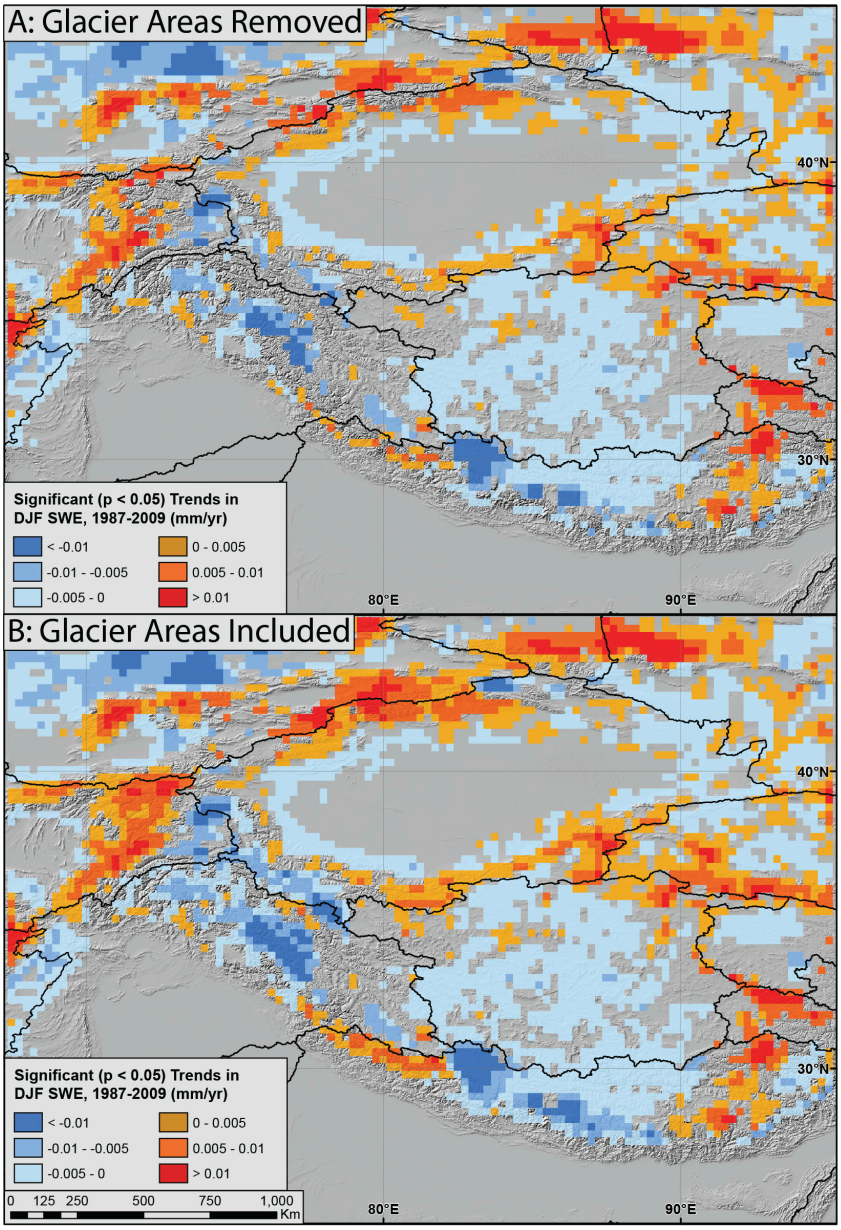

Figure B7 – DJF SWE trends with (A) glaciated areas (RGI V5, *(68)*) removed and (B) with glaciated areas maintained. We remove any pixel that contains more than 25% glacier cover for this analysis. While many pixels are removed, the large-scale spatial trends in the data are maintained, indicating that uncertainty over glaciers, while potentially important, does not strongly impact the spatial pattern of SWE trends.

Impacts of Measurement Uncertainty on Trend Values

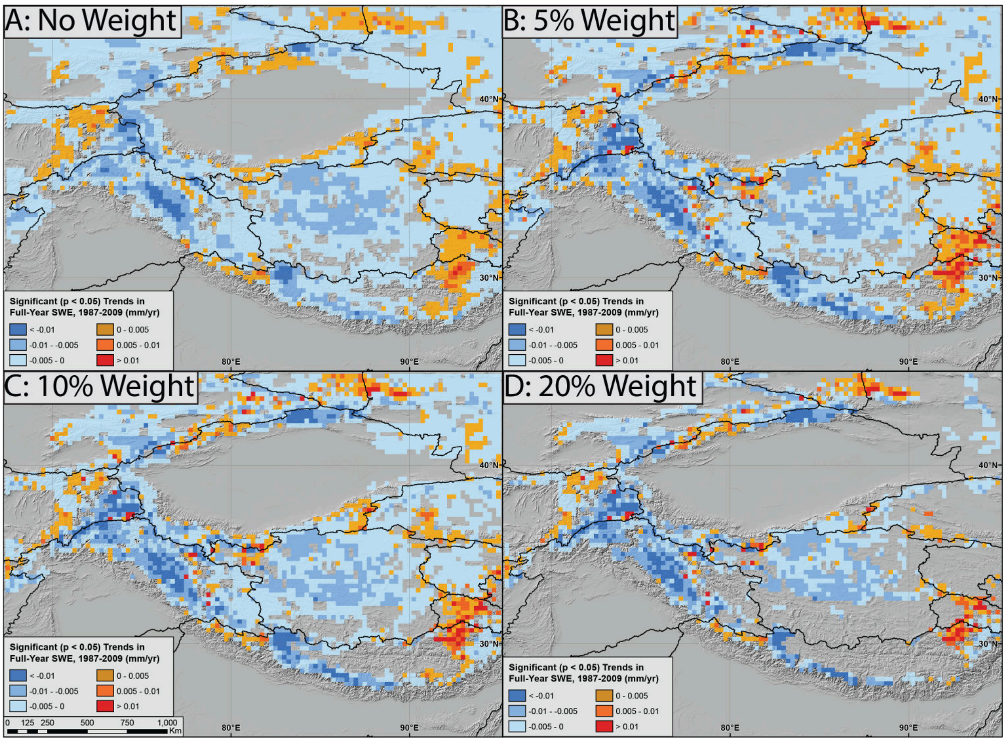

Figure B8 – Full-year SWE trends using (A) a simple linear model or (B) 5%, (C) 10%, and (D) 20% uncertainty weights based on SWE amount. While the large-scale patterns of SWE trends remain consistent, increasing uncertainty modifies the relative strength of the trends throughout the study area, and decreases the number of statistically significant trends.

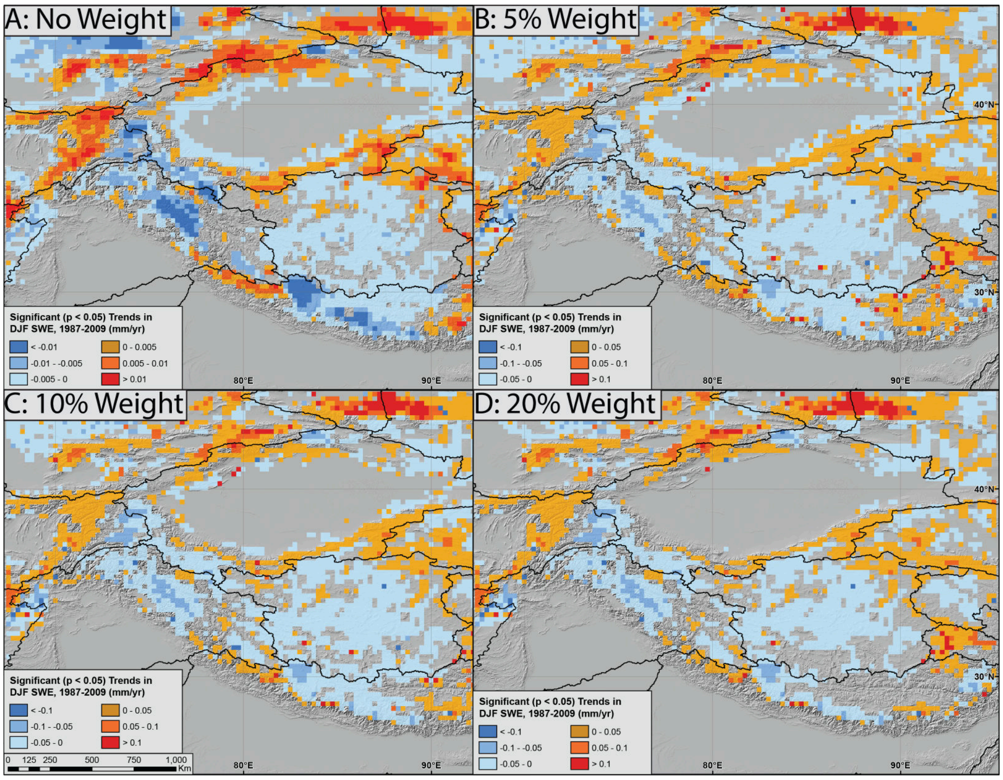

Figure B9 – DJF SWE trends using (A) a simple linear model or (B) 5%, (C) 10%, and (D) 20% uncertainty weights based on SWE amount. While the large-scale patterns of SWE trends remain consistent, increasing uncertainty modifies the relative strength of the trends throughout the study area, and decreases the number of statistically significant trends. In particular, the weighted regressions have larger trends by a factor of 2 as opposed to the simple linear trend in DJF data.

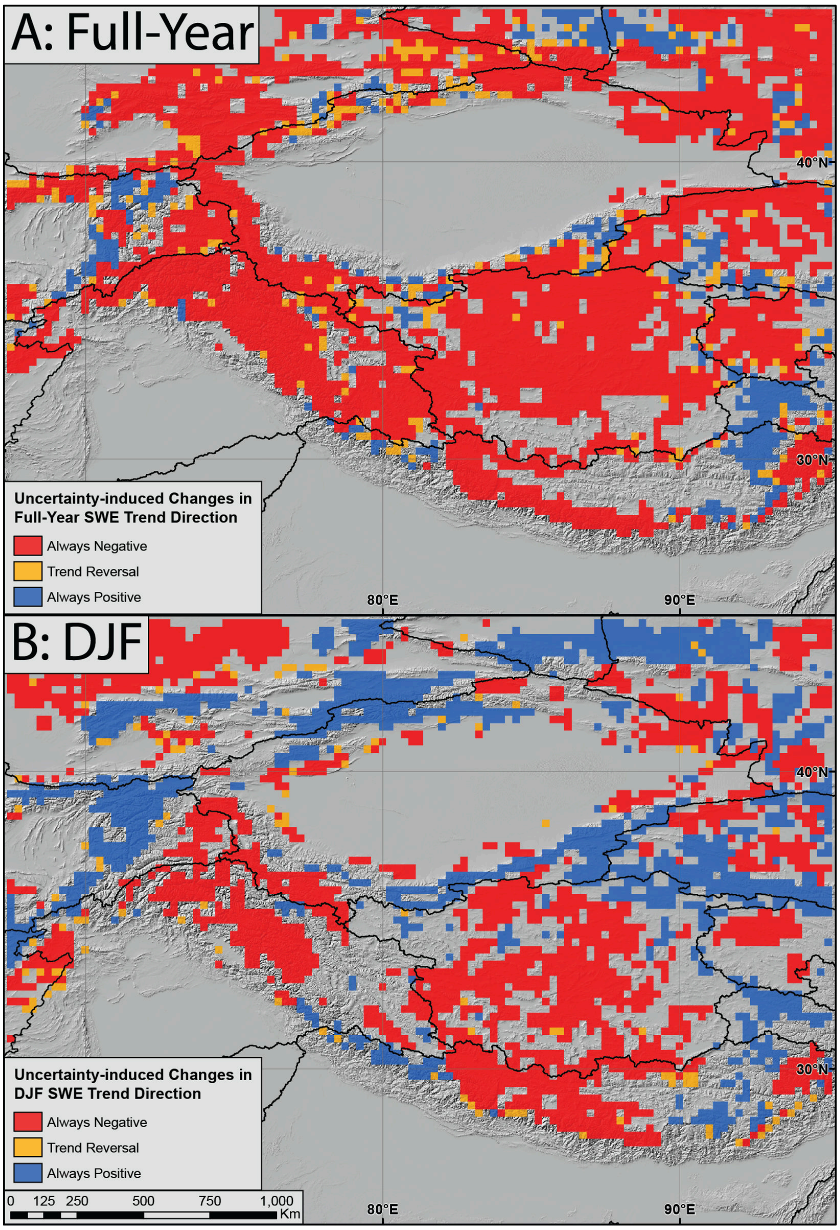

Figure B10 – Changes in (A) full-year and (B) DJF SWE trends when a 10% uncertainty margin is introduced (cf. Figs. S09-S10). While some areas change their trend direction (from negative to positive or positive to negative), the vast majority of points maintain the same trend direction in both cases. While the *magnitudes* of the trends may change between the regressions, the *direction* and *spatial distribution* of trends remains consistent.

By Catchment Average SWE (1987-2009)

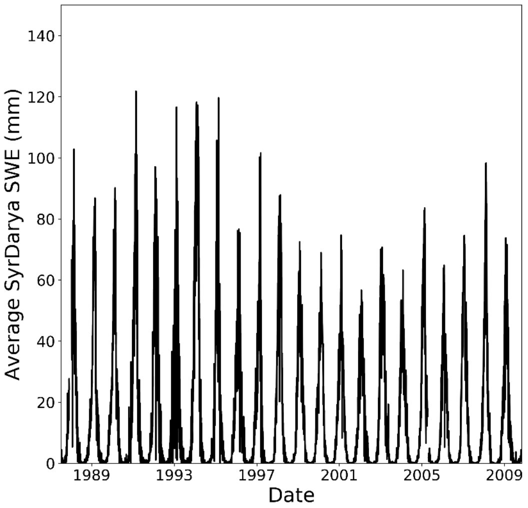

Figure B11 – Syr Darya catchment-averaged SWE (1987-2009).

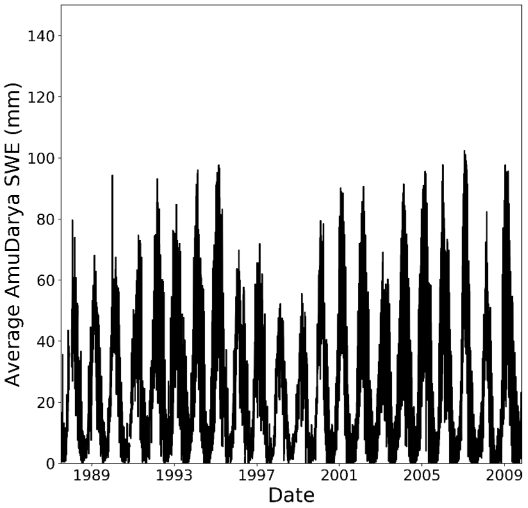

Figure B12 – Amu Darya catchment-averaged SWE (1987-2009).

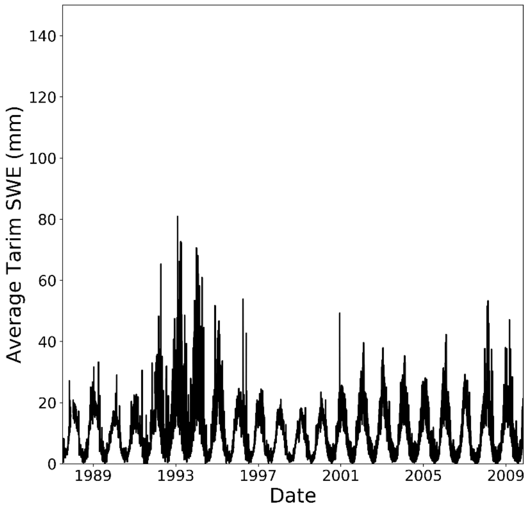

Figure B13 – Tarim catchment-averaged SWE (1987-2009).

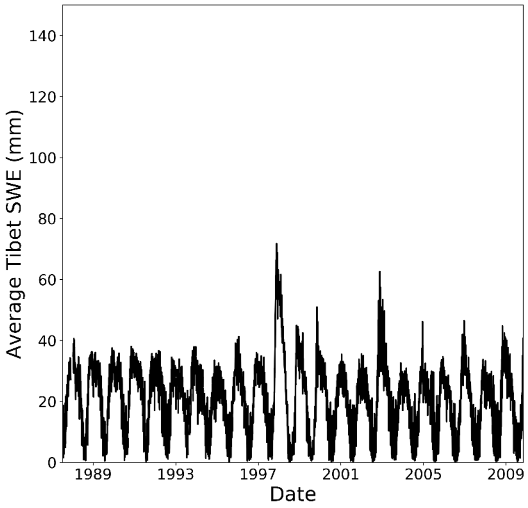

Figure B14 – Tibetan Plateau catchment-averaged SWE (1987-2009).

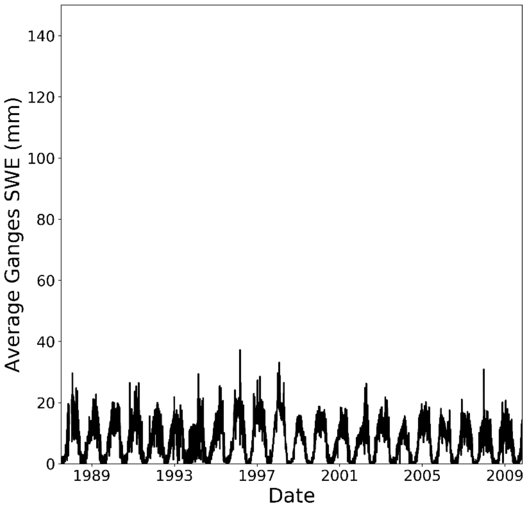

Figure B15 – Ganges catchment-averaged SWE (1987-2009).

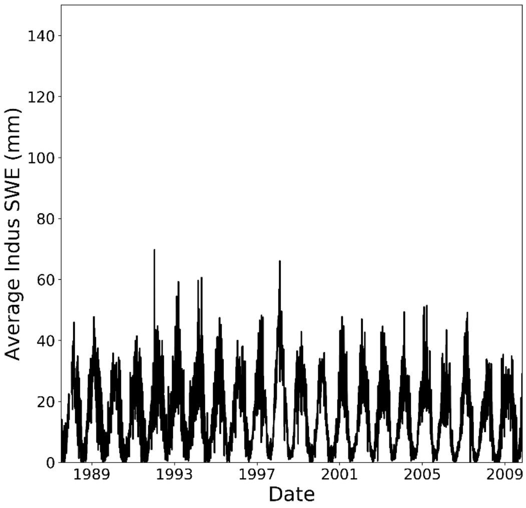

Figure B16 – Indus catchment-averaged SWE (1987-2009).

Appendix C

Appendix C - Supplementary Materials for Chapter 6

Properties of Passive Microwave Sensors

Table C1 – Characteristics of PM sensors. Temporal coverage, number of orbits, and processing algorithms.

Satellite	Temporal Coverage	Number of Orbits Used (Descending/Ascending)	Processing Level/Algorithm
SSMI (Wentz, 2013)	Aug 1987 - Apr 2009 (22 years)	176,460/176,460	FCDR V07
SSMI/S (Sun and Weng, 2008)	Jan 2008 - Apr 2015 (7 years)	41,896/41,896	FCDR V07
AMSR-E (Ashcroft and Wentz, 2013)	May 2002 - Oct 2011 (9 years)	49,083/49,079	L1B
AMSR2 (Imaoka et al., 2010)	Jul 2012 - Oct 2016 (4 years)	28,510/28,506	L1R
GPM (GPM Science Team, 2014)	Feb 2014 - Oct 2016 (2.5 years)	7,359/7,359	L1B

Flowchart of Melt Tracking Algorithm

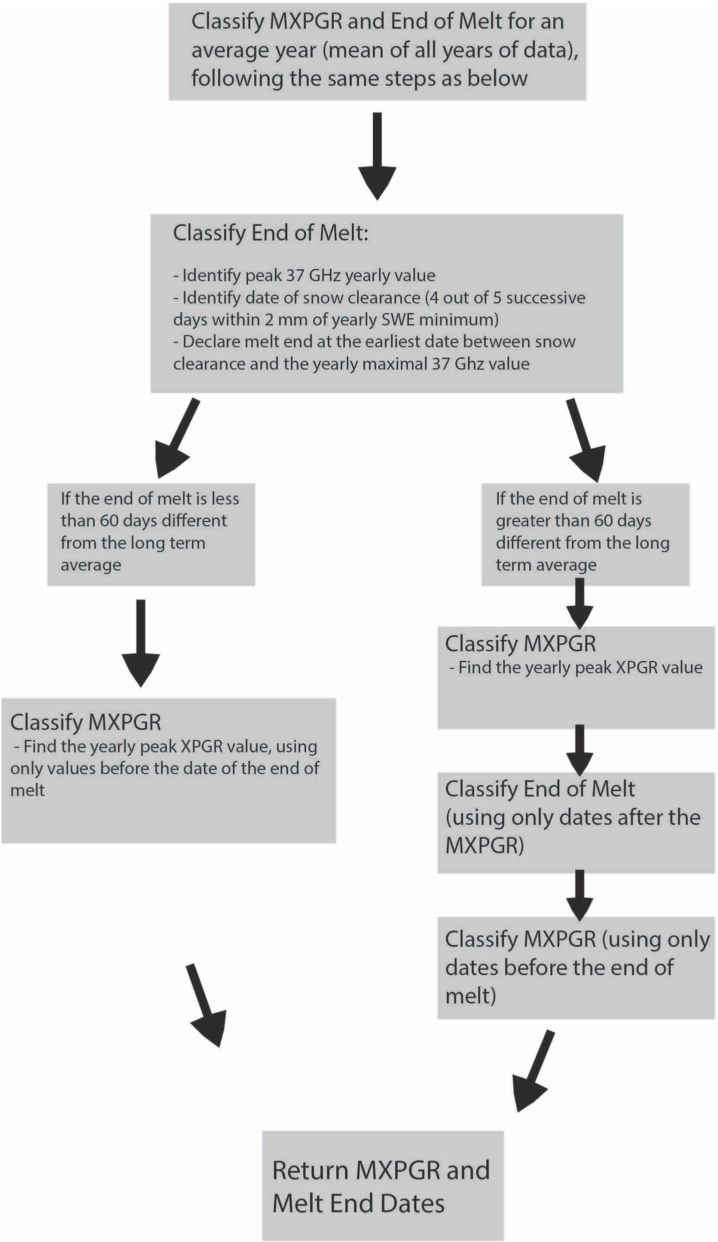

Figure C1 – Flowchart illustrating the steps for the melt tracking algorithm. A full description of the algorithm implementation is maintained on Github: https://github.com/UP-RS-ESP/SnowmeltTracking.

Algorithm Theoretical Considerations

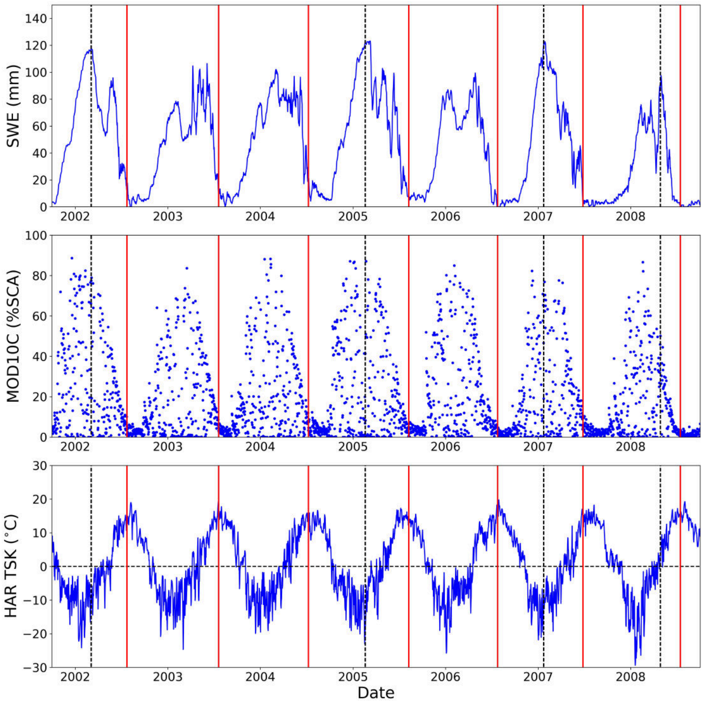

Figure C2 – (A) SWE, (B) MOD10C1 fractional snow-covered area, and (C) HAR daily average temperature. Melt dates in red, with MXPGR as dashed lines and snowmelt end as solid lines. Some years do not have a defined MXPGR date due to complex yearly SWE distributions. MXPGR dates generally correlate with the maximum MODIS snow-covered area and the point where the yearly temperature curve minimizes. End dates correlate well with MODIS snow clearance. Data taken from 71.25E, 36.75N.

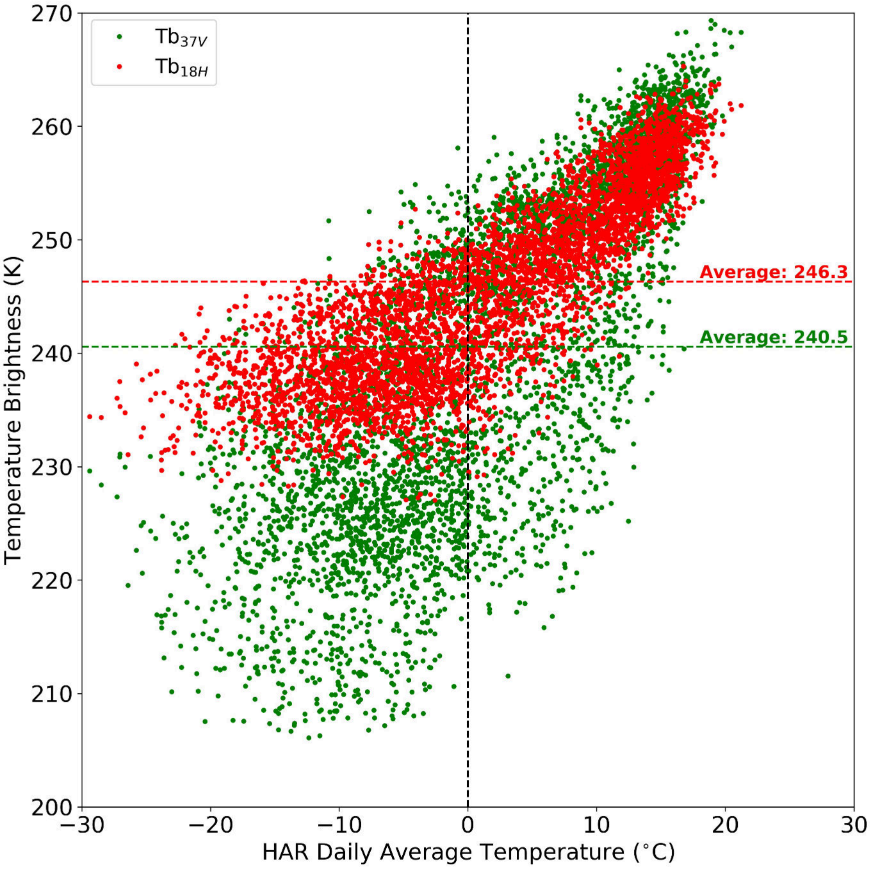

Figure C3 – HAR Average daily temperature vs Temperature Brightness (37V in green, 18H in red, 2000-2014). Both channels show correlations with air temperature, but show a wide spread. This observation indicates that there is no single Temperature Brightness threshold that can be used for snowmelt detection. Data taken from 71.25E, 36.75N.

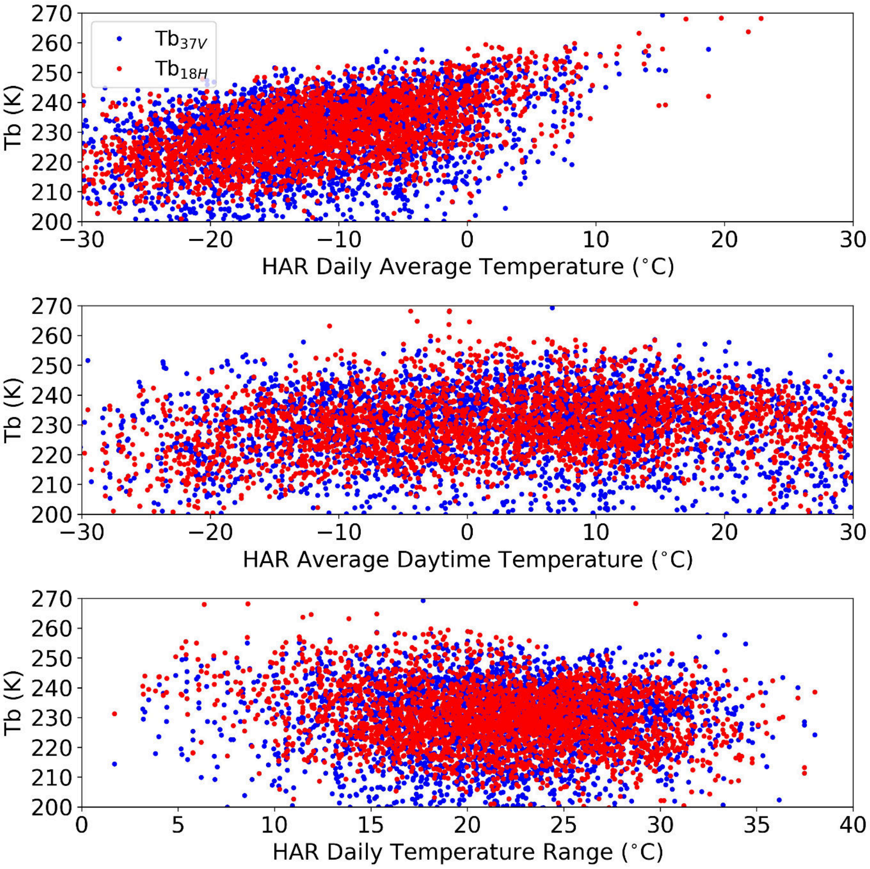

Figure C4 – HAR temperature metrics vs Tb at MXPGR. Both 37V (blue) and 18H (red) channels show significant spread. While there is a slight correlation between average daily temperature and Tb, average daytime temperature is very poorly related to Tb. This implies that the night-time passive microwave data used to identify MXPGR still captures the impacts of above-zero daytime temperatures. Data taken from 71.25E, 36.75N.

Standard Deviation in Snowmelt Period

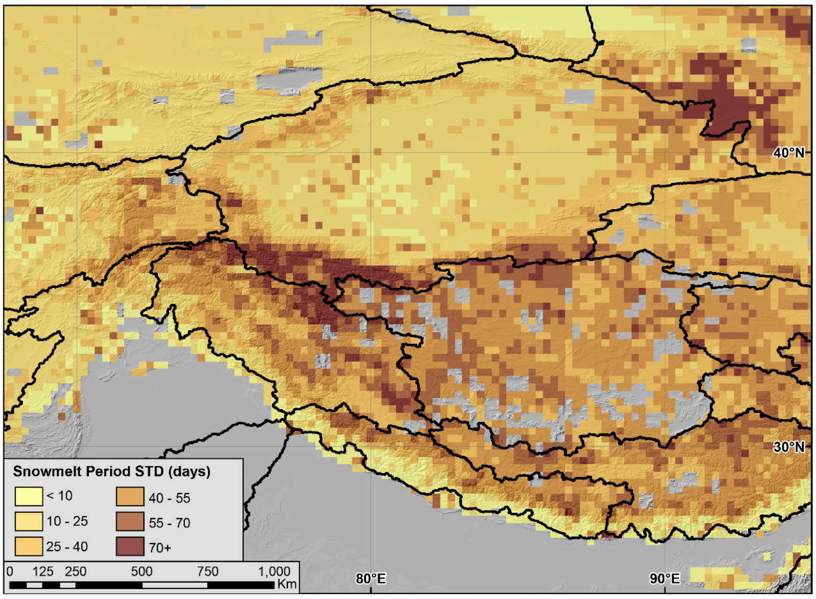

Figure C5 – Standard deviation in snowmelt period, showing higher snowmelt period variance at high elevations and in the orogen interior.

Linear Matching Regression Parameters

Table C2 – Linear matching parameters and statistics - SSMI to AMSR.

SSMI-AMSR			
37V	intercept	Mean	-19.63360131
		STD	35.83495628
		Range	1081.194363
37V	slope	Mean	1.080532984
		STD	0.144976002
		Range	4.12275082
37V	pval	Mean	5.61E-08
		STD	4.82E-06
		Range	0.000413347
37V	tval	Mean	208.7706349
		STD	75.80889139
		Range	476.9591168
18H	intercept	Mean	-21.99749485
		STD	39.91555202
		Range	1140.206255
18H	slope	Mean	1.095758046
		STD	0.164415637
		Range	4.199488203
18H	pval	Mean	1.30E-05
		STD	0.000790001
		Range	0.052541412
18H	tval	Mean	179.2705257
		STD	76.37323937
		Range	435.2829973

Table C3 – Linear matching parameters and statistics - SSMI to SSMIS.

SSMI-SSMIS			
37V	intercept	Mean	-11.82749674
		STD	26.99365273
		Range	1003.134398
37V	slope	Mean	1.046288015
		STD	0.112876411
		Range	4.118598352
37V	pval	Mean	6.75E-15
		STD	5.79E-13
		Range	4.97E-11
37V	tval	Mean	144.7377425
		STD	69.50580512
		Range	393.2536574
18H	intercept	Mean	-22.01065617
		STD	25.4825934
		Range	1003.973949
18H	slope	Mean	1.117712032
		STD	0.115147016
		Range	3.822440322
18H	pval	Mean	0.000122152
		STD	0.010421198
		Range	0.894333768
18H	tval	Mean	138.697067
		STD	74.55722512
		Range	396.2607783

Table C4 – Linear matching parameters and statistics - SSMIS to AMSR2.

SSMIS-AMSR2			
37V	intercept	Mean	-27.90708304
		STD	41.87667407
		Range	995.3410873
37V	slope	Mean	1.113591021
		STD	0.167733559
		Range	3.989960318
37V	pval	Mean	2.24E-17
		STD	1.92E-15
		Range	1.65E-13
37V	tval	Mean	166.7653894
		STD	62.51960823
		Range	398.7550507
18H	intercept	Mean	-32.35079224
		STD	45.3924612
		Range	1048.955192
18H	slope	Mean	1.134449236
		STD	0.188178861
		Range	3.882513428
18H	pval	Mean	3.07E-05
		STD	0.001843432
		Range	0.128179745
18H	tval	Mean	140.8474188
		STD	63.12218532
		Range	459.9962559

Table C5 – Linear matching parameters and statistics - AMSR2 to GPM.

AMSR2-GPM			
37V	intercept	Mean	-4.109791938
		STD	35.93862943
		Range	936.9121798
37V	slope	Mean	1.020145353
		STD	0.144607908
		Range	3.781385974
37V	pval	Mean	2.72E-19
		STD	2.19E-17
		Range	1.87E-15
37V	tval	Mean	79.40991596
		STD	27.93838517
		Range	193.4060824
18H	intercept	Mean	-3.172099946
		STD	41.4648854
		Range	989.3588298
18H	slope	Mean	0.99499014
		STD	0.166546112
		Range	3.592560572
18H	pval	Mean	3.14E-29
		STD	2.69E-27
		Range	2.31E-25
18H	tval	Mean	73.89142489
		STD	29.09024642
		Range	263.9399874

Hierarchical Clustering Metrics

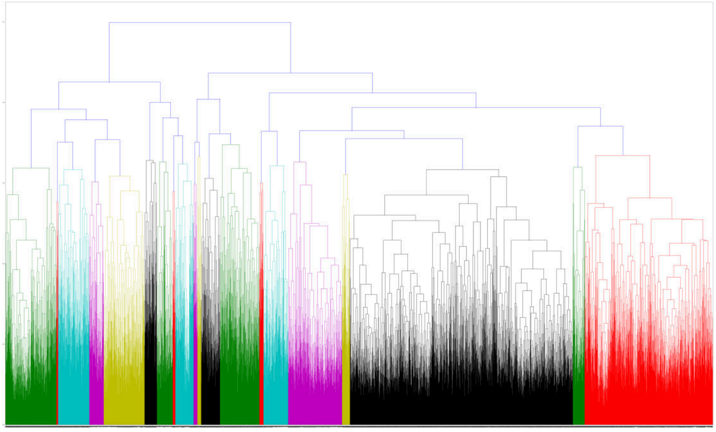

Figure C6 – Hierarchical clustering dendrogram. Clustering performed over Gaussian normalized XPGR values for the entire length of the study period. Methods described in detail in the Manuscript.

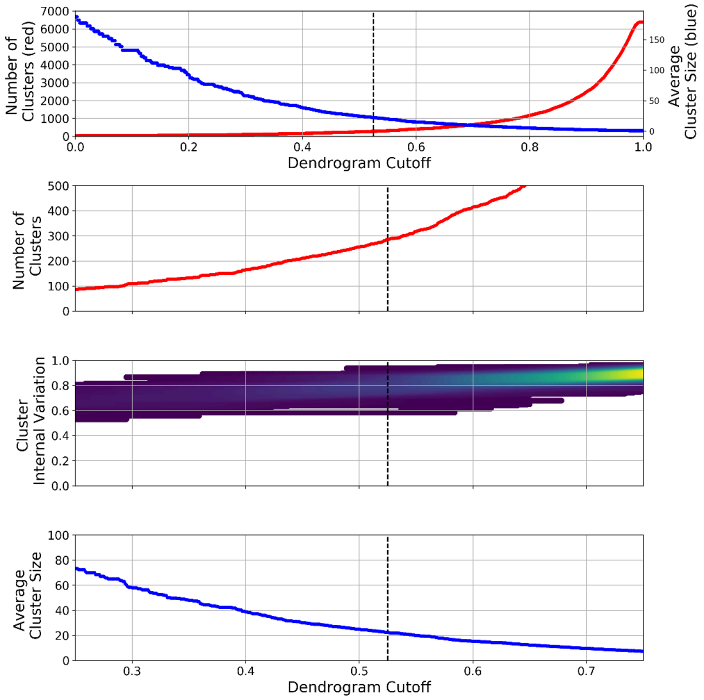

Figure C7 – Metrics used to choose the hierarchical clustering distance threshold. Chosen threshold shown on each chart in black.

Impact of Analysis Timeframe

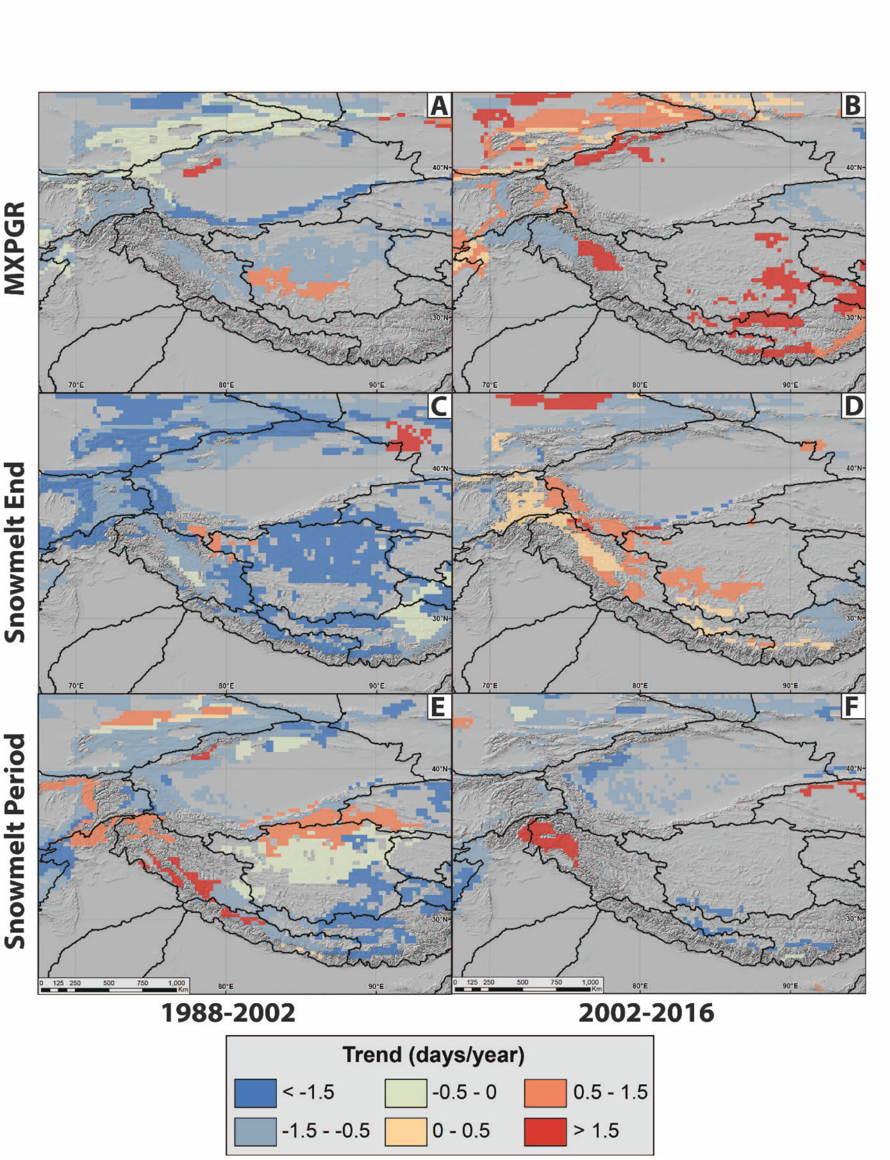

Figure C8 – Impact of analysis timeframe on (A, B) MXPGR, (C,D) snowmelt end, and (E,F) snowmelt period. The MXPGR and snowmelt end dates show a reversal of trend in many regions, from negative to positive.

Appendix D

Appendix D - Abstract of van der Veen et al. (in review)

Anthropogenic climate change has led to changes in seasonal and annual water storage and meltwater amounts. Increased rates of glacial and snowmelt not only increase river discharge and flood potential, but also the temporal heterogeneity in river discharge; areas downstream of rivers draining high mountain ranges are particularly vulnerable to changes in upstream hydrology. However, it, remains difficult to attribute changes in surface runoff to changes in a particular source. Here we present a stable isotope study of surface waters in the western Himalaya in northwest India, aimed to improve understanding of seasonal water sources and its climatological drivers. We present a new surface water δ^2H, δ^{18}O, and d-excess dataset containing 135 samples from three separate river catchments (Sutlej, Beas and Alaknanda Rivers) covering an altitudinal gradient from 457 to 4,417 m asl elevation. Additionally, two separate yearlong isotope datasets with a weekly sampling interval were obtained (at Tabo in the Spiti/Sutlej catchment at 3,285 m asl with 36 samples and at Manali in the Beas catchment at 1,900 m asl with 41 samples).

We find that δ^2H values of stream waters sampled in the post-monsoon season (September) in both the Sutlej and Alaknanda elevation transects show a significant negative correlation with mean catchment elevation. Both the lower Sutlej (<4,000 m asl) and Alaknanda showed a lapse rate of -8.8‰km^{-1}, while the high elevation Spiti/Sutlej has a significantly higher lapse rate (-32.7‰km^{-1}). Rayleigh distillation processes caused by orographic uplift of Indian Summer Monsoonal (ISM) moisture mainly drive the lapse rate in the lower Sutlej and Alaknanda. Deviations from the Rayleigh process predicted values in the upper part of the catchments are interpreted to reflect higher input of winter westerly-derived precipitation and snow and glacial meltwater input affected by post-depositional processes such as sublimation.

In the seasonal time series of surface waters at 2 locations a 6-25% increase in d-excess during the peak snowmelt season (March – June) was observed, coinciding with a decrease in remote- sensing derived snow cover from >90% in winter to <30% in summer, indicating a substantial input of snow and ice melt into the surface waters of high-elevation catchments in spring. These results suggest that snowmelt in high elevation catchments can significantly alter the surface water isotopic content, and can be used as a tracer for snow and ice melt waters.

Our modern results show that a stable-isotope monitoring system in combination with a remote sensing data approach can be used to understand seasonal variability in water-source contribution in these remote areas. More specifically, in the scope of global climate change, the timing and duration of snow- and glacier melt could be monitored using d-excess values in surface waters, and contribute to a hydrological budget in high- elevation Himalayan river catchments.

Declaration

This work has not been submitted to any other institution of higher education, and was prepared independently by Taylor Smith.

Potsdam, September 25, 2017
Taylor Smith